# Measurement of the Z boson pair-production cross section in proton-proton collisions at 7 and 8 TeV, and ECAL timing studies for the phase-2 upgrade of the CMS experiment

Luca Pernié

Université Libre de Bruxelles

Università degli studi La Sapienza

A thesis submitted for the degree of

*Doctor of Physics*

17 September 2015

Come sarebbe bello dire *per caso*? .. "
Tu credi davvero che ci sia qualcosa che succede *per caso*?
(A. B.)

La vida es un asunto de oportunidades.
(A. R.)

# Abstract

A measurement of the $Z$ boson pair production cross section using proton-proton collisions at 7 and 8 TeV center-of-mass energy, recorded by the CMS experiment, is presented. The $ZZ$ production cross section is measured via the decay channel $ZZ \rightarrow 2l2\nu$. The data used for the analysis have been recorded in years 2011 and 2012 by CMS and correspond to an integrated luminosity of about 5.1 fb$^{-1}$ at 7 TeV and 19.6 fb$^{-1}$ at 8 TeV. We measure $\sigma(\mathrm{pp} \rightarrow ZZ) = 5.1\,^{+1.5}_{-1.4}\,(\mathrm{stat})\,^{+1.4}_{-1.1}\,(\mathrm{syst}) \pm 0.1\,(\mathrm{lumi})$ pb at 7 TeV, and $7.2\,^{+0.8}_{-0.8}\,(\mathrm{stat})\,^{+1.9}_{-1.5}\,(\mathrm{syst}) \pm 0.2\,(\mathrm{lumi})$ pb at 8 TeV, in good agreement with the SM next-to-leading-order predictions. The selected data were also analyzed to search for anomalous triple gauge couplings (aTGC) involving the ZZ final state, and subsequently combined with the $ZZ \rightarrow 2l2l'$ final state data, in order to increase the sensitivity. In the absence of signs of new physics we set limits on the relevant aTGC parameters.

The last part of the thesis discusses the possible use of timing to mitigate the pileup contribution in object reconstruction, in the contest of the High Luminosity phase of LHC. Timing is included in different reconstruction algorithms, proving that a time resolution of about 30 ps could allow to reconstruct the $z$ position of the hard vertex with a O(cm) resolution, and to reject jets coming from pileup interactions with a rejection factor of about three.

# Résumé

Le Large Hadron Collider (LHC) marque une nouvelle ère dans la physique des particules. Grâce aux collisions proton-proton à haute énergie, et à la grande quantité de données recueillies au cours des années 2010-12, les physiciens du CERN peuvent tester le modèle standard (SM) de la physique des particules, explorer le secteur scalaire, et rechercher des indices de la présence d'une nouvelle physique.

Une mesure de la section efficace de production de paires de bosons $Z$ est obtenue dans les collisions proton-proton enregistrées par le détecteur CMS (Compact Muon Solenoid) à une énergie de 7 et 8 TeV dans le centre de masse. La production de paires de bosons au LHC est d'un intérêt particulier pour les raisons suivantes: elle permet d'étudier pour la première fois des processus rares du SM avec précision, de tester l'auto-interaction des bosons électro-faibles, et d'étudier des processus qui représentent des bruits de fond pour de nombreuses autres recherches, telles que la recherche du boson scalaire ou la recherche de particules supersymétriques.

La section efficace de la production de paires de bosons $Z$ est mesurée à travers le canal de désintégration $ZZ \to 2l2\nu$. Les données utilisées pour l'analyse ont été enregistrées dans les années 2011 et 2012, et correspondent à une luminosité intégrée d'environ 5.1 $\mathrm{fb}^{-1}$ à 7 TeV et 19.6 $\mathrm{fb}^{-1}$ à 8 TeV. Les données sont sélectionnées en exigeant la présence de deux leptons isolés (électrons ou muons) de même saveur et avec une grande impulsion transverse ($p_T$). En outre, les événements qui contiennent des jets de hadrons ou des leptons supplémentaires sont rejetés et, enfin, une sélection basée sur le $p_T$ et sur la masse invariante du système dileptonique et sur l'énergie transverse manquante ($E_T^{miss}$) est appliquée. Les principaux bruits de fonds du SM pour cette analyse sont le processus $Z/\gamma + jet$ (Drell-Yan), la désintégration totalement leptonique du $\bar{t}t$ et du top seul, et les processus dibosoniques $WW$ et $WZ$.

Toutes les distributions des bruits de fonds et leur normalisation sont contraintes par les données via un ajustement à la distribution d'une variable discriminante

(par exemple $E_T^{miss}$), permettant seulement à la normalisation du signal $ZZ$ de varier librement. Nous mesurons une section efficace de $\sigma(\mathrm{pp} \to ZZ) = 5.1\ ^{+1.5}_{-1.4}\,(\mathrm{stat})\,^{+1.4}_{-1.1}\,(\mathrm{syst}) \pm 0.1\,(\mathrm{lumi})$ pb à 7 TeV, et $7.2\ ^{+0.8}_{-0.8}\,(\mathrm{stat})\,^{+1.9}_{-1.5}\,(\mathrm{syst}) \pm 0.2\,(\mathrm{lumi})$ pb à 8 TeV, en accord avec les prédictions du modèle standard.

Les données sélectionnées ont ensuite été analysées pour rechercher la présence de couplages triples anomaux impliquant l'état final ZZ, et plus tard, les données ont été combinées avec celles de l'état final $ZZ \to 2l2l'$, pour augmenter la sensibilité. En l'absence de signes de nouvelle physique, nous avons mis des limites sur les paramètres liés aux couplages triples anormaux.

Entre 2024 et 2026, le détecteur CMS subira d'importantes transformations, nécessaires pour la prise de données à haute luminosité. Pendant les opérations à haute luminosité du LHC (HL-LHC), la luminosité instantanée devrait être supérieure à $10^{34}$ cm$^{-2}$ s$^{-1}$. L'augmentation de la luminosité engendrera une moyenne de 140 interactions simultanées (pileup), et représentera un défi pour la sélection et la reconstruction des objets physiques, la dégradation de la résolution en énergie des photons et des jets hadroniques, et toutes les quantités liées à l'isolation des objets. Il est donc essentiel d'éliminer la contribution des interactions d'empilement, et de corriger les variables associées. La dernière partie de cette thèse décrit l'utilisation d'une mesure de temps dans la reconstruction d'objets physiques. Une mesure du temps, estimée dans les simulations, est utilisée dans différents algorithmes de reconstruction, montrant des améliorations dans la reconstruction de vertex et dans l'atténuation des effets causés par le pileup.

Nous mesurons qu'une résolution de 30 ps permet de reconstruire la position en z du vertex de la collision dure avec une résolution de l'ordre du cm, et de rejeter les jets des interactions d'empilement avec un facteur de réjection de 3 environ.

# Riassunto

Il Large Hadron Collider (LHC) segna una nuova era per la fisica delle particelle. Grazie alle collisioni protone-protone ad alta energia, ed alla grande quantità di dati raccolti negli anni 2010-12, i fisici del CERN possono investigare il modello standard (SM) della fisica delle particelle, possono esplorare il settore scalare, e ricercare indizi sulla presenza di nuova fisica.

Viene presentata una misura della sezione d'urto della produzione di coppie di bosoni $Z$, ottenuta con collisioni protone-protone a 7 ed 8 TeV di energia nel centro di massa, registrate dall'esperimento CMS (Compact Muon Solenoid). La produzione di coppie di bosoni ad LHC è di particolare interesse per i seguenti motivi: permette di investigare per la prima volta rari processi dello SM con precisione, permette di testare l'auto-interazione dei bosoni elettro-deboli, e permette di studiare processi che rappresentano un fondo per molte altre ricerche, come la ricerca del bosone di Higgs o ricerche di supersimmetria.

La sezione d'urto per la produzione di coppie di bosoni $Z$ viene misurata attraverso il canale di decadimento $ZZ \to 2l2\nu$. I dati utilizzati per l'analisi sono stati registrati negli anni 2011 e 2012, e corrispondono ad una luminosità integrata di circa 5.1 fb$^{-1}$ a 7 TeV e 19.6 fb$^{-1}$ ad 8 TeV. I dati sono selezionati richiedendo la presenza di due leptoni isolati (elettroni o muoni) dello stesso sapore con alto momento trasverso ($p_T$). Inoltre, gli eventi che contengono getti adronici o leptoni supplementari sono rigettati, e viene applicata una selezione basata sul $p_T$ e la massa del sistema dei due leptoni, e sull'energia trasversa mancante ($E_T^{miss}$). I principali fondi dello SM per questa analisi sono il processo $Z/\gamma + jet$ (Drell-Yan), il decadimento leptonico di coppie $t\bar{t}$ e di singolo top, ed i processi dibosonici $WW$ e $WZ$.

Tutte le distribuzioni dei fondi e le relative normalizzazioni sono vincolati ai dati tramite un fit alla distributione della variabile $E_T^{miss}$, consentendo solo alla normalizzazione della distribuzione del segnale $ZZ$ di variare liberamente. È stata misurata una sezione d'urto di $\sigma(\mathrm{pp} \to ZZ) = 5.1\ ^{+1.5}_{-1.4}\,(\mathrm{stat})\,^{+1.4}_{-1.1}\,(\mathrm{syst})\ \pm$

0.1 (lumi) pb a 7 TeV, e 7.2 $^{+0.8}_{-0.8}$ (stat) $^{+1.9}_{-1.5}$ (syst) $\pm$ 0.2 (lumi) pb ad 8 TeV, in accordo con le predizioni del modello standard.

I dati selezionati sono stati successivamente analizzati per verificare la presenza di accoppiamenti tripli anomali nello stato finale $ZZ$, e successivamente i dati sono stati combinati con quelli dello stato finale $ZZ \to 2l2l'$, aumentando la sensibilità alla presenza di accoppiamenti tripli. In assenza di segni della presenza di nuova fisica, sono stati messi limiti sul valore degli accoppiamenti considerati.

Tra il 2024 e il 2026, il rivelatore CMS subirà delle importanti modifiche, necessarie per affrontare la successiva presa dati ad alta luminosità. Durante le operazioni ad alta luminosità di LHC (HL-LHC), la luminosità istantanea è prevista essere maggiore di $10^{34}$ cm$^{-2}$ s$^{-1}$. L'aumento di luminosità produrrà una media di 140 interazioni simultanee (pileup), e rappresenterà un problema per la selezione e la ricostruzione degli oggetti fisici, degradando la risoluzione dell'energia dei fotoni e dei getti adronici, e tutte le quantità di isolamento. È quindi fondamentale rimuovere il contributo dell'attività del pileup, e correggere le variabili misurate. L'ultima parte della tesi descrive l'utilizzo di una misura di tempo nella ricostruzione di oggetti fisici. Una misura del tempo, estratta dalla simulazione, sarà utilizzata in diversi algoritmi di ricostruzione, mostrando miglioramenti nella ricostruzione vertice e nella mitigazione degli effetti causati dal pileup.

Dimostriamo che a partire da una risoluzione temporale di 30 ps è possibile ricostruire la posizione del vertice lungo l'asse z con una risuluzione dell'ordine del centimetro, ed è possibile rimuovere jet provenienti da interazione di pilup con un fattore di reiezione di circa tre.

# Contents

# Nomenclature

e.g.: *Exempli gratia (for example)*
i.e.: *Id est (that is)*
Eq.: *Equation*
Fig.: *Figure*
SM: *Standard model*
QCD: *Quantum chromodynamics*
QED: *Quantum electrodynamics*
EWK: *Electroweak*
LHC: *Large Hadron Collider*
CMS: *Compact Muon Solenoid*
L1: *Level 1 trigger*
HLT: *High level trigger*
GCT: *L1 global calorimeter trigger*
GMT: *L1 global muon trigger*
GT: *L1 Global trigger*
DAQ: *Data acquisition system*
TCS: *Trigger control system*
EB: *ECAL barrel*
EE: *ECAL endcap*
ES: *ECAL preshower*
HB: *HCAL barrel*
HE: *HCAL endcap*
DT: *Drift tube*
CSC: *Cathode strip chamber*
RPC: *Resistive place chamber*
APD: *Avalanche photodiodes*
VPT: *Vacuum phototriodes*
SL: *Superlayer*
SC: *Supercluster*
IP: *Interaction point*
MC: *Monte carlo*
PU: *Pileup*
PF: *Particle flow*
IC: *Inter-calibration constant*
MVA: *Multivariate analysis*
Sec: *Section*
Chapt: *Chapter*
$M_e$: *Electron mass*
$p_T$: *Transverse momentum*
$q_T$: *Z boson transverse momentum*
$m_Z$: *Z boson mass*
$m_{ll}$: *Dilepton system mass*
$E_T^{miss}$: *Missing transverse energy*

# Introduction

The Large Hadron Collider (LHC) marks a new era for particle physics. Thanks to the very high energy of the proton beams, and to the large amount of data collected in years 2010-12, the physicists at CERN tested the standard model (SM) consistency, explored the scalar sector, and searched for any hint of new physics.

In this thesis we report a measurement of $Z$ boson pair production cross section, using proton-proton collisions at 7 and 8 TeV center-of-mass energy, recorded by the CMS (Compact Muon Solenoid) experiment. Diboson production at the LHC is of particular interest: it validates rare SM processes never tested before with high accuracy, it probes the electroweak boson self-interactions, and it constitutes a background for many searches such as the searches for the $H$ boson or supersymmetry. Furthermore, the gluon fusion contribution to the $ZZ$ production cross section, interferes with the production of the $H \rightarrow ZZ$ process. The study of the interference between these two processes allows to perform a measurement of the $H$ boson production and decay, which can be interpreted in a measurement of the $H$ boson total width.

The $ZZ$ production cross section here is measured via the decay channel $ZZ \rightarrow 2l2\nu$. The data used for the analysis have been recorded in years 2011 and 2012 by CMS and correspond to an integrated luminosity of about 5.1 fb$^{-1}$ at 7 TeV and 19.6 fb$^{-1}$ at 8 TeV. The data are selected requiring the presence of two isolated leptons (electrons or muons) of the same flavor with high transverse momentum ($p_T$). In addition, events containing jets or additional leptons are vetoed. A selection based on the dilepton $p_T$, on the dilepton invariant mass, and on the transverse momentum imbalance ($E_T^{miss}$) is also applied.

The main SM backgrounds for this analysis are the $Z/\gamma + jet$ (Drell-Yan) process, the fully leptonic $t\bar{t}$ and single-top decay, and the $WW$ and $WZ$ diboson processes. The $Z/\gamma+jet$ process has no neutrinos in the final state, thus it has no large $E_T^{miss}$, but its cross section at the $Z$-peak is four orders of magnitude larger than the $ZZ$ production. For this reason, even if the fraction of $Z/\gamma + jet$ events reconstructed with significant instrumental $E_T^{miss}$ is not large, a high $E_T^{miss}$ cut must be applied in order to improve the signal purity. High $E_T^{miss}$ in $Z/\gamma + jet$ events is due to misreconstruction of physical objects, and to the additional energy deposits arising from the other proton-proton interactions occurring in the same bunch crossing (pileup). These effects are not well described in simulation, for this reason a high statistic control sample is used in order to model these tails from data.

The fully leptonic $t\bar{t}$, the single-top decay, and the $WW$ processes have been estimated in control samples obtained requiring exactly one electron and one muon in the final state. The $WZ$ process instead, has been estimated directly from the simulation.

The distributions and normalizations of a discriminating variable (e.g. $E_T^{miss}$) of all the SM processes are then constrained to data from a fit. Backgrounds are allowed to vary within their uncertainty, while the $ZZ$ signal normalization is allowed to freely vary, in order to measure the $ZZ$ production cross section. The selected data were also analyzed to search for anomalous triple gauge couplings (aTGC) involving the $ZZ$ final state, and subsequently combined with the $ZZ \to 2l2l'$ final state data, to increase the sensitivity. In the absence of signs of new physics we set limits on the relevant aTGC parameters.

I contributed to this analysis from the very beginning. I performed studies on the $E_T^{miss}$ variable, in order to discriminate between the $ZZ$ signal and the $Z/\gamma + jet$ background, and I optimized the selection, in order to reject as much as background as possible, keeping high efficiency on the signal. I also performed the data-driven estimation of the (Drell-Yan) background and I took care of the systematic uncertainties on the final measurement, as for instance the uncertainty arising from the jet-veto. Finally, I introduced electroweak next-to-leading-order corrections to our simulation, and I derived limits on the anomalous couplings.

Between 2024 and 2026, to extend its discovery potential and/or characterize any new signal possibly discovered, the LHC will be upgraded to increase its instantaneous luminosity by a factor of 10 beyond its design value (phase 2 upgrade). The increase in luminosity will produce an average of 140 pileup (PU) interactions. This will represent an issue for the trigger and the reconstruction, degrading the jet and photon energy resolution and all the physics object isolation quantities.

In order to maintain full sensitivity, from low to high energy scales under severe pileup and radiation conditions, the L1 trigger, the tracker, the ECAL endcap and the HCAL, and the forward muon system will be upgraded. Moreover, in order to correct the measurement of the relevant variables, it will be fundamental to tag the extra activity from PU interactions. The last part of the thesis discusses the possible use of timing to mitigate the pileup contribution in the object reconstruction. Timing could be exploited for the association of photons, electrons and jets to their collision vertices, for particle identification, or to reject energy deposits coming from pileup vertices.

I developed these studies from scratch, presenting them several times to CMS upgrade meetings. Afterwards the "Fast Timing Studies" analysis group it has been instituted, with the purpose of producing, by the end of 2015, a scope document illustrating the effects of a time measurement on reconstruction performance, together with several proposals of time detectors that could be installed at CMS. The document is complementary to the CMS phase 2 scope document.

# Chapter 1

# Standard model and anomalous Triple Gauge Couplings

Particle physics is the science of the elementary components of matter and of their interactions. The discrete nature of matter, hypothesized by Democritus (370 BC) [1] was later established in the 19th century with the periodic behavior of the chemical properties of the elements, illustrated by Mendeleev's table [2].

The improvement of the experimental techniques in the last two centuries helped to investigate deeply the structure of matter and allowed a series of discoveries, such as the internal structure of atomic nuclei. After the discovery of the electron [3] and the formulation of the theory of electromagnetism [4], physics described the world in a different way in terms of forces and matter. With the discovery of positrons, muons and pions, the search for more particles was definitely opened [3].

In the late 1960, the standard model (SM) [5] of particle physics developed. The SM describes the electromagnetic, weak, and strong interactions, which mediate the dynamics of the known subatomic particles. This theory has been intensively tested by experimental physicists, most notably at high energy particle colliders, over the last three decades. It has been demonstrated to accurately describe fundamental particles and their interactions.

Today, thanks to the Large Hadron Collider (LHC) [6] at CERN, particle physics is in the middle of a unique period for the investigation of the constituents of the matter and their interactions, and physicists can test the standard model consistency and search for any hint of new physics.

## 1.1 Standard model of particle physics

The standard model is a theoretical framework that describes how matter is composed of fundamental constituents and the various types of interactions between these constituents. Experimental results confirmed in several occasions the accurate precision of this model.

According to the SM, all particles in the Universe can be included in two basic groups: *fermions*, particles with half-integer spin that compose the matter and obey to the Fermi-Dirac statistic, and *bosons*, particles with integer spin, obeying to the Bose-Einstein statistic, that carry the fundamental forces. The SM is a gauge invariant theory which obeys to $SU(3)_C \otimes SU(2)_L \otimes U(1)_Y$ symmetry, where $C$ means color charge, $L$ means weak isospin (since the $W$ boson only interacts with left-handed chiral components of the Dirac spinors), and $Y$ represents hyper-charge. The electromagnetic interaction is described by the unitary group $U(1)$. This interaction is mediated by massless particles (*photons*) and its theory is called Quantum Electrodynamics (QED). The weak interaction is mediated by 3 massive gauge bosons: the $W^{\pm}$ bosons, with mass of 80.4 GeV, and the $Z^0$ boson, with mass of 91.2 GeV. The strong interaction has eight generators, called *gluons*, which are massless and carry color charge. The gravity is not included in the SM.

In figure 1.1 all the SM particles are represented. Starting from the left column, the fermions are shown in three different generations. On the fourth column the bosons, mediators of the forces, are represented. The scalar ($H$) boson, theorized in 1964 [7, 8], is responsible for giving mass to the heavy vector bosons and to the fermions. In 2012 a $H$-like particle has been finally observed [9, 10] by the CMS and ATLAS experiments.

### 1.1.1 Electroweak interaction and the Brout-Englert-Higgs mechanism

Experimentally, the $W$ boson couples with a charged lepton and its corresponding neutrino, which is neutral. The Dirac fields of the two leptons can be regarded as a doublet under $SU(2)$. We can assume the interaction to be invariant under rotations defined by this symmetry group. A weak isospin multiplet can be identified by two conserved quantum numbers: the total isospin $T$ and its projection on a specific axis $T_3$. For the three lepton families we have $T = \frac{1}{2}$ and $T_3 = -\frac{1}{2}$ $(\frac{1}{2})$ for charged leptons (neutrinos).

In order to have a symmetric theory under gauge transformations of this group, the

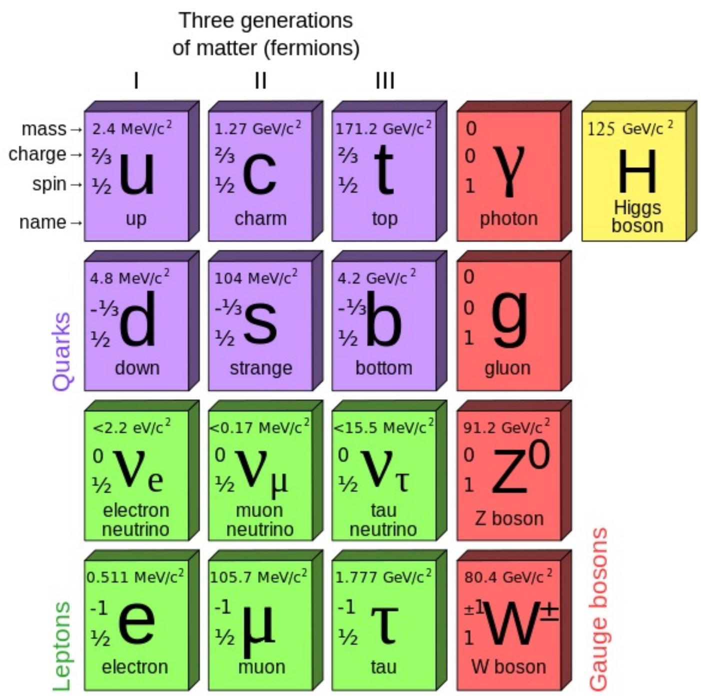


Figure 1.1: Fermions and bosons of the standard model.

Lagrangian needs to be invariant under:

$$\begin{pmatrix} \nu_e \\ e^- \end{pmatrix}_L \to \begin{pmatrix} \nu_e \\ e^- \end{pmatrix}_L^{'} = e^{i\alpha \cdot T} \begin{pmatrix} \nu_e \\ e^- \end{pmatrix}_L \tag{1.1}$$

where $T_i = \frac{1}{2}\tau_i$ (i=1,2,3) are the three generators of $SU(2)_L$, and $\tau_i$ are the Pauli matrices.

Since there is a gauge boson associated to each generator, we have a triplet of gauge bosons $W^\mu = (W_1^\mu, W_2^\mu, W_3^\mu)$, which creates the lepton-gauge interaction term:

$$g\bar{l}\gamma^\mu \frac{\tau_\alpha}{2} l W_\mu^\alpha \tag{1.2}$$

where $g$ is the coupling strength of the weak interaction, and $\gamma^\mu$ the Dirac matrices. We can write the $W^\mu$ boson experimentally observed as a combination of the gauge fields associated to the non-diagonal Pauli matrices $\tau_1$ and $\tau_2$:

$$W_\pm^\mu = \frac{W_1^\mu \mp W_2^\mu}{\sqrt{2}} \tag{1.3}$$

while the third gauge boson $W_3^\mu$ is neutral ($\tau_3$ is diagonal) and it cannot be identified with the $Z$ boson since the weak neutral current also has a right-handed component.

To include a weak neutral current Abdus Salam and Steven Weinberg in 1967 [11, 12] enlarged the symmetry group of the Lagrangian including U(1), gaining another gauge boson $B_\mu$. In this case the symmetry group of the unified electromagnetic and weak interactions is given by $SU(2)_L \otimes U(1)_Y$, and the photon ($A_\mu$) and the $Z$ boson ($Z_\mu$) are the results of a mixing of the gauge fields ($W^3_\mu$, $B_\mu$).

The Lagrangian that corresponds to the $SU(2)_L \otimes U(1)_Y$ gauge can be written as:

$$\mathcal{L}_{ewk} = \overline{\psi}_R(i\partial\!\!\!/ - m)\psi_R + \overline{\psi}_L(iD\!\!\!\!/ - m)\psi_L - \frac{1}{4}B_{\mu\nu}B^{\mu\nu} - \frac{1}{2}Tr(W_{\mu\nu}W^{\mu\nu}) \tag{1.4}$$

with:

$$B_{\mu\nu} = \partial_\mu B_\mu - \partial_\nu B_\nu \;\text{ and }\; W_{\mu\nu} = \partial_\mu W_\mu - \partial_\nu W_\nu - ig[W_\mu, W_\nu], \tag{1.5}$$

where $\partial\!\!\!/$ is equal to $\gamma^\mu\partial_\mu$, $D_\mu$ is equal to $\partial_\mu + i\frac{g}{2}W_\mu - i\frac{g'}{2}YB_\mu$, $g$ and $g'$ are the constant couplings of $SU(2)_L$ and $U(1)_Y$ respectively, $W^i_\mu$ that are the fields associated to $\mathrm{SU}(2)_L$, and $\mathrm{B}_\mu$ the fields associated to $\mathrm{U}(1)_Y$.

The vector-bosons associated to the weak force are massive, but the explicit insertion of bosonic mass terms spoils the invariance. Therefore there should be some mechanism that breaks the symmetry to explain their non-zero masses. This mechanism, proposed by Brout, Englert [7], and Higgs [8], is based on the spontaneous symmetry breaking, following the introduction of a complex weak isospin doublet with hypercharge $Y = 1$, called the $H$ doublet:

$$\phi = \begin{pmatrix} \phi^+ \\ \phi^0 \end{pmatrix} = \sqrt{\frac{1}{2}} \begin{pmatrix} \phi_1 + i\phi_2 \\ \phi_3 + i\phi_4 \end{pmatrix} \tag{1.6}$$

The $H$ Lagrangian, to be added to the electroweak one, can be written as the kinematic term of the $H$ doublet, minus the $H$ potential $V(\phi)$:

$$\mathcal{L}_H = (D_\mu\phi)^\dagger(D^\mu\phi) - V(\phi) \tag{1.7}$$

where $D_\mu$ is the covariant derivative and $V(\phi)$ is parametrized as $\mu^2\phi^\dagger\phi + \lambda(\phi^\dagger\phi)^2$. To have a stable theory, the $\lambda$ parameter have to be positive, while the $\mu$ parameter can be either positive or negative. The sign of $\mu$ will change the potential shape. In particular, for negative values of $\mu$, the potential has a set of minima given by the circle:

$$|\phi|^2 = \frac{1}{2}\left[\phi_1^2 + \phi_2^2 + \phi_3^2 + \phi_4^2\right] = -\frac{\mu^2}{2\lambda} \tag{1.8}$$

The vacuum state is degenerate, and it is given by all the field configurations that satisfy

Eq. 1.8. If we choose a single point in the circle to be the minima, the potential does not share anymore the same symmetry of the Lagrangian, and the symmetry is spontaneously broken. An arbitrary choice for the minimum could corresponds to set $\phi_1 = \phi_2 = \phi_4 = 0$ and $\phi_3 = \sqrt{\frac{-\mu^2}{\lambda}} \equiv \nu$.

In this way it is possible to write the vacuum state as:

$$\phi_0 = \sqrt{\frac{1}{2}} \begin{pmatrix} 0 \\ \nu \end{pmatrix} \tag{1.9}$$

Following the perturbation theory, we can expand the Lagrangian $\mathcal{L}_H$ around the vacuum by parametrizing the fluctuation around $\phi_0$ in terms of four real fields $\xi_1(x)$, $\xi_2(x)$, $\xi_4(x)$ and $h(x)$:

$$\phi(x) = \frac{1}{\sqrt{2}} \begin{pmatrix} \xi_1(x) + i\xi_2(x) \\ \nu + h(x) + i\xi_4(x) \end{pmatrix} \tag{1.10}$$

It is always possible to find a $SU(2)_L \otimes U(1)_Y$ transformation after which the $H$ doublet assumes the form:

$$\phi(x) = \frac{1}{\sqrt{2}} \begin{pmatrix} 0 \\ \nu + h(x) \end{pmatrix} \tag{1.11}$$

with only the real lower component different from zero. This particular gauge is called *unitarity gauge*. In the unitarity gauge there is only one scalar field left: the $H$ field identified by h(x).

Substituting the $H$ doublet in Eq. 1.11 in the kinetic energy term of the $H$ Lagrangian, and considering the $H$ doublet quantum numbers ($Y = 1$ and $T = \frac{1}{2}$) we find:

$$(D_\mu\phi)^\dagger(D^\mu\phi) = \left(\frac{1}{2}\nu g\right)^2 W_\mu^+ W^{-\mu} + \frac{1}{8}\nu^2 \begin{pmatrix} W_\mu^3 & B_\mu \end{pmatrix} \begin{pmatrix} g^2 & -gg' \\ -gg' & g'^2 \end{pmatrix} \begin{pmatrix} W^{3\mu} \\ B^\mu \end{pmatrix} \tag{1.12}$$

where $W^\mu$ is the the physical field represented by a combination of the gauge fields as shown in Eq. 1.3, and the mass term of the charged weak bosons is:

$$m_W = \frac{1}{2}\nu g \tag{1.13}$$

The other terms of the equation are off-diagonal in the $W_\mu^3$, $B_\mu$ basis. The mass term for the $A_\mu$ and $Z_\mu$ fields, corresponding to the photon and the $Z$ boson are derived diagonalizing the matrix:

$$\begin{pmatrix} g^2 & -gg' \\ -gg' & g'^2 \end{pmatrix} \tag{1.14}$$

Since its determinant is zero there is a null eigenvalue corresponding to the massless photon. The second eigenvalue is given by the trace $g^2 + g'^2$. In this case the mass of the neutral weak boson is:

$$m_Z = \frac{1}{2}\nu\sqrt{g^2 + g'^2} \tag{1.15}$$

The physical and the gauge fields are connected by a simple rotation:

$$\begin{pmatrix} Z_\mu \\ A_\mu \end{pmatrix} = \begin{pmatrix} \cos\theta_W & -\sin\theta_W \\ \sin\theta_W & \cos\theta_W \end{pmatrix} \begin{pmatrix} W^3_\mu \\ B_\mu \end{pmatrix} \tag{1.16}$$

where $\theta_W$ is called the Weinberg angle.

Imposing the field $A_\mu$ to have the null mass eigenvalue we obtain $g\sin\theta_W = g'\cos\theta_W$ and:

$$\sin\theta_W = \frac{g'}{\sqrt{g^2 + g'^2}}, \quad \cos\theta_W = \frac{g}{\sqrt{g^2 + g'^2}} \tag{1.17}$$

Now it is finally possible to rewrite the physical field as:

$$W^\pm_\mu = \frac{W^1_\mu \mp W^2_\mu}{\sqrt{2}} \quad \text{with} \quad m_W = \frac{1}{2}\nu g \tag{1.18}$$

$$Z_\mu = \frac{gW^3_\mu - g'B_\mu}{\sqrt{g^2 + g'^2}} \quad \text{with} \quad m_Z = \frac{1}{2}\nu\sqrt{g^2 + g'^2} \tag{1.19}$$

$$A_\mu = \frac{g'W^3_\mu + gB_\mu}{\sqrt{g^2 + g'^2}} \quad \text{with} \quad m_A = 0 \tag{1.20}$$

The mechanism leaves the photon field $A_\mu$ massless and it gives three masses to the physical fields of $\mathrm{SU}(2)_L$, implying the existence of a physical massive field, the $H$ boson, that couples with the massive gauge bosons and to itself. Three of the four degrees of freedom from the mechanism have been absorbed, allowing the gauge vector bosons to acquire mass, and the last degree of freedom becomes the mass of the $H$ boson.

The gauge group $SU(2)_L \otimes U(1)_Y$ is non-abelian. This implies the presence of a term $[W_\mu, W_\nu]$ into the $W_{\mu\nu}$ tensor. The $[W_\mu, W_\nu]$ term is responsible for the self interaction of the gauge fields, which includes interactions between three and four vector bosons.

The interaction term with three vector bosons can be written as [13]:

$$\begin{aligned}\mathcal{L}_{3V} = ig\cos\theta_W[(\partial_\mu W^+_\nu - \partial_\nu W^+_\mu)W^{-\mu}Z^\nu - (\partial_\mu W^-_\nu - \partial_\nu W^-_\mu)W^{+\mu}Z^\nu] + \\ ie[(\partial_\mu W^+_\nu - \partial_\nu W^+_\mu)W^{-\mu}A^\nu - (\partial_\mu W^-_\nu - \partial_\nu W^-_\mu)W^{+\mu}A^\nu] - \\ ig\cos\theta_W(\partial_\mu Z_\nu - \partial_\nu Z_\mu)W^{-\mu}W^{+\nu} - ie(\partial_\mu A_\nu - \partial_\nu A_\mu)W^{-\mu}W^{+\nu}\end{aligned}$$

It is important to notice that only the interactions between two $W^\pm$ bosons and a neutral boson are allowed, while couplings between neutral bosons are not possible.

### 1.1.2 Standard model shortcomings

The standard model describes successfully all features of electromagnetic, weak and strong interactions between matter constituents, up to energies of about 1 TeV. However, despite its incredible success, the SM has several shortcomings, preventing it to become the ultimate theory of particle interactions. For instance in the SM neutrinos are massless, but recent experimental observations, like neutrino oscillations [14], implies that the neutrinos are massive. Furthermore the SM does not provide candidates to account for the dark matter and dark energy in the Universe, while very strong evidence for their existence has been obtained observing the motions of stars and gas clouds, and from the Hubble Space Telescope observations [15]. The SM also does not explain the matter-antimatter asymmetry observed today in the Universe. This asymmetry seems inconsistent with the inflation picture of our early Universe, as the present structure of the SM treats particles and antiparticles almost similarly.

The Large Hadron Collider during Run2 will keep testing the SM consistency. Furthermore, thanks to the beyond standard model searches, like supersymmetry, performed by ATLAS and CMS, natural Dark Matter candidates could be discovered.

## 1.2 Z boson pair-production at the LHC

In this manuscript we focus on the measurement of the $ZZ$ production cross section in proton-proton collisions at two different center-of-mass energies: 7 TeV and 8 TeV. In this chapter we discuss the leading order and next-to-leading order contributions to the $ZZ$ production cross section.

### 1.2.1 Lowest-order contribution to the $ZZ$ production cross section

At tree level, pairs of $Z$ bosons are primarily pair-produced in the $t$ and $u$ channels from a quark-antiquark pair. These production modes account for about 90% of the total cross section and are depicted in Fig. 1.2 (left and center). The remaining contribution is expected to be due to gluon-gluon fusion through a quark-box diagram as depicted in Fig. 1.2 (right).

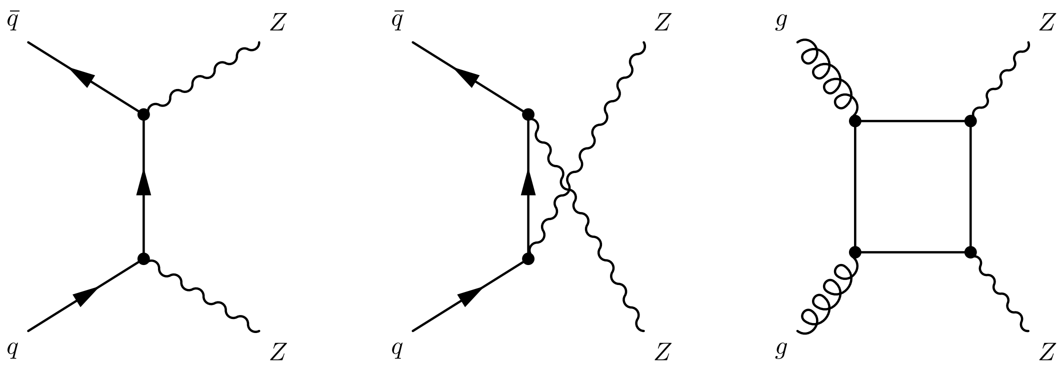


Figure 1.2: Lowest-order diagrams for the processes contributing to $Z$ boson pair production at the LHC. From left to right: $t-$channel, $u-$channel and gluon-gluon fusion.

Table 1.1 shows the total cross section of $Z$ boson pair production at leading-order (LO), at next-to-leading-order (NLO) in quantum chromodynamics (QCD) [16], and at NLO in QCD considering also electroweak (EWK) corrections [17]. The ratio between the NLO and LO cross section is called k$-$factor, and in the case of $ZZ$ pair production it reaches about 1.5.

| $\sqrt{s}$ [TeV] | $\sigma^{LO}$(ZZ) [pb] | $\sigma^{QCD\ NLO}$(ZZ) [pb] | $\sigma^{QCD+EWK\ NLO}$(ZZ) [pb] |
|---|---|---|---|
| 7 | 4.17 | 6.46 | 6.20 |
| 8 | 5.06 | 7.92 | 7.60 |
| 14 | 10.92 | 17.72 | 17.01 |

Table 1.1: Total cross section of $Z$ boson pair production at LO, at NLO in QCD [16], and at NLO in QCD considering also EWK corrections [17].

### 1.2.2 The factorization theorem and the hard process

The partons are the particles (as quarks or gluons) that constitute hadrons. In order to compute a cross section at hadron colliders one has to compute the cross section for the incoming partons, and convolute it with the description of the parton momenta inside the beam. The first part can be computed from Feynman diagrams. The second part is described by the parton density functions (PDFs). The PDF $f_{a/A}(x_a, Q^2)$ describes the probability to find a parton of type $a$ in the hadron $A$ with a Bjorken variable $x$. In high energy beams $x_a$ can be seen as the parton momentum fraction of the total momentum of $A$, and will be discussed in sec. 1.2.3. PDFs also depend on the energy scale $Q^2$ of the process. This scale can be either the transverse momentum of the outgoing partons with respect the beam, or invariant mass of the outgoing partons.

The QCD factorization theorem [18] can be used to calculate a wide variety of hard scattering cross sections in hadron-hadron collisions. It was first pointed out more than 30 years ago by Drell and Yan [19] that parton model ideas developed for deep inelastic scattering could be extended to certain processes in hadron-hadron collisions. The idea was that the production of a massive lepton pairs by $q\bar{q}$ annihilation (the Drell-Yan process) and the hadronic cross section $\sigma(AB \to l^+l^- + X)$ could be obtained by weighting the sub-process cross section $\hat{\sigma}$ for $q\bar{q} \to l^+l^-$ with the PDFs in the following way:

$$\sigma_{AB\to ll+X} = \int dx_a dx_b f_{a/A}(x_a, Q^2) f_{b/B}(x_b, Q^2) \hat{\sigma}_{ab\to ll+X}$$

where the $Q^2$ term could be for instance the dilepton mass or transverse momentum, $f_{a/A}(x_a, Q^2)$ represents the PDF, and, in the case of the Drell$-$Yan process, $AB = q\bar{q}, \bar{q}q$.

The cross section computation can be factorized in different orders:

$$\sigma_{AB\to ll+X} = \int dx_a dx_b f_{a/A}(x_a, \mu_F^2) f_{b/B}(x_b, \mu_F^2) \cdot [\hat{\sigma_0} + \alpha_S(\mu_R^2)\hat{\sigma_1} + ...]_{ab\to ll+X}$$

where $\hat{\sigma_0}$ and $\hat{\sigma_1}$ are coefficients, $\mu_F$ is the factorization scale and $\mu_R$ the normalization scale. We can think about $\mu_F$ as the scale that separates the long- and short-distance physics, and $\mu_R$ the scale for the QCD running coupling. In principle the cross section calculated to all orders in perturbation theory is invariant under changes in these parameters, but in the absence of a complete set of higher order corrections, it is necessary to make a specific choice for the two scales in order to make cross section computations.

### 1.2.3 PDFs

Parton distributions cannot be calculated perturbatively, but rather are determined by global fits to data from deep inelastic scattering (DIS), Drell-Yan (DY), and jets production.

Measurements of DIS structure functions in lepton-hadron scattering and of lepton pair production cross sections in hadron-hadron collisions provide the main source of information on quark distributions $f_{q/p}(x, Q^2)$ inside hadrons, where $Q$ is the momentum scale that characterize the hard scattering. At leading order, the gluon distribution function $f_{g/p}(x, Q^2)$ enters directly in hadron-hadron scattering processes with jet final states. The data from DIS, DY and jet processes utilized in PDF fits cover a wide range in $x$ and $Q^2$.

Parton distributions determined in a given range of $Q^2$ and can be evolved at higher $Q^2$ values. To determine the rate of change of parton densities when the energy scale chosen for their definition is varied, it is possible to use the DGLAP equations, derived by Gribov and Lipatov, Altarelli and Parisi, and Dokshitzer [20]. DGLAP-based NLO perturbative QCD calculation should provide an accurate description of the data (and of the evolution of the parton distributions) over the entire kinematic range.

### 1.2.4 Higher-order corrections

There are two higher-order corrections that contribute to the $ZZ$ production cross section: the NLO QCD corrections and the NLO EWK corrections [17, 21]. In the literature, the NLO QCD corrections include loop corrections with one gluon in the loops and the real emission corrections with one additional parton in the final state, and the gluon-gluon box contribution shown in Fig. 1.2. At the LHC, NLO QCD corrections are typically large, because of the high gluon density in the protons at the scale $Q^2$ of the processes considered.

The NLO contribution with an additional parton will be further denoted as: $\bar{q}q' \to VV'g$, where the gluon is radiated from an initial quark, and the gluon-quark induced contribution $qg \to VV'q'$, which is related to the gluon-quark radiated ones via crossing symmetry. They are both represented, in the case of $Z$ boson pair production, in Fig. 1.3 (left and right respectively). Both the virtual and real corrections are separately infra-red divergent, they

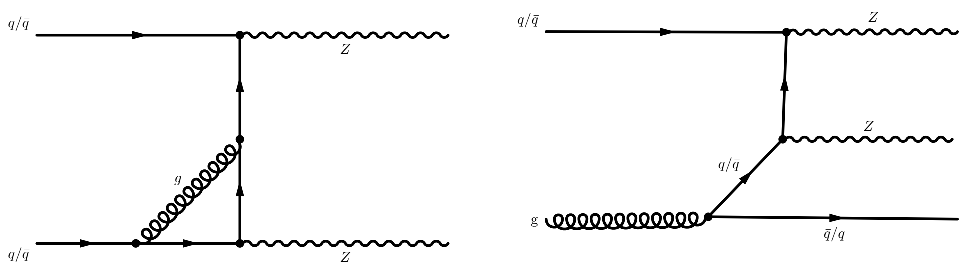


Figure 1.3: An example of Feynman diagrams for the $\bar{q}q \to ZZg$ (left) and $qg \to ZZq$ (right) NLO contribution.

cancel in the sum for infra-red-safe observables such as the total cross section and kinematic distributions of massive gauge bosons.

Two of the main kinematic distributions of $ZZ$ production are shown in Fig. 1.4 [21]: the $p_T$ spectrum of the second leading $Z$ boson, and the invariant mass of the pair of $Z$ boson, $M_{ZZ} = \sqrt{(E_{Z1} + E_{Z2})^2 - |\vec{p}_{Z1} + \vec{p}_{Z2}|^2}$, where $\vec{p}_Z$ denotes the tri-momentum of the $Z$ boson. The distributions are shown at LO and NLO in QCD and EWK processes. The theoretical uncertainties from missing higher orders is computed in [21] and [17] and it is found to be of the order of 4%.

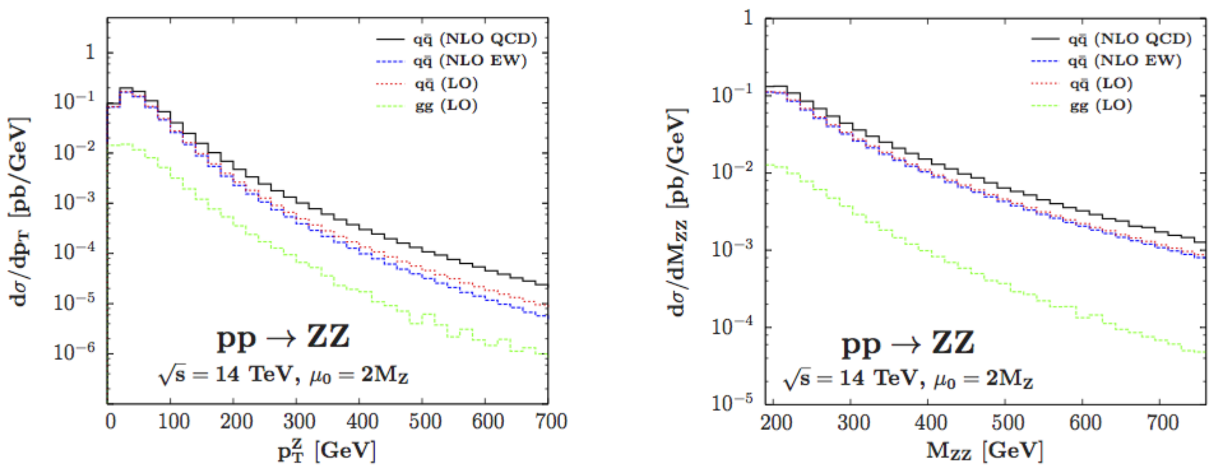


Figure 1.4: $pp \to ZZ$ cross section as a function of the transverse momentum ($p_T$) of the $Z$ boson (left) and of the invariant mass ($M_{ZZ}$) of the $Z$ boson pair (right), including NLO QCD and EWK corrections [21].

At the LHC, the production of a pair of $Z$ bosons is thus accompanied by the emission of initial-state quarks or gluons. If the $ZZ$ event sample is divided according to the multiplicity of jets accompanying the boson pair, then the uncertainty on the jet multiplicity bin and on the Z boson kinematic spectra is large.

In Fig. 1.5 we show the contributions of the $ZZ$ differential cross sections with no jets with $p_T > 30$ GeV, called $\sigma_{j0}$, and with at least one jet with $p_T > 30$ GeV, called $\sigma_{\geq 1j}$. These cross sections have been computed with the Monte Carlo for FeMtobarn processes (MCFM) [16] program, using a set of PDFs called MSTW [22]. The 0-jet category dominates at $Z$ boson $p_T$ between 80 and 200 GeV, while at $p_T$ less then 80 GeV and greater than 200 GeV, the category with at least 1 jet dominates.

An example of NLO EWK Feynman diagram is illustrated in Fig. 1.6. For $Z$ boson pair production these corrections are particularly large compared to other diboson processes.

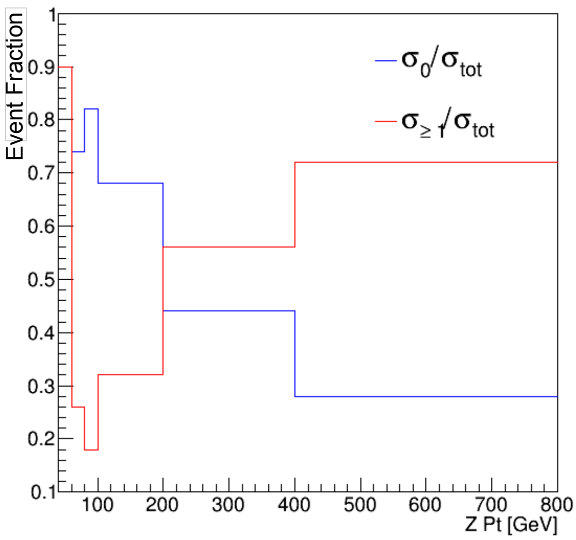


Figure 1.5: Contribution of the 0-jet category and the category with at least 1 jet to the $ZZ$ differential cross section as a function of the transverse momentum of one of the $Z$-bosons.

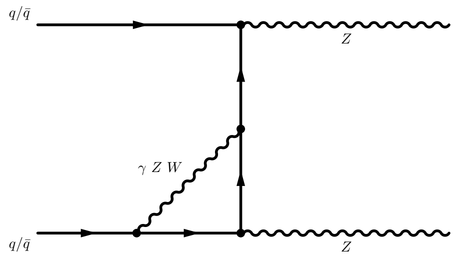


Figure 1.6: An example of NLO EWK Feynman diagram.

Fig. 1.7 shows the NLO EWK contribution for $WW$, $ZZ$, $WZ$ and $\gamma\gamma$ process. The contribution is negative and increasing in magnitude with the boson transverse momentum or the diboson invariant mass.

The authors of [17] provided us with tables of EWK corrections as a function of the Mandelstam variables $\hat{s}$ and $\hat{t}$ of the $q\bar{q} \to ZZ$ process, defined as:

$$\hat{s} = (p_1 + p_2)^2 = (p_3 + p_4)^2 \quad ; \quad \hat{t} = (p_1 - p_3)^2 = (p_2 - p_4)^2$$

where $p_1$ and $p_2$ is the quadri-momentum of the incoming partons and $p_3$ and $p_4$ the quadri-momentum of the outgoing $Z$ bosons.

The corrections depend on the electromagnetic and weak charges of the incoming quarks and their mass. They are therefore provided for different categories of quarks that contribute: $u$ and $c$, $d$ and $s$, and $b$ quarks. When these tables of corrections are applied to a $ZZ$ sample produced with MadGraph event generator [23], the spectrum is modified, and the relative difference, defined as:

$$\frac{\frac{dN}{dp_T}_{Mad.+NLOEWK} - \frac{dN}{dp_T}_{Mad.}}{\frac{dN}{dp_T}_{Mad.+NLOEWK}}$$

is shown in Fig. 1.8 and compared to the original calculation. The relative difference agrees with [17] as expected.

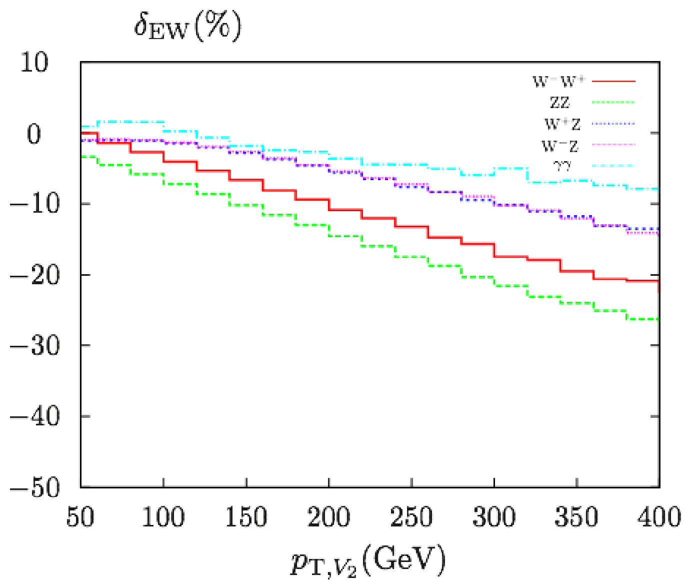


Figure 1.7: Electroweak corrections to the NLO cross section for different diboson processes as a function of the lower boson transverse momentum [17].

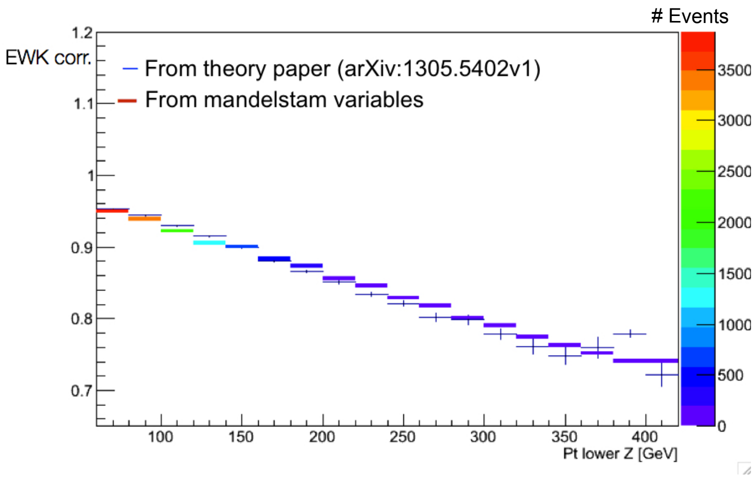


Figure 1.8: Electroweak corrections to the NLO cross section for the $ZZ$ process as a function of the lower boson transverse momentum. The blue distribution shows the published corrections [17], the colored one shows the corrections obtained with the parametrization.

## 1.3 Anomalous Triple Gauge Couplings

The existence of neutral trilinear gauge couplings (TGC) such as $ZZZ$, $ZZ\gamma$, $Z\gamma\gamma$, $\gamma\gamma\gamma$, is forbidden at the tree level in the SM, while it is allowed in some of its extensions. The study of these self-interactions of the neutral gauge bosons can thus provide evidence of new phenomena, or exclude them. The $ZZ$ production process provides a way to probe the existence of such anomalous couplings at the $ZZZ$ and $\gamma ZZ$ vertices. In the presence of anomalous triple gauge couplings (aTGCs) the $ZZ$ final state is also expected to be produced through the diagrams shown in Fig. 1.9.

Neutral couplings $VZZ$ ($V = Z$, $\gamma$) can be described using the following effective Lagrangian [24]:

$$\mathcal{L}_{\mathrm{VZZ}} = -\frac{e}{M_{\mathrm{Z}}^2}\left\{\left[f_4^\gamma\left(\partial_\mu F^{\mu\alpha}\right)+f_4^Z\left(\partial_\mu Z^{\mu\alpha}\right)\right]Z_\beta\left(\partial^\beta Z_\alpha\right)-\left[f_5^\gamma\left(\partial^\mu F_{\mu\alpha}\right)+f_5^Z\left(\partial^\mu Z_{\mu\alpha}\right)\right]\tilde{Z}^{\alpha\beta}Z_\beta\right\} \tag{1.21}$$

where $F^{\mu\nu}$ is the electromagnetic tensor, $Z_{\mu\nu}$ corresponds to $\delta_\mu Z_\mu - \delta_\nu Z_\nu$ and $\tilde{Z}_{\mu\nu}$ corresponds to $\frac{1}{2}\epsilon_{\mu\nu\rho\sigma}Z^{\mu\nu}$ ($\epsilon_{\mu\nu\rho\sigma}$ is the Levi-Civita symbol). The coefficients $f_i^\gamma$ and $f_i^Z$ correspond to couplings $\gamma ZZ$ and $ZZZ$, respectively. All the operators in Eq. (1.21) are Lorentz-invariant and $\mathrm{U}(1)_{EM}$ gauge-invariant, but not invariant under $\mathrm{SU}(2)_L \otimes \mathrm{U}(1)_Y$ gauge symmetry. The terms corresponding to $f_4^V$ parameters violate the $CP$ symmetry, while the terms corresponding to $f_5^V$ parameters conserve $CP$.

The general vertex between three neutral gauge bosons is shown in Fig. 1.10. In our case

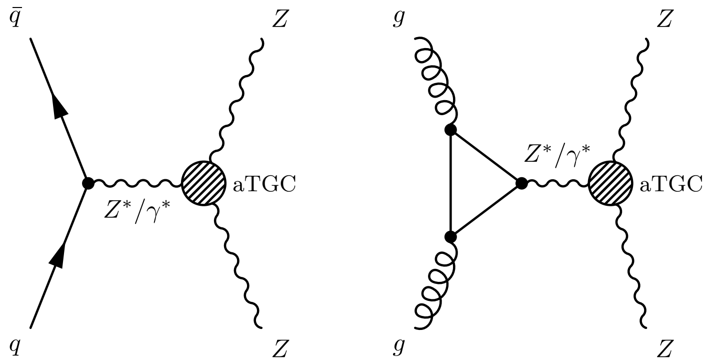


Figure 1.9: Diagrams representing the generation of $ZZ$ final states in the presence of anomalous triple gauge couplings in proton-proton collisions. Left: $s-$channel; right: gluon-gluon fusion.

$V_1$ and $V_2$ are two on-shell $Z$ bosons, and $V_3$ is an off-shell photon or an off-shell $Z$ boson. The coupling $\Gamma$ at this vertex can be expressed as:

$$\Gamma^{\alpha\beta\mu}_{ZZV} = \frac{i(s - m_V^2)}{m_Z^2}[f_4^V(P^\alpha g^{\mu\beta} + P^\beta g^{\mu\alpha}) - f_5^V \epsilon^{\mu\alpha\beta\rho}(q_1 - q_2)_\rho] \tag{1.22}$$

where $V$ denotes the off-shell boson, and where the momenta $P$, $q_1$, and $q_2$ are defined in Fig. 1.10. In Eq. 1.22, $s$ denotes $P^2$, $m_V$ represents the pole mass of the off-shell boson, $g^{\mu\nu}$ is the metric tensor, and $\epsilon^{\mu\alpha\beta\gamma}$ is the Levi-Civita fully anti-symmetric tensor.

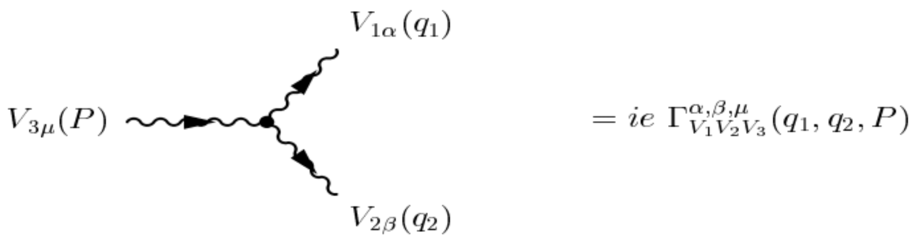


Figure 1.10: General vertex between neutral gauge bosons.

None of these couplings exist at tree level in the standard model. In the SM contributions to neutral TGCs can arise only from fermion loops such as the one shown in Fig. 1.11. These are CP-conserving processes, so $f_4^\gamma$ and $f_4^Z$ are identically zero in the standard model. The contribution to $f_5^\gamma$ and $f_5^Z$ is shown as a function of $s$, the invariant mass of the $ZZ$ pair, in Fig. 1.12, and is of the order of $10^{-4}$ [24].

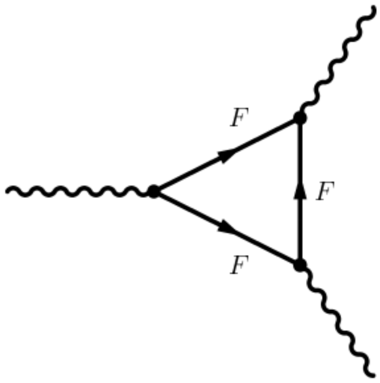


Figure 1.11: Triangular fermions loop.

## 1.4 Previous limits on aTGCs

Previous studies on neutral anomalous triple gauge couplings were performed at LEP2 [25], Tevatron [26, 27], and at the LHC [28][29]. No deviation from the SM expectation has been observed so far, and the best limits were set by the LHC measurements with integrated luminosities of about 5 $\mathrm{fb}^{-1}$ at 7 TeV. Published existing measurements are summarized in Table 1.2. The limits have to be considered as one-dimensional limits on anomalous couplings, and no correlation among different parameters has been considered.

To ensure that the theory does not violate unitarity, often the anomalous couplings are multiplied by so-called *form factors*: $\frac{1}{1+\hat{s}/\Lambda^2}$. Form factors are arbitrary and depend on the energy $\Lambda$ on which new physics appear and the scale energy $\hat{s}$ for which the limits are derived. While ATLAS, D0 and CDF in general derive limits on anomalous couplings that include form factors, in CMS limits are generally set without the use of form factors, or equivalently with the form factor scale set at infinity. This approach is justified from several reasons. First of all the effective theory that fits data will not violate unitarity, since we are in the case where the new physics scale is higher than the values $\hat{s}$ probed in the $ZZ$ production. Moreover form factors introduce a theory dependent interpretation of the results. For these reasons form factors will not be used in this analysis.

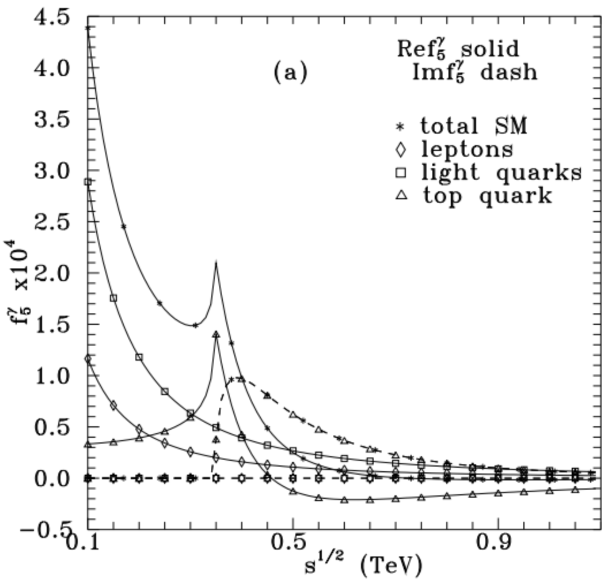


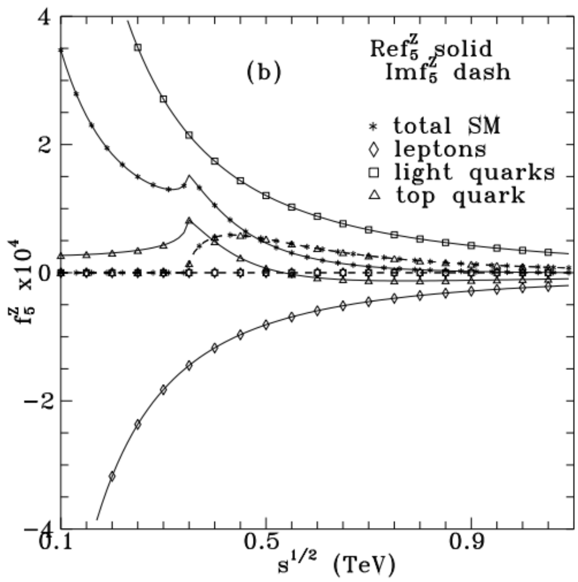


Figure 1.12: SM contribution to the real and imaginary part of $f_5^\gamma$ and $f_5^Z$ couplings [24].

Table 1.2: Summary of existing 95% C.L. intervals for the neutral aTGC coefficients.

| Experiment | $f_4^Z$ | $f_4^\gamma$ | $f_5^Z$ | $f_5^\gamma$ | Comments |
|---|---|---|---|---|---|
| LEP [25] | [-0.30; 0.30] | [-0.17; 0.19] | [-0.34; 0.38] | [-0.32; 0.36] | LEP combination No form factors, 1D |
| CDF [26] | [-0.12; 0.12] | [-0.10; 0.10] | [-0.13; 0.12] | [-0.11; 0.11] | $\Lambda$ = 1.2 TeV |
| DØ [26] | [-0.28; 0.28] | [-0.26; 0.26] | [-0.31; 0.29] | [-0.20; 0.28] | 1 fb$^{-1}$, $\Lambda$ = 1.2 TeV |
| CMS [27] | [-0.011; 0.012] | [-0.013; 0.015] | [-0.012; 0.012] | [-0.014; 0.014] | No form factors |
| ATLAS [29] | [-0.013; 0.013] | [-0.015; 0.015] | [-0.013; 0.013] | [-0.016; 0.015] | No form factors |
| ATLAS [29] | [-0.019; 0.019] | [-0.022; 0.023] | [-0.020; 0.019] | [-0.023; 0.023] | $\Lambda$ = 3 TeV |

# Chapter 2

# The Large Hadron Collider and the CMS detector

## 2.1 Large Hadron Collider

To answer to the open questions left by the SM, and to investigate any signal that new physics can produce, the Large Hadron Collider (LHC) [6] has been built. LHC is an accelerator and a collider built at the European Organization for Nuclear Research (CERN). It is located on the the Swiss-French border, at about 100 m underground. It has a 27 km circumference and it was installed during the years 2000 to 2008 in the existing tunnel complex of the Large Electron Positron (LEP) collider.

The LHC had the first beams injected in the summer of 2008. On 23rd November 2009, the first LHC collisions became available at 900 GeV center-of-mass. Then few months later, on 30th March 2010, protons were accelerated up to energies of 3.5 TeV, resulting in a centre-of-mass energy of $\sqrt{s} = 7$ TeV. In 2012 the LHC run at 8 TeV energy in the centre-of-mass, and in 2015, after a two years technical stop, it reached 13 TeV.

### 2.1.1 Overview

Fig. 2.1 shows the CERN accelerator complex. Prior to being injected into the LHC, the particles are prepared by a series of accelerators that successively increase their energy:

- Linac2 and Linac3: two linear accelerators generating low energy particles: the first, 50 MeV protons, the other, heavy ions;
- PSB: the Proton Synchrotron Booster, where the protons are accelerated to 1.4 GeV and injected into the Proton Synchrotron;

- PS: the Proton Synchrotron, it accelerates the protons to 26 GeV;
- SPS: the Super Proton Synchrotron. An accelerator of 2 km radius used to further increase the proton energy to 450 GeV before they are at last injected;
- LHC: where the proton bunches are accumulated and accelerated to their peak energy, while collisions occur at four intersection points.

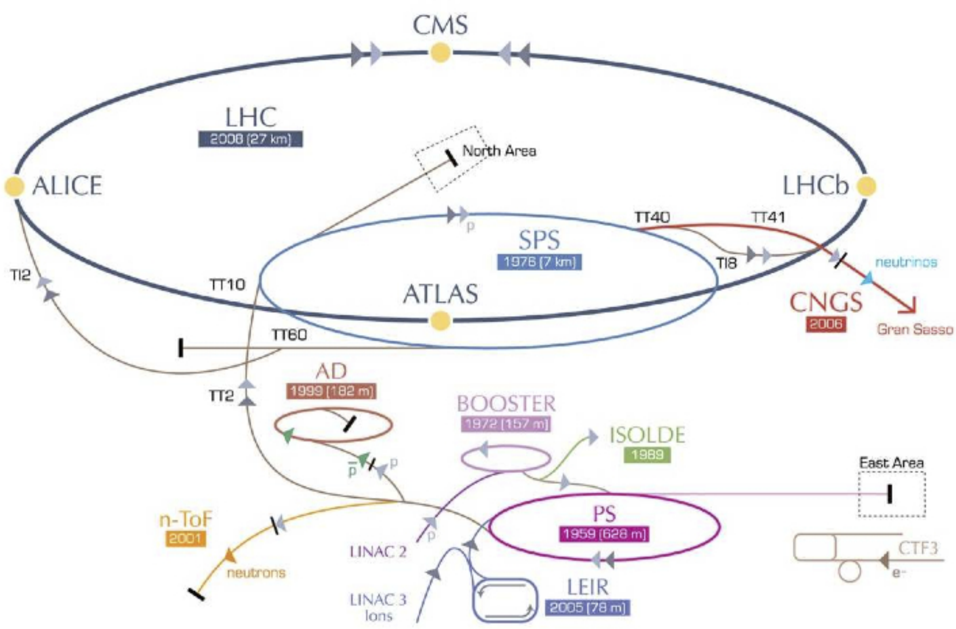


Figure 2.1: Overview of the CERN accelerator complex [6].

### 2.1.2 Luminosity and center-of-mass energy

Since LHC is a hadron accelerator, the interactions are produced at partonic level and the center-of-mass energy will depend on the momentum fraction carried by the partons that interact.

The rate of events $R_i$ of the physics process $i$, defined by the cross section $\sigma_i$, can be expressed as the number of events per unit of time:

$$R_i = \frac{\delta N_i}{\delta t} = \sigma_i \mathcal{L} \tag{2.1}$$

where the luminosity $\mathcal{L}$ is measured per square centimeter and per second. $\mathcal{L}$ depends on the parameters of the accelerator and can be expressed as:

$$\mathcal{L} = f \frac{n_b N_1 N_2}{4\pi\sigma_x\sigma_y} \tag{2.2}$$

where $f$ is the frequency revolution of the $n_b$ bunches in each beam. $N_1$ and $N_2$ are the number of protons in the bunches, while $\sigma_x$ and $\sigma_y$ are the beam size over the two axes at the interaction points. Tab. 2.1 shows the main parameters for the LHC during 2011 and 2012.

| Parameters | Values for 2012 (2011) |
|---|---|
| $\sqrt{S}$ | 8 (7) TeV |
| Maximum luminosity | $7.7 \cdot 10^{33}$ $(3.6 \cdot 10^{33})$ cm$^{-2}$ s$^{-1}$ |
| Number of interactions per bunch | 20.7 (9.1) |
| Protons for bunch | $1.6 \cdot 10^{11}$ $(1.2 \cdot 10^{11})$ |
| Bunches per beam | 1854 (1380) |
| Transverse dimension of the beam | 18.8 $\mu$m |
| Time between bunches | 50 ns |
| Circumference | 26.7 km |
| Injection energy | 450 GeV |
| Crossing points | 4 |
| Number of dipoles | 1232 |
| Number of quadrupoles | 520 |
| Number of hexapoles | 2464 |
| Number of octopoles | 1232 |

Table 2.1: LHC parameter in 2012 (2011) [6].

During the year 2015 the design luminosity of $10^{34}$ cm$^{-2}$s$^{-1}$ will be reach and, after major upgrades during future shut-down periods, the luminosity will reach $5 \cdot 10^{34}$ cm$^{-2}$s$^{-1}$ for the high-luminosity LHC phase (HL-LHC).

### 2.1.3 Main experiments at the LHC

Proton beams collide in four interaction points (IP), at which four detectors are installed:

- CMS (Compact Muon Solenoid) [30];
- ATLAS (A Toroidal LHC ApparatuS) [31];
- LHCb (Large Hadron Collider Beauty experiment) [32];

- ALICE (A Large Ion Collider Experiment) [33].

CMS and ATLAS are general purpose detectors. Their aim is to investigate a wide range of physics: from the search for the scalar boson of the standard model, to searches for new physics beyond the SM, to the precision measurements of processes predicted in the SM. The two experiments have different technical solutions and a different design for the magnet system. ALICE is designed to study heavy ions physics and is an ion-ion/proton-ion collision experiment, accelerated up to total energy of 2.76 TeV/nucleon. LHCb is designed to investigate the physics of B mesons and to perform precision measurements of CP violation in the B meson sector.

## 2.2 The CMS detector

The CMS detector is a hermetic, $4\pi$ multi-purpose detector. All sub-detectors are arranged concentrically around the cylindrical beam pipe and the interaction point (IP). The CMS detector is divided into a central region, called barrel and two endcap regions. The main feature of the CMS detector is the 3.8 T magnetic field, created by a superconducting solenoid, which allows an excellent momentum resolution of reconstructed charged particles. Furthermore, it has three different sub-detectors for the detection of muons. The sandwich-like arrangement of the muon detectors and the iron return yoke give rise to the characteristic appearance of the CMS detector. The weight of the solenoid including the iron return yoke is 11,500 tons, the total weight of the whole detector is 14,000 tons. Its dimensions are a length of 28.7 m and a diameter of 15 m.

Fig. 2.2 shows the CMS experiment. Its main components and features can be summarized as:

- The inner track system: able to guarantee high track reconstruction efficiency and a good momentum resolution of charged particles. Pixel detectors close to the impact region are needed to provide an efficient on-line and off-line $\tau$ and $b$ tagging;
- The electromagnetic calorimeter (ECAL): providing a good energy resolution for photons and electrons, resulting in a good invariant mass resolution for photons pairs (1% at 100 GeV);
- The hadronic calorimeter (HCAL): complementing the ECAL energy measurement and improve the jet energy resolution;
- The magnet: a superconducting magnet of 6 m diameter and 12.5 m length, generating a magnetic field of 3.8 T;

- Muons chambers: able to identify muons, helped by tracker and calorimetric information.

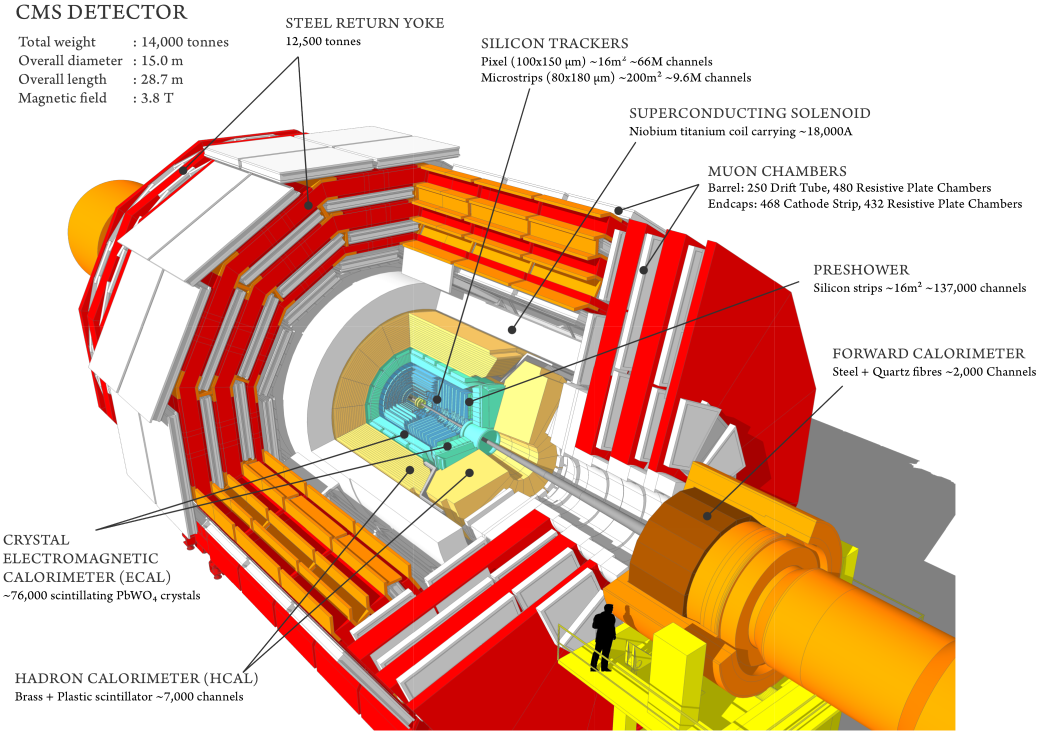


Figure 2.2: Overview of the CMS detector [30].

### 2.2.1 The coordinate system

The coordinate system adopted by CMS has the origin centered at the nominal interaction point inside the experiment. Furthermore:

- the $x$-axis points radially inward toward the center of the LHC;
- the $y$-axis points vertically upward;
- the $z$-axis points along the beam direction, and $xyz$ form a right-handed system;
- the azimuthal angle $\phi$ is defined from the $x$-axis in the x-y projection;
- the polar angle $\theta$ is defined from the $z$-axis;
- the radial coordinate is denoted by r.

For hadron colliders the polar angle $\theta$ is more conveniently replaced by the rapidity $y$, since it is invariant for boost along the $z$-axis. It is defined as:

$$y = \frac{1}{2}\ln\left(\frac{E + p_Z}{E - p_Z}\right), \tag{2.3}$$

where $E$ is the particle energy and $p_z$ is the projection of the momentum along the $z$-axis. For most particles in the final state, $E >> m$, and then the rapidity can be substituted by the pseudorapidity:

$$\eta = -\ln\left(\tan\frac{\theta}{2}\right). \tag{2.4}$$

In the following sections we will discuss all the CMS sub-detectors. The magnet is not a detector but, since it has a fundamental role, it will be treated first.

### 2.2.2 The magnet

CMS uses a solenoidal magnetic field to bend the charged tracks. It is generated by a superconducting magnet of 6 m diameter and 12.5 m length. It is placed after the tracker, the ECAL, and the HCAL, and it generates a magnetic field of 3.8 T [34]. The external muon system instead uses the magnetic properties of the iron yoke that surrounds CMS. The magnetic field lines are forced into the iron of the end-caps and barrel and this provides an additional 2 T magnetic field that is used in conjunction with the muon chambers placed in between the iron yokes to independently measure the momentum of the muons. The solenoid is cooled to 4.5 K, to reach the superconducting phase, and it is traversed by about 19 kA, in order to produce its magnetic field. Due to the large current several hours are needed for its charge and discharge under normal conditions.

### 2.2.3 The tracker

The inner tracking system [35] of CMS is designed to provide a precise and efficient reconstruction of the trajectories of charged particles coming from the collisions, as well as a precise position of secondary vertices.

The tracker is placed in the inner part of the apparatus, immersed in the 3.8 T magnetic field. The high number of particles traversing the tracker for each bunch-crossing requires high granularity in order to identify and reconstruct the trajectories, and a fast response to assign them to the correct bunch crossing. The large particle flux is also an intense source of radiation, hence the detector and its electronics has to be resistant to radiation damage.

Fig. 2.3 shows an r−z view of the modules in one quarter of the CMS tracker.

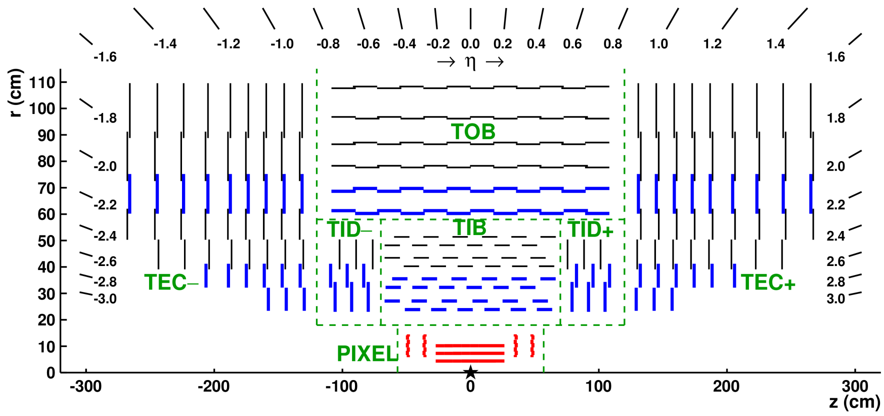


Figure 2.3: Schematic cross section through the CMS tracker in the $r$-$z$ plane [36].

#### 2.2.3.1 The pixel detector

The pixel detector consist of three cylindrical barrel layers at radii of 4.4, 7.3 and 10.2 cm and two disks in each endcap. This system allows to keep the occupancy lower than 1%. The pixel detector counts 66 million pixels with a size of 100 x 150 $\mu m^2$. Additionally, there are two pixel endcaps, which both have two pixel layers at distances of $|z|$ = 34.5 and 46.5 cm. The main task of the pixel tracker is to provide information about the primary interaction point (primary vertex) and displaced decays (secondary vertices) from long-lived unstable particles, like bottom or charm mesons.

#### 2.2.3.2 The strip detector

The silicon strip tracker system provides a coverage of $|\eta| < 2.5$ and consists of almost 15000 modules, which are mounted on a carbon-fiber structure. The strip tracker covers a region between $20 < r < 110$ cm, where the particle flux decreases with respect to the innermost region of the pixel tracker. Therefore silicon micro-strip detectors are used. The barrel sector of the detector is divided in two parts: the inner part called TIB and the outer part called TOB. Similarly the endcaps are divided in two parts called TID and TEC.

The TIB consists of four layers of strip detectors. In the first two layers of the TIB, double-side modules are mounted as stereo modules with an angle of 100 mrad in order to provide a measurement in the $(r - \phi)$ and $(r - z)$ directions. The outermost region of the inner tracking system is referred to as the TOB, which covers a radius between $55 < r < 110$ cm. The significantly lower particle flux allows for the use of larger-pitch silicon micro-strip detectors with a good signal-to-noise ratio. The TOB comprises six layers of strip detectors, where the first two layers are also mounted as stereo modules. In the forward region, there are nine layers of micro-strips in each of the two TECs. The modules are concentric in rings, and rings 1, 2 and 5 have stereo modules. Additionally, there are three layers of TID on each side, in order to fill the gap in the transition region between TIB and TEC.

#### 2.2.3.3 Tracker performances

The interesting $p_T$ range for muons produced from $Z$-boson decays is in general between the 20 and 100 GeV. The reconstruction efficiencies is above 98% for muons and 90% for electrons for $p_T \geq 1$ GeV. The tracking efficiency inside jets is over 95% for particles with $p_T$ larger than 10 GeV and 85% for $p_T \geq 1$ GeV. Fig. 2.4 shows the resolution, as a function of pseudorapidity, on the transverse momentum for isolated muons with $p_T$ = 1, 10, and 100 GeV. The efficiencies on primary and secondary vertices reconstruction are given in Secs. 3.4.1 and 3.4.6.

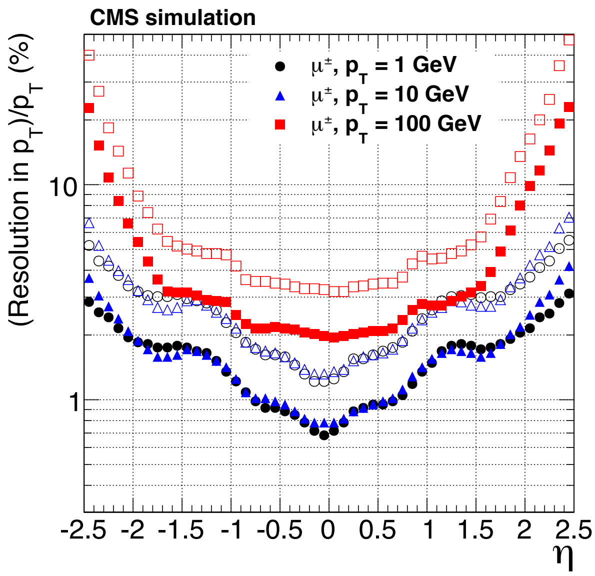


Figure 2.4: Resolution, as a function of pseudorapidity, on the transverse momentum for isolated muons with $p_T$ = 1, 10, and 100 GeV. For each bin in $\eta$, the solid (open) symbols correspond to the half-width for 68% (90%) intervals centered on the mode of the distribution in residuals [36].

### 2.2.4 The electromagnetic calorimeter

The electromagnetic calorimeter (ECAL) plays an essential role in the study of the electroweak symmetry breaking, particularly through the exploration of the scalar sector. The

ECAL is also an important detector element for a large variety of SM and other new physics processes. Consequently, one of the principal CMS design objectives was to construct a very high performance electromagnetic calorimeter. Some considerations based on physics requirements drive the design of the electromagnetic calorimeter:

- optimize the interface with the inner tracking system in front of the ECAL;
- ensure the best possible hermeticity
- minimize the space and material between ECAL and hadron calorimeter to ensure the best jet and missing transverse energy measurements;

To satisfy these requests it has been chosen a scintillating crystal calorimeter, that offers the best performance for energy resolution for electrons and photons.

The ECAL [37] is an hermetic homogeneous calorimeter made of 61200 lead tungstate ($PbWO_4$) crystals mounted in a central barrel and of 7324 crystals in each of two endcaps (Fig. 2.5). This system is completed with a preshower, based on lead absorbers equipped with silicon strip sensors, placed in front of the endcap crystals. The main parameters to

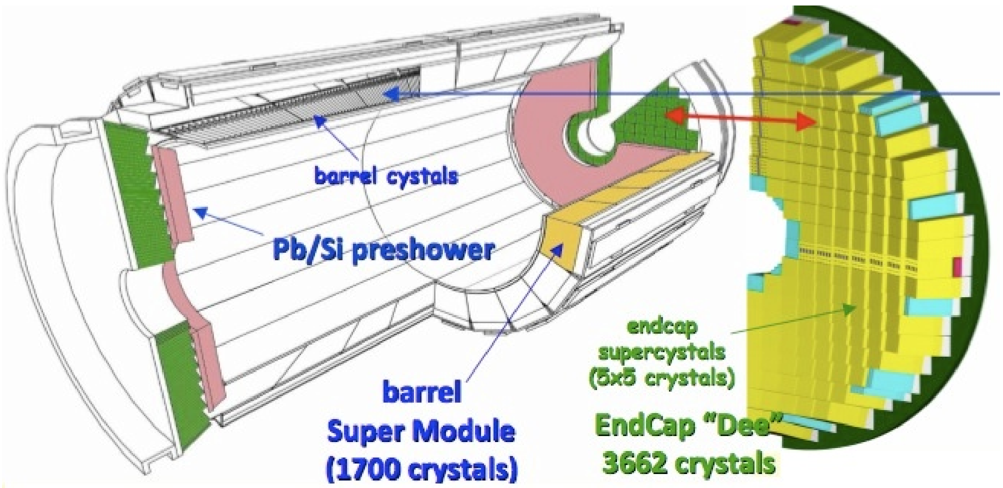


Figure 2.5: A 3-D view of the electromagnetic calorimeter.

define the $PbWO_4$ crystals are the following:

- $X_0$: *radiation length*, characteristic distance by which an electron looses all but $1/e$ of its energy. With the common energies at CMS, 25 $X_0$ give a containment of 98% of the total electron and photon energy;
- $R_M$: *Molière radius*, useful to describe the transversal behavior of the shower, since 90% of the energy is contained into a region of radius $R_M$.

- $LY$: *light yield*, numbers of photons emitted per MeV of energy deposited inside the crystal;
- $\tau$: *emission time* of the crystal. Given the high rate of collisions it has to be very short (few nanoseconds).

In Fig. 2.6 the $PbWO_4$ crystals are compared to other scintillating crystals, commonly used in electromagnetic calorimeters.

| | NaI(Tl) | BGO | CSI | $BaF_2$ | $CeF_3$ | $PbWO_4$ |
|---|---|---|---|---|---|---|
| Density [g/cm$^3$] | 3.67 | 7.13 | 4.51 | 4.88 | 6.16 | 8.28 |
| Radiation length [cm] | 2.59 | 1.12 | 1.85 | 2.06 | 1.68 | 0.89 |
| Interaction length [cm] | 41.4 | 21.8 | 37.0 | 29.9 | 26.2 | 22.4 |
| Molière radius [cm] | 4.80 | 2.33 | 3.50 | 3.39 | 2.63 | 2.19 |
| Light decay time [ns] | 230 | 60<br>300 | 16 | 0.9<br>630 | 8<br>25 | 5 (39%)<br>15 (60%) |
| Refractive index | 1.85 | 2.15 | 1.80 | 1.49 | 1.62 | 2.30 |
| Maximum of emission [nm] | 410 | 480 | 315 | 210<br>310 | 300<br>340 | 440 |
| Temperature coefficient [%/°C] | ~0 | –1.6 | –0.6 | –2/0 | 0.14 | –2 |
| Relative light output | 100 | 18 | 20 | 20/4 | 8 | 1.3 |

Figure 2.6: $PbWO_4$ properties compared to other scintillating crystals [37]

A total thickness of about 26 radiation lengths at $|\eta| = 0$ is required to limit the longitudinal shower leakage of high-energy electromagnetic showers to an acceptable level. This corresponds to a crystal length of 23 cm in the barrel region. The presence of a preshower (a total of $3X_0$ of lead) in the endcap region allows the use of slightly shorter crystals (22 cm). The geometrical crystal coverage extends up to $|\eta| = 3$.

The system has to be maintained to a constant temperature with high precision. In order to preserve energy resolution it requires, hence, a cooling system to keep the temperature of crystals and photo-detectors stable within $\pm$ 0.05 ℃. The nominal operating temperature of the ECAL is 18 ℃, and the cooling system employs water flow to stabilize the detector.

In Fig. 2.7 a longitudinal section of the electromagnetic calorimeter is shown.

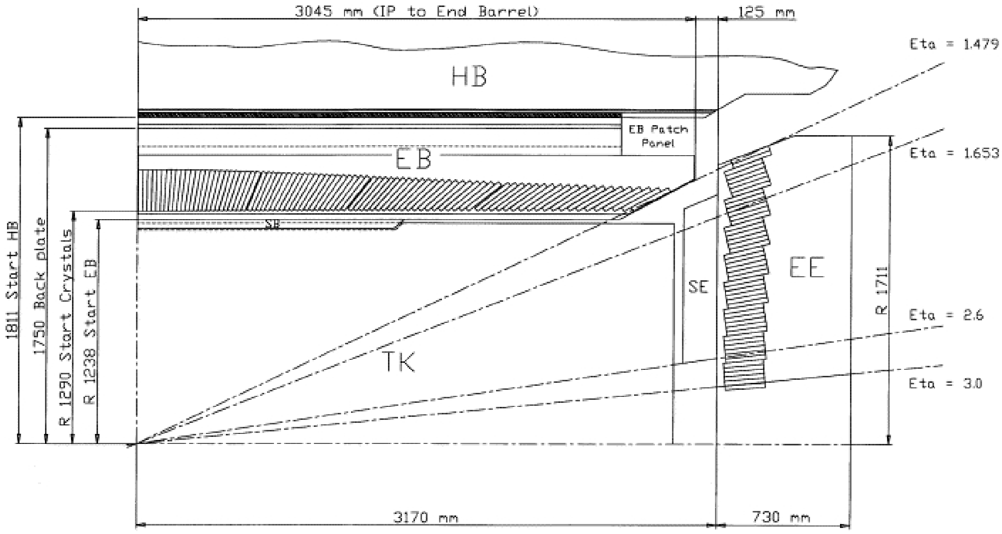


Figure 2.7: Longitudinal section of the electromagnetic calorimeter (one quadrant) [37].

#### 2.2.4.1 The barrel

The barrel (EB) part of the ECAL covers the pseudo-rapidity range $|\eta| < 1.479$ (see Fig. 2.7). The front face of the crystals is at a radius of 1.29 m from the beam axis and each crystal has a front face of 22 x 22 mm$^2$, a rear face of 26 x 26 mm$^2$, and a length of 230 mm, corresponding to 25.8 $X_0$. The truncated pyramid-shaped crystals are mounted in a geometry which is off-pointing with respect to the mean position of the primary interaction vertex, with a 3 ° tilt in both $\phi$ and in $\eta$. The crystal cross-section corresponds to $\Delta\eta$ x $\Delta\phi = 0.0174$ x 0.0174. The barrel granularity is 360-fold in $\phi$ and 2 x 85-fold in $\eta$, resulting in a total number of 61200 crystals. Crystals for each half-barrel are grouped in 18 *super-modules*. Each super-module comprises four modules with 500 crystals in the first module and 400 crystals in each of the remaining three modules. For simplicity of construction and assembly, crystals have been grouped in arrays of 2 x 5 crystals which are contained in a very thin wall (200 $\mu m$) alveolar structure and form a *sub-module*.

The scintillation light is detected by silicon avalanche photodiodes (APDs), especially developed for the CMS ECAL. Each APD has an active area of 5 x 5 mm$^2$ and a pair is mounted on each crystal. The sensitivity to the nuclear counter effect is given by the effective thickness of 6 $\mu$m. It translates a signal from a minimum ionizing particle traversing an APD equivalent to about 100 MeV deposited in the $PbWO_4$. The gain stability directly affects the ECAL energy resolution. Since the APD gain has a high dependence on the bias voltage the APDs require a very stable power supply system.

#### 2.2.4.2 The endcaps

The endcaps (EE) of ECAL covers a pseudo-rapidity range from 1.48 to 3.0. Despite that the design of the endcaps provides precision energy measurement up to $|\eta| \leq 2.6$.

The mechanical design of the endcap calorimeter is based on an off-pointing pseudo-projective geometry using crystals of the same shape and dimensions. Each crystal has a front face of 28.6 x 28.6 mm$^2$, a rear face of 30 x 30 mm$^2$, and a length of 220 mm, corresponding to 24.7 $X_0$. Crystals are grouped together into units of 25, referred to as *super-crystals*. A total of 268 identical super-crystals will be used to cover each endcap with a further 64 sectioned super-crystals used to complete the inner and outer perimeter. Each endcap contains 7324 crystals, corresponding to a volume of 1.52 m$^3$. Both endcaps are identical.

In the endcaps, the photodetectors are vacuum phototriodes (VPTs). Vacuum phototriodes are photomultipliers having a single gain stage. These particular devices have an anode of very fine copper mesh (10 $\mu$m pitch) allowing them to operate in the 3.8 T magnetic field. Each VPT is 25 mm in diameter, with an active area of approximately 280 mm$^2$; one VPT is glued to the back of each crystal.

#### 2.2.4.3 The preshower

The preshower (ES) detector covers a smaller $\eta$ range compared to the EE, it starts at $|\eta| =$ 1.65 to reach 2.61. The main purpose of the preshower is the $\gamma$-$\pi^0$ separation.

The preshower detector, placed in front of the endcaps crystals, contains two lead converters of a total thickness of 2 $X_0$ and 1 $X_0$ respectively, thus about 95% of single incident photons start showering before the second sensor plane. The orientation of the strips in the two planes is orthogonal. Each silicon sensor measures 63 x 63 mm$^2$, with an active area of 61 x 61 mm$^2$ divided into 32 strips (1.9 mm pitch). The nominal thickness of the silicon is 320 $\mu$m; a minimum ionizing particle will deposit 3.6 fC of charge in this thickness (at normal incidence).

The impact position of the electromagnetic shower is determined by the centre-of-gravity of the deposited energy. The accuracy is typically 300 $\mu m$ at 50 GeV. In order to correct for the energy deposited in the lead converter, the energy measured in the silicon is used to apply corrections to the energy measurement in the crystal. The fraction of energy deposited in the preshower (typically 5% at 20 GeV) decreases with increasing incident energy.

The ES information is important for the reconstruction of low energy $\pi^0$, and it provides information not only on the energy deposited in the preshower, but also a more accurate estimation of the $\pi^0$ position, since the strip dimensions are $\sim$ 10 time smaller than the crystal one.

#### 2.2.4.4 Performance

The energy resolution of a calorimeter can be parametrized as:

$$\left(\frac{\sigma}{E}\right)^2 = \left(\frac{S}{\sqrt{E}}\right)^2 + \left(\frac{N}{E}\right)^2 + C^2 \tag{2.5}$$

where $S$ is a stochastic term, that takes into account fluctuations in the number of produced and collected photons, $N$ is the noise term, that reproduces the electronic noise and the signal pileup due to simultaneous collisions, and $C$ is the constant term, that takes into account contributions such as:

- the stability of working conditions, such as temperature and high voltage;
- the presence of dead material between the crystals and the rear and lateral leakage of the electromagnetic shower;
- the non-uniformity of the longitudinal light collection, due to the truncated pyramidal shape of the crystals and to the high refractive index;
- the inter-calibrations between the crystals;
- the radiation damage of the crystals, the exposition of the crystals to high radiation dose, resulting in a change of detector response to the deposited energy.

The values of the stochastic, noise, and constant terms have been derived at test beam [38], and they are 0.028 $\sqrt{\text{GeV}}$ for $S$, 0.12 GeV for $N$, and 0.3 for $C$.

In Fig. 2.8 photon resolution has been computed in situ and it has been compared to simulation. The resolution estimation uses $Z \to ee$ events, where the electrons are reconstructed as photons [39] in different $\eta$ ranges. The events have been divided in two $R_9$ category, defined as the energy sum of the 3x3 crystals centered on the most energetic crystal in the supercluster divided by the energy of the supercluster. $R_9$ discriminates between unconverted, or late converted photons, from converted photons.

#### 2.2.4.5 ECAL calibration strategy

The signals from the ECAL channels are first shaped and then amplified with multiple gains before subsequent digitization by a multiple channel ADC. Signals are digitized by the ADC every 25 ns and in standard operation the signal from an event is read out as a series of 10

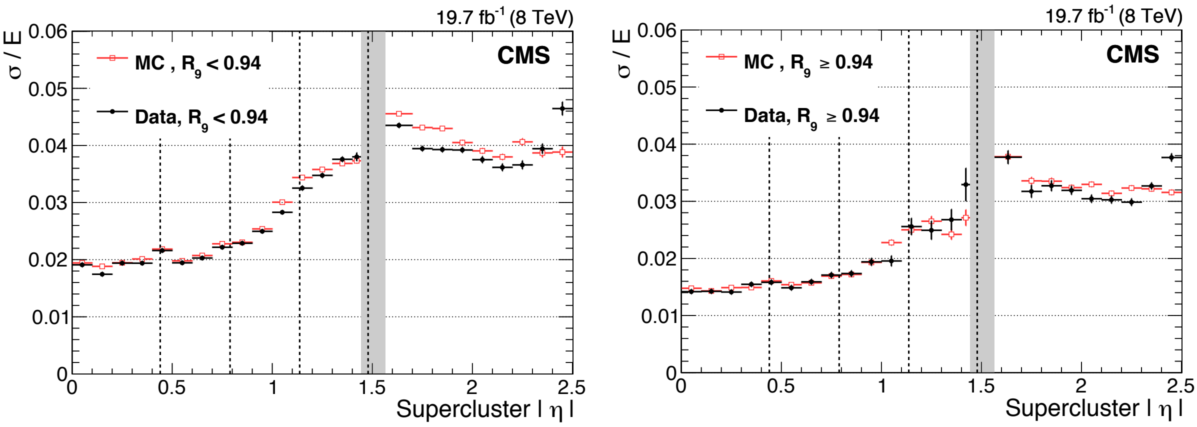


Figure 2.8: Photon resolution in data and simulation using $Z \to ee$ events, reconstructing the electrons as photons in different $\eta$ ranges. Left plot shows the $R_9 < 0.94$ category, right plot shows the $R_9 > 0.94$ category. [39].

samples. The amplitude of the signal is reconstructed from crystals that are uncalibrated using a linear combination of these samples: $A = \Sigma_i w_i \cdot S_i$, where $S_i$ is the sample value in ADC counts and $w_i$ is a weight. For each crystal an ADC to GeV conversion factor is applied, as well as the inter-calibration factor ($C_i$) of the corresponding channel to calibrate the signal.

The ECAL was pre-calibrated before installation using several methods. The final calibration is done in-situ using collision data. The estimated particle energy, obtained from the ECAL, can be expressed as:

$$E = F \cdot \Sigma_i G(GeV/ADC) \cdot C_i \cdot A_i \tag{2.6}$$

where the sum is over the crystals in a cluster and $G$ is the ECAL energy scale. The factor $F$ is defined as an additional energy correction which depends on the type of the particle, its energy and pseudorapidity and in particular takes into account shower leakage and bremsstrahlung losses for electrons. In addition, variations in the crystal light output and transparency are monitored with a laser-based system.

The inter-calibration of the ECAL detector represents a fundamental part of the reconstruction path. In fact the energy measured from the ECAL crystals do not enter only in the photon reconstruction, but also into the jet reconstruction and the missing transverse energy computation. For high energy particles (more than few tens of GeV) the resolution is dominated by the constant term. The main contribution to the constant term is the calibration precision. To fully exploit the CMS and ECAL physics potential (in particular for the measurement of $H \to \gamma\gamma$), it is necessary to maintain an inter-calibration precision of 0.5% level or better.

There are several methods to derive inter-calibration constants, that are combined in order to provide the final inter-calibration to CMS. The $\phi$-symmetry inter-calibration provides a fast inter-calibration exploiting invariance around the beam axis of energy flow. This method inter-calibrates crystals at the same pseudorapidity. The $\pi^0$ and $\eta$ calibration uses the photon pairs selected as $\pi^0(\eta) \to \gamma\gamma$ candidates. Finally isolated electrons from $W \to e\nu$ and $Z \to ee$ decays can be used to compare the energy measured in ECAL to the track momentum measured in the silicon tracker.

During my thesis I worked on the derivation of the inter-calibration constants [40] using $\pi^0$ and $\eta$ resonances. The $C_i$ parameters are derived using the reconstructed invariant mass of known resonances ($\pi^0$ and $\eta$) decaying in a pair of photons. The photons are reconstructed using a cluster of 3x3 crystals. The ES information has been used to correct the photon energy for energy deposited in the preshower, furthermore it provides a more accurate estimation of the photon position, thanks to the ES strips dimension, $\sim$ 10 time smaller than the crystal one. The photon energy is also corrected using a multivariate analysis, that takes into account the energy loss due to the crack between the ECAL modules or super-modules. From the ratio between the reconstructed mass of the mesons, and the true mass value, it is possible to extract the energy correction to be applied on the crystals, that restore the correct invariant mass value.

The precision achieved on the inter-calibration constants are shown in Fig. 2.9. The precision is computed as the spread of the difference between the constants derived with data and the ones computed in the test beam in the barrel (left), and in beam splashes in the endcaps (right). Different inter-calibration methods are compared.

### 2.2.5 The hadronic calorimeter

The hadronic calorimeter [42], in complement to the tracker and the ECAL, allows the measurement of the energy and position of the hadrons. It plays an essential role in the identification of the quarks and gluons. Moreover, it helps to indirectly detect particles that do not interact with any detector such as neutrinos. This is possible since the collinear beams have a initial momentum on the transverse plane ($p_T$) close to zero; summing vectorially the total transverse energy in the event the unbalanced energy can be attributed to the neutrinos ($E_T^{miss}$) that escape the detection. The hadron calorimeter will also help in the identification of electrons, photons and muons in conjunction with the electromagnetic calorimeter and the muon system.

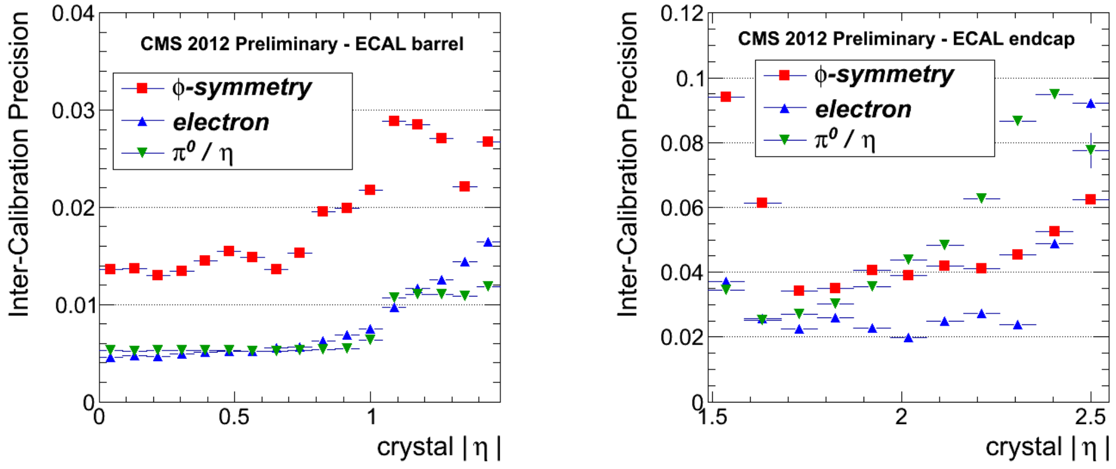


Figure 2.9: Precision achieved on the inter-calibration constants, computed as the spread of the difference between the constants derived with data and the ones computed in the test beam in the barrel (left), and in beam splashes in the endcaps (right). Different inter-calibration methods are compared. [41].

Since most of the calorimeter is located inside the CMS superconducting magnet coil the design of HCAL is strongly influenced by the choice of magnet parameters. An important requirement of the HCAL is to minimize the non-Gaussian tails in the energy resolution and to provide good containment of hadronic shower and hermeticity for missing energy measurements. The HCAL design maximizes the material inside the magnet coil in terms of interaction lengths. The requirement of maximizing the amount of absorber before the magnet, results into minimum space for the active medium. The brass has been chosen as absorber material as it has reasonable short interaction length and it is non-magnetic material. The scintillator tile technology makes an ideal choice. It consists of plastic scintillator tiles having wavelength-shifting (WLS) fibers to transport the light. The WLS fibers are spliced to high attenuation-length clear fibers outside the scintillator that carry the light to the readout system-photo-detectors. The photo-detection readout is based on multi-channel hybrid photo-diodes (HPDs). The gap between the barrel and the endcap HCAL, through which the cable services of the ECAL and inner tracker pass, is inclined at 53 ° and points away from the center of the detector.

In order to contain as much energy as possible the HCAL (Fig. 2.10) is split into three main components:

- HB: that covers $|\eta| < 1.26$;
- HE: composed from 2 identical endcaps, that reach $|\eta| = 3$;

- HF: the only one outside the solenoid, extending up to $|\eta| = 5.3$.

#### 2.2.5.1 The barrel and the endcaps

The HB part is divided in 18 wedges in $\phi$ and 16 in $\eta$; each towers cover a $\Delta\eta$ x $\Delta\phi \approx 0.084$ x 0.084.

Each wedge is composed of 17 layers of absorber and active elements. Since this part is operated inside the magnetic field the absorber is non-magnetic brass composed by 90% Cu and 10% Zn plus some trace of stainless steel for the innermost and outermost layers to provide more structural strength. The brass has a short interaction length, needed to keep the detector as compact as possible.

The layers of active material are composed of 4-mm-thick plastic scintillators. Optical guides collect the light they emit. Some additional scintillators have been placed before the muon chambers, outside the solenoid (HO), to measure the most energetic jets that cannot be fully contained by the HB.

The HE contains tower with the same technology, their area for the region $|\eta| < 1.7$ is the same than in the HB with cells of size $\Delta\eta$ x $\Delta\phi \approx 0.175$ x 0.175.

#### 2.2.5.2 The forward region

The HF is divided into 36 wedges in $\phi$ and 12 segments in $\eta$ and since no magnetic field is present it does not have the same non-ferromagnetic requirements. On, the other hand, it has to resist to radiation. The material used is quartz in this case. The quartz fibers emit Cherenkov light detected by photo-multipliers located in areas with less radiations exposure.

#### 2.2.5.3 Performance

Parts of the various HCAL subsystems have been exposed in 2008 to beams of electrons, pions, protons and muons, to measure their characteristics and to obtain a reference calibration. The hadronic energy resolution of the HCAL and ECAL combination can be parametrized as $\sigma/E = a/\sqrt{E} \oplus b$, where $a$ corresponds to a stochastic term and $b$ to a constant term. It has been measured $a$= 0.847 $\pm$ 0.016 GeV and $b$ = 0.074 $\pm$ 0.008, with E measured in GeV, in the barrel. The energy resolution in the endcaps is similar, and the corresponding values for HF are $a$ = 1.98 GeV and $b$ = 0.09 [43]. From 2011 in situ measurements the total energy scale uncertainty is smaller than 3% for $p_T > 50$ GeV in the region $|\eta| < 3.0$. In the forward region, $3.0 < |\eta| < 5.0$, the energy scale uncertainty for calorimeter jets increases to 5%. The jet $p_T$-resolution has been studied, using the dijet and

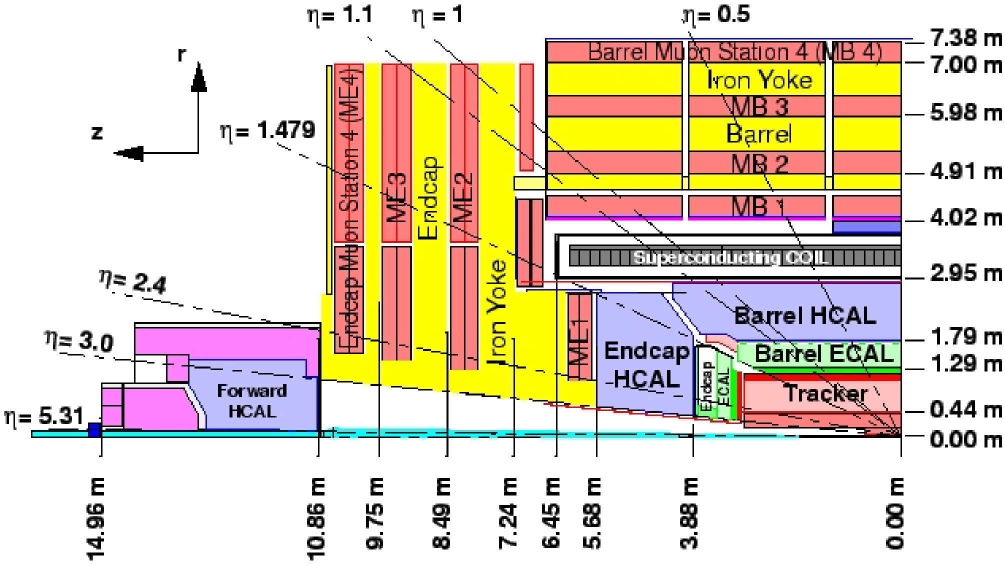


Figure 2.10: Longitudinal view of one quadrant of CMS. HB, HE and HF are shown [42].

$\gamma$+jets samples in both data and simulation. For particle-flow (PF) [44] jets in the region $|\eta| < 0.5$ with a $p_T$ of 100 GeV the measured resolution in the data is better than 10% [45].

### 2.2.6 The muon chamber

The muon system [46] is the outermost part of the CMS detector and it is divided into three main subsystems according to their location inside the detector and their use. Due to the shape of the solenoid magnet, the muon system was naturally driven to have a cylindrical, barrel section and 2 planar endcap regions. In the barrel region, where the neutron-induced background is small, the muon rate is low, and the 3.8 T magnetic field is uniform and mostly contained in the steel yoke, drift tube chambers (DT) with standard rectangular drift cells are used. In the 2 endcap regions of CMS, where the muon rates and background levels are high and the magnetic field is large and non-uniform, the muon system uses cathode strip chambers (CSC). Because of the uncertainty in the eventual background rates and in the ability of the muon system to measure the correct beam-crossing time when the LHC reaches full luminosity, a complementary, dedicated trigger system consisting of resistive plate chambers (RPC) was added in both the barrel and endcap regions. In figure 2.11 the different sub-detectors are shown.

The whole system has been designed to achieve the best transverse momentum measurement for muons in a wide range of energies, from a few GeV up to the TeV scale.

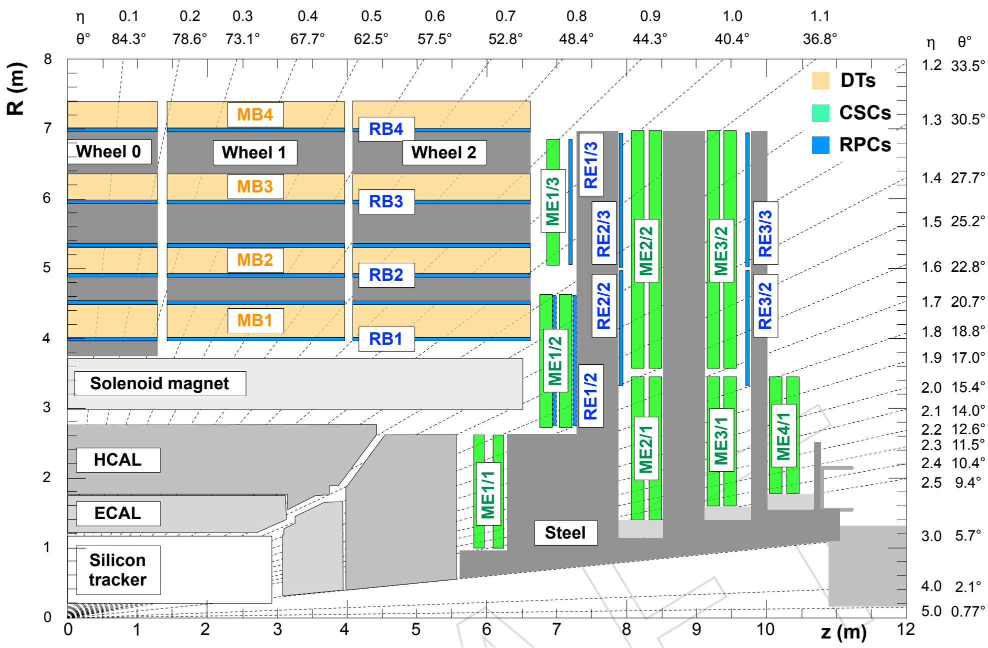


Figure 2.11: Longitudinal view of three muon sub-detectors [46].

#### 2.2.6.1 Drift tube chambers

The drift tube chambers muon subsystem, reach a pseudo-rapidity $|\eta| < 1.2$. They are made of five wheels, each divided into 12 sectors, covering an azimuthal region of 30 degrees. Each sector is organized into 4 stations interspersed among the layers of the flux return plates. The first 3 stations contain 12 chambers, in 3 groups (super-layers) of 4 layers, which measure the muon coordinate in the $r - \phi$ bending plane, and 4 layers which provide a measurement in the $z$ direction, along the beam line. The fourth station does not contain the $z$-measuring planes. The 2 super-layers (SL) measuring the $r - \phi$ plane are separated as much as possible to achieve the best angular resolution.

In Fig. 2.12 (left) is shown a sector. Each SL is made of 4 layers of long rectangular drift cells staggered by half a cell. The drift cell is 2.4 m long with a section of 13 x 42 mm$^2$. The characteristic dimension of the drift cell is 21 mm, thus the maximum drift time is 380 ns in the gas mixture of 85% Ar and 15% $CO_2$. The super-layer is a basic measuring unit of the DT station.

Since one SL is a group of 4 consecutive layers of thin tubes staggered by half a tube, it gives excellent time-tagging capability, with a time resolution of a few nanoseconds. This capability provides local, stand-alone and efficient bunch crossing identification. The time tagging is delayed by a constant amount of time equal to the maximum possible drift-time, which is determined by the size of the tube, the electrical field and the gas mixture. The design and the precise mechanical construction of the DT chamber allowed them to achieve 100 $\mu m$ precision in global $r - \phi$ position measurement.

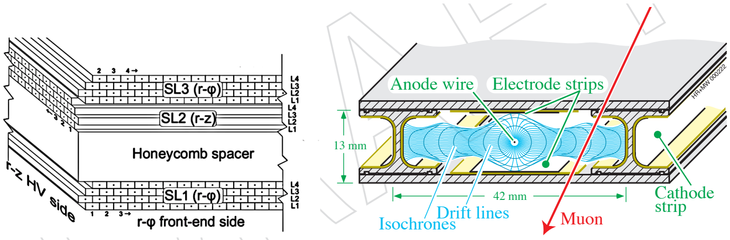


Figure 2.12: Left: Schematic view of a DT chamber. Right: Section of a drift tube cell showing the drift lines [46].

#### 2.2.6.2 Cathode strip chambers

The Cathode Strip Chambers (CSC) provide precise tracking and triggering of muons in the endcaps. The region $0.9 < |\eta| < 1.2$ is covered by DT and CSC. The two muon endcaps contain 468 CSCs, each endcap is divided into four stations (ME1, ME2, ME3 and ME4) perpendicular to the beam direction. They increase the distance from the interaction point from 6 to 10 meters.

Each CSC (Fig. 2.13) is trapezoidal in shape and consists of 6 gas gaps, each gap having a plane of radial cathode strips and a plane of anode wires running almost perpendicularly to the strips. The gas ionization and subsequent electron avalanche caused by a charged particle traversing each plane of a chamber produces a charge on the anode wire and an image charge on a group of cathode strips. Thus, each CSC measures the space coordinates (r, $\phi$, z) in each of the 6 layers.

#### 2.2.6.3 Resistive plate chamber system

Resistive Plate Chambers (RPC) are gaseous parallel-plate detectors that combine adequate spatial resolution with a time resolution comparable to that of scintillators. They complement the muon tracking system: drift tubes (DT) in the barrel and cathode strip chambers (CSC) in the endcaps.

The RPC time resolution of a ionizing particle is much shorter than the 25 ns time separation between LHC bunch crossings, so it allows the identification of the relevant bunch crossing to which a muon track is associated with [47].

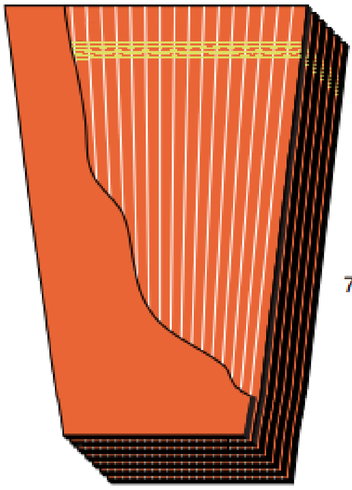


Figure 2.13: Cathode strip chambers [46].

#### 2.2.6.4 Performance

The measurement of the muon transverse momentum is highly sensitive to the alignment of the tracker and of the muon chambers, to the composition of material and its distribution inside the tracking volume, and to the knowledge of the magnetic field inside and outside the solenoid volume. The momentum scale and resolution of muons have been studied using different approaches in different $p_T$ ranges. At low and intermediate $p_T$ ($\leq$ 100 GeV), the mass constraint of dimuon decays from the $J/\psi$ and $Z$ resonances is used to calibrate the momentum scale and measure the momentum resolution. In the high-$p_T$ range ($\geq$ 100GeV), the muon momentum scale and resolution can be measured using cosmic-ray muons (with the exception of the high-$|\eta|$ region). A sample of muons produced in the decays of $Z$ bosons is well suited for measuring the muon momentum scale and resolution in the intermediate range of transverse momentum, $20 < p_T < 100$ GeV.

The momentum resolution for muons reconstructed only with the muon system (standalone muons) is estimated using the $p_T$ of the tracker track as reference:

$$R^{sta}(\frac{1}{p_T}) = \frac{\left((\frac{1}{p_T})^{sta} - (\frac{1}{p_T})^{trk}\right)}{(\frac{1}{p_T})^{trk}} \tag{2.7}$$

As the resolution of the tracker tracks at low and intermediate $p_T$ is expected to be about an order of magnitude better than the resolution of the standalone-muon tracks, Eq.2.7 provides a good estimate of the resolution for standalone muons. The resolution of standalone-muon tracks is shown in Fig. 2.14. The relative difference between the resolutions measured with respect to the tracker-track $p_T$ and the true $p_T$ was evaluated from simulation and found to be smaller than 1% in the barrel and smaller than 5% in the endcaps.

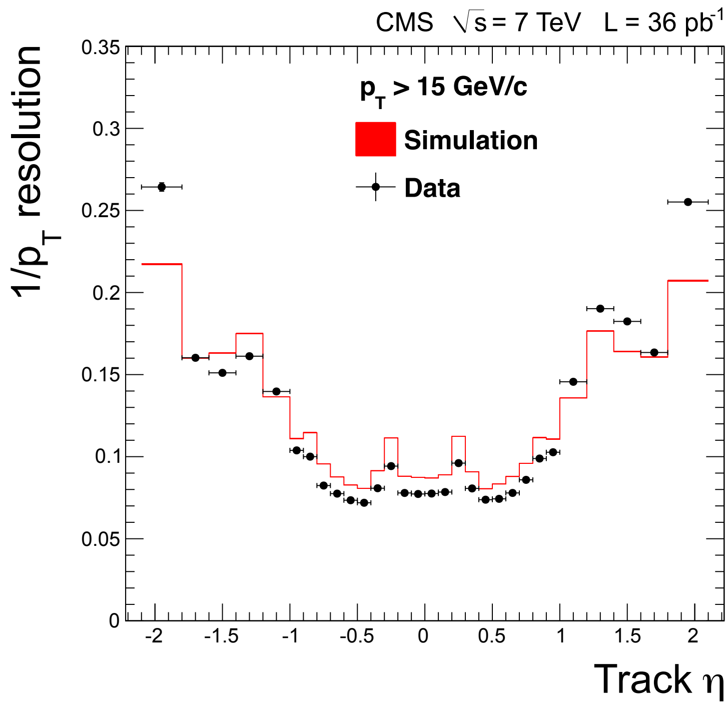


Figure 2.14: Resolution of standalone-muon tracks with respect to tracker tracks, as a function of $\eta$ of the tracker track for muons with $p_T > 15$ GeV. Resolution is estimated as the $\sigma$ of a Gaussian fit to $R^{sta}(\frac{1}{p_T})$ [48].

### 2.2.7 The Trigger

The design luminosity will provide a rate of 40 MHz and a size for the single event of 1 MB. Due to the impossibility to store such amount of information an advanced trigger system is required in order to reduce the selected event rate to few hundreds Hz.

The trigger system achieves this goal reducing the rate in two steps:

- Level-1 (L1) Trigger;
- High-Level Trigger (HLT).

#### 2.2.7.1 Level 1 trigger

L1 consists of custom-designed, largely hardware based, programmable electronics, whereas the HLT is a software based system implemented in a farm of about one thousand computer processors.

The reduction needed is a factor $10^6$, combining in series the two triggers. This means that L1 will provide an output of 100 kHz to HLT, implemented as a computer processing farm that is designed to achieve a rejection factor such that few hundred events/second are written to mass computer storage.

The L1 trigger is subdivided into three subsystems: L1 Global Calorimeter trigger (GCT), the L1 Global Muon trigger (GMT) and the L1 Global trigger (GT). The Muon trigger is organized in three sub-system that represent the three different muon detector systems, the Drift Tube Trigger in the barrel, the Cathode Strip Chamber trigger in the endcap and the Resistive Plate Chamber (RPC) trigger covering both barrel and endcap. Combining the trigger information from the DT, CSC and RPC trigger into a L1 Global trigger, it is possible to take the decision to reject an event or to accept it for further evaluation by the HLT.

Fig. 2.15 shows all these processes. The global Muon decision is based on algorithm calculations and on the readiness of the sub-detectors and the Data Acquisition System (DAQ), which is determined by the Trigger Control System (TCS).

The processing must therefore be pipelined in order to enable a quasi-deadtime-free operation. The L1 Trigger electronics is housed partly on the detectors, partly in the underground control room located at a distance of approximately 90 m from the experimental cavern.

#### 2.2.7.2 High level trigger

Thus the main purpose of High-Level Trigger (HLT) system is to read the CMS detector event information for those events that are selected by the Level-1 Trigger and to select, from among those events, the most interesting ones for output to mass storage.

The HLT contains many trigger paths, each corresponding to a dedicated trigger. A path consists of several steps (software modules), each module performing a well-defined task such as unpacking (raw to digi), reconstruction of physics objects (electrons, muons, jets, $E_T^{miss}$, etc.), making intermediate decisions triggering more refined reconstructions in subsequent modules, or calculating the final decision for a trigger path. The CMS framework ensures that if an intermediate filter decision on a trigger path is negative, the rest of the path is not executed and the specific trigger is regarded as rejecting the event. In order to save CPU time, each reconstruction step is followed by a filter in order to avoid running

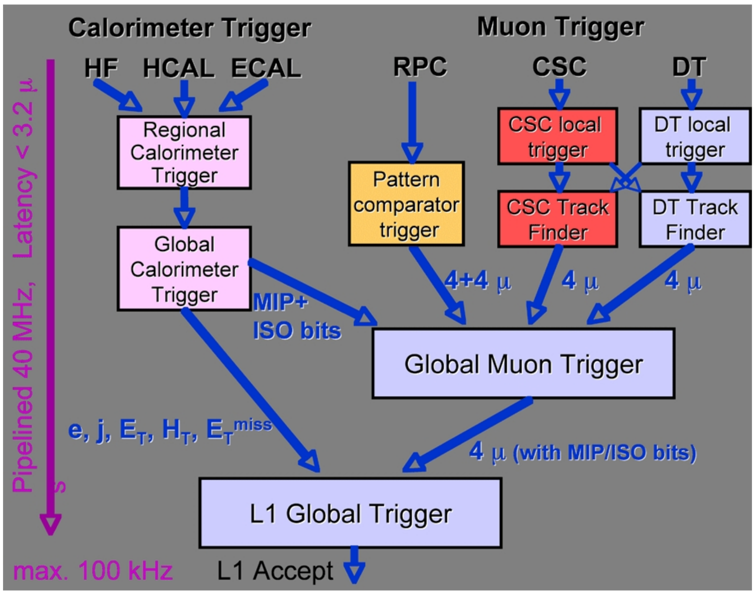


Figure 2.15: Level 1 trigger [49].

time-consuming code if it is already clear it will not be needed.

# Chapter 3

# Measurement of the Z boson pair production cross section

In this chapter, the measurement of the $Z$ boson pair production cross section is described.

Sec. 3.1 describes the analysis strategy, Sec. 3.2 briefly explains the event simulation programs used in the analysis to compare the data to the SM predictions, and to correct for the detector acceptance and for the selection efficiency. In Sec. 3.4 and 3.5 the physic objects reconstruction and the simulation weights used to correct for discrepancy between the data and the simulation are discussed. Then in Sec. 3.6 and 3.7 the reduced missing transverse energy variable and the final selection used to measure the cross section are presented. Finally in Sec. 3.8, 3.9 and 3.10 the data driven estimation of the backgrounds, the systematic uncertainty on the final measure, and the measurement of the cross section are explained.

## 3.1 The $2l2\nu$ final state and the analysis strategy

The $Z$ boson decays into a lepton or a quark pair, hence the $ZZ$ production could produce different final states. Two channels have been exploited for the $ZZ$ cross section measurement. In the first channel one $Z$ boson decays into a $e^+e^-$ or a $\mu^+\mu^-$ pair and the other boson into a $e^+e^-$, $\mu^+\mu^-$ or $\tau^+\tau^-$ pair. This channel will be further denoted as $2l2l'$, where $l$ stands for $e$ or $\mu$ and $l'$ stands for $e$, $\mu$, or $\tau$ (the $4\tau$ final state has not been used since it has too large background). In the second channel one $Z$ boson decays into a $e^+e^-$ or $\mu^+\mu^-$ pair, and the other decays into neutrinos. This channel will be denoted $2l2\nu$.

The $2l2\nu$ final state benefits from higher branching ratio that the $2l2l'$ channel. This allows data to be collected in the tails of the kinematic distributions. In particular, the tail of the visible $Z$ boson transverse momentum is sensitive to the presence of aTGCs. Competitive limits can thus be set in the $2l2\nu$ final channel.

The selection requires two high $p_T$ leptons plus a significant momentum imbalance in the transverse plane, measured by the missing transverse energy $E_T^{miss}$. Since $Z+jet$ production is four orders of magnitude larger than $ZZ$ production, but it only produces instrumental $E_T^{miss}$, a high $E_T^{miss}$ cut must be applied in order to improve the signal purity.

The remaining contamination is still significant since the detailed detector simulation is not sufficient to describe the tails of the instrumental $E_T^{miss}$ in the $Z+jet$ events. Thus a high statistic control sample has to be used in order to model these tails. In addition, since fake $E_T^{miss}$ mostly comes from mismeasured jets, a jet veto is applied. This veto causes a systematic uncertainty in the $Z$ boson $p_T$ spectrum, that needs to be carefully evaluated. Eventually, as high order electroweak corrections to $ZZ$ production are significant at high $Z$ transverse momentum, these corrections have to be included in the modeling of the $ZZ$ cross section. These corrections are not included in the standard generation, therefore a dedicated table of corrections provided by theorist has been applied (see Sec. 1.2.4).

The trigger used in this analysis requires data to contain at least two high-$p_T$ leptons. The typical $p_T$ cut applied at trigger level is 17 GeV on the leading $p_T$ lepton (see Sec. 3.3.3 for more details). There are several SM processes that can fulfill such requests in addition to $ZZ$. The most important are:

- Drell-Yan (DY) process: dilepton production from a $\gamma$ or a $Z$. This process has high cross section but no genuine $E_T^{miss}$;
- Fully leptonic $t\bar{t}$ and single-top decay: lead to b-jet in the final state;
- Dibosons production: $WW$ and $WZ$.

Part of these backgrounds can be rejected requesting further constrains, others are called *irreducible* backgrounds since they simulate perfectly the signal, i.e. $WW \to l\nu l\nu$ process and the $WZ \to l\nu ll$ process, where the lepton from the $W$ boson is produced out from the CMS acceptance. We can also divide these backgrounds into *resonant* or *non-resonant* backgrounds, depending on the presence of a $Z$ or not.

As shown in Sec. 1.2.4 the $ZZ$ process has a low cross section. To reduce the background, a tight selection is applied (see Sec. 3.7). The efficiency of the selection is accounted for the cross section estimation. In a counting analysis, the observed number of events $N^{data}$ is related to the cross section of the process by the following formula:

$$\sigma = \frac{N^{data} - N^{back}}{\mathcal{L}^{int} \cdot A \cdot \epsilon} \tag{3.1}$$

where $N^{back}$ is the number of background events, $\mathcal{L}^{int}$ is the integrated luminosity, $A$ is the geometrical acceptance, and $\epsilon$ is the selection efficiency. The number of background events $N^{back}$ is estimated from data in the case of non resonant background and DY, and taken from the simulation otherwise.

A method that provides a better precision relies on the difference between the distribution of a discriminating variable for the signal and the backgrounds (e.g. $E_T^{miss}$). The signal and the background distributions are constrained to the data through a fit. During the fit the signal is free to vary, while the backgrounds are constrained to their expected values. In this way is possible to extract the signal normalization, measuring the $ZZ$ production cross section. This method is called *shape analysis*, and it improves the total precision of the measurement, as it allows to make use of the intervals of the discriminating variables where the signal-to-background ratio is small. This method will be explained in Chap. 3.10.

In summary the main features of this measurements are:

- a dataset containing two energetic leptons ($e$ or $\mu$);
- the request of significant $E_T^{miss}$ and the jet-veto;
- a data-driven modeling of the instrumental $E_T^{miss}$ from $\gamma + jet$ events;
- an estimation of systematic uncertainty from the jet-veto that is consistent with the ATLAS and CMS prescriptions for scalar boson searches;
- the application of the NLO EWK corrections in the $ZZ$ and $WZ$ production;
- a shape analysis of the $E_T^{miss}$ distribution in order to extract the cross section.

## 3.2 Simulation tools

The prediction should describe how a physical process, from the standard model or from new physics, could be seen in the experiment.

Once all the relevant SM processes are simulated, comparing expectation with data is possible. Having a reliable Monte Carlo (MC) simulation allow to separate the different processes composing the data.

The event generation consists in the following steps:

- generate the Feynman diagrams involved in the hard process;
- compute the matrix elements from the Feynman diagrams;

- convolute it with the parton distribution function in order to compute the total and differential cross-section;
- generate random events according the full differential cross section and create the four momentum vectors of the final state particles.

Quarks and gluons cannot exist in the bare state since they are colored particles. The interactions of these particles, as they move apart, are simulated by the so-called *parton shower*. In the parton shower a cascade of colored particles are produced. Gluons are emitted from the colored partons, and also split into pairs of quark and antiquarks. Partons that are close in the phase space can combine into hadrons. This phase is called fragmentation. Fragmentation is described by a parametrization of the non-perturbative QCD physics. Short lived articles are also decayed by the generator. For particles that reach the detector, the detector simulation takes their decay in charge.

In proton-proton collision, the remnants of the protons that did not participate in the hard process are colored. Their interaction is modeled by parametrizing additional partonic interactions. Eventually several proton-proton interactions occur at the same bunch crossing for all the luminosity values in which the data analyzed in this thesis are taken.

The $ZZ \to 2l2\nu$ signal process is simulated using MadGraph5_aMC@NLO [23], an event generator that computes SM cross sections at NLO accuracy. MadGraph has been used also to generate $WW \to 2l2\nu$, $WZ \to 3l\nu$, $Z$+jets, $W$+jets, and the $tt$+jets background processes. Single top-quark processes are simulated with POWHEG [50]: a general computer framework for implementing NLO calculations in shower Monte Carlo programs. Finally *SHERPA* [51] has been used to generate the SM plus anomalous coupling $ZZ$ production. Sherpa is LO generator and once again $k$-factors have been derived from MCFM as it will be explained in Sec. 4.

### 3.2.1 MCFM

The Monte Carlo for FeMtobarn processes (MCFM) is a parton-level Monte Carlo program which gives NLO predictions for a range of processes at hadron colliders [16].

MCFM gives the possibility to compute NLO cross sections modifying the parton density functions (PDF), or the renormalization and factorization scales, and to specify the generation cuts to be used in the computation. Such possibility will be used to estimate some of the systematic errors related to the cross section measurement (Sec. 3.9).

### 3.2.2 Detector simulation

Simulated events should be as close as possible to real data events. Hence the primary goal of the detector simulation program is to model closely the interactions of particles with the detector material and the detector performance. The CMS full simulation is based on the Geant4 [52] simulation toolkit, which accurately simulate the passage of particles through matter. The response of the sensitive detectors and the simulation of the readout electronics is described by dedicated programs written by CMS physicists [53].

## 3.3 Dataset, simulation and trigger

### 3.3.1 Dataset

The collision data used for our measurements correspond to the one that fired the trigger called: SingleMu, DoubleMu and DoubleElectron. The list of the primary datasets (PD) are shown in Table 3.1. The same datasets are used for the measurement of trigger and selection efficiencies. Data samples used for background measurements are listed in Table 3.2.

Table 3.1: Datasets used for analysis. The integrated luminosity and the run-ranges are shown for each data period. PD is used as an abbreviation for DoubleElectron, DoubleMu and SingleMu.

| Dataset | $\int \mathcal{L}$ [pb$^{-1}$] | Run range |
|---|---|---|
| **7 TeV** | | |
| /PD/Run2011A-HZZ-08Nov2011-v1/AOD | 2312 | 160431-173692 |
| /PD/Run2011B-HZZ-19Nov2011-v1/AOD | 2739 | 175860-180252 |
| Total for the 2011 dataset | 5051 | |
| **8 TeV** | | |
| /PD/Run2012A-13Jul2012/AOD | 890 | 190459-193621 |
| /PD/Run2012B-13Jul2012/AOD | 4430 | 193834-195947 |
| /PD/Run2012C-24Aug/AOD | 490 | 197774-198913 |
| /PD/Run2012C-PromptReco-v2/AOD | 6390 | 198913-200601 |
| /PD/Run2012D-PromptReco-v1/AOD | 7380 | 203768-208686 |
| Total for the 2012 dataset | 19580 | |

### 3.3.2 Simulated samples

The Monte Carlo datasets for signal and various background processes relevant to this analysis are listed in Table 3.3, along with the respective cross sections. Most cross sections are taken from the official CMS recommendations [54, 55] with the exception of the diboson

Table 3.2: Datasets used for background estimation.

| | |
|---|---|
| **Top/$WW$ Estimation** | /MuEG/Run2011A-HZZ-08Nov2011-v1/AOD<br>/MuEG/Run2011B-HZZ-19Nov2011-v1/AOD<br>/MuEG/Run2012A-13Jul2012/AOD<br>/MuEG/Run2012B-13Jul2012/AOD<br>/MuEG/Run2012C-24Aug/AOD<br>/MuEG/Run2012C-PromptReco-v2/AOD<br>/MuEG/Run2012D-PromptReco-v1/AOD |
| **DY Estimation** | /Photon/Run2011A-16Jan2012-v1/AOD<br>/Photon/Run2011B-16Jan2012-v1/AOD<br>/Photon/Run2012A-13Jul2012/AOD<br>/Photon/Run2012B-13Jul2012/AOD<br>/Photon/Run2012C-24Aug/AOD<br>/Photon/Run2012C-PromptReco-v2/AOD<br>/Photon/Run2012D-PromptReco-v1/AOD |

processes. For diboson normalization we use either the measured cross section at CMS for $WW$ [56, 57] or the result obtained using MCFM [16]. For the $ZZ$ case the cross section value is irrelevant given that this is the measured quantity. The value is only used as the base normalization of the simulation. All theoretical cross sections (multiplied by branching ratios) are computed at NLO and NNLO approximation where available.

The $ZZ$ cross section is computed at NLO with the MCFM program version 6.2 [16]. It includes contributions from the gluon-gluon box diagram, and the computation is performed for an invariant mass of the dilepton system greater than 40 GeV. The $Z$ boson decaying into a neutrino pair, instead, is generated with a mass greater than 12 GeV. The sample produced with MadGraph, which is used to model the signal spectrum in the $ZZ$ cross section measurement, may show kinematic differences from the more accurate MCFM computation, especially visible in the transverse momentum of the dilepton system. Since our measurement is performed by fitting the $E_T^{miss}$ spectrum, that is fully correlated with the $Z$-boson $p_T$ spectrum, we study the sensitivity of this distribution to the generator used. Fig. 3.1 shows a comparison between the dilepton transverse momentum spectra obtained with MCFM and MadGraph (no POWHEG $2l2\nu$ sample was available at the time of the analysis). The distributions show minor disagreement in the low $p_T$ region which will not be probed by our analysis, while they show an acceptable agreement in the high $p_T$ region. Hence, no dynamical re-weighting of the $Z$ $p_T$ is therefore applied.

The generation of SM plus anomalous coupling $ZZ$ production is obtained through *SHERPA* . It simulates both the parton-level scattering and the subsequent parton shower. We produce samples including up to two jets in the matrix-element computation: as can

Table 3.3: Simulation samples used for the analysis. For the different processes (signal and background) the expected cross sections are quoted [54, 55, 56, 57].

| Process | Dataset | $\sigma$ [pb] |
|---|---|---|
| | **7 TeV** | |
| $W \to \ell\nu$ | /WJetsToLNu_TuneZ2_7TeV-madgraph-tauola/F11-S6-v1 | 31314 |
| $Z \to \ell\ell$ | /DYJetsToLL_TuneZ2_M-50_7TeV-madgraph-tauola/F11-S4-v1 | 3048 |
| $t\bar{t}$ | /TTJets_TuneZ2_7TeV-madgraph-tauola/F11-S4-v1 | 165 |
| Single top | /T_TuneZ2_tW-channel-DR_7TeV-powheg-tauola/F11-S6-v1 | 7.87 |
| | /Tbar_TuneZ2_tW-channel-DR_7TeV-powheg-tauola/F11-S6-v1 | 7.87 |
| | /T_TuneZ2_t-channel_7TeV-powheg-tauola/F11-S6-v1 | 41.92 |
| | /Tbar_TuneZ2_t-channel_7TeV-powheg-tauola/F11-S6-v1 | 22.6 |
| | /T_TuneZ2_s-channel_7TeV-powheg-tauola/F11-S6-v1 | 3.19 |
| | /Tbar_TuneZ2_s-channel_7TeV-powheg-tauola/F11-S6-v1 | 1.44 |
| Dibosons | /ZZJetsTo2L2Nu_TuneZ2_7TeV-madgraph-tauola/F11-v1 | $6.83 \times 0.0386$ |
| | /WWJetsTo2l2Nu_TuneZ2_7TeV-madgraph-tauola/F11-S6-v1 | 52.4 |
| | /WZJetsTo3LNu_TuneZ2_7TeV-madgraph-tauola/F11-S6-v1 | $18.5 \times 0.033$ |
| | **8 TeV** | |
| $W \to \ell\nu$ | /WToENu_TuneZ2star_8TeV_pythia6/S12-S50-v1<br>/WToMuNu_TuneZ2star_8TeV_pythia6/S12-S50-v1<br>/WToTauNu_TuneZ2star_8TeV_pythia6_tauola_cff/S12-S50-v1 | 12085 |
| $Z \to \ell\ell$ | /DYJetsToLL_M-50_TuneZ2Star_8TeV-madgraph-tarball/S12-S52-v2 | 35041 |
| $t\bar{t}$ | /TTJets_MassiveBinDECAY_TuneZ2star_8TeV-madgraph-tauola/S12-v1 | 225 |
| Single top | /Tbar_tW-channel-DR_TuneZ2star_8TeV-powheg-tauola/S12-S52 ($\bar{t}$) | 11.2 |
| | /T_tW-channel-DR_TuneZ2star_8TeV-powheg-tauola/S12-S52 ($t$) | 11.2 |
| | /Tbar_t-channel_TuneZ2star_8TeV-powheg-tauola/S12-S52 ($\bar{t}$) | 55.5 |
| | /T_t-channel_TuneZ2star_8TeV-powheg-tauola/S12-S52 ($t$) | 30.0 |
| | /Tbar_s-channel_TuneZ2star_8TeV-powheg-tauola/S12-S52 ($\bar{t}$) | 3.9 |
| | ($t$) | 1.76 |
| Dibosons | /ZZJetsTo2L2Nu_TuneZ2star_8TeV-madgraph-tauola/S12-S52-v3 | $8.38^{+0.37}_{-0.24} \times 0.03$ |
| | /WWJetsTo2L2Nu_TuneZ2star_8TeV-madgraph-tauola/S12-S52-v1 | $69.9 \pm 9.3$ |
| | /WZTo3LNu_TuneZ2star_8TeV_pythia6_tauola/S12-S52-v1 | $22.9^{+1.2}_{-0.9} \times 0.03$ |

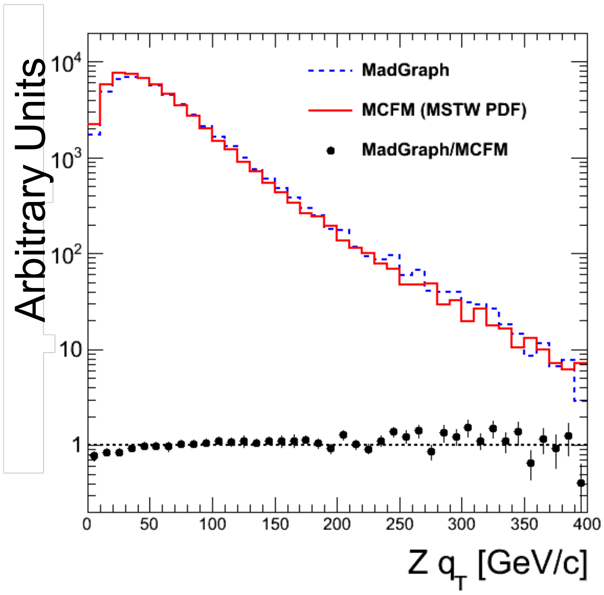


Figure 3.1: $Z$-boson transverse momentum spectrum generated by MadGraph compared to the NLO MCFM prediction.

be seen in Fig. 3.2, this provides an acceptable agreement, at few percent level, between MadGraph and MCFM in the dilepton $p_T$ spectrum, which is the main variable used in the limit extraction.

The DY background will be estimated by a data-driven technique (Sec. 3.8.1). This technique is tested on simulated data using the samples listed in Table 3.4.

### 3.3.3 Trigger

We select events using unprescaled triggers which require the presence of two electrons (for the $ee$ final state) or two muons (for the $\mu\mu$ final state). Each trigger requires minimum $p_T$ thresholds which may differ depending on each one of the two leptons. Given the varying conditions of the LHC luminosity throughout the 2011 and 2012 runs, the $p_T$ thresholds vary throughout the data-taking period considered. In electron triggers, isolation requirements are also applied. Table 3.5 lists all the triggers used in the analysis. In addition to the $ee$ and $\mu\mu$ triggers we use dedicated triggers for the control samples (electron + muon triggers to control the flavor-symmetric backgrounds such as the fully leptonic $t\bar{t}$ decay; photon triggers to control the instrumental missing transverse energy from the DY process).

Table 3.4: Data and MC samples analyzed for the estimation of the Drell-Yan process.

| Process | Dataset | $\sigma$ [pb] |
|---|---|---|
| | **7 TeV** | |
| $\gamma$+jets | G_Pt-30to50_TuneZ2_7TeV_pythia6/F11_S6_V9B-v1 | $1.67\times10^{4}$ |
| | G_Pt-50to80_TuneZ2_7TeV_pythia6/F11_S6_V9B-v1 | $2.72\times10^{3}$ |
| | G_Pt-80to120_TuneZ2_7TeV_pythia6/F11_S6_V9B-v1 | $4.47\times10^{2}$ |
| | G_Pt-120to170_TuneZ2_7TeV_pythia6/F11_S6_V9B-v1 | 84.2 |
| | G_Pt-170to300_TuneZ2_7TeV_pythia6/F11_S6_V9B-v1 | 22.6 |
| | G_Pt-300to470_TuneZ2_7TeV_pythia6/F11_S6_V9B-v1 | 1.49 |
| | G_Pt-470to800_TuneZ2_7TeV_pythia6/F11_S6_V9B-v1 | 0.132 |
| | G_Pt-800to1400_TuneZ2_7TeV_pythia6/F11_S6_V9B-v1 | $3.48\times10^{-3}$ |
| | G_Pt-1400to1800_TuneZ2_7TeV_pythia6/F11_S6_V9B-v1 | $1.26\times10^{-5}$ |
| QCD | QCD_Pt-20to30_EMEnriched_TuneZ2_7TeV-pythia6/F11_S6_V9B-v1 | 2502660 |
| | QCD_Pt-30to80_EMEnriched_TuneZ2_7TeV-pythia6/F11_S6_V9B-v1 | 3625840 |
| | QCD_Pt-80to170_EMEnriched_TuneZ2_7TeV-pythia6/F11_S6_V9B-v1 | 142813.8 |
| | QCD_Pt-170to250_EMEnriched_TuneZ2_7TeV-pythia6/F11_S6_V9B-v1 | 3263.4 |
| | QCD_Pt-250to350_EMEnriched_TuneZ2_7TeV-pythia6/F11_S6_V9B-v1 | 368.0 |
| | QCD_Pt-350_EMEnriched_TuneZ2_7TeV-pythia6/F11_S6_V9B-v1 | 55.0 |
| $Z\to\nu\nu$ | ZGToNuNuG_TuneZ2_7TeV-madgraph/S4-v2 | 3.425 |
| | ZJetsToNuNu_50_HT_100_7TeV-madgraph/F11_S6_V14B-v1 | 309.5 |
| | ZJetsToNuNu_100_HT_200_7TeV-madgraph/F11_S6_V14B-v1 | 125.2 |
| | ZJetsToNuNu_200_HT_inf_7TeV-madgraph/F11_S6_V14B-v1 | 32.92 |
| $W\gamma$ | WGToEEG_TuneZ2_7TeV-madgraph/F11_S6_V14B-v1 | 114.7 |
| | WGToMuMuG_TuneZ2_7TeV-madgraph/F11_S6_V14B-v1 | 114.6 |
| | WGToTauNuG_TuneZ2_7TeV-madgraph-tauola/F11_S6_V14B-v1 | 104.6 |
| | **8 TeV** | |
| $\gamma$+jets | G_Pt-30to50_TuneZ2star_8TeV_pythia6_Z2/S12-S52-v1 | $1.99\times10^{4}$ |
| | G_Pt-50to80_TuneZ2star_8TeV_pythia6/S12-S52-v1 | $3.32\times10^{3}$ |
| | G_Pt-80to120_TuneZ2star_8TeV_pythia6/S12-S52-v1 | $5.58\times10^{2}$ |
| | G_Pt-120to170_TuneZ2star_8TeV_pythia6/S12-S52-v1 | 108 |
| | G_Pt-170to300_TuneZ2star_8TeV_pythia6/S12-S52-v1 | 30.1 |
| | G_Pt-300to470_TuneZ2star_8TeV_pythia6/S12-S52-v1 | 2.14 |
| | G_Pt-470to800_TuneZ2star_8TeV_pythia6/S12-S52-v1 | 0.212 |
| | G_Pt-800to1400_TuneZ2star_8TeV_pythia6/S12-S52-v1 | $7.08\times10^{-3}$ |
| QCD | QCD_Pt-30to80_EMEnriched_TuneZ2star_8TeV-pythia6/S12-S52-v1 | 4677993 |
| | QCD_Pt-80to170_EMEnriched_TuneZ2star_8TeV-pythia6/S12-S52-v1 | 183295 |
| | QCD_Pt-170to250_EMEnriched_TuneZ2star_8TeV-pythia6/S12-S52-v1 | 4587 |
| | QCD_Pt-250to350_EMEnriched_TuneZ2star_8TeV-pythia6/S12-S52-v1 | 557 |
| | QCD_Pt-350_EMEnriched_TuneZ2star_8TeV-pythia6/S12-S52-v1 | 89 |
| EWK | WJetsToLNu_TuneCUETP8M1_8TeV-madgraphMLM-pythia8/S12-S52-v1 | 44146 |
| | WGToLNuG_TuneZ2star_8TeV-madgraph-tauola/S12-S52-v1 | 461.6 |
| | ZG3JetsToLL_8TeV-madgraph/S12-S52-v1 | 123.9 |

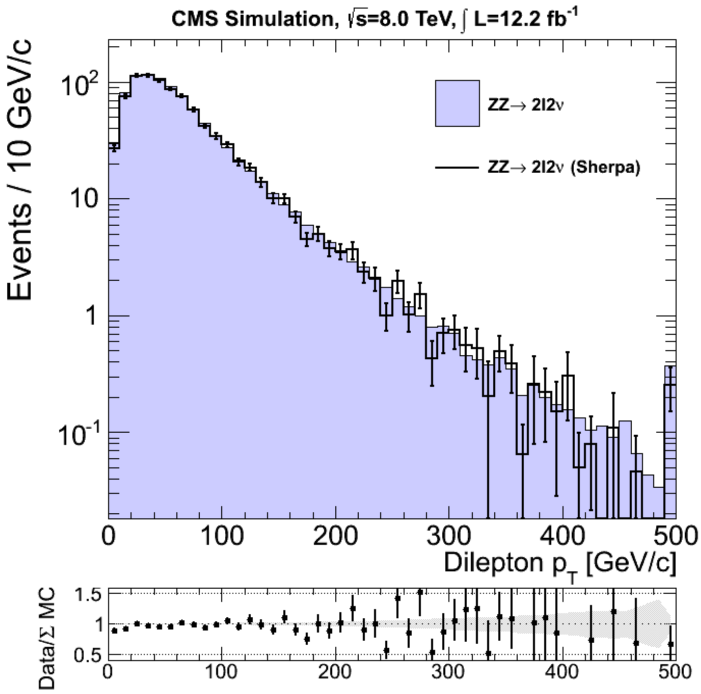


Figure 3.2: $Z$-boson transverse momentum spectrum before the parton shower in MadGraph and *SHERPA* samples at 8 TeV .

## 3.4 Object reconstruction and selection

The data passing the trigger contain at least two charged leptons. In order to clean data from misreconstructed leptons (e.g. a jet exchanged for an electron) or leptons not coming from the interaction vertex, we reconstruct our physical objects applying a tighter selection, using the standard particle identification and isolation criteria of the CMS collaboration [48, 58]. The outcome of such selection provides useful information to understand the background composition. In addition, to overcome the huge background for fake $E_T^{miss}$ in $Z + jet$ events, we investigate several $E_T^{miss}$ definitions. We compare these $E_T^{miss}$ variables in terms of the efficiency for the $ZZ$ signal, and the rejection for $Z + jet$ background in simulation.

### 3.4.1 Primary vertex

Primary vertices are reconstructed from the tracks of charged particles. Each event is required to contain at least one primary vertex (PV), reconstructed with the deterministic annealing algorithm [59], and selected with the following quality requirements:

- the vertex fit must have at least 4 degrees of freedom (3 tracks);

Table 3.5: List of trigger thresholds used to select signal and control data samples during 2011 and 2012 data-taking. Different thresholds for the same trigger correspond to different data-taking periods.

| Channel | Dataset Name | 2011 $p_T$ thresholds [GeV, GeV] | 2012 $p_T$ thresholds [GeV, GeV] |
|---|---|---|---|
| $ee$ | DoubleElectron | 17, 8 | 17, 8<br>33, 33 |
| $\mu\mu$ | DoubleMu | 7, 7<br>13, 8<br>17, 8 | 17, 8 |
| $e\mu$ | MuEG | 17 ($\mu$), 8 ($e$)<br>17 ($e$), 8 ($\mu$) | 17 ($\mu$), 8 ($e$)<br>17 ($e$), 8 ($\mu$) |
| $\gamma$ | Photon,SinglePhoton, DoubleElectron | 20,30,50,75,90<br>125,135,200 | 22,36,50,75,90 (EB only)<br>135,150,160,250,300 |

- the transverse distance of the vertex from the beam spot center must be less than 2 mm;
- the longitudinal distance of the vertex from the beam spot center must be less than 24 cm.

If an event contains more than one primary vertex, the one with the highest $\sum_{tracks} {p_{\mathrm{T}}}^2$ is chosen, where the sum runs over the transverse momentum of all the tracks used in the vertex fit.

The average track reconstruction efficiency for promptly-produced charged particles with transverse momenta of $p_T > 0.9$ GeV is about 94% for pseudorapidities of $|\eta| < 0.9$, and 85% for $0.9 < |\eta| < 2.5$. The resolution in a reconstructed primary-vertex position depends strongly on the number of tracks used to fit the vertex and the $p_T$ of those tracks, but in general is below 50 $\mu$m for vertices with more than 15 tracks. The primary vertex reconstruction efficiency is close to 100% [36].

### 3.4.2 Muon identification

Muons leave information mainly in the tracker and in the muon chambers. Reconstruction proceeds by first identifying hits in the detection layers of a muon station, and by then building straight-line track segments from these hits. This is referred to as local reconstruction.

The segments reconstructed in the muon chambers are used to generate seeds consisting of position and direction vectors and an estimate of the muon transverse momentum, from the direction of the segment in the transverse plane, assuming that the origin of the muon is the beam spot center. These initial estimates are used as seeds for the track fit in the muon system, which is performed using segments and hits from DTs, CSCs and RPCs. The result is a collection of muon tracks, which are referred to as standalone muons.

For each standalone muon track, a search for tracks matching it among those reconstructed in the inner tracking system is performed, and the best-matching tracker track is selected. For each tracker track and standalone muon pair, the fit using all hits is performed. The result is called global muon. The muon system can also be used purely to tag extrapolated tracks from the central tracker; such tracks are called tracker muons. For muons with transverse momenta below $\simeq 300$ GeV, tracker muons have better resolution than standalone muons. As the $p_T$ value increases, the additional hits in the muon system gradually improve the overall resolution. Global muons exploit the full bending of the CMS solenoid and return yoke to achieve the ultimate performance in the TeV region.

The muons used to reconstruct a $Z$ candidate are selected inside the fiducial region of the muon spectrometer, $|\eta| < 2.4$, with a minimum $p_T$ of 20 GeV, and using standard CMS identification criteria [48]. The identification and isolation criteria differ depending on the dataset analysed, i.e. for 2011 and 2012. In 2011 muons must be identified by both the global muon and tracker muon algorithms, while in 2012 they are also required to be identified by the so-called particle-flow (PF) algorithm for muons [48]. Further track quality requirements based on number of hits, $\chi^2$ of the fit and relative $p_T$ uncertainty are imposed on the muons. They also need to be associated to the primary vertex of the event by transverse and longitudinal impact parameter cuts. The muon tracks are required to be isolated by summing the momenta of tracks and energy deposits, or the particle flux reconstructed in a cone built around the track. Relative isolation is therefore defined for the 2011 period as:

$$I_{\text{rel}} = \frac{1}{p_T}(I_{\text{tracker}} + I_{\text{cal}}) \tag{3.2}$$

where $I_{\text{tracker}}$ is the sum of the transverse momenta of all the charged particle tracks inside a cone of size $\Delta R = \sqrt{(\Delta\phi)^2 + (\Delta\eta)^2} = 0.3$ around the muon track (excluding the muon itself), and $I_{\text{cal}}$ is the sum of the ECAL and HCAL energy deposits inside the same cone.

In order to reduce the dependence of the isolation cut on the number of pileup interactions, only tracks coming from the muon primary vertex are used. Moreover, the calorimeter deposits are corrected for the average energy density $\rho$ in the event: $I_{\text{cal}} = \max(0,\, I_{\text{cal}}^{\text{uncorr}} - \pi \cdot 0.3^2 \cdot \rho)$.

For the 2012 period, PF based isolation is used instead, and it is defined as

$$I_{\text{rel}} = \frac{1}{p_T} \left[ I_{\text{ch}} + \max(0,\ I_{\text{nh}} + I_\gamma - 0.5 \cdot I_{ch,PU}) \right] \tag{3.3}$$

where the isolation sums correspond to the sums of charged (ch), neutral hadrons (nh) or photon ($\gamma$) candidates reconstructed by the PF algorithm inside a $\Delta R = 0.4$ cone. The last term, $-0.5 \cdot I_{\text{ch,PU}}$, is intended to subtract the contribution from pileup interactions to the neutral component of the isolation, and is derived looking at the number of tracks pointing to pileup vertices. The factor 0.5 corresponds to a naive average ratio of neutral to charged particle multiplicity, and it has been measured in jets in [44]). In Table 3.6, the details of muon selection are reported. The values reported here have been optimized by CMS [48, 44] and they represent the standard CMS identification criteria.

Table 3.6: Muon identification for $Z$ candidate selection.

| Variable | 2011 | 2012 |
|---|---|---|
| $\|\eta\|$ | $< 2.4$ | |
| $p_T$ | $> 20$ GeV | |
| GlobalMuon | true | |
| TrackerMuon | true | |
| PF | – | true |
| Valid muon hits | $> 0$ | |
| Muon matched stations | $> 1$ | |
| Valid tracker hits | $> 10$ | – |
| Tracker layers with measurement | – | $>5$ |
| Valid pixel hits | $> 0$ | |
| Global track $\chi^2$ | $< 10$ | |
| $\sigma(p_T)/p_T$ | $< 0.1$ | – |
| Transverse IP | $< 0.02$ cm | $< 0.2$ cm |
| Longitudinal IP | $< 0.1$ cm | $< 0.5$cm |
| Detector-based relative isolation | $< 0.15$ | – |
| PF relative isolation | – | $< 0.2$ |

### 3.4.3 Electron identification

Electron and photon showers deposit their energy in several crystals in the ECAL. Approximately 94% of the incident energy of a single electron or photon is contained in 3x3 crystals and 97% in 5x5 crystals. Summing the energy measured in such fixed arrays gives the best performance for unconverted photons, or for electrons in the test beam. The presence in

CMS of material in front of the calorimeter results in bremsstrahlung and photon conversions. Because of the strong magnetic field the energy reaching the calorimeter is spread in $\phi$. The spread energy is clustered by building a cluster of clusters, a *supercluster*, which is extended in $\phi$.

Electron reconstruction in particular uses two complementary algorithms at the track seeding stage: *tracker driven* seeding, more suitable for low $p_T$ electrons and electrons inside jets, and *ECAL driven* seeding. The *ECAL driven* algorithm starts by the reconstruction of ECAL *superclusters* (SC) of transverse energy $E_T > 4$ GeV and is optimized for isolated electrons in the $p_T$ range relevant for $Z$ or $W$ decays and down to 5 GeV in $p_T$ . The SC is a group of one or more associated clusters of energy deposits in the ECAL, constructed using an algorithm which takes into account their characteristic narrow width in the $\eta$ coordinate and their characteristic spread in $\phi$ due to the bending of the tracks of electrons and the radiation of Bremsstrahlung photons in the tracker material. As a first filtering step, SCs are matched to track seeds (pairs or triplets of hits) in the inner tracker layers, and electron tracks are built from these track seeds. Trajectories are reconstructed using a dedicated modeling of the electron energy loss and fitted with a Gaussian Sum Filter (GSF) [60].

Electrons used to build a $Z$ candidate are selected inside the fiducial region of the electromagnetic calorimeter ECAL, $|\eta_{SC}| < 2.5$, excluding the transition region between the barrel and the endcaps, $1.4442 < |\eta_{SC}| < 1.566$. The electron candidates must have a minimum $p_T$ of 20 GeV, and satisfy tight identification criteria, based on shower shape, track quality and cluster-track matching, in order to reject misidentified hadrons. Criteria for rejection of conversion candidates from photons are also applied [58], exploiting tracker and shower shape information. As in the case of muons, the electrons are required to be isolated and originate from the primary vertex. As for the muon case, the criteria differ slightly depending on the data period analysed. The isolation is computed similarly as for the muon case (explained in Sec. 3.4.2).

Table 3.7 summarizes the electron selection criteria separately for barrel and endcaps for both data periods. The variable $\sigma_{i\eta i\eta}$ represents the spread between the $\eta$ of the seed and the other crystals of the SC, weighted for the fraction of the crystal energy. The variables $\Delta\phi(track, SC)$ and $\Delta\eta(track, SC)$ are the distance between the electron track and the supercluster, $H/E$ the ratio of the energy deposited in the hadronic and electromagnetic calorimeter, and the isolation quantities are defined in the previous section. The variable $|1/E - 1/p|$ has been proved to be robust for high energetic electrons.

Table 3.7: Electron identification for $Z$ candidate selection. EB and EE are used as abbreviations for ECAL barrel and endcap correspondingly.

| Variable | 2011 EB | 2011 EE | 2012 EB | 2012 EE |
|---|---|---|---|---|
| $p_T$ | $> 20$ GeV | | $> 20$ GeV | |
| $\|\eta\|_{SC}$ | $< 1.4442$ | $1.566 < \|\eta\| < 2.5$ | $< 1.4442$ | $1.566 < \|\eta\| < 2.5$ |
| $\sigma_{i\eta i\eta}$ | $< 0.01$ | $< 0.03$ | $< 0.01$ | $< 0.03$ |
| $\Delta\phi(track, SC)$ | $< 0.06$ | $< 0.04$ | $< 0.06$ | $< 0.03$ |
| $\Delta\eta(track, SC)$ | $< 0.004$ | $< 0.007$ | $< 0.004$ | $< 0.007$ |
| $H/E$ | $< 0.04$ | $< 0.1$ | $< 0.12$ | $< 0.1$ |
| Transverse IP | $< 0.02$cm | | $< 0.02$cm | |
| Longitudinal IP | $< 0.1$cm | | $< 0.1$cm | |
| Missing hits | 0 | | 1 | |
| Conversion vertex fit prob. | $10^{-6}$ | | $10^{-6}$ | |
| $\|1/E - 1/p\|$ | - | | $< 0.05$ | |
| $\Delta R$ from muon candidates | $> 0.1$ | | $> 0.1$ | |
| Detector-based relative isolation | $< 0.1$ | | – | |
| Relative isolation | – | | $< 0.15$ | |

### 3.4.4 Z candidate selection

$Z$ candidates are selected in events with a pair of same-flavor charged leptons which pass the identification and isolation criteria described in the previous sections. Although we expect the leptons to have opposite charge sign we do not apply this requirement in the selection. In order to suppress all backgrounds that do not include a $Z$ boson, the lepton pair is required to have an invariant mass compatible with the $Z$ boson nominal mass of 91.2 GeV. Moreover, the transverse momentum of the $Z$ candidate is required to be greater than 30 GeV. The boost of the $Z$ is required for two reasons: in $ZZ$ events each boson recoils against the other at LO and is boosted, and the data-driven estimate of the DY background is done using a photon sample in which the trigger thresholds suffer high prescales below 30 GeV.

Fig. 3.3 and 3.4 show, respectively, the invariant mass and transverse momentum distributions of selected muon and electron pairs in both data periods. A shift of few hundreds MeV between the mass distribution in data and in simulation is visible. Furthermore a small under-estimation of the DY simulation can be observed for high values of the dilepton the invariant mass. Since the dominant contribution to the $E_T^{miss}$ resolution is given from jet resolution, and we select events within 7.5 GeV around $Z$ mass peak, these effects do not represent an issue to our analysis. The lack of Monte Carlo events at 7 TeV below 50 GeV in the dilepton distribution, is due to generator cuts in the samples production; nevertheless this region is not relevant in our analysis.

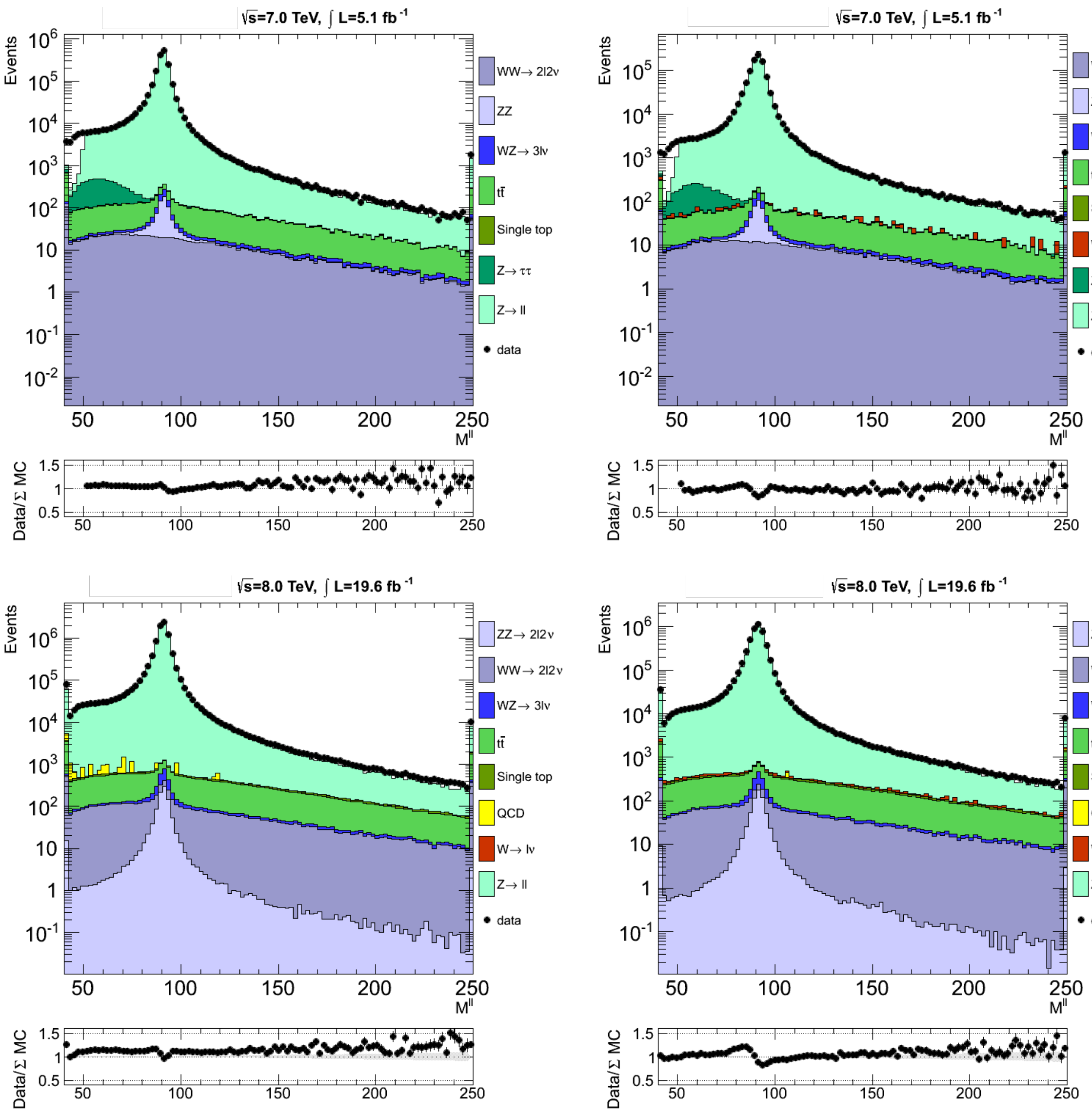


Figure 3.3: Dilepton invariant mass in $\mu\mu$ (left) and $ee$ (right) channels at 7 (*up*) and 8 (*down*) TeV. For the 7 TeV DY simulation, the generator cut on the invariant mass of the dilepton system is 40 GeV (CMS data).

### 3.4.5 Jets and missing energy

The jet reconstruction at CMS uses the PF [44] method. The PF event reconstruction aims at reconstructing and identifying all stable particles in the event, i.e. electrons, muons,

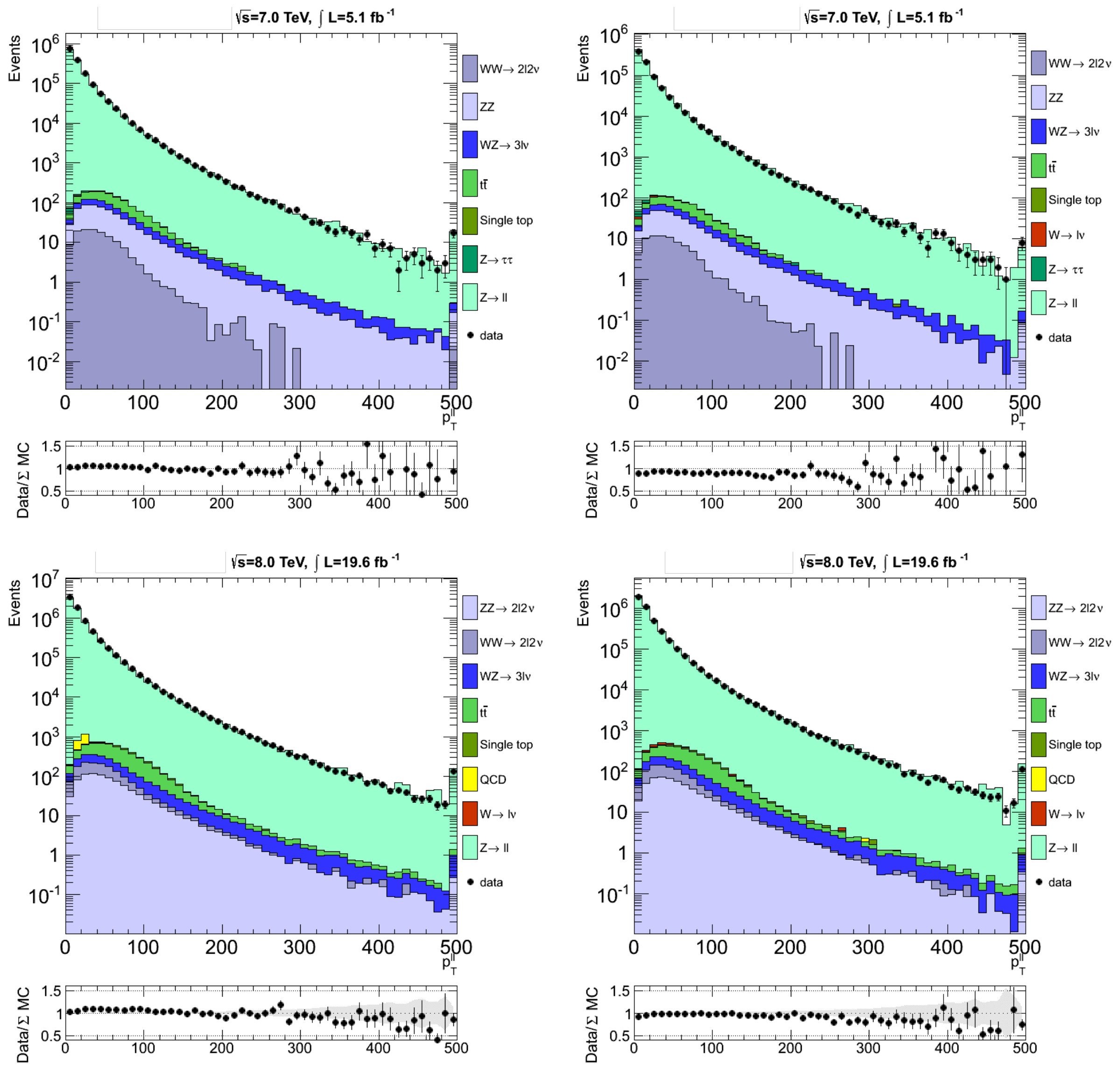

Figure 3.4: Dilepton transverse momentum in $\mu\mu$ (left) and $ee$ (right) channels at 7 (*up*) and 8 (*down*) TeV, for events with dilepton mass within $91 \pm 7.5$ GeV (CMS data).

photons, charged hadrons and neutral hadrons, with a thorough combination of all CMS subdetectors towards an optimal determination of their direction, energy and type. This list of individual particles is then used, as if it came from a Monte Carlo event generator, to build jets (from which the quark and gluon energies and directions are inferred), to determine the missing energy $E_T^{miss}$, to reconstruct and identify $\tau$ from their decay products, to quantify charged lepton isolation with respect to other particles, etc.

The silicon tracker, with coverage in $\eta$ up to 2.5, the uniform axial 3.8 T magnetic field, and $4\pi$ calorimeter allow to distinguish all the different particle topologies. Charged-particle tracks can be reconstructed with large efficiency and adequately small fake rate down to a momentum transverse to the beam of 150 MeV. Photons are reconstructed with an excellent energy resolution in ECAL, electrons are reconstructed by a combination of tracks and of energy deposits, from the electron itself and from possible Bremsstrahlung photons radiated by the electron in the tracker material. Muons are reconstructed and identified with very large efficiency and purity from a combination of the tracker and muon chamber information. Charged and neutral hadrons deposit their energy in the hadron calorimeter with a similar pseudo-rapidity coverage. The hadron energy resolution in the combined ECAL-HCAL system is of the order of 10% at 100 GeV. This resolution allows neutral hadrons to be detected as an energy excess on top of the energy deposited by the charged hadrons pointing to the same calorimeter cells. The charged hadrons are reconstructed with the superior angular and energy resolutions of the tracker. Particles with pseudo-rapidities between 3.0 and 5.0 are more coarsely measured with the forward calorimeter.

For this analysis, PF jets are reconstructed with an algorithm called *anti-*$k_{\mathrm{T}}$ ([61, 62]), with a $\Delta R = 0.5$ parameter.

The presence of additional pileup interactions, and the imperfections of the detector response, require the jets to be corrected [45]. A first level correction removes the pileup contribution from the jets, based on the event by event computation of pileup density per unit of area. A second level correction unifies the detector response, as a function of the $\eta$ and the $p_T$ of the jet.

Only jets with a corrected transverse momentum greater than 10 GeV within $|\eta|$ <5.0 are used in our analysis. An extra correction is applied to jets in MC to match the resolution as observed in data. The procedure consists in applying a smearing on each jet $p_T$, that vary from five to about ten percent, depending on its $p_T$ and $\eta$ [45].

Finally, the presence of neutrinos and other weakly interacting particles can be inferred by transverse missing energy $E_T^{miss}$, defined as the modulus of the vector sum of the transverse momenta of all reconstructed particles. The $E_T^{miss}$ variable also need to be corrected for the pileup contribution and for the inhomogeneous detector response. This is done by replacing the vector sum of transverse momenta of particles which can be clustered as jets with the vector sum of the transverse momenta of the jets to which the corrections explained above are applied.

### 3.4.6 B quark tagging

The $b$ quark detection gives powerful information about single-top and $t\bar{t}$ production processes. Since top quarks decay at $\sim$ 100% into $Wb$, rejecting events containing a $b$ quark allow the suppression of most of these backgrounds.

A $b$ quark hadronizes into a $B$ hadron. Thanks to its lifetime of the order of few picoseconds, it will decay at a measurable distance from the primary vertex. Vetoing such events is possible looking at secondary vertex information. The CMS detector, with its precise charged particle tracking system, robust lepton identification and finely segmented calorimetry, is well matched to the task of $b$-jet identification ($b$ tagging).

The impact parameter is defined as the distance between the track and the primary interaction vertex at the point of closest approach. The IP is positive (negative) if the track is produced downstream (upstream) with respect to the PV along the jet direction. The IP is calculated in 3 dimensions thanks to the good x-y-z resolution provided by the pixel detector. An important feature of the IP is that it is approximately independent of the boost of the B-hadron. Due to the B-hadron lifetime, the typical IP scale is set by $c\tau \sim 600$ $\mu$m. In practice, the impact parameter significance IP/$\sigma$(IP) is used in order to take into account resolution effects. Thanks to the long lifetime of the B-hadrons the IP of the tracks from the b-hadron decay are expected to be mainly positive, while for tracks in light jets, it is almost symmetric with respect to zero.

Secondary Vertex tagging algorithms rely on the reconstruction of at least one secondary vertex (SV). The significance of the 3D flight distance is used as a discriminating variable. Two variants based on the number of tracks at SV are considered: N$\geq$2 for high efficiency, and N$\geq$3 for high purity. The combined secondary vertex (CSV) algorithm includes this information and provides discrimination even when no secondary vertices are found. Furthermore the flight distance significance in the transverse plane, the vertex mass, the number of tracks at the vertex, the ratio of the energy carried by tracks at the vertex with respect to all tracks in the jet, the pseudorapidities of the tracks at the vertex with respect to the jet axis, and the 3D IP significance for each track in the jet are combined to build the CSV discriminator.

Jets with $p_T > 60$ GeV in a sample of simulated multijet events are used to obtain the efficiencies and mis-identification probabilities. For loose selections with 10% mis-identification probability for light-parton jets a b-jet, tagging efficiency of $\sim$ 80-85% is achieved. For tight selections with mis-identification probabilities of 0.1%, the typical b-jet tagging efficiency values are $\sim$ 45-55%. For medium and tight selections the CSV algorithm shows the best performance compared to other algorithms [63].

## 3.5 Monte Carlo corrections

Several aspects of the simulation, as the trigger efficiencies and the lepton identification and isolation, do not described with high accuracy the data.

In order to correct for these effects, the efficiencies of our selections have been computed from data using the *tag and probe* technique. The tag and probe is a tool developed to measure the efficiency of a selection from data, exploiting di-object resonances, and to correct the simulation in order to have a better description of data.

It could be summarized in the following steps:

- a resonance, like the $Z$-boson, is reconstructed as pair of leptons. One lepton passes a tight identification (tag) and the other one passes a loose identification (probe);
- the probe selection is the one of which we want to measure the efficiency from data, while the tag selection has a know efficiency;
- the events passing the tag selection on one lepton and the probe selection on the other, and the events passing the tag selection, but failing the probe, are fitted separately to measure the signal yields;
- the efficiency is computed from the ratio of the signal yields in the two line-shapes;
- the procedure is repeated in bins of the probe variables (e.g. $p_T$ and $\eta$) to compute efficiency histograms as a function of those variables.

The invariant mass of the reconstructed pair must be compatible with a SM candle and for the region of interest of the kinematics we are probing we choose the dilepton to be compatible with a $Z$ boson decay. The trigger efficiencies are about 98% for the double electron channel and about 94% for the double muon channel.

Furthermore, as it has been described in Sec. 1.2.4, a correction for the NLO EWK contribution to the $ZZ$ and $WW$ processes have been included in the analysis.

Finally, the pileup activity in data is poorly described in the simulation. To have a better description of the number of pileup per event, the number of simultaneous interactions in the simulation is weighted using the distribution of the number of pileup computed in data. The uncertainty on the reweighting is described in Sec. 3.9.10.

## 3.6 Reduced missing transverse energy

Missing transverse energy ($E_T^{miss}$) is computed from the flux of the transverse momenta of all PF candidates reconstructed in the event. Its resolution is critical for the extraction of the $ZZ \to 2l2\nu$ signal given that it is the distinctive hallmark with respect to DY background. Since the $E_T^{miss}$ of the signal is moderate in average as it reflects the boost of the second $Z$ in the event, we cannot afford to cut simply on a high $E_T^{miss}$ threshold.

We follow the approach of constructing a reduced-$E_T^{miss}$ variable. The general concept behind a reduced-$E_T^{miss}$ is, on an event-by-event basis, to reduce the $E_T^{miss}$ by considering possible contributions to fake $E_T^{miss}$. An event with high value for reduced-$E_T^{miss}$ is one which has a very robust $E_T^{miss}$ signature that is very unlikely to come from mismeasurement. The reduced-$E_T^{miss}$ can be thought of as a minimum plausible value for the $E_T^{miss}$, and not as an unbiased estimator of the true $E_T^{miss}$. This approach was used effectively in the DØ experiment's analysis of the same process [64], and before that in the analysis of similar final states in the OPAL experiment [65].

### 3.6.1 Definition

The reduced-$E_T^{miss}$ for each event is calculated by decomposing $E_T^{miss}$, jet and lepton $p_T$ information along an orthogonal set of axes within the transverse plane of the detector, such that projection onto one axis is insensitive to hadronic recoil, and projection onto the other axis is insensitive to lepton resolution. Since the signal is characterized by events with two well-measured leptons, we are only concerned with constructing reduced-$E_T^{miss}$ for those events. Two-dimensional $\overrightarrow{p_T}$ vectors are defined for the $E_T^{miss}$, both leptons ($\overrightarrow{p_T}(\ell_1)$ and $\overrightarrow{p_T}(\ell_2)$, ordered by $p_T$), and each jet ($\overrightarrow{p_T}(jet)$) within the event. The orthogonal set of axes are also defined as two unit vectors: a transverse axis $\widehat{a}_t$ and a longitudinal axis $\widehat{a}_l$. If the angle $\phi$ between the two leptons is less than $\frac{\pi}{2}$, then

$$\widehat{a}_l = \frac{\overrightarrow{p_T}(\ell_1) + \overrightarrow{p_T}(\ell_2)}{|\overrightarrow{p_T}(\ell_1) + \overrightarrow{p_T}(\ell_2)|} \tag{3.4}$$

and $\widehat{a}_t$ is defined such that $\widehat{a}_l \cdot \widehat{a}_t = 0$, and $\overrightarrow{p_T}(\ell_1) \cdot \widehat{a}_t > 0$.

However, if $\phi \geq \frac{\pi}{2}$, then

$$\widehat{a}_l = \frac{\overrightarrow{p_T}(\ell_1) - \overrightarrow{p_T}(\ell_2)}{|\overrightarrow{p_T}(\ell_1) - \overrightarrow{p_T}(\ell_2)|} \tag{3.5}$$

and $\widehat{a}_t$ is defined such that $\widehat{a}_l \cdot \widehat{a}_t = 0$ and $\overrightarrow{p_T}(\ell_1) \cdot \widehat{a}_t > 0$.

After defining these axes, the lepton and hadron sources of instrumental $E_T^{miss}$ are isolated as follows. The dilepton components are defined as:

$$a_i^{\ell\ell} = (\overrightarrow{p_T}(\ell_1) + \overrightarrow{p_T}(\ell_2)) \cdot \widehat{a_i} \tag{3.6}$$

where $i$ represents the longitudinal and transverse axis. The hadronic activity that recoils against the dilepton system is estimated in two different ways. The clustered hadron recoil components are defined from the energy clustered in jets:

$$a_i^{clus} = \sum_j \overrightarrow{p_T}(jet_j) \cdot \widehat{a_i} \tag{3.7}$$

The measured hadron recoil components are defined from the $E_T^{miss}$ and the leptons:

$$a_i^{unclus} = -(E_t^{miss} + \overrightarrow{p_T}(\ell_1) + \overrightarrow{p_T}(\ell_2)) \cdot \widehat{a_i}. \tag{3.8}$$

The reduced-$E_T^{miss}$ components are then defined in two possible ways again. In the first way, further noted D∅ reduced-$E_T^{miss}$, the components are defined as [65]:

$$C_i = a_i^{\ell\ell} + W_{recoil} \cdot min(a_i^{clus}, -a_i^{unclus}, 0) \tag{3.9}$$

where $W_{recoil}$ is an additional free parameter of the definition, that can be optimized. In the second way, further denoted reduced-$E_T^{miss}$, the components are defined as:

$$C_i = min\left(\left|a_i^{\ell\ell} + W_{recoil} \cdot a_i^{clus}\right|, \left|a_i^{\ell\ell} + W_{recoil} \cdot a_i^{unclus}\right|\right) \tag{3.10}$$

Eventually, the magnitude of the reduced-$E_T^{miss}$ variable is defined as: $\sqrt{C_l^2 + W_t \cdot C_t^2}$, where $W_t$ is a weight that can also be optimized. In our analysis the weights $W_{recoil}$ and $W_t$ are set to unity. No significant improvement has been seen with optimized $W_{recoil}$ and $W_t$.

### 3.6.2 Stability

Before finding the optimal selection we need to focus on a $E_T^{miss}$ definition which:

- Has a good data description;
- Provides a good background rejection;
- Is stable under pileup and energy scale variations.

We compare different $E_T^{miss}$ definitions:

- Standard Particle Flow $E_T^{miss}$ (PF $E_T^{miss}$);
- D∅ reduced-$E_T^{miss}$;
- Reduced-$E_T^{miss}$.

In Fig. 3.5, the signal efficiency is shown in simulation as a function of the Drell-Yan background efficiency, for the three $E_T^{miss}$ definitions and for different cuts. The two reduced-$E_T^{miss}$ show a better signal efficiency compared to the standard PF $E_T^{miss}$. The efficiencies are computed after the full signal selection in table 3.8, without the $E_T^{miss}$ cut. Since the stability with respect to pileup is very important at high luminosity, we re-compute the different $E_T^{miss}$ variables and their efficiencies varying the PU weight distribution (left) and the jet energy (right) within their uncertainties, as explained in Sec. 3.9. The working points of interest

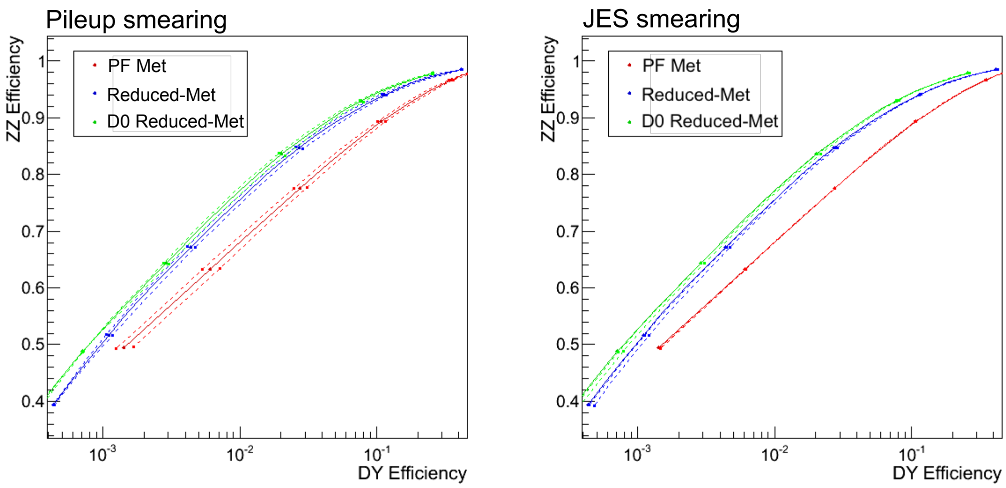


Figure 3.5: Signal efficiency for simulated $ZZ$ events as a function of the Drell-Yan background efficiency, for different $E_T^{miss}$ definitions and different cut points. In red it is shown the PF $E_T^{miss}$, in green the D∅ reduced-$E_T^{miss}$, in blue the reduced-$E_T^{miss}$. The efficiencies are computed after the full signal selection, except the $E_T^{miss}$ cut. The dashed lines are the efficiencies after changing the PU weight (left) and the jet energy scale (right) using the 2012 data conditions.

for the cross section measurements are in the range of $10^{-2}$-$10^{-3}$ for the DY background rejection. In this range, it can be seen that the two reduced-$E_T^{miss}$ definitions yield better efficiency than PF $E_T^{miss}$, and both are stable under variation in the PU distribution and jet energy calibration. The original D0 reduced-$E_T^{miss}$ definition shows a slightly better performance compared to the standard reduced-$E_T^{miss}$, nevertheless the difference is marginal and to be consistent with the definition used in the CMS H $\rightarrow$ ZZ $\rightarrow$ $2l2\nu$ analysis [66], we select the reduced-$E_T^{miss}$.

Fig. 3.6 shows the distributions of the $E_T^{miss}$ and the reduced-$E_T^{miss}$ in data and MC after the dilepton mass and $p_T$ selection, the b-tagged jet veto, and the jet veto. This figure already indicates that simulation does not describe well the instrumental $E_T^{miss}$ distribution. The method to model instrumental $E_T^{miss}$ from data will be described later in Sec. 3.8.1.

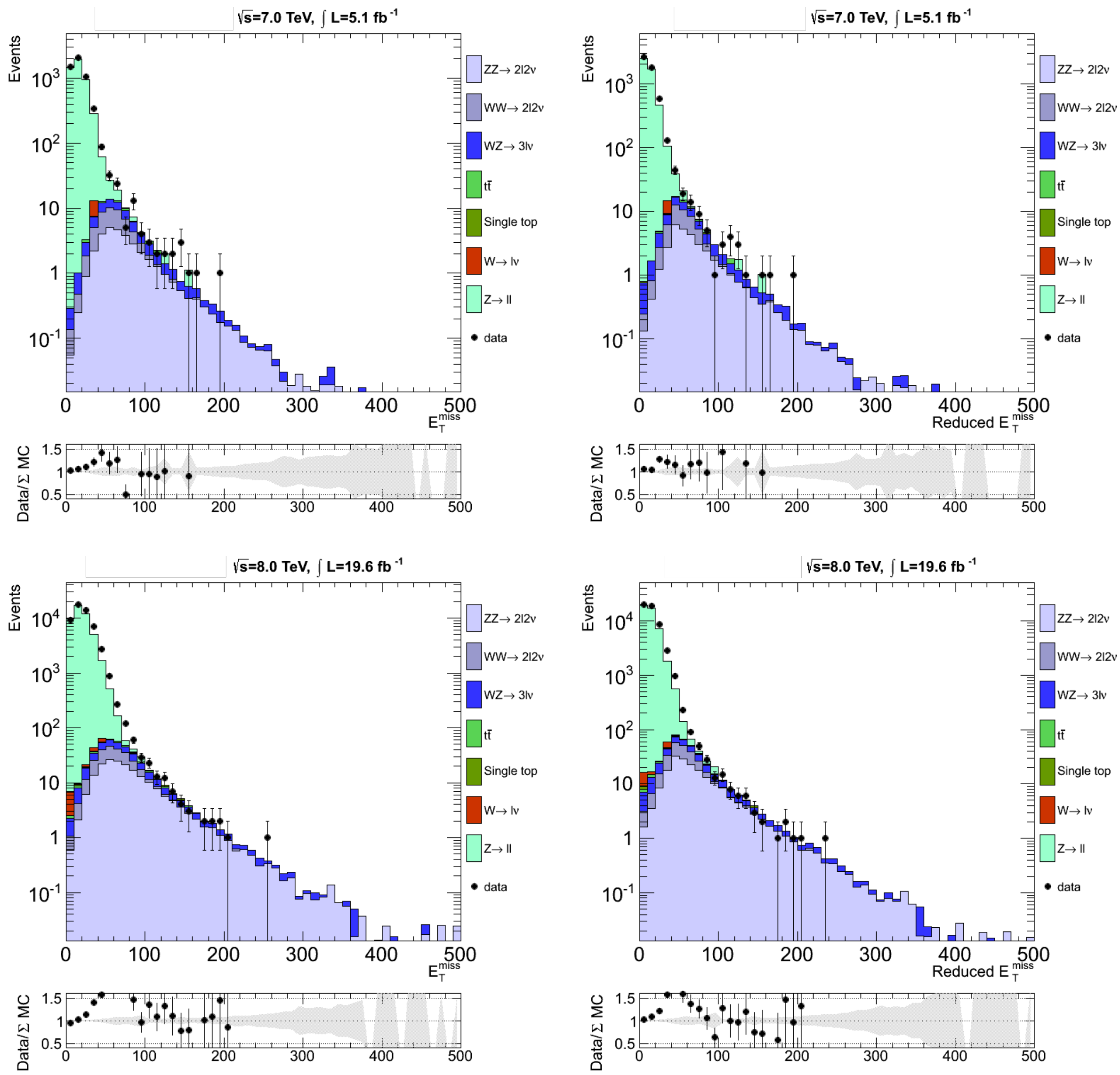


Figure 3.6: Particle Flow $E_T^{miss}$ (left) and reduced-$E_T^{miss}$ (right) distributions, for the *ee* channel at 7 (up) and 8 (down) TeV, after the dilepton mass and $p_T$ selection, the b-tagged jet veto, and the jet veto (CMS data).

## 3.7 Selection optimization

In figures 3.3 and 3.6 the data-Monte Carlo comparison is shown after vetoing jets with a $p_T$ greater then 30 GeV and the request of the dilepton $p_T$ to be greater then 45 GeV. Due to its high cross section, the DY process is the dominant background to be removed.

In the optimization we used both the data-driven predictions for the DY and non-resonant backgrounds (Sec. 3.8) and the MC estimation. The optimization has been done after vetoing jets with a $p_T$ greater than 30 GeV, vetoing jets tagged as b-jet (CSV $< 0.244$) with a $p_T$ greater than 20 GeV and $\eta < 2.4$, vetoing the presence or a third lepton, and applying a minimal cut of 40 GeV to the dilepton invariant mass. Data-driven background estimation (Sec. 3.8) is used.

We optimize the selection in order to minimize the total statistical and systematic uncertainty on the cross section measured at 8 TeV. For this purpose we scan a series of cuts on:

- dilepton $p_T$ ;
- the $Z$ mass window;
- jet $p_T$ threshold used in the computation of the reduced-$E_T^{miss}$ variable;
- reduced-$E_T^{miss}$ minimum threshold.

The following set of cuts ensures the lowest uncertainty on the cross section measurement: $p_T^Z$ >45 GeV, $|M_{ll} - M_Z|$ <7.5 GeV, $p_T^{\text{jet}}$ >10 GeV, and reduced-$E_T^{miss}$ >65 GeV. The most important cut is the one on the reduced-$E_T^{miss}$, that allow to reject the DY contribution. The value chosen by the optimization represents a good compromise between DY rejection and signal efficiency.

The final selection is shown in table 3.8, and it has been applied both at 7 TeV and 8 TeV.

Fig. 3.7 shows the number of jets with $p_T > 30$ GeV per event. A fair agreement is observed overall, except for the 0-jet bin in the $\mu\mu$ category at 8 TeV. The discrepancy does not affect out measurement since the Drell-Yan background in the 0-jet category is estimated from data.

Fig. 3.8 shows the number of b-tagged jets per event, with $p_T$ above 20 GeV. The poor agreement is probably due to the disagreement in the jet multiplicity shown in the previous figure, and partially due to the higher mis-tag rate in data compared to simulation. Since we

Table 3.8: Summary of signal selection cuts.

| Variable | Cut |
|---|---|
| Dilepton $p_T$ | $q_{\mathrm{T}} > 45$ GeV |
| Dilepton invariant mass | $\|m(\ell\ell) - 91\| < 7.5$ GeV |
| Lepton veto | no extra loose $\mu/e$ with $p_T > 3/10$ GeV |
| Jet veto | no jets with $p_T > 30$ GeV |
| b-tag veto | CSV discr. $< 0.244$ ($p_{\mathrm{T,jet}} > 20$ GeV) |
| $\Delta\phi(E_T^{miss}$,jet) | $> 0.5$ rad |
| $E_T^{miss}$ balance | $0.4 < B < 1.8$ |
| $\Delta\phi(E_T^{miss}$,ll) | $> 0.2$ rad (if $E_T^{miss} > 60$ GeV) |
| Reduced-$E_T^{miss}$ | $> 65$ GeV |

only keep events without any jet with $p_T > 30$ GeV and without any $b$-jet with $p_T > 20$, the mis-modeling of b-tagging performance has a negligible effect on the cross section uncertainty.

The $E_T^{miss}$ balance variable is here defined as the ratio between the $E_T^{miss}$ and the transverse momentum of the $Z$ boson ($q_T$). This variable identifies events in which the $Z$ candidate is not well balanced by natural $E_T^{miss}$ from neutrinos, but recoils against jets or fake $E_T^{miss}$ from mismeasurement of jets or leptons. In Fig. 3.9 distributions of the balance variable are shown after the dilepton mass and $p_T$ selection, the reduced-$E_T^{miss}$ cut, the b-tagged jet veto, and the jet veto. The selected sample can still be contaminated by events with jets of $p_T$ below the veto threshold. A mis-measurement of the jet energy can produce fake $E_T^{miss}$ aligned with the jet direction on the transverse plane. These events are thus characterized by a small transverse angle between the $E_T^{miss}$ and the closest jet with $p_T > 30$ GeV, $\Delta\phi(E_T^{miss}$,jet).

Likewise, a mis-measurement of the transverse momentum of a lepton can produce fake $E_T^{miss}$. Although this effect is generally negligible, given the good lepton momentum resolution, events are found where a large $E_T^{miss}$ value ($> 60$ GeV) is accompanied by a small angle between the $E_T^{miss}$ and the $p_T$ of a lepton, generally, an electron (Fig. 3.10). This cut is expected to have a negligible effect on the signal efficiency, and can be safely used. Events with $E_T^{miss} > 60$ GeV and $\Delta\phi(E_T^{miss},ll) < 0.2$ rad. are rejected.

In order to suppress the $WZ$ background, with both bosons decaying leptonically, events are required not to have any additional leptons, other than the muon or electron pair from the $Z$ candidate. To improve the rejection power, the $p_T$ threshold is lowered to 3 GeV for additional muons, and 10 GeV for electrons. Furthermore, muons and electrons are selected with looser criteria than those described in Sections 3.4.2 and 3.4.3, as reported in Tab. 3.9 and 3.10.

Fig. 3.11 shows the number of additional leptons (electrons and muons with $p_T > 10$

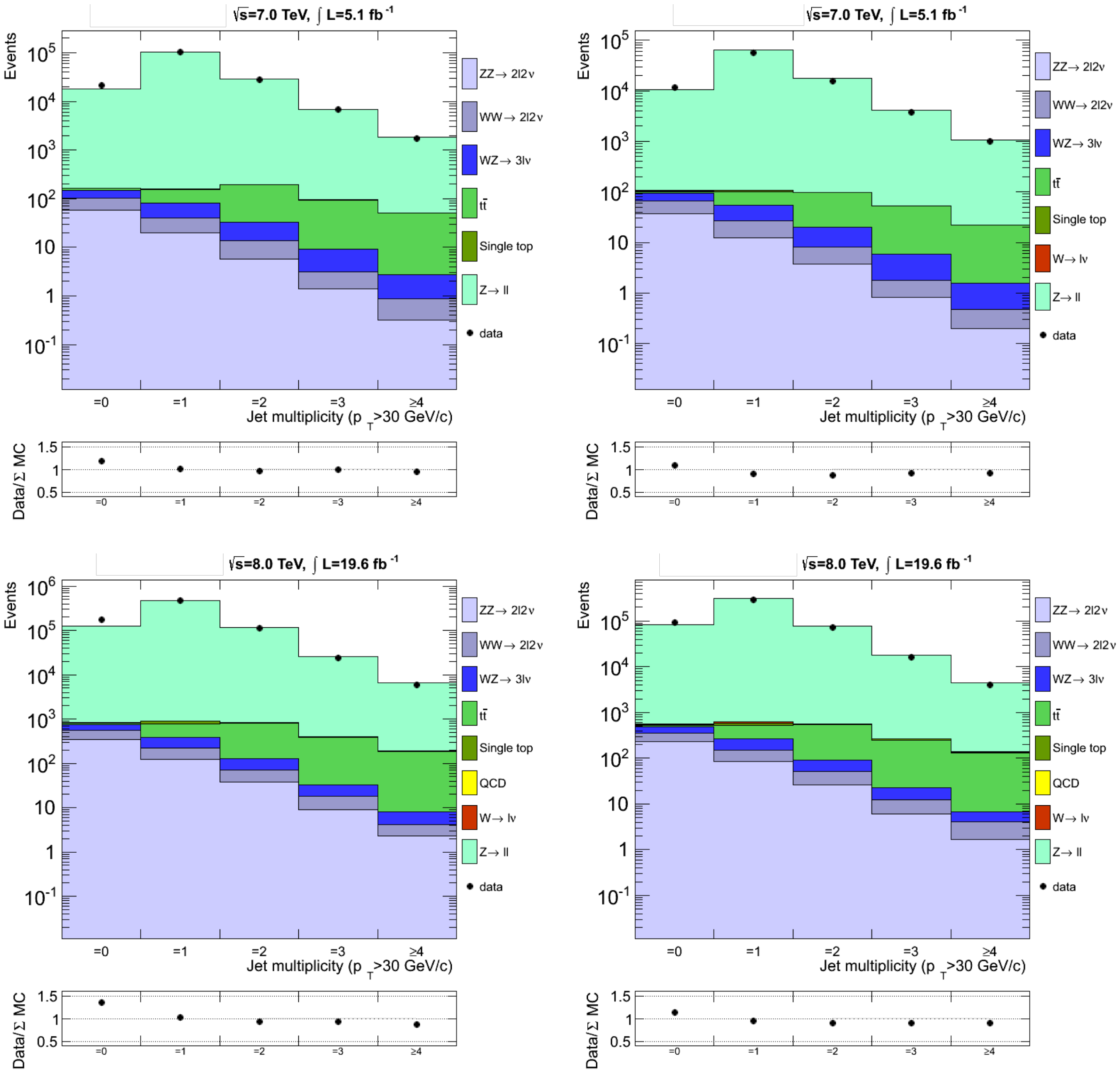

Figure 3.7: Number of jets with $p_T$ above 30 GeV per event, in $\mu\mu$ (left) and $ee$ (right) channels at 7 (top) and 8 (bottom) TeV, after the dilepton mass and $p_T$ selection (CMS data).

GeV) per event. While the category with two leptons in the final state is well reproduced in simulation, categories with more leptons are affected from a different fake rate in data and simulation.

Fig. 3.12 shows the event yield after each cut, for 7 and 8 TeV data. A general agreement with the Monte Carlo simulation is observed. It is also possible to see how top-based processes are reduced by the jet-veto and the DY background is strongly reduced by the cut on the reduced-$E_T^{miss}$.

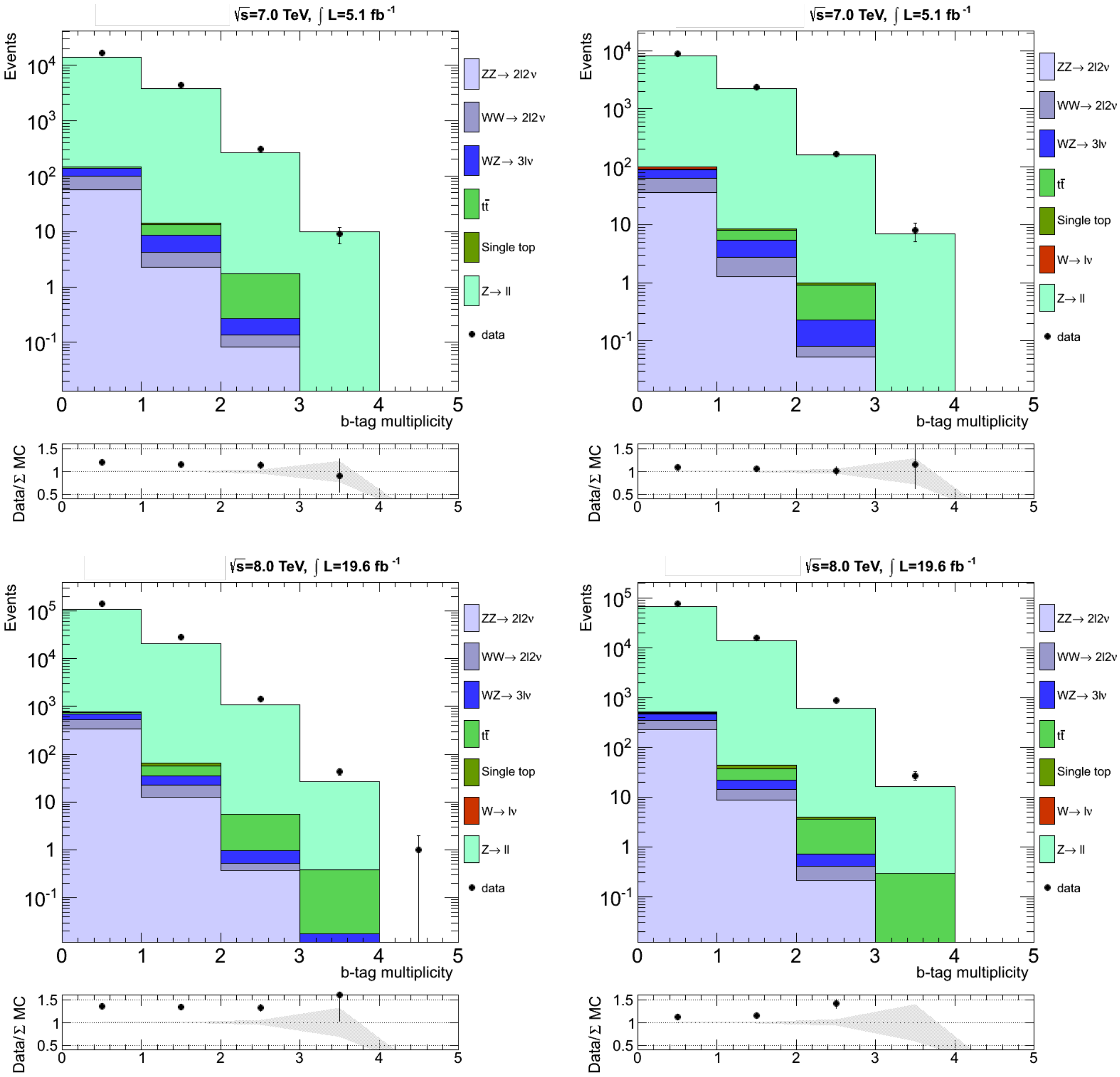


Figure 3.8: Number of $b$-tagged jets (CSV $< 0.244$) with $p_T > 20\ GeV$, in $\mu\mu$ (left) and $ee$ (right) channels at 7 (top) and 8 (bottom) TeV, after the dilepton mass and $p_T$ selection, and the jet veto (CMS data).

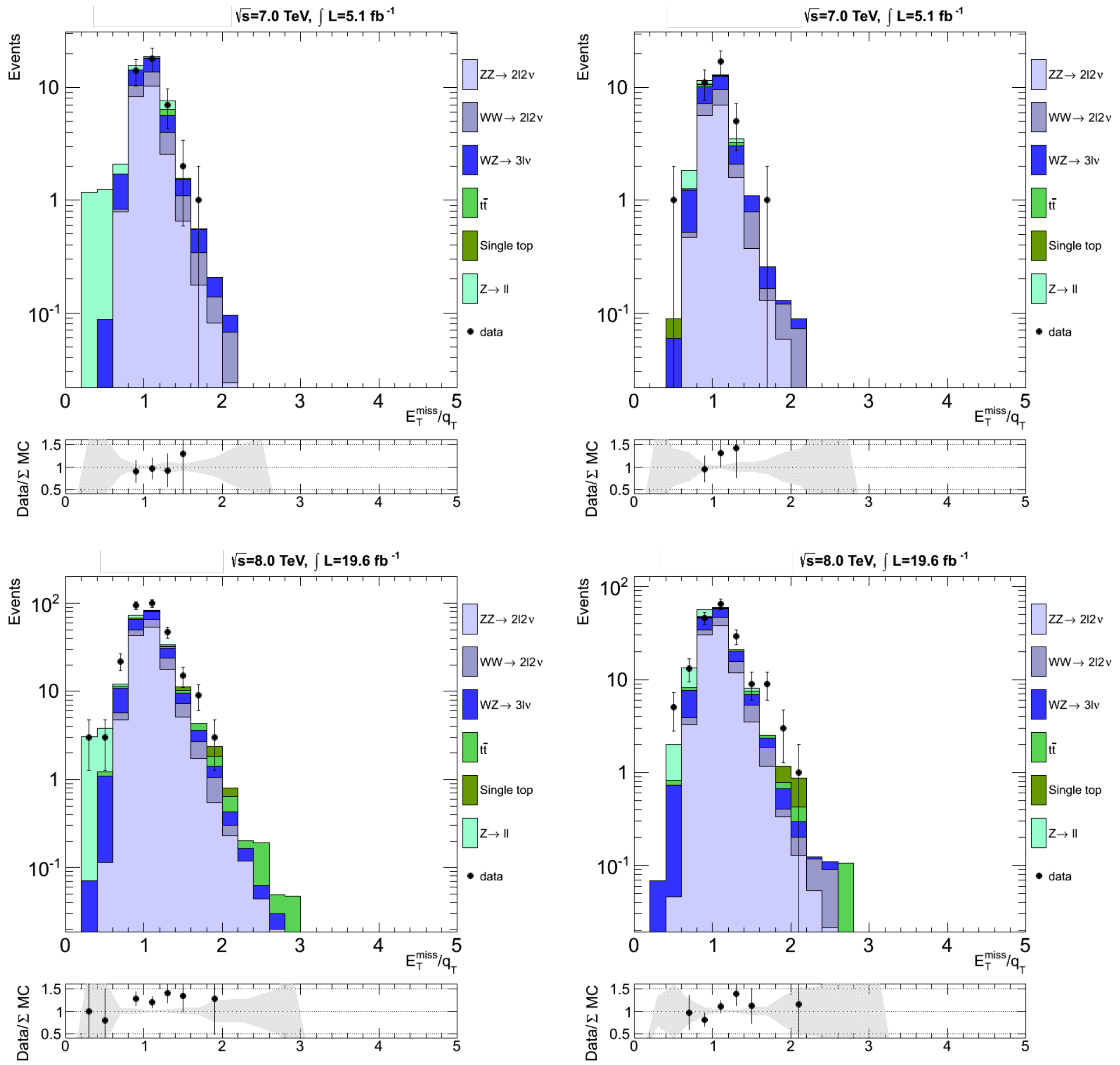


Figure 3.9: Distributions of the $E_T^{miss}$ balance variable $B$, in $\mu\mu$ (left) and $ee$ (right) channels at 7 (top) and 8 (bottom) TeV (CMS data), after the dilepton mass and $p_T$ selection, the reduced-$E_T^{miss}$ cut, the b-tagged jet veto, and the jet veto.

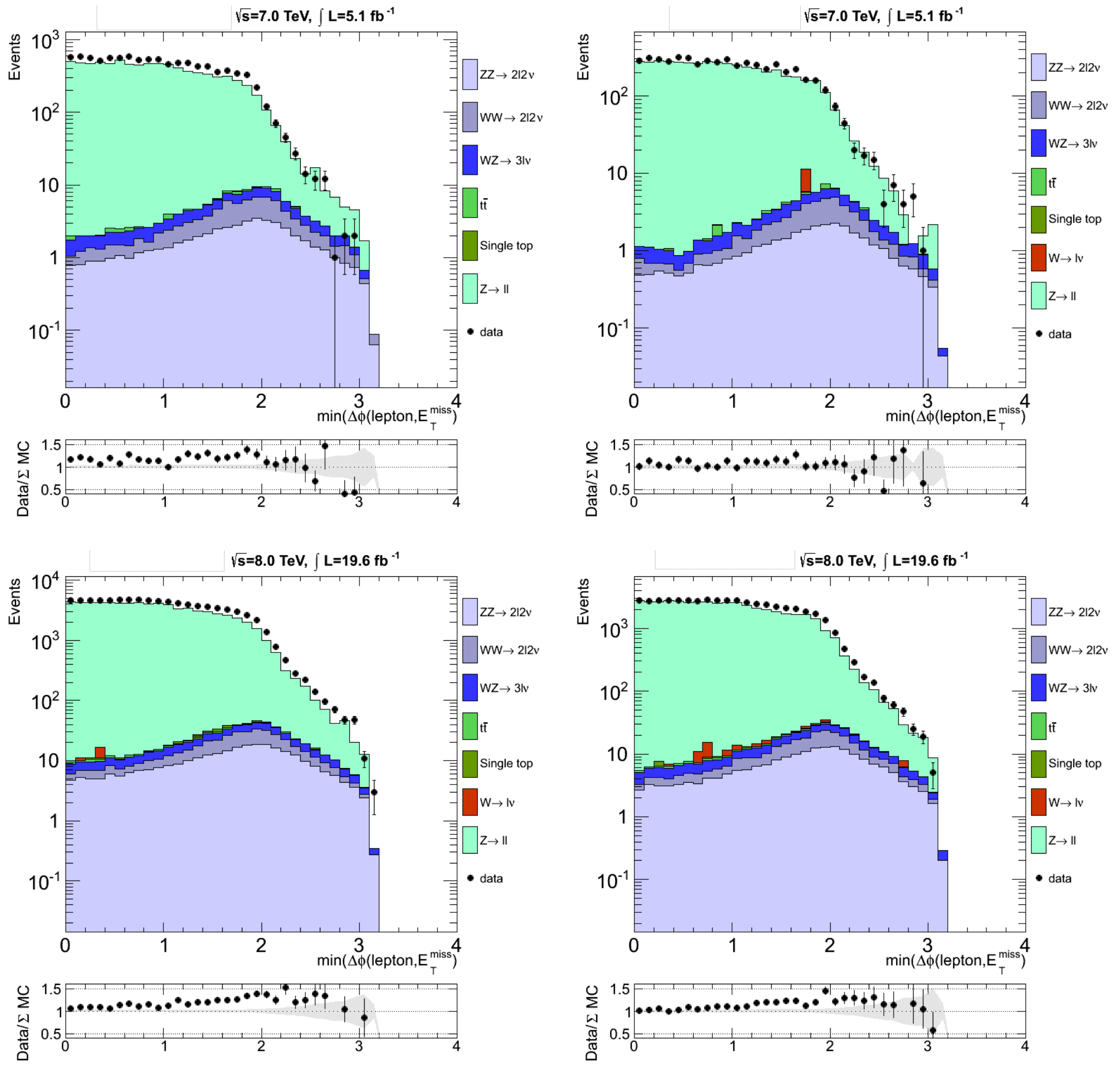

Figure 3.10: Distributions of the $\Delta\phi$ angle between the $E_T^{miss}$ and the closest lepton, in $\mu\mu$ (left) and $ee$ ( right) channels, after the dilepton mass and $p_T$ selection, the $b$-tagged jet veto, the jet veto, and the 3rd lepton veto (CMS data).

Table 3.9: Muon identification for $WZ$ background suppression.

| Variable | 2011: Tight OR Soft ID | |
|---|---|---|
| | Tight ID | Soft ID |
| $\|\eta\|$ | $< 2.4$ | $< 2.4$ |
| $p_T$ | $> 10$ GeV | $> 3$ GeV |
| GlobalMuon | true | - |
| TrackerMuon | true | true |
| Muon ID | - | "TMOneStationTight" |
| Muon matched stations | $> 1$ | - |
| Valid muon hits | $> 0$ | - |
| Valid tracker hits | $> 10$ | $> 10$ |
| Valid pixel hits | $> 1$ | - |
| Pixel layers with hits | - | $> 1$ |
| Transverse IP | $< 0.2$cm | $< 3$cm |
| Longitudinal IP | - | $< 30$cm |
| $\chi^2$/d.o.f. of inner track | - | $< 1.8$ |
| $\chi^2$/d.o.f. of global track | $< 10$ | - |
| Detector-based relative isolation | $< 0.15$ | - |

| Variable | 2012: Loose OR Soft ID | |
|---|---|---|
| | Loose ID | Soft ID |
| $\|\eta\|$ | $< 2.4$ | $< 2.4$ |
| $p_T$ | $> 10$ GeV | $> 3$ GeV |
| PFMuon | true | true |
| GlobalMuon | true (OR TrackerMuon) | true |
| TrackerMuon | true (OR GlobalMuon) | true |
| Muon ID | - | "TMOneStationTight" |
| Tracker layers with hits | - | $> 5$ |
| Pixel layers with hits | - | $> 1$ |
| $\chi^2$/d.o.f. of inner track | - | $< 1.8$ |
| Transverse IP | - | $< 3$cm |
| Longitudinal IP | - | $< 30$cm |
| PF relative isolation | $< 0.2$ | - |

Table 3.10: Electron identification for $WZ$ background suppression. Note that the selection in 2011 is the same as for signal electrons, except for the $p_T$ threshold.

| Variable | 2011 | | 2012 | |
|---|---|---|---|---|
| | Barrel | Endcap | Barrel | Endcap |
| $\|\eta\|$ | $< 1.4442$ | $> 1.566$ | $< 1.4442$ | $> 1.566$ |
| $p_T$ | $> 10$ GeV | | $> 10$ GeV | |
| $\sigma_{i\eta i\eta}$ | $< 0.01$ | $< 0.03$ | $< 0.01$ | $< 0.03$ |
| $\Delta\phi(track, SC)$ | $< 0.06$ | $< 0.04$ | $< 0.8$ | $< 0.7$ |
| $\Delta\eta(track, SC)$ | $< 0.004$ | $< 0.007$ | $< 0.007$ | $< 0.01$ |
| $H/E$ | $< 0.04$ | $< 0.1$ | $< 0.15$ | – |
| Transverse IP | $< 0.02$cm | | $< 0.04$cm | |
| Longitudinal IP | $< 0.1$cm | | $< 0.2$cm | |
| $\|1/E - 1/p\|$ | – | | $< 0.05$ | |
| Conversion vertex fit prob. | $10^{-6}$ | | – | |
| $\Delta R$ from muon candidates | $> 0.1$ | | $> 0.1$ | |
| Detector-based relative isolation | $< 0.1$ | | – | |
| PF relative isolation | – | | $< 0.15$ | |

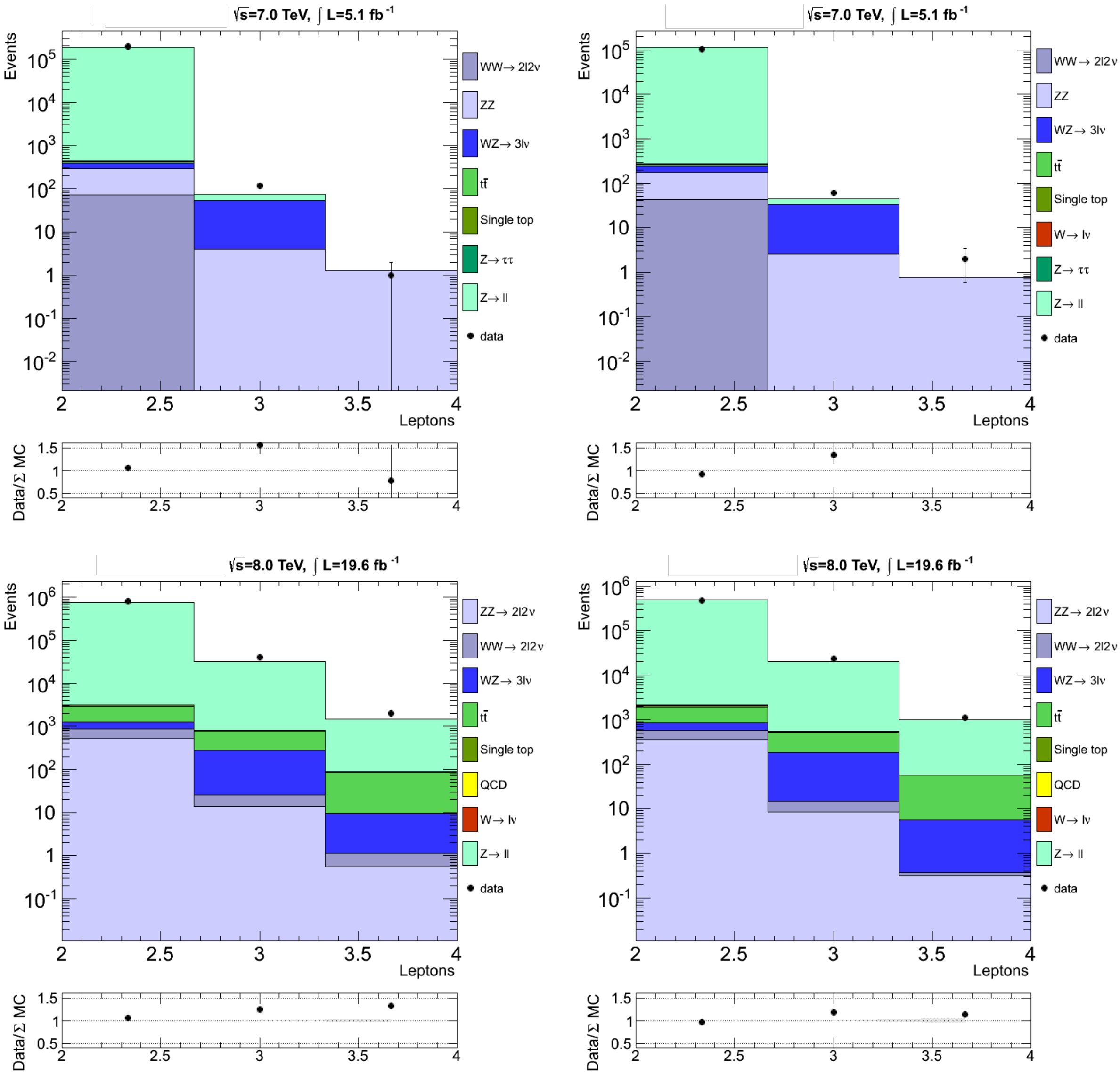


Figure 3.11: Number of loose leptons ($e$ and $\mu$ with $p_T > 10$ GeV) per event, in $\mu\mu$ (left) and $ee$ (right) channels at 7 (up) and 8 (right) TeV, after the dilepton mass and $p_T$ selection (CMS data).

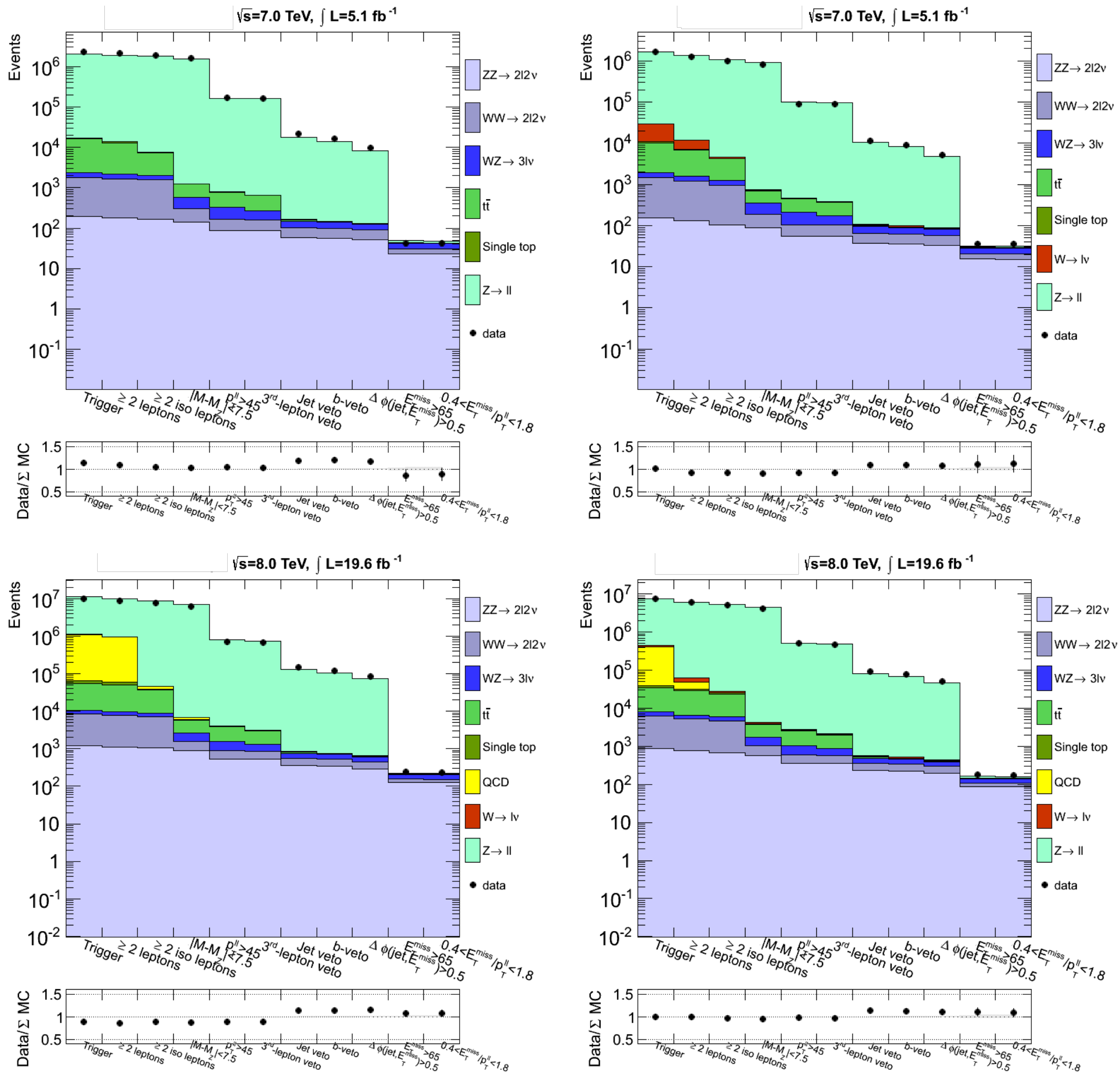


Figure 3.12: Event yield distribution after each selection cut for $\mu\mu$ (left) and $ee$ (right) channels and 7 (up) and 8 (right) TeV (CMS data).

## 3.8 Background estimation

### 3.8.1 Drell-Yan background

Although the $Z \to e^+e^-$ and the $Z \to \mu^+\mu^-$ processes do not include genuine $E_T^{miss}$ from neutrinos, the tail of the $E_T^{miss}$ distribution can be contaminated by these events due to detector energy resolution, jet energy mismeasurements and pileup energy fluctuations and instrumental noise. Although rare, these extreme cases are significant given the large cross section of DY with respect to the $ZZ$ signal.

Given the fact that the simulation does not fully reproduce detector and pileup effects on the $E_T^{miss}$ distribution, especially in the tails, and that the simulation is limited in statistics, we build a data-driven model of the DY. For this purpose we use a process which is similar to the DY production, but which has much higher cross section: the production of prompt isolated photons in association with jets (i.e. $\gamma$+jets).

Single photons are produced through Compton- and annihilation-like processes involving quarks and gluons from the protons. The characteristics of these events (kinematics of the boson, jet multiplicity, underlying event and pileup conditions) are expected to resemble the characteristics of the DY process. We expect therefore that a reasonable description of the $E_T^{miss}$ distribution is obtained from the photon sample. However some corrections must be applied to the $\gamma$+jets sample to ensure a good modeling of the DY process. These corrections account for the difference in the kinematics distributions of the photon and the $Z$-boson. These differences affect also the distributions of the hadronic system that recoils against the boson. Therefore, if not corrected, they would affect the instrumental $E_T^{miss}$.

The yield of photon events is scaled to the observed dilepton yield as function of the transverse momentum. This accounts for differences in the selection efficiency of the dileptons and photon candidates, but most of all it corrects the trigger prescales which are applied on the low $p_T$ photon triggers. More specifically, due to trigger constraints, only photons with $p_T > 30$ GeV are considered for the study and the same cut is applied to the off-line reconstructed $\gamma$. This also drives the minimum $p_T$ threshold applied to dilepton events for consistency. The reweighting is performed after applying a jet veto (for jets with $p_T > 30$ GeV, as in Sec. 3.7) to both the dilepton and photon samples: this corrects possible discrepancies in jet multiplicity between the two processes. Only photons in the barrel region are used given that both the purity and the resolution are better in that region. The selection of photon events is summarized in Table 3.11. It is based on electromagnetic shower shape variables, the ratio between the energy measured in the ECAL and in the HCAL ($H/E$), the isolation in the tracker and the calorimeters, taking into account the pileup contribution to the cluster ($\rho_{25}$). After this selection, several processes with instrumental $E_T^{miss}$ contribute to the photon sample: single $\gamma$ events, double $\gamma$ events where either photon escapes detection or fails the identification, and multi-jet events with a fake photon.

Processes with real $E_T^{miss}$ can also contaminate this sample: $W/Z{+}\gamma$, with the $Z$ decaying to $2l/2\nu$ or the W decaying to $l\nu$, with the lepton faking a photon or converting while into the tracker region. Although these processes have generally lower cross sections, they are characterized by large $E_T^{miss}$ values, and thus contribute to the tails of the distribution, where it is most important to measure the residual instrumental background. In order to reduce their contribution, specific selections are applied, but to ensure a fully pure $\gamma$ + jet sample, we subtract the remaining contributions estimated from simulation from our data, as explained in the following. The specific selections are:

- the event must have exactly one photon and no leptons;
- only jets with $\Delta R > 0.4$ from photons are considered, with no jet b-tagged;
- the photon has to be unconverted [58].

The same photon selection is applied to both 2011 and 2012 data periods.

Table 3.11: Photon identification for Drell-Yan background modeling.

| Variable | Value |
|---|---|
| $E_T$ | $> 5$ GeV |
| $\lvert\eta\rvert$ | $< 1.4442$ |
| $H/E$ | $< 0.05$ |
| $\sigma_{i\eta i\eta}$ | $0.001 < \sigma_{i\eta i\eta} < 0.011$ |
| $\sigma_{i\phi i\phi}$ | $> 0.001$ |
| Track isolation (cone 0.4) | $< 2.0$ GeV $+0.001\,E_T + 0.0167\,\rho_{25}$ |
| ECAL isolation (cone 0.4) | $< 4.2$ GeV $+0.006\,E_T + 0.183\,\rho_{25}$ |
| HCAL isolation (cone 0.4) | $< 2.2$ GeV $+0.0025\,E_T + 0.062\,\rho_{25}$ |

The weights to be applied to each $\gamma$+jet event are derived dividing the fit to the shape of the dilepton $p_T$ spectra and the fit to the photon $p_T$ spectra (Fig. 3.13). To include the effect of the prescale in photon data (bottom), the fit has been performed in $p_T$ bins, depending on the number of presacales present in data. Assuming $N$ $p_T$ bins, the fit parametrization in each bin is of the form:

$$4i\frac{x^{(4i+2)}}{4i+1} \cdot \frac{e^{-x/(4i+1)}}{1+e^{(Tr_i)/(4i+3)}} \text{ for } Tr_i < x < Tr_{i+1} \quad i = 0, 2...N-1. \tag{3.11}$$

where $i$ is the number of the $p_T$ bin, $Tr_i$ and $Tr_{i+1}$ represent the $p_T$ boundaries of the bin. The numerator of the second term represents the exponentially decreasing part of the distribution, while the denominator and the first term allow to parametrize the transition between prescales.

Both data and MC photon events are reweighted separately to the dilepton $p_T$ spectrum by multiplying the events by the weight computed in data and in simulation respectively. Fig. 3.14 shows the photon $p_T$ spectrum in MC before reweighting. It can be seen that the contribution from $W\gamma$ and $Z\gamma$ processes is small, about 1% or less of the total, across the whole spectrum. Therefore, their effect on the weights is negligible.

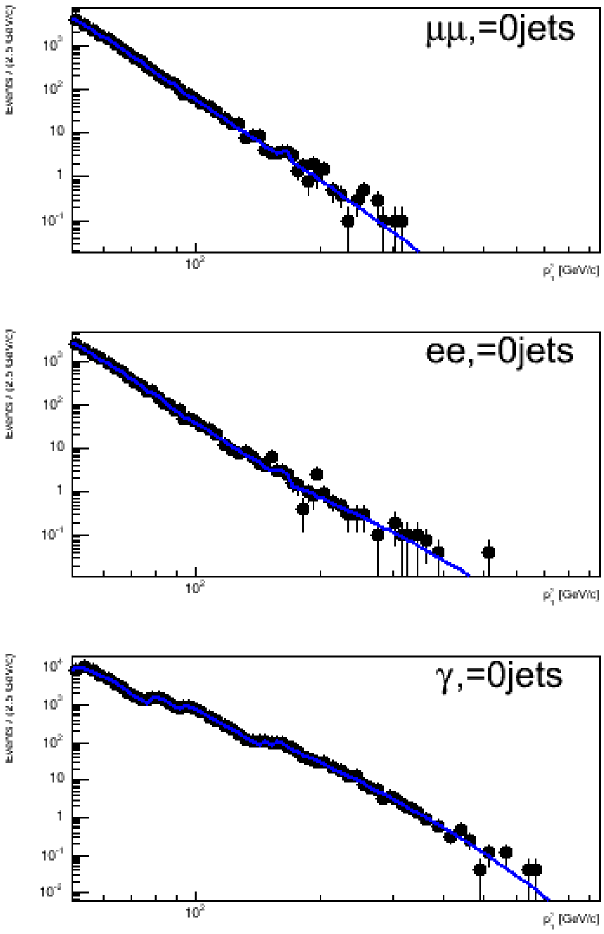


Figure 3.13: Dilepton $\mu\mu$ (top), dilepton $ee$ (center) and photon (bottom) $p_T$ spectra at 8 TeV in data. The blue line represents the fit to the distribution. The photon data distribution shows the effect of trigger prescales at different $p_T$ thresholds.

Given that the main variable of interest to select the $ZZ$ candidates is the reduced-$E_T^{miss}$ we have adapted its construction for the $\gamma$ event case. The longitudinal and perpendicular

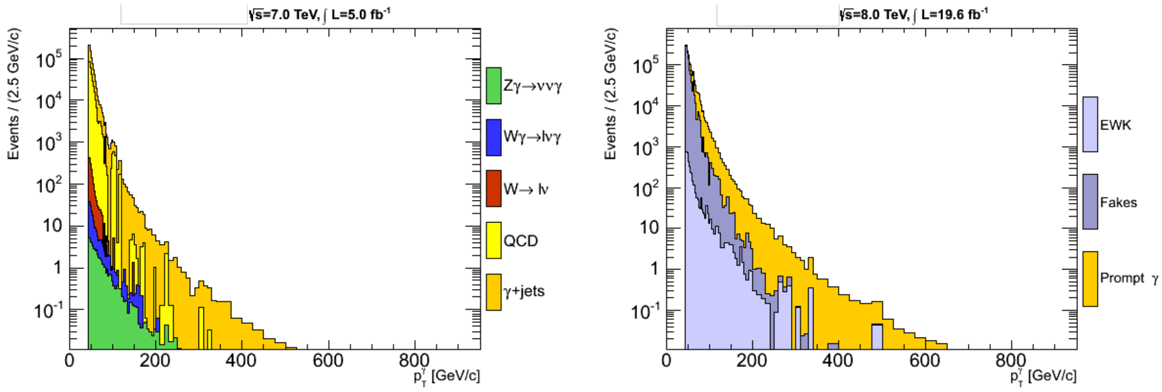


Figure 3.14: Photon $p_T$ spectra in MC at 7 TeV (left) and 8 TeV (right), before reweighting. In the 8 TeV plots, the $W$ + jets and $\gamma + W/Z$ processes are grouped as "EWK", and QCD processes are labelled as "FAKE".

projections are defined with respect to the $\gamma$ direction. Fig. 3.15 shows the distribution of the longitudinal component (left) and the transversal component (right), of the reduced-$E_T^{miss}$ variable, after the reweighting of the data and the simulation to the dilepton $p_T$ separately. It can be seen that the $W + jet$ and $\gamma + W/Z$ events are not fully suppressed and still contaminate the tail of the distribution (in the 8 TeV plots, they are collectively shown as $EWK$). Fig. 3.16 shows the reduced-$E_T^{miss}$ distribution. As in the dilepton case, also the reduced-$E_T^{miss}$ distribution in $\gamma + jet$ events shows a poor agreement between data and MC. This is expected, given the imperfect description of the instrumental background in simulation. The EWK processes with real $E_T^{miss}$, however, are expected to be modeled better, so we subtract them bin by bin from the reweighted photon kinematic distributions after applying the full selection.

We assume that the prediction obtained from the reweighted photon sample after the EWK subtraction in the $ZZ$ selection region ($N_{\mathrm{DY}}^{\mathrm{data}}$) is the central value of the actual contribution from the DY process. This is affected by several sources of uncertainty: other than the statistical error and the theoretical uncertainty on the cross sections of the EWK processes, we assign a conservative systematic uncertainty estimated as the relative difference between the DY event yields in data and simulation, in a control region obtained by imposing: reduced-$E_T^{miss} < 60$ GeV (see Fig. 3.17). This gives a systematic uncertainty of about 25% at 7 TeV and 40% at 8 TeV.

Fig. 3.18 shows the final reduced-$E_T^{miss}$ distributions in the photon template after the reweighting procedure, with the contribution from electroweak processes in MC, which is finally subtracted to estimate the residual instrumental background. The agreement is poor, but this is expected, since at this level the Monte Carlo description is expected to be at the

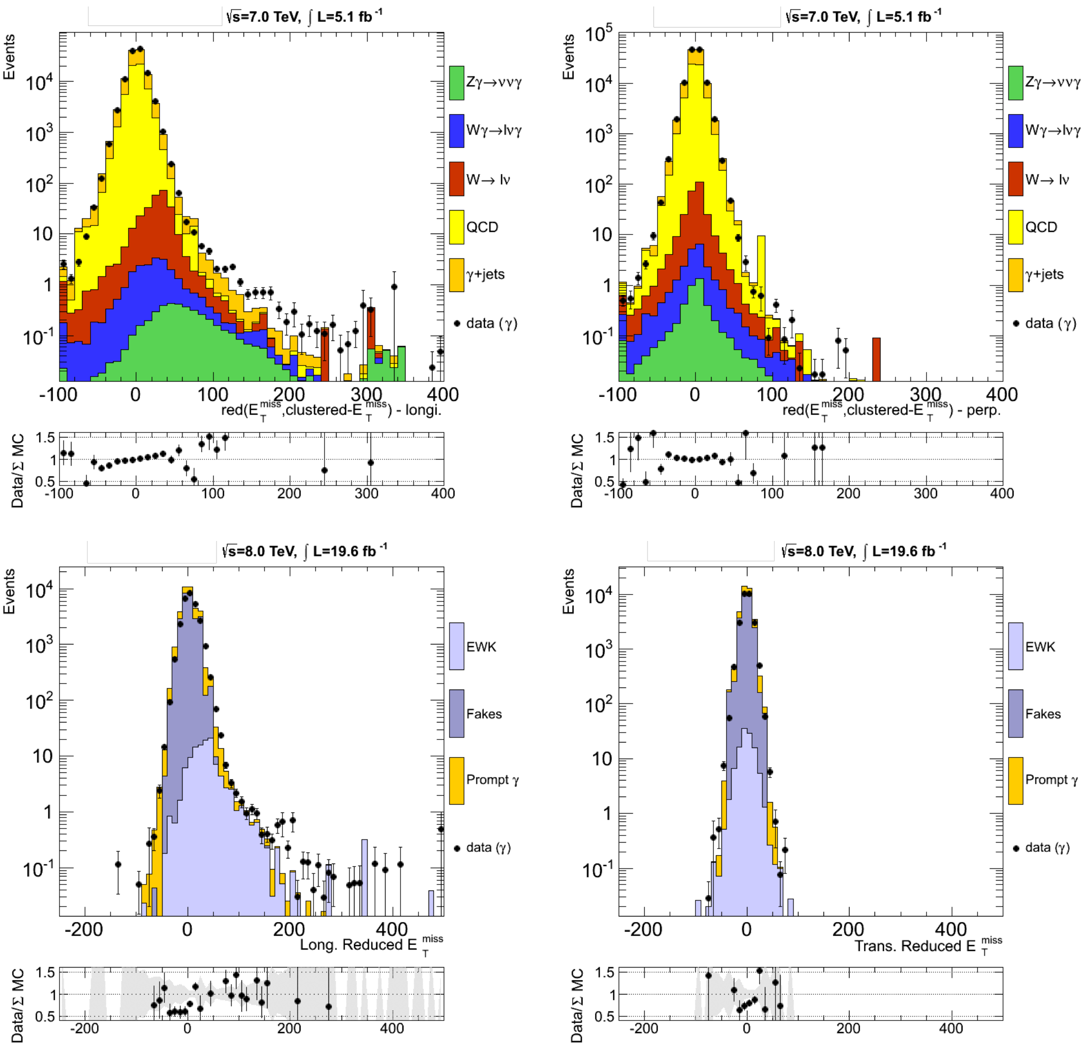


Figure 3.15: Longitudinal (left) and transverse (right) components of the reduced-$E_T^{miss}$ variable in the photon sample, after the reweighting of the data and the simulation to the dilepton $p_T$ separately. In the 8 TeV plots (bottom), the $W$ + jets and $\gamma + W/Z$ processes are grouped as "EWK", and QCD processes are labelled as "FAKE" (CMS data).

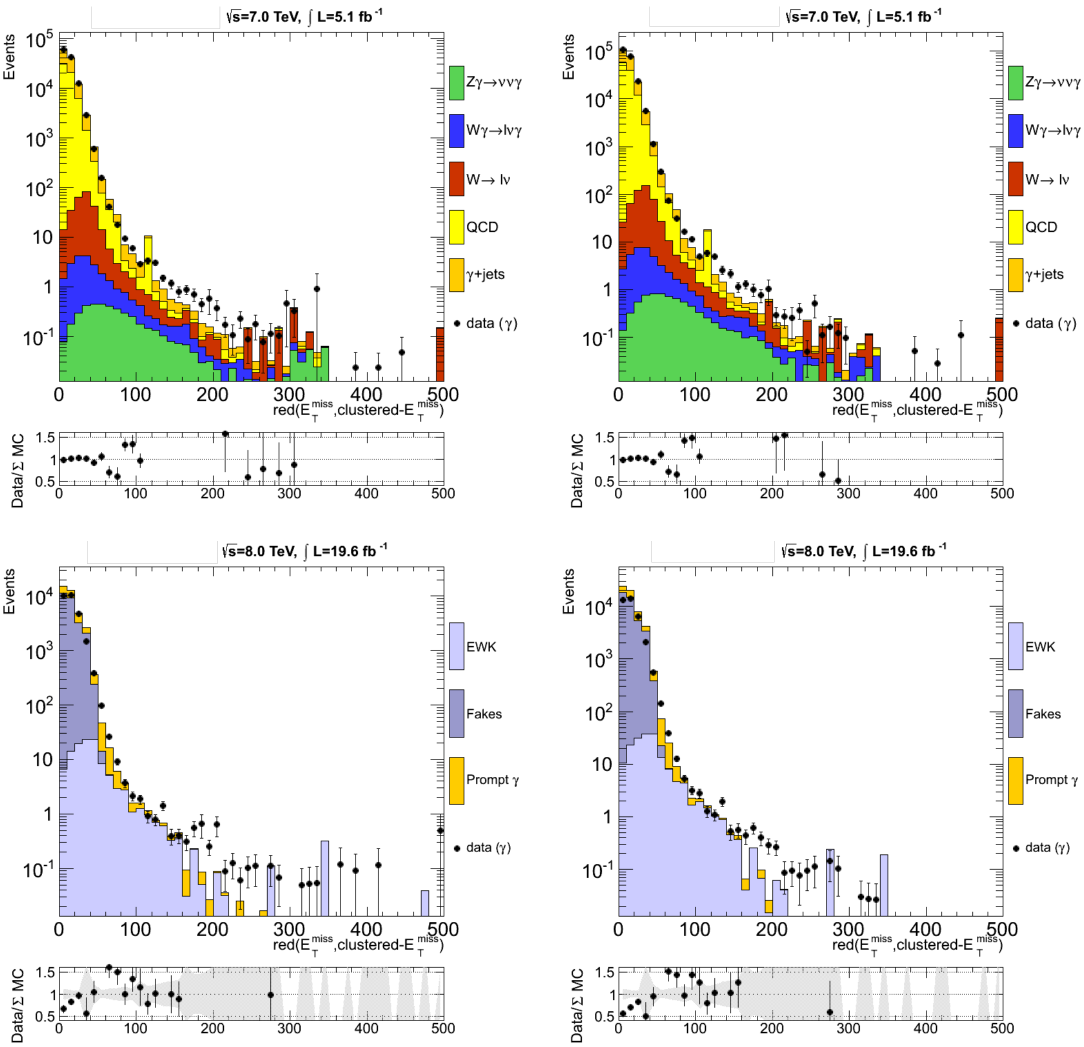


Figure 3.16: Reduced-$E_T^{miss}$ spectrum in the photon sample ($ee$ on the left and $\mu\mu$ on the right), after the reweighting of the data and the simulation to the dilepton $p_T$ separately. In the 8 TeV plots (bottom), the $W$ + jets and $\gamma$ + $W/Z$ processes are grouped as "EWK", and QCD processes are labelled as "FAKE" (CMS data).

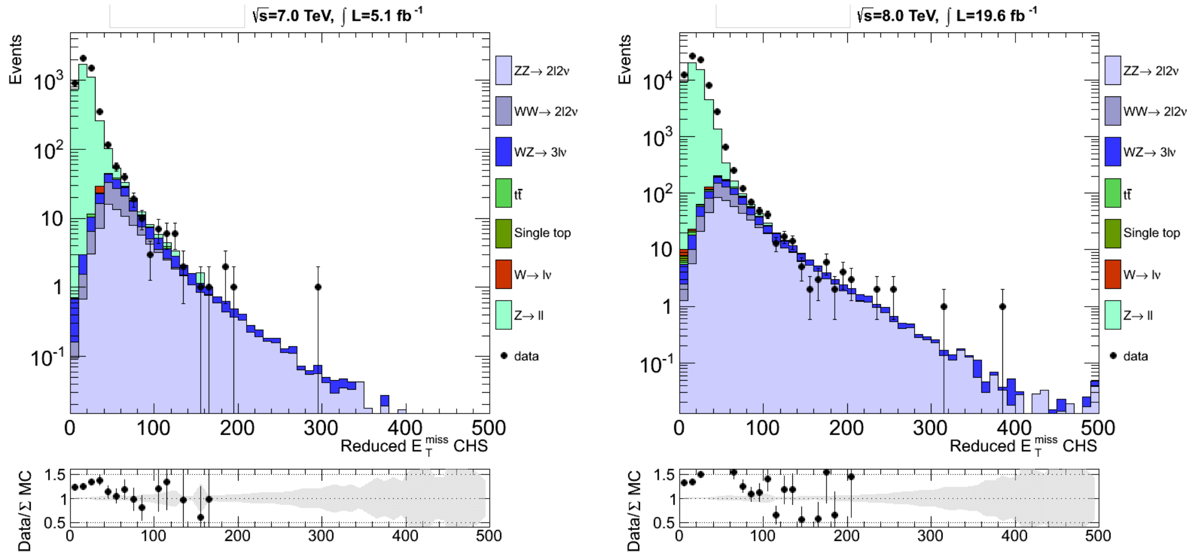


Figure 3.17: Reduced-$E_T^{miss}$ distributions in data and simulation at 7 TeV (left) and 8 TeV (right), after the full selection except for the reduced-$E_T^{miss}$ cut (CMS data).

same level of the Drell-Yan one, and this represents the reason why a data-driven estimation is needed.

Figures 3.19 and 3.20 show the distribution for the reduced-$E_T^{miss}$ and the $Z$ $p_T$ variables using the data-driven prediction for the DY contribution. A fair agreement is found in all cases.

The performance of this data-driven estimate is also evaluated as function of the pileup by profiling the spectrum of the reduced-$E_T^{miss}$ variable. For this purpose we compute the average reduced-$E_T^{miss}$ in dilepton and photon events as function of the average energy density in the event, i.e. the $\rho$ variable. The result is shown in Fig. 3.21 and shows a good agreement in between the different samples.

The whole procedure could be summarized as follow:

- a preselection is used to select a pure $\gamma$+jets sample;
- the yield of photon events is scaled to the observed dilepton yield as function of the transverse momentum;
- the whole selection of the main analysis is applied to the weighted $\gamma$+jets sample;
- the contamination from electroweak processes is subtracted to the reduced-$E_T^{miss}$ distribution of the $\gamma$+jets sample;

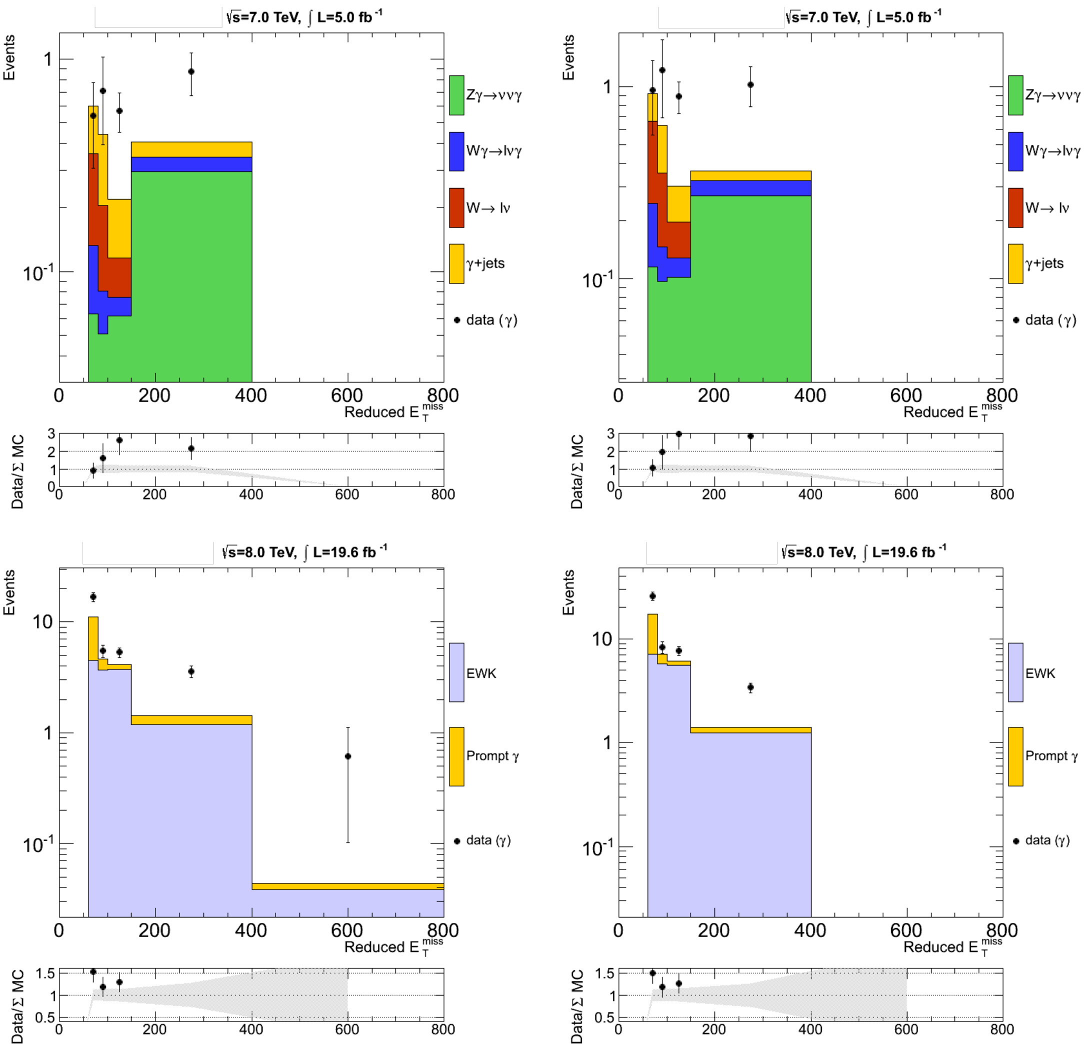


Figure 3.18: Reduced-$E_T^{miss}$ distributions in the photon template after reweighting to the $ee$ (left) and $\mu\mu$ (right) $p_T$ spectra, after the full selection. The contribution from electroweak processes in MC is also shown. In the 8 TeV plots (bottom), the $W$ + jets and $\gamma + W/Z$ processes are grouped as "EWK", and QCD processes are labelled as "FAKE".

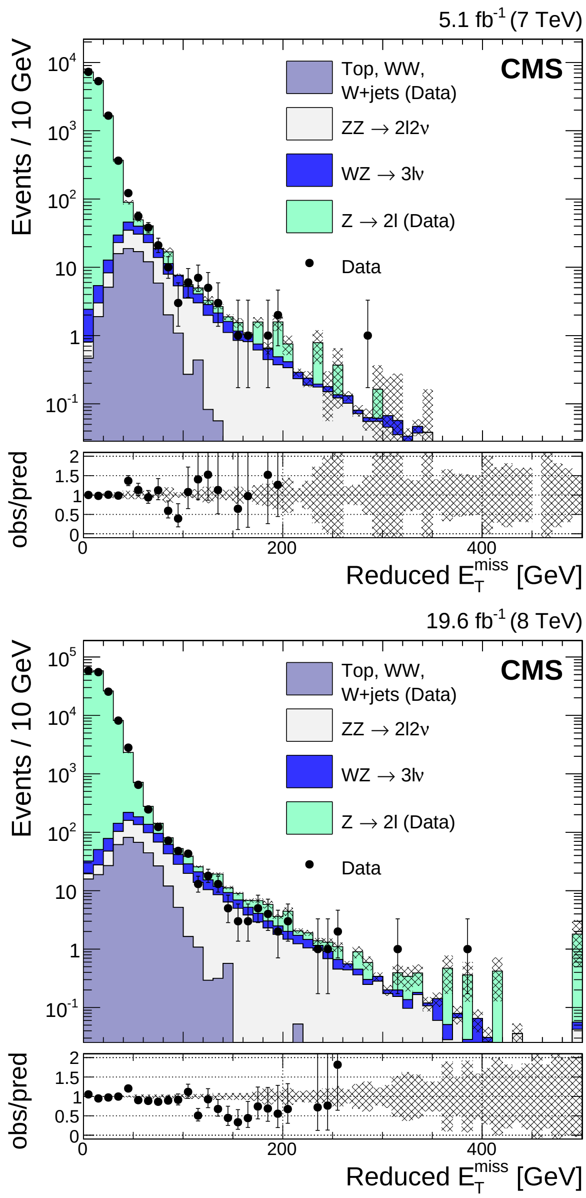


Figure 3.19: Reduced-$E_T^{miss}$ spectrum at 7 (up) and 8 (down) TeV using the photon model to describe the DY contribution, after a selection on the dilepton invariant mass and $p_T$, jet veto, b-tagged jet veto, third lepton veto, and $\Delta\phi(E_T^{miss}, jet)$. The gray error band represents the statistical uncertainty in the predicted yields [67].

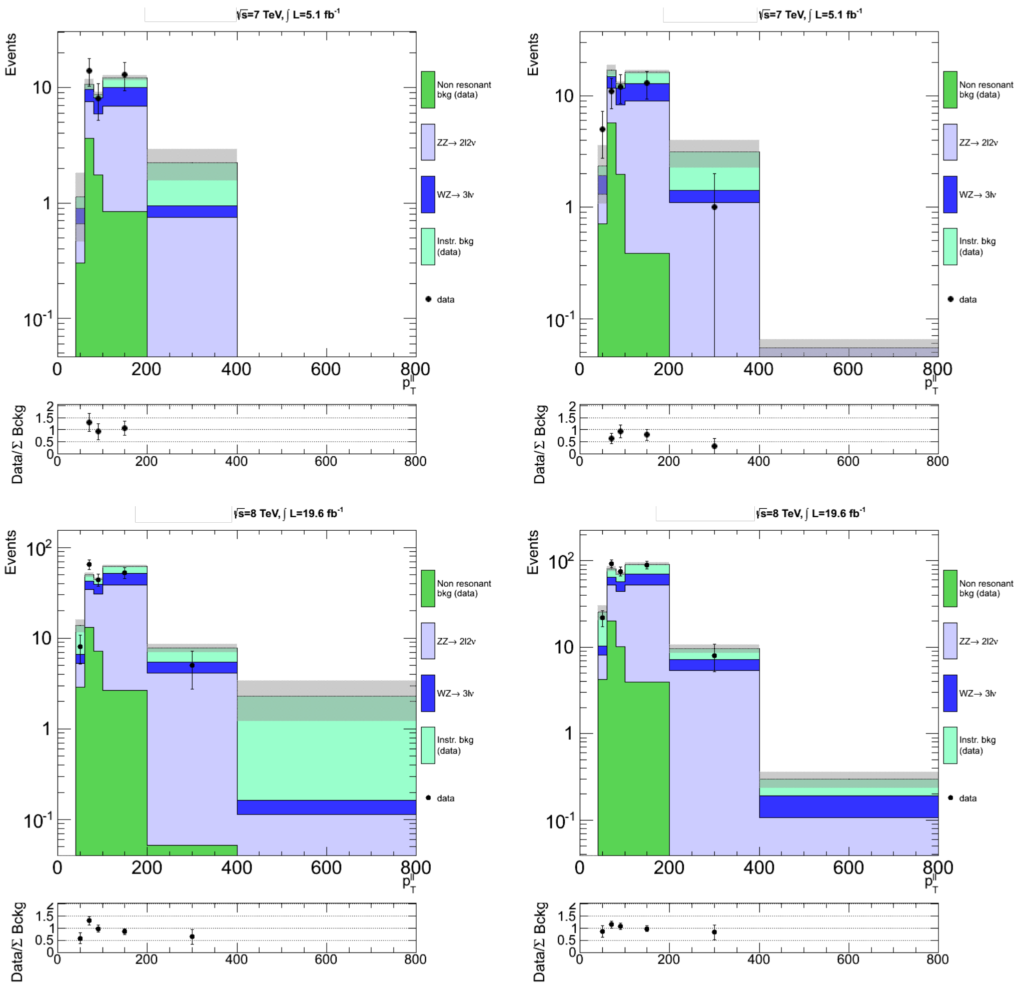


Figure 3.20: $Z$ $p_T$ spectrum after the full selection in $ee$ (left) and $\mu\mu$ (right) events using the template derived from the photon sample at 7 (up) and 8 (down) TeV (CMS data).

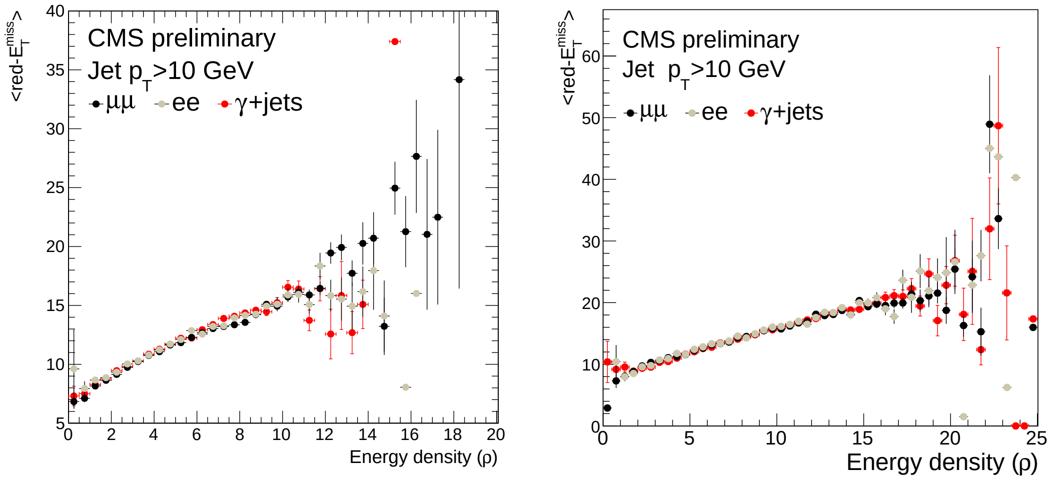


Figure 3.21: Profile of the reduced-$E_T^{miss}$ variable as function of $\rho$ for 7 TeV (left) and 8 TeV (right) data.

- the final reduced-$E_T^{miss}$ distribution is used as a estimation of the DY contamination in data

### 3.8.2 Non-Resonant background: $WW$ and top

We use a data-driven method to estimate the total number of background events from processes which do not involve a $Z$ boson, i.e. $WW$ pair production and top-induced background. We denominate these as non-resonant background (NRB).

In order to measure this contribution, a control sample is selected by applying the same requirements as in the main analysis, but looking at the side-bands of the $Z$ mass peak region, i.e. in the regions 55-70 GeV and 110-200 GeV. The non-resonant background yields in the same-flavor channels ($ee$ and $\mu\mu$) are obtained by scaling the number of events in the control sample. The rescaling is done by means of data-driven factors, derived in a sample selected by applying the same requirements as in the main analysis, bur removing the jet veto and requiring at least one b-jet. The scale factors are defines as follow:

$$\alpha_{ll} = N_{ll}^{\rm SB}/N_{e\mu}^{\rm SB}\,, \tag{3.12}$$

The NRB contamination in the $Z$-peak regions is then found as follows:

$$N_{ll}^{\rm peak} = \alpha_{ll} \times N_{e\mu}^{\rm peak}\,. \tag{3.13}$$

Two main sources of uncertainty affect the measurement of the $\alpha_{ll}$ factors and lead to a systematic mismeasurement of the non-resonant background:

- the statistical limitation of the control samples used to compute the scale factors. The relative uncertainties on the $\alpha_{ll}$ factors are thus assigned as systematic uncertainties on the background estimations, and are found to be about 10% and 5% at 7 and 8 TeV, respectively;

- the composition of the samples used for $\alpha_{ll}$ measurement does not reflect exactly the composition of the $e\mu$ control region (i.e. the region where $N_{e\mu}^{\text{peak}}$ is computed). In particular, requesting a b-tagged jet, the $WW$ component is reduced in favor of the top component. The bias induced by this effect is studied in simulation, as described below.

The $\alpha_{ll}$ factors include the branching ratios between $e\mu$ and $ee/\mu\mu$ final states, and also possible differences between lepton and trigger efficiencies in the different final states. The branching fractions to $e\mu$ and $ee/\mu\mu$ final states are clearly the same in $t\bar{t}$ and $WW$ processes. Both $t\bar{t}$ and from $WW$ produce isolated, high-$p_T$ leptons, but differences in efficiency can arise from the different kinematics of the two processes.

A closure test is performed by comparing the yields of non-resonant backgrounds in simulation ($N_{true}$, including $WW$, top, and $W$ + jets) with the prediction from the method described above ($N_{pred}$). A relative bias is estimated as $(N_{pred} - N_{true})/N_{true}$. The percentage bias of the method has been assigned as a total uncertainty of 20% on the estimated non-resonant background.

### 3.8.3 Control sample for top backgrounds

Besides the data-driven method described in the previous section, we checked if the simulation prediction is accurate enough for the top sample ($t\bar{t}$ and single top) in a high-statistics control region defined as:

- dilepton $p_T > 30$ GeV;

- dilepton mass in the side-bands of the $Z$-peak, i.e. 40-70 or 110-200 GeV;

- at least one jet with $p_T > 20$ GeV which is $b$-tagged.

The $E_T^{miss}$ spectrum is obtained in this region for both $ee$ and $\mu\mu$ events as well as for $e\mu$ events. We expect the high $E_T^{miss}$ region to be populated by $t\bar{t}$ dilepton events with a residual contribution from the $tW$ channel. Fig. 3.22 depicts this feature. We observe, independently of the poor simulation in the low $E_T^{miss}$ region (still dominated by DY in the same flavor channels), that the top contribution has a fair agreement to data. The $WW$ contribution is anyway estimated using the data-driven method described in the previous section.

### 3.8.4 Control sample for $WW$ background

As in the case of the top backgrounds, a control sample can be selected to enhance the $WW$ production and check the agreement between data and simulation.

To isolate a region dominated by the $WW$ production, the full selection described in Table 3.8 is applied, except for the dilepton invariant mass cut. Fig. 3.23 shows the dilepton mass distribution for the three channels, $\mu\mu$, $ee$ and $e\mu$, after such selection. Despite some contamination from other backgrounds, especially in the $ee$ channel, the side-bands of the $Z$ peak in $\mu\mu$ and $ee$ channels are dominated by the $WW$ background. The main sources of the discrepancy are the low statistic available on the $W \to l\nu$ sample and the difference between the fake rate in data and in simulation. Since we are using a data-driven technique to estimate the $WW$ contribution, this does not affect our measurement.

### 3.8.5 Control sample for $WZ$ background

The $WZ$ background is strongly reduced by means of the lepton veto described in Sec. 3.7. The veto is however inefficient if the lepton fails the CMS detector acceptance for charged leptons or if the lepton is a $\tau$ lepton as we don't apply a $\tau$ veto. In the first case the $WZ$ state becomes indistinguishable from the $ZZ \to 2\ell 2\nu$ final state. In the second case the $\tau$ is counted as a jet if it decays hadronically and the event will resemble a $ZZ + 1$ jet final state.

We try to select a pure $WZ$ control sample by selecting trilepton final states: $\mu\mu\ell$ and $ee\ell$, with $\ell = e, \mu$. The following selection has been used to define the control sample:

- Dilepton $p_T > 30$ GeV + lepton with $p_T > 10$ GeV;
- Dilepton mass consistent with the $Z$ nominal mass;
- $b$-jet veto.

Fig. 3.24 shows distributions of the transverse mass, defined as:

$$m_T = \sqrt{2 p_T(l) E_T^{miss} (1 - cos(\phi(l) - \phi(\nu)))} \tag{3.14}$$

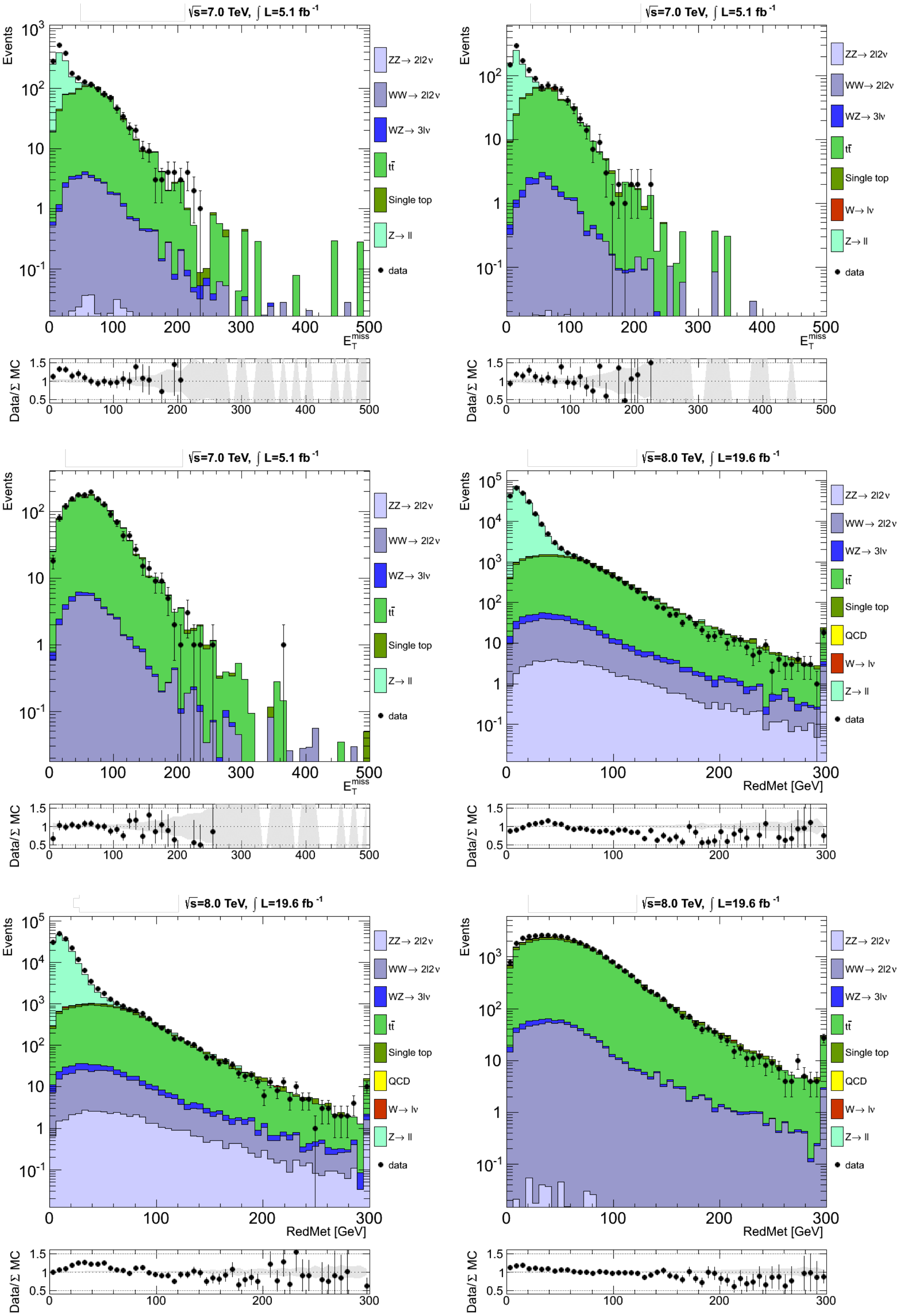


Figure 3.22: $E_T^{miss}$ distribution in the control region created to isolate the top contribution. The first three plots show the $\mu\mu$, $ee$ and $e\mu$ final state at 7 TeV, and the last three plots show the same final states at 8 TeV (CMS data).

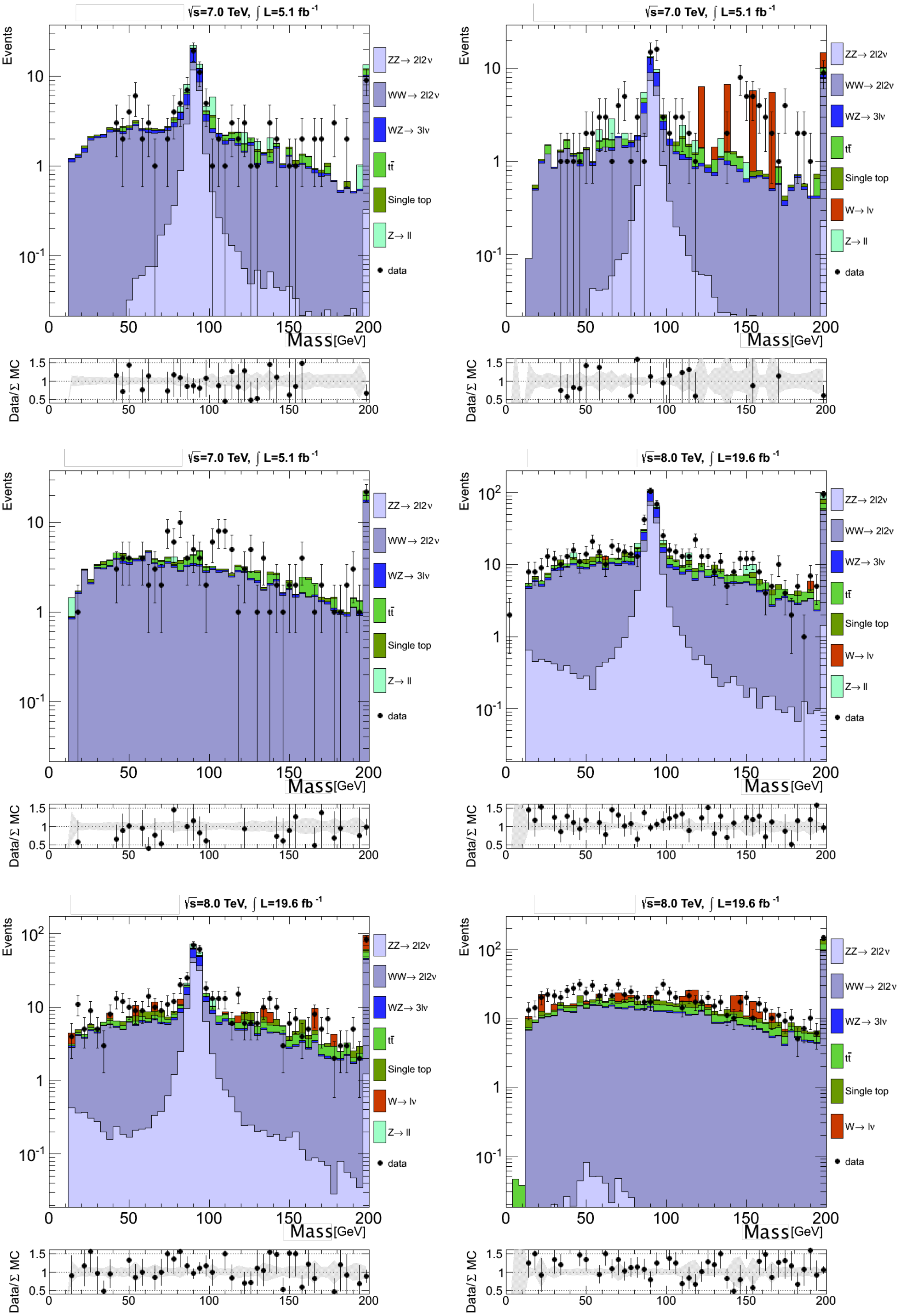

Figure 3.23: Dilepton invariant mass distributions in the control region created to isolate the $WW$ contribution. The first three plots show the $\mu\mu$, $ee$ and $e\mu$ final state at 7 TeV, and the last three plots show the same final states at 8 TeV (CMS data).

computed between the $E_T^{miss}$ and the third lepton system for such control sample, in $\mu\mu$ and $ee$ final states.

For $M_T > 50$ GeV the spectrum is dominated by the $WZ$ process, but due to the low statistic it is not possible to perform an accurate comparison between data and simulation. However, as mentioned in 3.3.2, the $WZ$ cross section has been taken from the measured cross section at CMS.

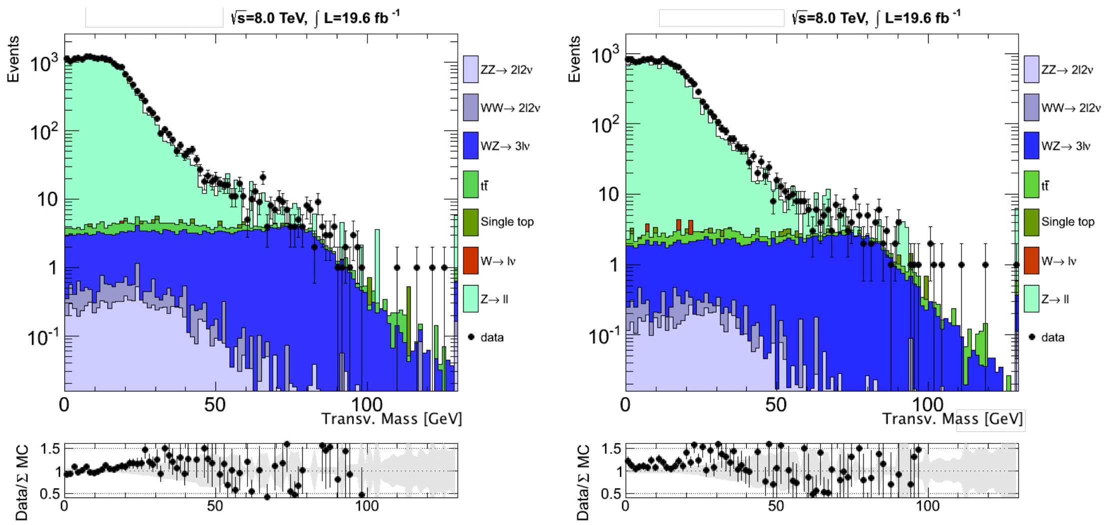


Figure 3.24: Distributions of transverse mass in $\mu\mu$ (left) and $ee$ (right) channels for trilepton events at 8 TeV (CMS data).

## 3.9 Systematic uncertainties

In the computation of the $ZZ$ cross section, different sources of systematic uncertainties might affect the number of observed events. The main sources of systematic uncertainties are summarized and estimated in the following paragraphs.

### 3.9.1 Monte Carlo and control sample statistics

For the processes estimated from simulation, $ZZ$ and $WZ$, the available statistics of the MC sample limits the precision of the modeling, and is therefore taken as a systematic uncertainty on the shape of the kinematic distributions used in the cross section measurement and aTGCs limit setting. The uncertainty has been approximated as correlated bin-by-bin. Fig. 3.25 shows the systematic variations in the $ZZ$ reduced-$E_T^{miss}$ distributions due to the limited statistics in simulation.

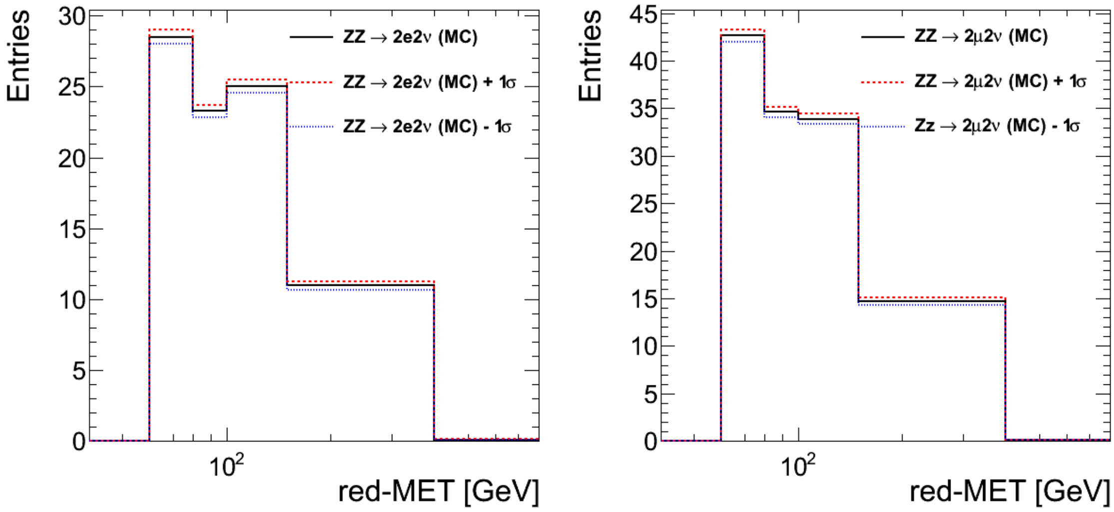


Figure 3.25: Systematic variations in the $ZZ \to 2l2\nu$ reduced-$E_T^{miss}$ distributions at 8 TeV for electrons (left) and muons (right) due to the limited statistics in simulation.

Similarly, the precision of the backgrounds estimated from data is limited by the available statistics in the control samples described in Sections 3.8.1 and 3.8.2: the $e\mu$ sample for non-resonant backgrounds, and the $\gamma +$ jets sample for Drell-Yan. For these uncertainties, the same treatment is used as in the case of MC statistical uncertainties. Fig. 3.26 shows the systematic variations in the DY reduced-$E_T^{miss}$ distributions due to the limited statistics in the control data samples.

Table 3.12 summarizes the uncertainties from the size of the MC samples or control

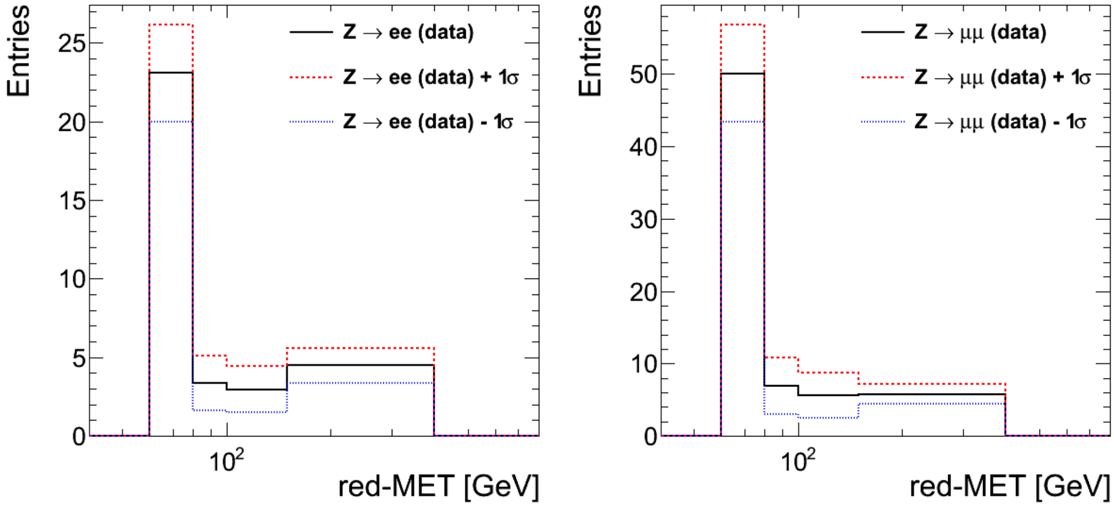


Figure 3.26: Systematic variations in the $Z \to 2l$ + jets reduced-$E_T^{miss}$ distributions at 8 TeV for electrons (left) and muons (right) due to the limited statistics in the $\gamma + jet$ control samples.

regions.

Table 3.12: Uncertainty stemming from the limited size of MC and control samples.

| | Sample | Uncertainty [%] 7 TeV $ee$ | 7 TeV $\mu\mu$ | 8 TeV $ee$ | 8 TeV $\mu\mu$ |
|---|---|---|---|---|---|
| MC | $ZZ$ | 2.3 | 1.8 | 2.0 | 1.7 |
| | $WZ$ | 6.1 | 4.9 | 3.1 | 2.6 |
| Control samples | Non resonant | 35 | 34 | 24 | 24 |
| | Drell-Yan | 48 | 48 | 21 | 21 |

### 3.9.2 $ZZ$ and $WZ$ cross sections: PDF's and QCD scales

The cross sections for pp $\to ZZ \to 2\ell 2\nu$ + X and pp $\to WZ \to 3\ell\nu$ + X are calculated using MCFM version 6.2 [16], and using parton density functions from the Les Houches accord PDF (LHAPDF) program, version 5.8.7 [68]. These versions represent the latest releases available at the time when this analysis was performed. To estimate the uncertainty on the PDF modeling, the NLO cross sections are recomputed using three different PDF sets (MSTW2008 represents the set of PDFs used to compute the cross section central value), according to the PDF4LHC recommendations [69, 70, 71, 72]. For each PDF set, the renormalization ($\mu_R$) and factorization ($\mu_F$) scales were changed simultaneously to $\mu = 45$, 90, and 180 GeV. The results are reported in Table 3.13 for $ZZ$, and in Tables 3.14 and 3.15 for $W^+Z$ and $W^-Z$.

Table 3.13: pp $\rightarrow$ ZZ $\rightarrow$ $2e2\nu$ + X NLO cross sections computed with MCFM 6.2, using LHAPDF 5.8.7.

| PDF Set | $\sigma_{\mathrm{NLO}}^{7TeV}(\mathrm{pp} \rightarrow \mathrm{ZZ} \rightarrow 2e2\nu + \mathrm{X})$ [fb] | | |
|---|---|---|---|
| | $\mu = 45$ GeV | $\mu = 90$ GeV | $\mu = 180$ GeV |
| MSTW2008nlo68cl | $92.227 \pm 0.015$ | $87.975 \pm 0.016$ | $85.273 \pm 0.016$ |
| CT10 | $89.987 \pm 0.020$ | $86.015 \pm 0.020$ | $83.462 \pm 0.020$ |
| NNPDF22_nlo_100 | $91.695 \pm 0.012$ | $87.663 \pm 0.012$ | $84.964 \pm 0.012$ |

| PDF Set | $\sigma_{\mathrm{NLO}}^{8TeV}(\mathrm{pp} \rightarrow \mathrm{ZZ} \rightarrow 2e2\nu + \mathrm{X})$ [fb] | | |
|---|---|---|---|
| | $\mu = 45$ GeV | $\mu = 90$ GeV | $\mu = 180$ GeV |
| MSTW2008nlo68cl | $112.618 \pm 0.015$ | $108.151 \pm 0.015$ | $104.650 \pm 0.015$ |
| CT10 | $110.178 \pm 0.019$ | $105.785 \pm 0.019$ | $102.862 \pm 0.019$ |
| NNPDF22_nlo_100 | $112.304 \pm 0.012$ | $107.413 \pm 0.012$ | $104.099 \pm 0.012$ |

Table 3.14: pp $\rightarrow$ W$^+$Z $\rightarrow$ $\mu\nu 2e$ + X NLO cross sections computed with MCFM 6.2, using LHAPDF 5.8.7.

| PDF Set | $\sigma_{\mathrm{NLO}}^{7TeV}(\mathrm{pp} \rightarrow \mathrm{W^+Z} \rightarrow \mu\nu ee + \mathrm{X})$[fb] | | |
|---|---|---|---|
| | $\mu = 45$ GeV | $\mu = 90$ GeV | $\mu = 180$ GeV |
| MSTW2008nlo68cl | $46.206 \pm 0.016$ | $43.918 \pm 0.016$ | $42.042 \pm 0.016$ |
| CT10 | $45.732 \pm 0.022$ | $43.421 \pm 0.022$ | $41.675 \pm 0.022$ |
| NNPDF22_nlo_100 | $46.503 \pm 0.013$ | $44.047 \pm 0.013$ | $42.262 \pm 0.013$ |

| PDF Set | $\sigma_{\mathrm{NLO}}^{8TeV}(\mathrm{pp} \rightarrow \mathrm{W^+Z} \rightarrow \mu\nu ee + \mathrm{X})$ [fb] | | |
|---|---|---|---|
| | $\mu = 45$ GeV | $\mu = 90$ GeV | $\mu = 180$ GeV |
| MSTW2008nlo68cl | $56.048 \pm 0.016$ | $53.607 \pm 0.016$ | $51.603 \pm 0.016$ |
| CT10 | $56.072 \pm 0.022$ | $53.004 \pm 0.022$ | $51.143 \pm 0.022$ |
| NNPDF22_nlo_100 | $56.486 \pm 0.013$ | $53.659 \pm 0.013$ | $51.690 \pm 0.013$ |

The PDF uncertainty is evaluated as the maximum spread of the cross sections computed at $\mu = 90$ GeV with the three PDF sets, including the respective errors, and it results to be 1.15% (1.12%) at 7 (8) TeV for $ZZ$, and 1.20% (1.16%) at 7 (8) TeV for $WZ$. The uncertainty from the renormalization and factorization scales is evaluated as the maximum spread of the cross section central values computed at different scales $\mu$ for each PDF set.

Table 3.15: pp $\to$ W$^-$Z $\to \mu\nu ee$ + X NLO cross sections computed with MCFM 6.2, using LHAPDF 5.8.7.

| PDF Set | $\sigma_{\rm NLO}^{7TeV}$(pp $\to$ W$^-$Z $\to \mu\nu ee$ + X) [fb] | | |
|---|---|---|---|
| | $\mu = 45$ GeV | $\mu = 90$ GeV | $\mu = 180$ GeV |
| MSTW2008nlo68cl | $26.080 \pm 0.018$ | $24.747 \pm 0.018$ | $23.677 \pm 0.018$ |
| CT10 | $25.029 \pm 0.024$ | $23.746 \pm 0.024$ | $22.823 \pm 0.024$ |
| NNPDF22_nlo_100 | $26.058 \pm 0.015$ | $24.697 \pm 0.015$ | $23.736 \pm 0.015$ |

| PDF Set | $\sigma_{\rm NLO}^{8TeV}$(pp $\to$ W$^-$Z $\to \mu\nu ee$ + X) [fb] | | |
|---|---|---|---|
| | $\mu = 45$ GeV | $\mu = 90$ GeV | $\mu = 180$ GeV |
| MSTW2008nlo68cl | $32.691 \pm 0.017$ | $31.102 \pm 0.017$ | $29.846 \pm 0.017$ |
| CT10 | $31.369 \pm 0.023$ | $29.813 \pm 0.023$ | $28.796 \pm 0.023$ |
| NNPDF22_nlo_100 | $32.605 \pm 0.014$ | $31.012 \pm 0.014$ | $29.847 \pm 0.014$ |

An uncertainty of about 5.0% (4.5%) at 7 (8) TeV is found for $ZZ$ process, and 5.9% (5.4%) for $WZ$ process. For the $ZZ$ signal, however, these values are not used, and are instead replaced by a more accurate estimation, including the requirement of 0 jets with $p_T > 30$ GeV.

Since in our analysis we only select events with no jets with $p_T > 30$ GeV, we evaluate the systematic uncertainty on the theoretical definition of exclusive production of $ZZ$ in association with 0 jets, following the prescription described in [73, 74] for the case of the $H$ cross section. With MCFM we compute the inclusive cross sections of $ZZ + n$ jets (jet $p_T > 30$ GeV), with $n \geq 0$ and $n \geq 1$, and deduce the exclusive cross section of $ZZ$ + 0 jets by subtracting the two inclusive results. As explained above, we vary the QCD scales $\mu$ from 90 GeV to 45 and 180 GeV, and use the variations to evaluate errors on the inclusive cross sections $\sigma_{\geq 0j}$ and $\sigma_{\geq 1j}$, which we call $\epsilon_{\geq 0j}$ and $\epsilon_{\geq 1j}$ respectively. According to [74], the relative uncertainty on the exclusive cross section $\sigma_{0j}$ depends on two independent terms, related to the errors on $\sigma_{\geq 0j}$ and $\sigma_{\geq 1j}$:

$$\epsilon_{\geq 0j} \simeq \; 7.0\% \; (9.4\%) \text{ at } 7 \; (8)\text{TeV} \; ,$$

$$\epsilon_{\geq 1j} \simeq \; 8.3\% \; (7.4\%) \text{ at } 7 \; (8)\text{TeV} \; .$$

Since the errors are uncorrelated, we can sum them in quadrature, obtaining about 11% at 7 TeV and 12% at 8 TeV. Comparing these results with the QCD scale errors for $ZZ$ obtained in the previous section (5.0% and 4.5%), we can deduce the effect of the jet veto on the theoretical uncertainty.

Due to the importance of the $Z$ $p_T$ and $E_T^{miss}$ distributions for aTGC searches, we compute this uncertainty as a function of the $Z$ $p_T$, and we use it as a shape uncertainty. As we expect from Sec. 1.2.4, and in particular from Fig. 1.5, the uncertainty of the 0 jet category is much higher at high $p_T$, due to the fact that total cross section will be composed mostly from the $\geq 1$ jet category.

The uncertainty in the NLO EWK correction to $ZZ$ production, corresponding to missing higher order terms in the computation, is estimated as the product of the NLO QCD and EWK corrections [17]. The uncertainty on the EWK correction to $WZ$ production is estimated as 100% of the correction, to account for the poorly-known fraction of photon+quark-induced events [21] passing the jet veto.

### 3.9.3 Acceptance

The kinematic acceptance is computed with MCFM using the MSTW2008nlo68cl PDF, comparing the cross sections with and without kinematic cuts at generator level resembling the cuts in the signal selection:

- di-lepton $p_T > 45$ GeV;
- lepton $p_T > 20$ GeV;
- lepton $|\eta| < 2.5$;
- dilepton mass in the range $|m_{ll} - m_Z| < 7.5$ GeV;
- missing transverse momentum greater than 75 GeV (same signal efficiency as the reduced-$E_T^{miss}$ cut applied in the selection).

The acceptance value is about 12% at 7 and 8 TeV, as described in Table 3.16. The acceptance is recomputed after varying the scales on QCD, as described in Sec. 3.9.2, and the maximum difference is taken as systematic uncertainty. The result is about 0.3% at 7 TeV, and 1.8% at 8 TeV.

### 3.9.4 Luminosity

The uncertainty on the luminosity measurements is estimated to be 2.2% in 2011, and 2.6% in 2012 data taking [75].

Table 3.16: Kinematic acceptance of process pp $\rightarrow ZZ \rightarrow ee\nu\nu$ + X at 7 and 8 TeV with MSTW2008nlo68cl PDF set and various QCD scale values, obtained using MCFM 6.2 and LHAPDF 5.8.7.

| PDF Set | Acceptance of pp $\rightarrow$ ZZ $\rightarrow ee\nu\nu$ + X at 7 TeV | | |
|---|---|---|---|
| | $\mu = 45$ GeV | $\mu = 90$ GeV | $\mu = 180$ GeV |
| MSTW2008nlo68cl | $0.1162 \pm 0.0023$ | $0.1160 \pm 0.0024$ | $0.1156 \pm 0.0025$ |

| PDF Set | Acceptance of pp $\rightarrow$ ZZ $\rightarrow ee\nu\nu$ + X at 8 TeV | | |
|---|---|---|---|
| | $\mu = 45$ GeV | $\mu = 90$ GeV | $\mu = 180$ GeV |
| MSTW2008nlo68cl | $0.1190 \pm 0.0023$ | $0.1156 \pm 0.0023$ | $0.1149 \pm 0.0024$ |

### 3.9.5 Trigger and lepton identification and isolation efficiencies

The trigger efficiency and the lepton identification efficiency are computed with the Tag and Probe method as explained in Sec. 3.5. The systematic uncertainty of the method has been computed varying separately, by the conservative values of 1%, the trigger and the reconstruction efficiencies for each lepton. These variations give a systematic uncertainty of about 3.3% for the muon trigger efficiency (for 7 and 8 TeV), and about 3.7% and 3.4% for the reconstruction efficiency (for 7 and 8 TeV) for electrons and muons respectively. The uncertainties refer to the final yield of the $ZZ$ process estimated in MC.

### 3.9.6 Lepton momentum scale

The lepton momentum scale uncertainty is computed by varying the momentum of the leptons within their uncertainties. We assume conservatively the uncertainty on the muons to be 1% and the uncertainty on the electrons to be 2% for the barrel and 3.5% for the endcaps.

This procedure yields a systematic uncertainty of about 2.5% for the $ee$ channel, and 1.0% for the $\mu\mu$ channel. These uncertainties are also propagated to the evaluation of the $E_T^{miss}$ systematic uncertainty, computing the new $E_T^{miss}$ after the lepton momentum scale variation and recomputing the reduced-$E_T^{miss}$. The shape of kinematic distributions is expected to vary in this procedure, so the varied distributions are used as shape errors in the fit of the cross section.

### 3.9.7 Jet Energy Scale and Resolution

The uncertainty in the calibration of the jet energy scale (JES) affects directly the jet veto, the $E_T^{miss}$ computation and all the cuts related to jets. Note that this effect contributes to an overall increase/decrease of the number of selected events due to miscalibration of the $E_T^{miss}$ measurement.

The impact of the jet energy scale uncertainty is estimated by varying independently the jet energy scale up and down by one time the resolution as measured by the JET/MET group [45]. The variation corresponds to a simple rescaling of the jet 4-momentum as follows: $P \to P \cdot (1 \pm \frac{\sigma_{JES}}{P_T})$, where $\sigma_{JES}$ is the absolute uncertainty on the jet energy scale which is parametrized as function of the $P_T$ and $\eta$ of the jet. This variation affects the energy imbalance of the detector and it is therefore propagated to re-compute the $E_T^{miss}$ measurement as

$$\vec{E}_t^{miss\prime} = \vec{E}_t^{miss} - \Delta\vec{P}_{\mathrm{T}}^{\mathrm{jet}} \tag{3.15}$$

where $\Delta\vec{P}_{\mathrm{T}}^{\mathrm{jet}}$ is the difference between the $\vec{P}_{\mathrm{T}}$ of the jets before and after the smearing that is computed twice, according to up/down smearing of the JES. Starting from this new $E_T^{miss}$ we compute the new reduced-$E_T^{miss}$ and we apply the selection (in particular the jet-veto and the cut on $\Delta\phi$ between the $E_T^{miss}$ and the closest jet) using the new varied jets. The systematic uncertainty related to the JES is 3.3% for both $ee$ and $\mu\mu$ final states at 7 TeV, and about 7.8% at 8 TeV. The higher uncertainty at 8 TeV is due to the higher number of jets in the data, due to the different pileup condition at 8 TeV.

We perform a similar strategy to evaluate the systematic related to the jet energy resolution (JER). The momentum of the jets used in this analysis is smeared as $P_{\mathrm{T}}' = P_{\mathrm{T}} \cdot shift$, where

$$shift = \frac{max[0, P_{\mathrm{T}}^{\mathrm{GEN}} + Gauss(\mathrm{JER}, \sigma_{\mathrm{JER}}) \cdot (P_{\mathrm{T}}^{\mathrm{GEN}} - P_{\mathrm{T}})]}{P_{\mathrm{T}}}, \tag{3.16}$$

in order to reproduce in Monte Carlo the jet resolution measured in data. Not only the $E_T^{miss}$ is corrected with this procedure, but all the observables depending on the jet energy. The values of jet energy resolution and errors are taken from the official CMS recommendations for 2011 [45]. To evaluate the systematic uncertainty coming from the jet energy resolution, the jet energy (and all the related quantities) are over-smeared and under-smeared by shifting the central value of the JER by one $\sigma$. An uncertainty of 0.4% at 7 TeV, and 0.8% at 8 TeV is found in both $ee$ and $\mu\mu$ channels.

Since the shape of the distributions is expected to be affected by such variations, the systematic uncertainties on JES and JER are treated as shape uncertainties in the cross section fit.

### 3.9.8 Missing transverse energy

The $E_T^{miss}$ variable exploits the whole detector, and its systematic uncertainty is therefore divided among several pieces. First of all the jet-related uncertainties, like the JER and the JES, but also the lepton momentum scale and the unclustered $E_T^{miss}$. When varying the jet and the lepton, as described above, the reduced-$E_T^{miss}$ has been recomputed each time and its effect has been included the such uncertainties. Recomputing the reduced-$E_T^{miss}$ after varying each of these components, we can compute the different contributions to this uncertainty.

Smearing the JER as described before we find the uncertainty to be 0.02% for electrons and 0.16% for muons, for the JES we find a variation of 1.95% for the electron channel and 2.68% for the muon channel, and for the lepton momentum scale 3% for the electron channel and 1% for the muon channel.

The mismodeling of the true $E_T^{miss}$ can be estimated also using the $t\bar{t}$ control sample. Since it contains two real neutrinos, it offers the possibility to smear with a Gaussian the $E_T^{miss}$ distribution and compute the $\chi^2$ between data and simulation for each smearing value. The smearing that provides the best $\chi^2$ is the best representation of all the resolutions and the energy/momentum scale effects at the same time.

We select a pure $t\bar{t}$ control sample requiring at least two b-jets, $e$-$\mu$ final state, and veto on the $3^{rd}$ lepton. We consider four number of vertices categories, and for each we apply a different smearing. The four categories are: below 6 vertices, between 6 and 9, between 9 and 13 and over 13 (Fig. 3.27).

A Gaussian smearing is then applied to the $E_T^{miss}$ projection on the x- and y-axis, varying the RMS of the smearing from 0 to 50 GeV. The $\chi^2$ between data and Monte Carlo has been computed. Fig. 3.28 suggest that an extra-smearing, not bigger than 10 GeV, in the $E_T^{miss}$ projection on the x-axis leads to slightly better agreement between data and Monte Carlo. On the $y$-axis instead, no extra-smearing seems needed, due to the different modulations in $\phi$ of the $E_T^{miss}$. Once the optimal $\sigma$ is found, the $ZZ$ Monte Carlo sample is smeared accordingly. The difference in the signal yield is taken as cross-check on the estimate of the systematic uncertainty related to the true $E_T^{miss}$ modeling. We find a 2.4% uncertainty in the electron channel, and 2.6% in the muon channel, in agreement with what is expected from varying the lepton momentum scale and the jet energy resolution and scale.

### 3.9.9 B-Jet veto

The b-tagging efficiency for the CSV discriminator is computed elsewhere [63]. In simulation, the cut value on the CSV discriminator is shifted in order to reproduce the efficiency

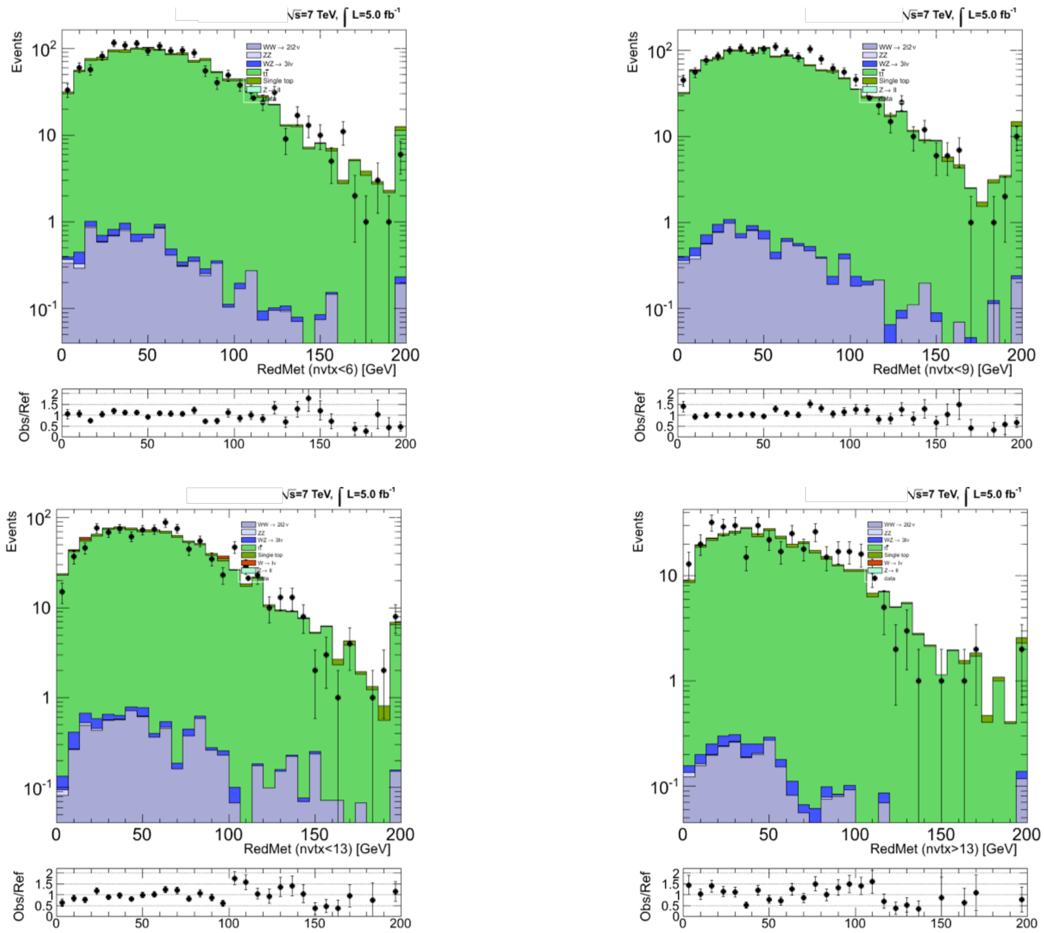

Figure 3.27: Reduced-$E_T^{miss}$ distribution for the $t\bar{t}$ control sample for 4 different bins. From the left: events with less than 6 vertices, between 6 and 9, between 9 and 13 and over 13 (CMS data).

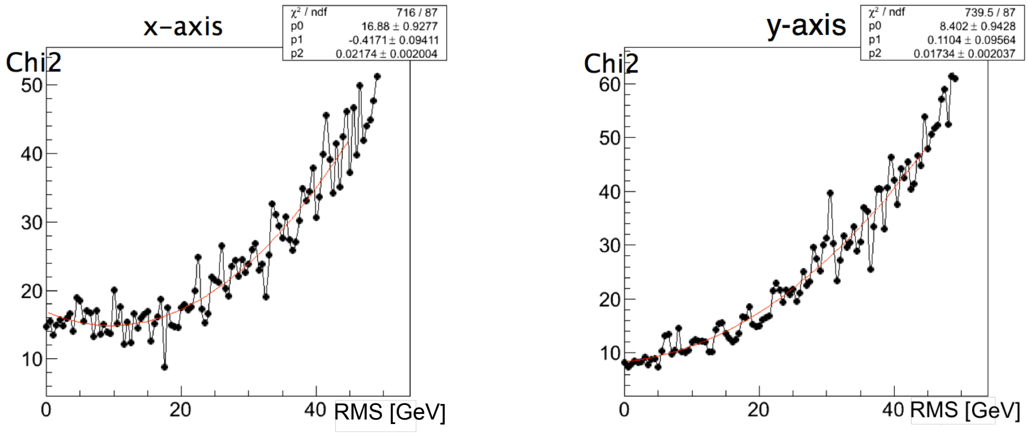


Figure 3.28: $\chi^2$ between data and MC $E_T^{miss}$ distribution in the $t\bar{t}$ control sample as a function of the RMS of the Gaussian smearing applied to the $E_T^{miss}$ in simulation. Left: x-axis; right: y-axis. Here are reported the result in the event category with less then 6 vertices.

observed in data. The resulting uncertainty on the measured efficiency is propagated to the event yields processes estimated from simulation ($ZZ$, $WZ$) by shifting the discriminator threshold. A very small uncertainty on the final yields of the MC samples is found: about 0.1-0.15% both at 7 and 8 TeV.

### 3.9.10 Pileup

In this analysis, Monte Carlo samples are re-weighted in order to reproduce the pileup conditions observed in data. The correction is applied following the official CMS prescription. To compute the uncertainty related to this re-weighting procedure, we shift the mean of the distribution of real interaction in MC by 8%. The variation of the final yields induced by this procedure is less than 1% in simulations. However, the shape of kinematic distributions can vary in this procedure, so the varied distributions are used as uncertainty errors in the fit of the cross section.

### 3.9.11 Drell-Yan background

We estimate the Drell-Yan contribution using the data-driven technique described in Sec. 3.8.1. As explained, an uncertainty of 25% (40%) at 7 (8) TeV is assigned to the DY estimate.

### 3.9.12 Non-resonant backgrounds

The uncertainty on the estimate of the non-resonant backgrounds, obtained with the data-driven method explained in Sec. 3.8.2, is derived from the closure test, performed by comparing the yields of non-resonant backgrounds in simulation with the prediction. It is found to be about 20% at 7 and 8 TeV.

### 3.9.13 Summary

Table 3.17 summarizes the systematic uncertainties described in the previous sections. The percentage errors are referred to the event yields of the relevant processes. The uncertainties marked with an asterisk ($*$) are those which affect significantly the shape of the kinematic distributions, and are thus used as shape errors in the maximum-likelihood fit. The values shown in the tables is the average value of the uncertainty, obtained from the variations in the integrals of the reduced-$E_T^{miss}$ distribution when applying variations of $\pm 1\sigma$ for the corresponding source.

| Source of uncertainty | Systematic uncertainty [%] 7 TeV | 8 TeV |
|---|---|---|
| (*) MC statistics: $ZZ$ ($ee$) | 2.3 | 2.0 |
| (*) MC statistics: $ZZ$ ($\mu\mu$) | 1.8 | 1.7 |
| (*) MC statistics: $WZ$ ($ee$) | 6.1 | 3.1 |
| (*) MC statistics: $WZ$ ($\mu\mu$) | 4.9 | 2.6 |
| (*) Ctrl. sample statistics: DY ($ee$) | 48 | 21 |
| (*) Ctrl. sample statistics: DY ($\mu\mu$) | 48 | 21 |
| (*) Ctrl. sample statistics: NRB ($ee$) | 35 | 24 |
| (*) Ctrl. sample statistics: NRB ($\mu\mu$) | 34 | 24 |
| $ZZ$ cross section: PDF | 1.15 | 1.12 |
| $ZZ$ cross section: QCD scales | 11 | 12 |
| $WZ$ cross section: PDF | 1.20 | 1.16 |
| $WZ$ cross section: QCD scales | 5.9 | 5.4 |
| Signal acceptance | 0.3 | 1.8 |
| Luminosity | 2.2 | 2.6 |
| (*) Pileup | 0.5 | 0.7 |
| Trigger ($\mu\mu$) | 3.3 | 3.3 |
| Electron Reconstruction, ID, Isolation | 3.7 | 3.7 |
| Muon Reconstruction, ID, Isolation | 3.4 | 3.4 |
| (*) Electron Momentum Scale | 2.5 | 2.5 |
| (*) Muon Momentum Scale | 1 | 1 |
| (*) Jet Energy Scale | 3.3 | 7.8 |
| (*) Jet Energy Resolution | 0.4 | 0.8 |
| (*) Unclustered $E_T^{miss}$ | 1 | 1.3 |
| (*) b-jet veto | 0.1 | 0.14 |
| Drell-Yan Estimation | 25 | 40 |
| Top & WW Estimation | 20 | 20 |

Table 3.17: Systematic uncertainties on the event yields of the corresponding processes. The uncertainties marked with an asterisk (*) are used as shape errors in the maximum-likelihood fit to extract the $ZZ$ cross section.

## 3.10 Cross section measurement

### 3.10.1 Profile likelihood method

We extract the $ZZ$ production cross section using a profile likelihood fit to the reduced-$E_T^{miss}$ distribution (see Fig. 3.29), which takes into account the expectations for the different background processes and the $ZZ$ signal. The expectations for the signal in a given $E_T^{miss}$ bin and the expectations for a background process in the same bin can be written as depending on:

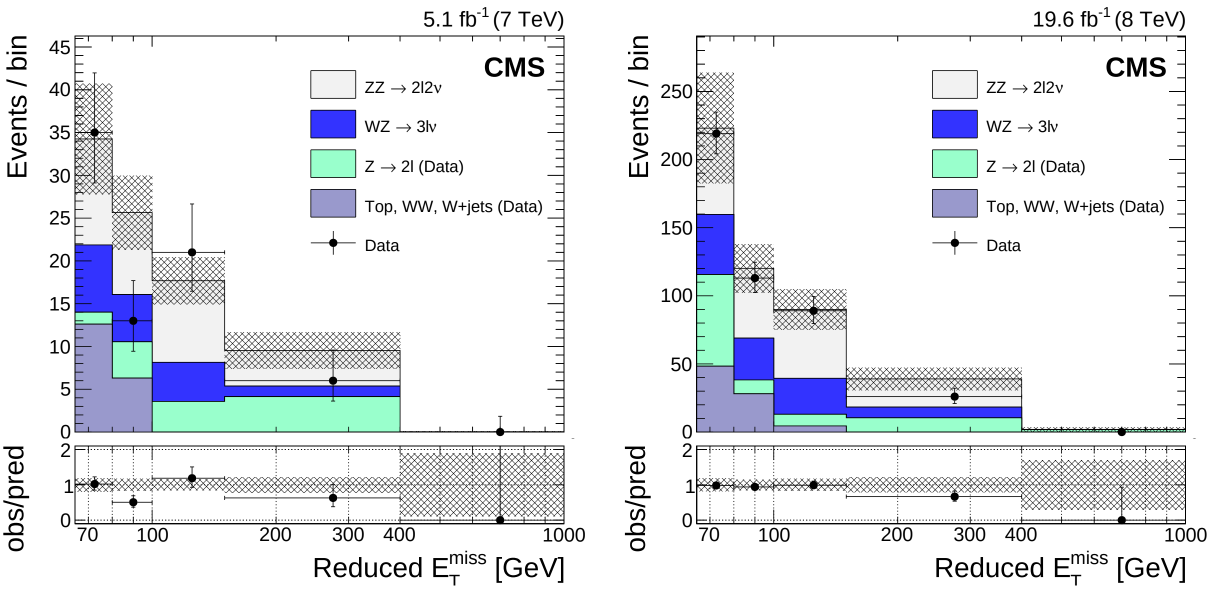


Figure 3.29: Reduced-$E_T^{miss}$ distribution after the full selection at 7 TeV (left) and 8 TeV (right). The error bands on data include statistical and systematic uncertainties, while the gray bands are the uncertainties on the simulation [67].

- the average values obtained from simulation or from a data-driven method ($\hat{s}$ or $\hat{b}$ for signal and background correspondingly);
- nuisance parameters ($\theta_i$) which parametrize the effect of the systematic uncertainties associated to the estimate of these average values.

The nuisance parameters are usually expressed as multiplicative factors which affect the nominal prediction of the event yields of each process, $N \to (1 + r_i\theta_i)N$, where $r_i$ represents a Gaussian distribution centered in zero with the width equal to one. The relative values of the nuisances are estimated in the previous section and we assign to each one a Gaussian PDF to constrain these parameters in the fit to be performed. This constraint allows the nuisance to float in the neighborhood of its expected value enabling a fine adjustment of their values in the data. For the signal we fit a multiplicative factor, which is the ratio of the cross section to be measured in data to the expected theoretical value, i.e. the signal strength $\boldsymbol{\mu} = \sigma/\sigma_{\mathrm{th}}$. For each channel ($k = ee, \mu\mu$) we write therefore the total number of expected events as:

$$\hat{N}_k(\boldsymbol{\mu}, \theta_i) = \hat{N}_k^s(\boldsymbol{\mu}, \theta_i) + \hat{N}_k^b(\theta_i) = \boldsymbol{\mu} \cdot \hat{s}_k \cdot \prod_i (1 + r_i^s \theta_i) + \sum_{\mathrm{b} \in \mathrm{bkg}} \hat{b}_k \cdot \prod_i (1 + r_i^b \theta_i) \tag{3.17}$$

In the expression above $r_i^s \theta_i$ ($r_i^b \theta_i$) denote the relative shift on the signal (background) yields due to the $i$-th source of uncertainty. Using Eq. (3.17) we write the likelihood as a product of Poisson distributions and nuisance distributions:

$$\mathcal{L}(\boldsymbol{\mu}, \theta_i) = \prod_k \mathcal{P}_{oisson} \left[ N_k | \hat{N}_k(\boldsymbol{\mu}, \theta_i) \right] \cdot \prod_i \mathcal{G}_{auss}(r_i, \theta_i) \tag{3.18}$$

where $N_k$ is the number of events observed in the $k$-th category and $\mathcal{G}_{auss}(r_i, \theta_i)$ is a Gaussian distribution centered on zero with RMS $= \theta_i$. The nuisance constraints are written as normal distributions and correspond directly to the relative systematic uncertainty ascribed to the $i$-th source. Based on the likelihood expressed in Eq. (3.18) we define the profile likelihood ratio (PLR) test statistics as:

$$\lambda(\boldsymbol{\mu}) = \frac{\mathcal{L}(\boldsymbol{\mu}, \hat{\hat{\theta}}_i)}{\mathcal{L}(\hat{\boldsymbol{\mu}}, \hat{\theta}_i)} \tag{3.19}$$

The quantities $\hat{\hat{\theta}}$ corresponds to the values of $\theta$ which maximize the likelihood for the specified signal strength. The denominator is called the un-conditional likelihood function and its estimators are $\hat{\boldsymbol{\mu}}$ and $\hat{\theta}$, that correspond to the parameters that globally maximize the likelihood. This approach allows to cover the effect of the systematic uncertainties in the fit: in the presence of floating nuisance parameters the likelihood as function of $\boldsymbol{\mu}$ tends to be broader with respect to the one obtained if the nuisance values are fixed. This reflects the loss of information in $\boldsymbol{\mu}$ due to systematic effects. More details can be found in [76].

For the computation and maximization of the PLR described in Eq. (3.19) we use the CMS Higgs working group combination tool [74]. After maximizing the PLR we obtain the cross section and its uncertainty for the $ZZ$ production from the fitted signal strength. In the next section we discuss the optimization of the final selection used to measure the cross section.

### 3.10.2 Results

The cross sections are extracted from individual fits to the $ee$ and $\mu\mu$ channels and from a simultaneous fit to both channels. Table 3.18 reports the measured $pp \to ZZ \to 2l2\nu$ exclusive cross section, i.e. the production cross section of $ZZ$ pairs with mass $60 < M_Z < 120$ GeV, with no restrictions on lepton acceptance nor jet number, times the branching fraction to final states with two charged leptons of a given flavor and two neutrinos of any flavor. This is obtained by rescaling the theoretical prediction for the exclusive cross section in the same kinematic range by the fitted signal strength. These theoretical predictions are computed at NLO in QCD with MCFM in the mass range $60 < M_Z < 120$ GeV. The cross section has been also corrected for NLO EWK effects [16].

Table 3.18: Cross sections [fb] for process $pp \to ZZ \to 2l2\nu$ (where $l$ denotes a charged lepton of a given flavor, $\nu$ a neutrino of any flavor) at 7 and 8 TeV, with both $Z$ boson masses in the range 60 to 120 GeV, measured in the $ee$ and $\mu\mu$ channels and the two channels combined.

| Channel | $\sqrt{s} = 7$ TeV | $\sqrt{s} = 8$ TeV |
|---|---|---|
| $ee$ | $98^{+35}_{-31}\,(\text{stat})\,^{+27}_{-22}\,(\text{syst}) \pm 2\,(\text{lumi})$ fb | $83^{+17}_{-16}\,(\text{stat})\,^{+26}_{-19}\,(\text{syst}) \pm 2\,(\text{lumi})$ fb |
| $\mu\mu$ | $47^{+24}_{-21}\,(\text{stat})\,^{+20}_{-19}\,(\text{syst}) \pm 1\,(\text{lumi})$ fb | $98^{+14}_{-14}\,(\text{stat})\,^{+29}_{-22}\,(\text{syst}) \pm 3\,(\text{lumi})$ fb |
| Combined | $66^{+20}_{-18}\,(\text{stat})\,^{+18}_{-14}\,(\text{syst}) \pm 1\,(\text{lumi})$ fb | $92^{+11}_{-10}\,(\text{stat})\,^{+25}_{-19}\,(\text{syst}) \pm 2\,(\text{lumi})$ fb |
| Theory | $79^{+4}_{-3}\,(\text{theo})$ fb | $97^{+4}_{-3}\,(\text{theo})$ fb |

The measured $ZZ$ inclusive cross section is obtained by rescaling the theoretical inclusive cross section, by the signal strength obtained from the combined fit. The theoretical inclusive cross section is computed in this case with the zero-width approximation using MCFM version 6.2. The results are [67]:

$$\text{7 TeV} \qquad \sigma(\text{pp} \to ZZ) = 5.1^{+1.5}_{-1.4}\,(\text{stat})\,^{+1.4}_{-1.1}\,(\text{syst})\; \pm 0.1\,(\text{lumi})\text{ pb} \tag{3.20}$$

$$\text{8 TeV} \qquad \sigma(\text{pp} \to ZZ) = 7.2^{+0.8}_{-0.8}\,(\text{stat})\,^{+1.9}_{-1.5}\,(\text{syst})\; \pm 0.2\,(\text{lumi})\text{ pb.} \tag{3.21}$$

Table 3.19 shows the value of the expected signal and background yields, and the corresponding values after the simultaneous fit to both $ee$ and $\mu\mu$ channels. The errors on the predicted yields are statistical only. The errors on the post-fit yields are obtained from pseudo-experiments in MC, and they include the contribution from systematic errors. The p-values of the simultaneous fit to the $ee$ and $\mu\mu$ channels are 0.335 (0.569) at 7 (8) TeV. The data are also consistent with the reduced-$E_T^{miss}$ spectra uncorrected for NLO EWK effects, with only slightly smaller $p$-values of 0.322 (0.477) at 7 (8) TeV. Because of the large uncertainty associated to the photon template, the estimated yields of the DY process obtained after the simultaneous fit are then used as DY estimation in the limits computation.

The pre-fit and post-fit values and uncertainties reveal expected features. The uncertainties on the event yields for the Drell-Yan and the non resonant backgrounds processes, that have been estimated using a control sample, decrease after the fit, due to the additional constrain imposed by data. The signal is let free to vary, and it is constrained to data. At 7 TeV its uncertainty is dominated by statistic, while at 8 TeV systematic uncertainties predominate.

Table 3.19: Predicted signal and background yields at 7 and 8 TeV, and corresponding values after the simultaneous fit to both $ee$ and $\mu\mu$ channels. The uncertainties include both the statistical and systematic components.

| Dataset | Process | Channel | Predicted yield | Fitted yield |
|---|---|---|---|---|
| 7 TeV | $ZZ \to 2l2\nu$ | $ee$ | $14.0 \pm 1.9$ | $12.0 \pm 4.4$ |
| | | $\mu\mu$ | $21.7 \pm 3.2$ | $18.4 \pm 6.8$ |
| | $WZ \to 3l\nu$ | $ee$ | $7.7 \pm 0.9$ | $7.9 \pm 1.0$ |
| | | $\mu\mu$ | $11.5 \pm 1.6$ | $11.6 \pm 1.2$ |
| | Z + jets | $ee$ | $5.0 \pm 2.7$ | $4.8 \pm 2.3$ |
| | | $\mu\mu$ | $8.3 \pm 4.8$ | $4.8 \pm 3.0$ |
| | Non resonant | $ee$ | $7.7 \pm 3.1$ | $7.4 \pm 2.3$ |
| | | $\mu\mu$ | $11.2 \pm 4.8$ | $9.2 \pm 2.9$ |
| 8 TeV | $ZZ \to 2l2\nu$ | $ee$ | $77 \pm 16$ | $69 \pm 13$ |
| | | $\mu\mu$ | $109 \pm 23$ | $100 \pm 19$ |
| | $WZ \to 3l\nu$ | $ee$ | $45 \pm 6$ | $43.9 \pm 5.6$ |
| | | $\mu\mu$ | $64 \pm 4$ | $63.8 \pm 7.3$ |
| | Z + jets | $ee$ | $36 \pm 12$ | $27.7 \pm 7.9$ |
| | | $\mu\mu$ | $63 \pm 21$ | $52 \pm 14$ |
| | Non resonant | $ee$ | $31 \pm 9$ | $34.1 \pm 7.2$ |
| | | $\mu\mu$ | $50 \pm 14$ | $54 \pm 12$ |

Table 3.20 shows the post-fit value of the systematic uncertainties in the cross sections due to each source separately.

### 3.10.3 Discussion

These results represent the first measurement of the $ZZ$ cross section using the $2l2\nu$ channel at 8 TeV [67]. They are less than one standard deviation away from the SM predictions at

Table 3.20: Post-fit value of the systematic uncertainties in the cross sections due to each source separately, after the maximum likelihood fit to extract the $ZZ$ cross section. The uncertainties marked with an asterisk ($*$) are used as shape uncertainties in the fit.

| Source of uncertainty | Uncertainty [%] | |
|---|---|---|
| | 7 TeV | 8 TeV |
| ($*$) MC statistics: $ZZ$ ($ee$) | 0.8 | 0.9 |
| ($*$) MC statistics: $ZZ$ ($\mu\mu$) | 1.3 | 1.0 |
| ($*$) MC statistics: $WZ$ ($ee$) | 1.7 | 0.8 |
| ($*$) MC statistics: $WZ$ ($\mu\mu$) | 1.7 | 1.0 |
| ($*$) Ctrl. sample statistics: DY ($ee$) | 6.5 | 4.3 |
| ($*$) Ctrl. sample statistics: DY ($\mu\mu$) | 5.8 | 5.0 |
| ($*$) Ctrl. sample statistics: NRB ($ee$) | 6.3 | 3.0 |
| ($*$) Ctrl. sample statistics: NRB ($\mu\mu$) | 8.2 | 4.4 |
| $WZ$ cross section: PDF+$\alpha_S$ | 1.9 | 2.6 |
| ($*$) $ZZ + WZ$ cross section: scales | 17 | 16 |
| ($*$) $ZZ + WZ$ cross section: NLO EWK corr. | 2.4 | 2.3 |
| Signal acceptance | 2.8 | 2.8 |
| ($*$) Pileup | 0.5 | 1.0 |
| Muon trigger, ID, isolation | 4.1 | 3.6 |
| Electron trigger, ID, isolation | 1.7 | 2.0 |
| ($*$) Lepton momentum scale | 2.7 | 3.7 |
| ($*$) JES | 6.0 | 12 |
| ($*$) JER | 0.8 | 1.4 |
| ($*$) Unclustered $E_T^{miss}$ | 2.0 | 3.2 |
| ($*$) b-jet veto | 0.3 | 0.3 |
| Drell–Yan bkg. normalization | 6.6 | 8.5 |
| Top-quark & $WW$ bkg. normalization | 7.7 | 7.1 |
| Total systematic uncertainty | 24.0 | 24.3 |
| Statistical uncertainty | 28.0 | 12.1 |

both 7 TeV and 8 TeV. The statistical uncertainties are comparable to the ones of the $4l$ channel published by CMS [28]. This is due to the small acceptance of the analysis, around 10%. The acceptance in the $4l$ final state analysis is about 57% (a factor 6 larger), which compensate the larger branching fraction of the $2l2\nu$ channel.

The total systematic uncertainties are almost 25%. The larger ones are the QCD scale uncertainties, around 15%, the JES, 12% and the normalization of the Drell-Yan and non-resonant backgrounds, about 8% each. The QCD scale uncertainty is mainly due to the jet veto. Generators are made available for $ZZ$+jet production at NLO, which could lead to a reduction of this uncertainty in the future. The systematic uncertainty in the $4l$ channel is at the level of 5-6% for both the 8 TeV measurement at CMS [28] and ATLAS [77], thanks to the absence of neutrinos in the final state and the negligible level of backgrounds. In these analysis the main systematic contributions are given from the uncertainties on the lepton energy scale and the trigger efficiencies.

# Chapter 4

# Search for anomalous triple gauge couplings

In the following, we present a search for neutral triple gauge couplings using the datasets described in Sec. 3.3. Limits on the four $f_i^V$ parameters, described in Sec. 1.3, are set by comparing data with theoretical predictions of yields at high $Z$ $p_T$. Finally the limits at 7 and 8 TeV have been combined with each other and with the limits obtained from the four charged-lepton final state analysis.

## 4.1 Limit setting

We produced several MC samples for the pp $\to$ ZZ $\to 2\ell 2\nu$ ($\ell = e,\ \mu$) process that include $\mathrm{V}^{(*)}ZZ$ couplings with different $f_i^V$ values. Currently, no NLO generator includes simulation of the $ZZ$ process with aTGC. The $ZZ$ + aTGC process is simulated with *SHERPA* (version 1.2.2 for 7 TeV and 1.4.0 for 8 TeV). The simulated samples are produced at LO with up to 2 additional jets in the final state. The aTGC contribution is obtained by subtracting the SM spectrum computed with *SHERPA* to the SM + aTGC spectrum. The aTGC signal is then added to the SM $ZZ$ spectrum. To be consistent with the $ZZ$ cross section analysis, the $ZZ$ spectrum is simulated with MadGraph (see Sec. 3.3).

NLO effects are accounted for by multiplying the aTGC contribution by an average $k$-factor. This $k$-factor has been computed comparing the *SHERPA* SM cross section with the cross section computed at NLO by MCFM. The $k$-factors at 7 and 8 TeV are given in table 4.1, they differ because of the different version of *SHERPA* used in the generation of the samples at 7 and 8 TeV.

Considering the existing limits from previous experiments, and the sensitivity of this analysis at 7 and 8 TeV, we produced a set of MC samples varying each parameter independently in a range from -0.02 to 0.02. The set of values is reported in Table 4.1, along with the corresponding LO cross sections for the $2l2\nu$ final state.

A quadratic interpolation is used in order to interpolate the $p_T$ spectrum for parameter values for which we have no MC sample. The quadratic dependence of the event yields with the aTGC parameter values was verified. The result of these tests is shown in Fig. 4.1, where the number of events expected after the full selection in the $Z$ $p_T$ bin [400,800] GeV is given as a function of $f_4^Z$. The interpolation of the event yield is performed only for the last two $p_T$ bins: 200-400 GeV and $\geq$ 400 GeV.

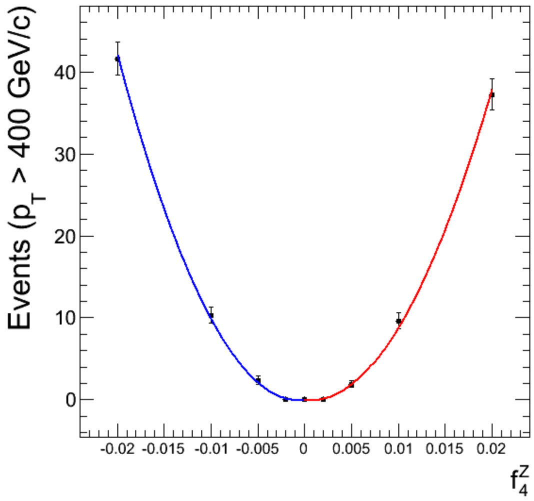


Figure 4.1: Signal yields for different values of the $f_4^Z$ parameter in the $p_T$ bin 400-800 GeV at 8 TeV, in the $\mu\mu$ channel, after the full selection.

Fig. 4.2 shows the generated dilepton $p_T$ spectrum for different values of the parameters produced with Sherpa, compared to the SM expected spectrum produced with MadGraph . Fig. 4.3 instead, shows the generated dilepton $p_T$ spectrum for a sample including aTGC and SM processes (black) and for a sample including only the SM process (red), both generated with *SHERPA*. In blue the difference of the spectra is shown.

As can be seen in Fig. 4.2 and 4.3, the presence of triple gauge couplings enhances the high-$p_T$ region of the dilepton system. This provides a good way to probe the existence of aTGCs. In the four charged-lepton channel, another possibility is to use the invariant mass of the four charged-leptons [28]. This variable cannot be measured in the $2l2\nu$ final state, thus the transverse mass $m_T = \sqrt{2p_T E_T^{miss}(1 - cos(\Delta\phi)}$, has been tested and it has been found less sensitive to the presence of aTGC. In the formula $p_T$ refers to the transverse momentum of the dilepton system, and $\Delta\phi$ is computed between the $E_T^{miss}$ and the dilepton

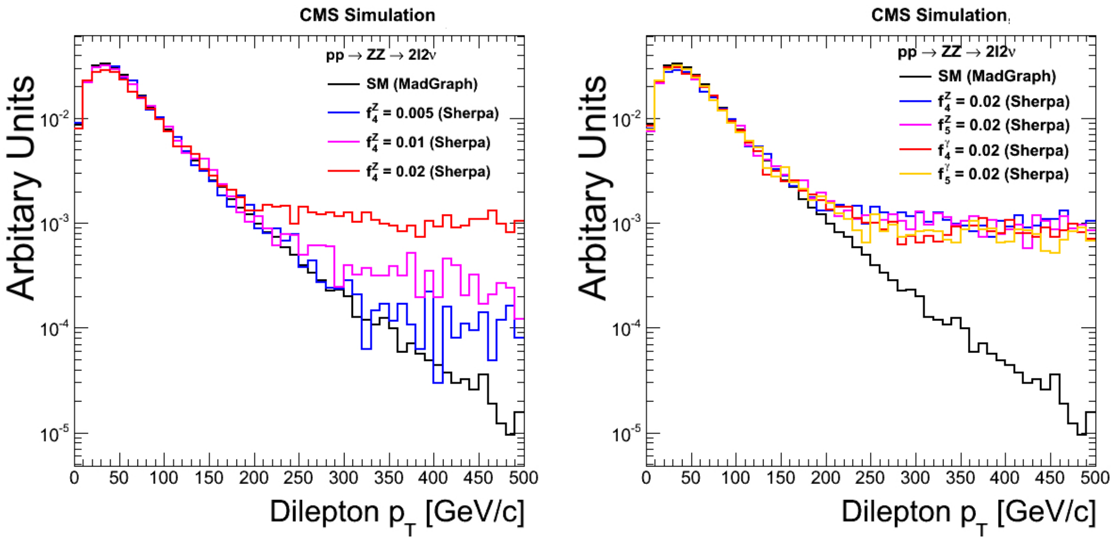


Figure 4.2: Dilepton transverse momentum spectrum in samples generated with *SHERPA* at 8 TeV for different values of the $f_4^Z$ parameter (left), or for different parameters (right), compared to the SM expected spectrum produced with MadGraph .

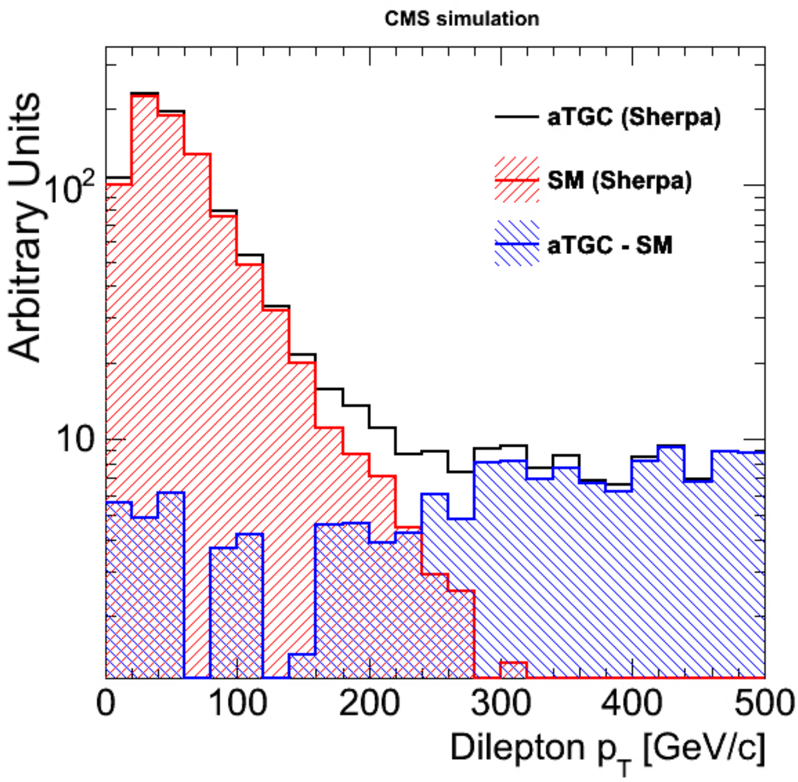


Figure 4.3: Dilepton transverse momentum spectrum in samples generated with *SHERPA* at 8 TeV: $f_4^Z = -0.02$ (black), SM (red), and their difference (blue), which represents our signal.

Table 4.1: LO cross section for different aTGCs couplings at 7 and 8 TeV center-of-mass energy.

| | 7 TeV *SHERPA* cross sections [pb] | | | | | | | | |
|---|---|---|---|---|---|---|---|---|---|
| Parameter | -0.02 | -0.01 | -0.005 | -0.002 | 0 | 0.002 | 0.005 | 0.01 | 0.02 |
| $f_4^Z$ | 0.1293 | 0.1211 | 0.1210 | - | 0.1209 | - | 0.1203 | 0.1224 | 0.1297 |
| $f_5^Z$ | 0.1285 | 0.1224 | 0.1212 | | | | 0.1209 | 0.1219 | 0.1280 |
| $f_4^\gamma$ | 0.1255 | 0.1206 | 0.1202 | | | | 0.1203 | 0.1225 | 0.1255 |
| $f_5^\gamma$ | 0.1264 | 0.1209 | 0.1204 | | | | 0.1196 | 0.1226 | 0.1263 |
| | MCFM /*SHERPA* $k$-factor = 1.6077 | | | | | | | | |

| | 8 TeV *SHERPA* cross sections [pb] | | | | | | | | |
|---|---|---|---|---|---|---|---|---|---|
| Parameter | -0.02 | -0.01 | -0.005 | -0.002 | 0 | 0.002 | 0.005 | 0.01 | 0.02 |
| $f_4^Z$ | 0.2691 | 0.2380 | 0.2305 | 0.2284 | 0.2275 | 0.2283 | 0.2297 | 0.2382 | 0.2670 |
| $f_5^Z$ | 0.2684 | 0.2382 | 0.2314 | 0.2290 | | 0.2286 | 0.2296 | 0.2368 | 0.2681 |
| $f_4^\gamma$ | 0.2578 | 0.2376 | 0.2269 | 0.2290 | | 0.2273 | 0.2305 | 0.2351 | 0.2604 |
| $f_5^\gamma$ | 0.2572 | 0.2361 | 0.2298 | 0.2282 | | 0.2281 | 0.2311 | 0.2354 | 0.2581 |
| | MCFM /*SHERPA* $k$-factor = 1.0264 | | | | | | | | |

system.

Fig. 4.4 shows the dilepton $p_T$ distribution in data and in simulation, after the full selection described in Sec. 3.7, and the background estimation described in Sec. 3.8. Samples with aTGC contribution with different values of the $f_4^Z$ parameter are also superimposed, to show the yields that are expected. The binning is chosen in order to have significant MC statistics in the high-$p_T$ bins and avoid non-physical fluctuations of the background estimation. The last bin includes the overflow events.

In the computation of the limits, the DY and the non-resonant backgrounds are estimated with the data-driven methods described in Sections 3.8.1 and 3.8.2, respectively. Given the large uncertainty associated with the photon template used to model the DY background, we replace its estimated yields with the fitted shape obtained from the profile-likelihood fit performed for the $ZZ$ cross section, described in Sec. 3.10.

Using the dilepton $p_T$ distributions shown in Fig. 4.4, we compute one-dimensional limits for the four parameters, i.e. we vary a single parameter at a time, while fixing the other three to 0. For each $f_i^V$ value we set one-side limits, computing an upper limits at 95% C.L. on the ratio of the cross section excluded to the signal cross section expected, using the modified frequentist construction $\text{CL}_\text{S}$ [74], with a binned profile likelihood test statistics (the binning is the same as Fig. 4.4). The 95% C.L. one-dimensional limits on the four parameters are shown in Table 4.2 and in Figures 4.5, 4.6, and 4.7 for the 7 TeV, 8 TeV, and the combined

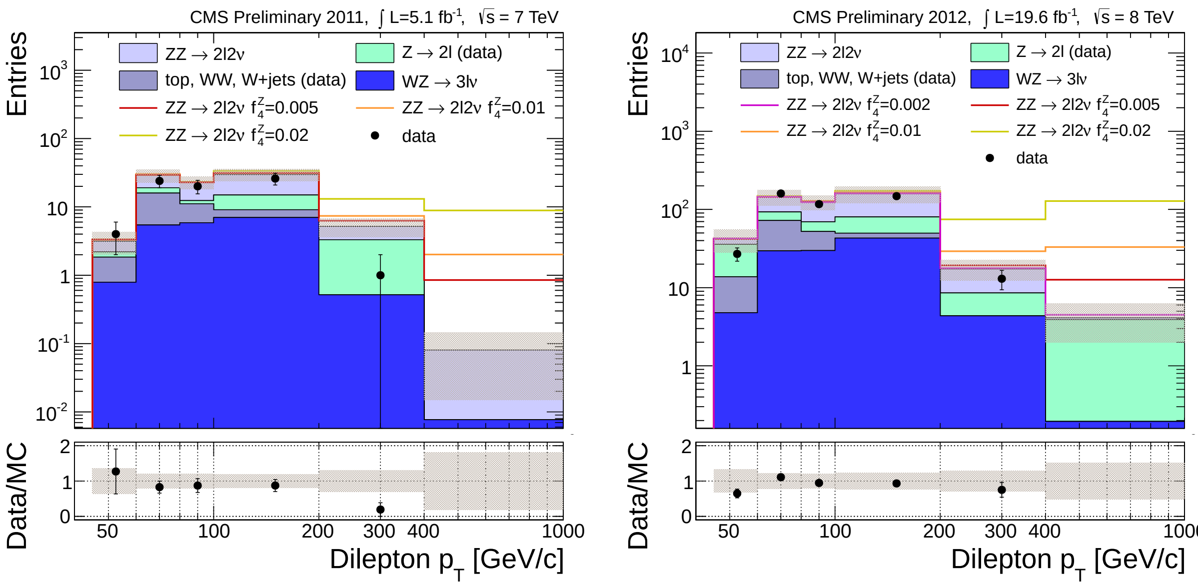


Figure 4.4: Dilepton transverse momentum distributions at 7 TeV (left) and 8 TeV (right). DY and non-resonant backgrounds are estimated with data-driven methods. The uncertainty band includes statistical and systematic uncertainties. The last bin includes the overflow events [67]

.

datasets respectively.

Table 4.2: Summary of 95% C.L. limits for the neutral aTGC coefficients, set by the $2l2\nu$ analysis using the 7 and 8 TeV CMS datasets. The expected 95% C.L. intervals obtained using the 7 and 8 TeV simulated samples are also shown.

| Dataset | $f_4^Z$ | $f_4^\gamma$ | $f_5^Z$ | $f_5^\gamma$ |
|---|---|---|---|---|
| 7 TeV | [-0.010; 0.011] | [-0.011; 0.013] | [-0.010; 0.010] | [-0.013; 0.013] |
| 8 TeV | [-0.0033; 0.0037] | [-0.0044; 0.0038] | [-0.0033; 0.0035] | [-0.0039; 0.0044] |
| Combined | [-0.0028; 0.0032] | [-0.0037; 0.0033] | [-0.0029; 0.0031] | [-0.0033; 0.0037] |
| Expected (7 and 8 TeV) | [-0.0048; 0.0051] | [-0.0060; 0.0053] | [-0.0048; 0.0050] | [-0.0057; 0.0062] |

## 4.2 Combined limits from the $ZZ \to 4l$ and $ZZ \to 2l2\nu$ channels

We now proceed with the combination of the results of the previously-published ZZ→ $4l$ analyses [28, 67] with the present results. In doing this, the analysis of the 4l channel is

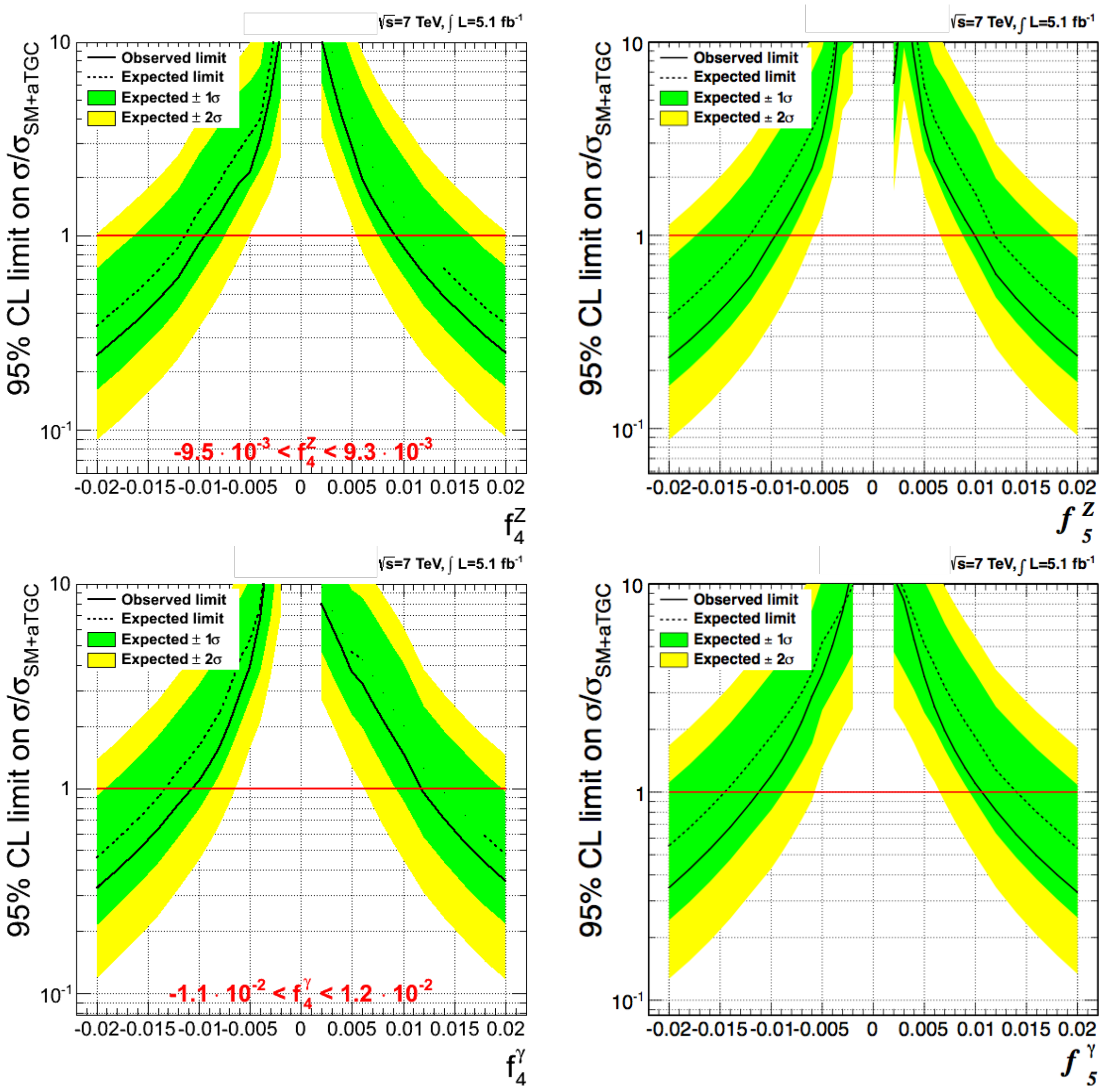


Figure 4.5: Expected and observed one-dimensional exclusion limits at 95% C.L. on the anomalous neutral trilinear $ZZZ$ and $\gamma ZZ$ couplings for the analysis of the $2l2\nu$ channel. The green and yellow bands represent the one and two-standard deviation variations from the expected limit. The results correspond to an integrated luminosity of about 5.1 fb$^{-1}$ at 7 TeV centre-of-mass energy.

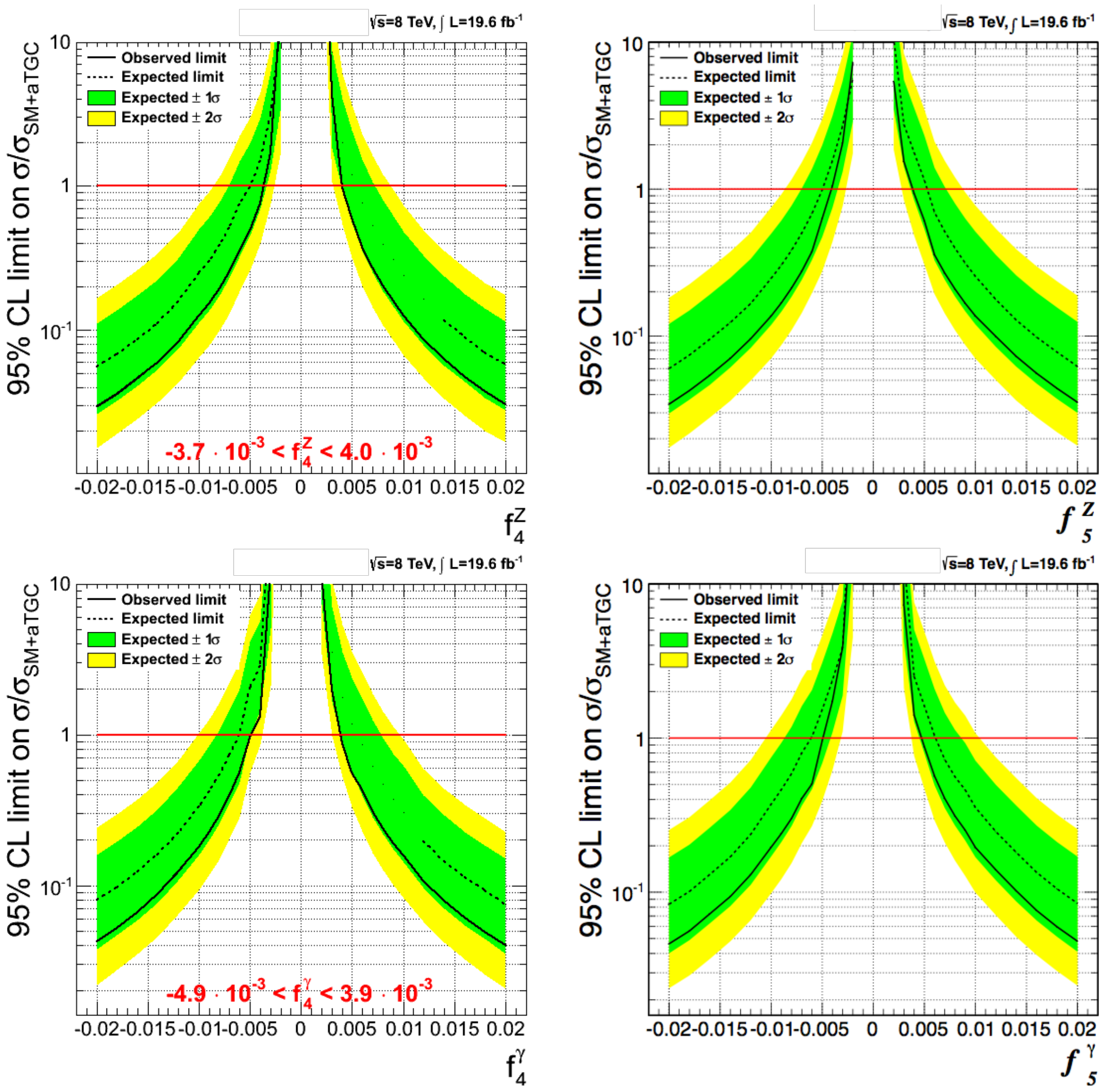


Figure 4.6: Expected and observed one-dimensional exclusion limits at 95% C.L. on the anomalous neutral trilinear $ZZZ$ and $\gamma ZZ$ couplings for the analysis of the $2l2\nu$ channel. The green and yellow bands represent the one and two-standard deviation variations from the expected limit. The results correspond to an integrated luminosity of about 19.6 fb$^{-1}$ at 8 TeV centre-of-mass energy.

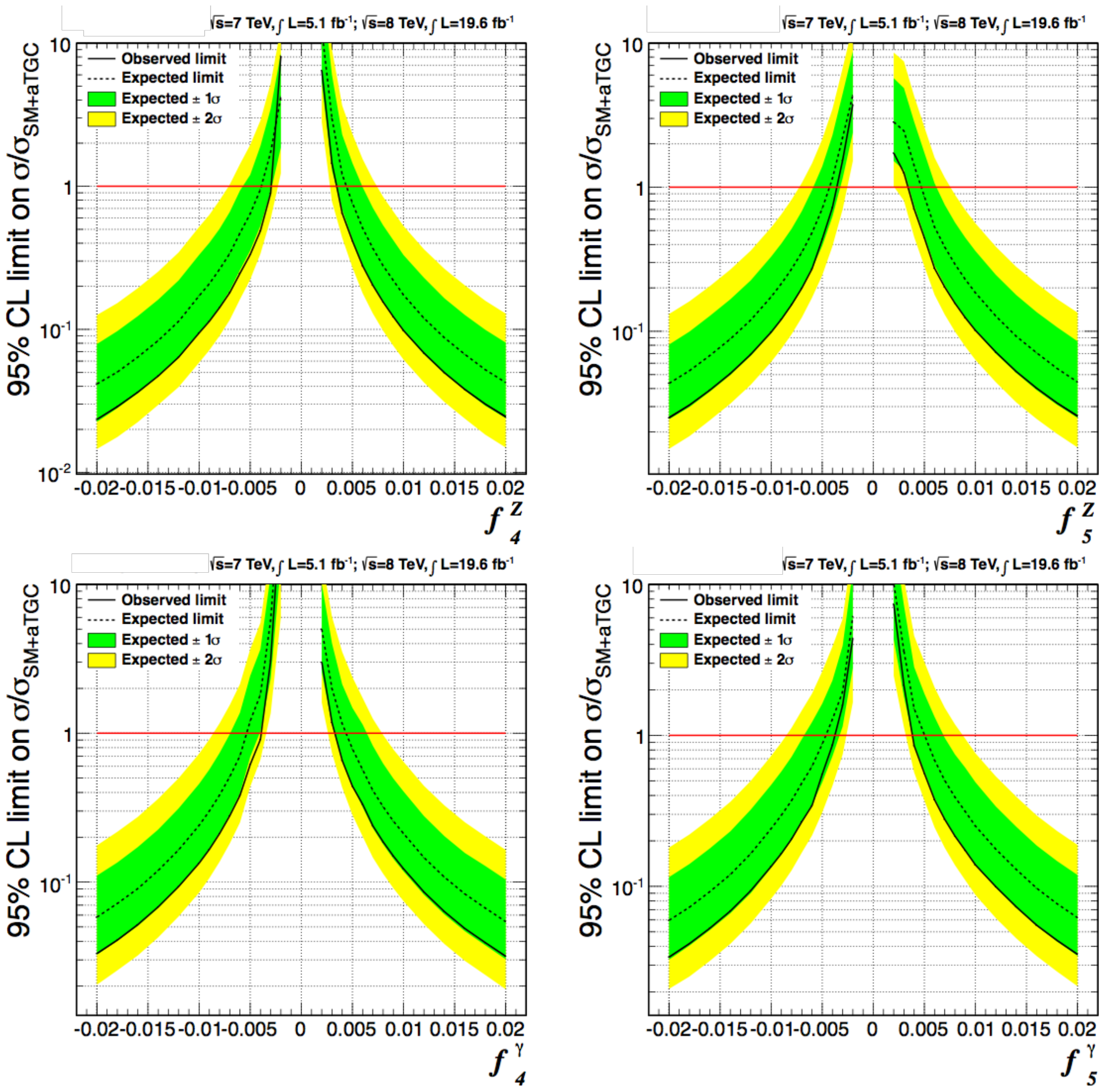


Figure 4.7: Expected and observed one-dimensional exclusion limits at 95% C.L. on the anomalous neutral trilinear $ZZZ$ and $\gamma ZZ$ couplings for the analysis of the $2l2\nu$ channel. The green and yellow bands represent the one and two-standard deviation variations from the expected limit. The results correspond to an integrated luminosity of 5.1 fb$^{-1}$ at 7 TeV, plus 19.6 fb$^{-1}$ at 8 TeV centre-of-mass energy.

unchanged compared to the published analysis, except that NLO EWK corrections to the SM ZZ$\rightarrow 4l$ background are accounted for in the same way as in the present analysis. In the combination, the procedure used in the $4l$ analysis to set limits on the aTGC parameters is adopted for both channels. Instead of setting one-side limits on the cross section, a profile likelihood method is used to extract from the best fit value the central values of the limits. It is then possible to define a 95% confidence interval around such value to derive the limits.

The systematic uncertainties in the signal and diboson background cross sections, in the integrated luminosity, and in the lepton efficiencies are treated as fully correlated between the two channels.

Table 4.3 shows the intervals obtained using the four separate data sets, and combining them. The combined analysis improves the sensitivity of the two separate channels, and the limits are the most stringent ever published.

Table 4.3: Summary of 95% CL intervals for the neutral aTGCs coefficients, set by the combined analysis of $4l$ and $2l2\nu$ final states. The intervals obtained separately by the two analyses using the 7 and 8 TeV CMS data sets are shown, as well as their combination. The expected 95% CL intervals obtained using the 7 and 8 TeV simulated samples of both analyses are also shown.

| Dataset | $f_4^Z$ | $f_4^\gamma$ | $f_5^Z$ | $f_5^\gamma$ |
|---|---|---|---|---|
| 7 TeV, $4l$ | [-0.010; 0.011] | [-0.012; 0.013] | [-0.011; 0.011] | [-0.013; 0.013] |
| 7 TeV, $2l2\nu$ | [-0.010; 0.011] | [-0.012; 0.013] | [-0.010; 0.010] | [-0.013; 0.013] |
| 8 TeV, $4l$ | [-0.0041; 0.0044] | [-0.0052; 0.0048] | [-0.0041; 0.0040] | [-0.0048; 0.0045] |
| 8 TeV, $2l2\nu$ | [-0.0033; 0.0037] | [-0.0044; 0.0038] | [-0.0033; 0.0035] | [-0.0039; 0.0043] |
| Combined | [-0.0022; 0.0026] | [-0.0029; 0.0026] | [-0.0023; 0.0023] | [-0.0026; 0.0027] |
| Expected (4l and $2l2\nu$, 7 and 8 TeV) | [-0.0036; 0.0039] | [-0.0046; 0.0041] | [-0.0036; 0.0037] | [-0.0043; 0.0043] |

## 4.3 Discussion

The best fit values of the anomalous couplings derived in the $2l2\nu$ [67] and $4l$ [28] analysis are all consistent at 95% C.L. with zero. The two channels produce similar results, as can be seen from the observed limits in Table 4.3. For the $2l2\nu$ channel, the observed limits are tighter than the expected ones, which is due to an under-fluctuation in data compared to the expected SM contribution, as visible in Fig. 4.4. The observed limits are within $1\sigma$ of the expected ones, as shown in Figs. 4.5, 4.6, and 4.7.

In the case of the cross section measurement, where the low part of the $Z$ $p_T$ distribution is leading the measurement, the $2l2\nu$ final state is affected from low acceptance and background contamination. In the case of anomalous couplings, the tail of the $Z$ $p_T$ distribution has higher statistic due to the $2l2\nu$ branching fraction and is less affected from background contamination.

Combining the two analysis, the limits improve by about 30%. The combined limits represent the most stringent limits ever published.

The contribution to the limits due to the systematic uncertainties of the analysis has been tested by varying the uncertainty on the DY estimation up to 200% and the jet-veto uncertainty up to 100%. The observed limits does not depend strongly from the uncertainty on the DY, since DY mostly affect the first bins, that are not sensitive on anoumalous couplings. The limits also do not depend strongly from the jet-veto uncertainty, because of the under-fluctuation observed in the last bins in data.

The current limits are about a factor 10 greater than the SM contribution to neutral aTGC (see Sec. 1.3). From a simple scaling of the expected event yields, it can be expected to reach the sensitivity to the SM contribution to neutral aTGC during the High Luminosity phase of LHC, when the luminosity collected will reach about 3000 $\text{fb}^{-1}$.

The effect of some categories of beyond the SM physics has been translated in terms of aTGC in [24]. For example, for some particular parameters of the Minimal Supersymmetric Standard Model (MSSM) theory, the effect on neutral aTGC would be of the same order than the effect coming from the SM contribution. During the High Luminosity phase of LHC, it will be then possible to constrain such model parameters.

# Chapter 5

# Timing studies for the phase 2 upgrade

Timing is of particular interest in data-taking period with high luminosity, when the number of proton-proton collisions in the same bunch crossing is expected to be very high. This chapter presents a study on the use of calorimetric timing information to mitigate the effect from pileup (PU) at high luminosity. Timing could be exploited for the association of photons, electrons and jets to their collision vertices, for particle identification, or to reject energy deposits coming from pileup vertices.

The chapter is divided in three sections. Sec. 5.1 summarizes the High Luminosity LHC project, Sec. 5.2 presents the electromagnetic calorimeter (ECAL) shower timing studies, and finally Sec. 5.3 shows the improvement in the reconstruction testing different time resolution scenarios.

## 5.1 The High Luminosity LHC

The LHC has been exploring the high-energy frontier since 2010, producing proton-proton collisions at the centre-of-mass energy of 7 and 8 TeV. In 2012 the LHC has delivered to CMS about 25 fb$^{-1}$ of integrated luminosity and has reached approximately 75% of its nominal instantaneous luminosity. From 2015 to 2024 new runs of data-taking will collect about 300 fb$^{-1}$ of integrated luminosity, reaching twice the nominal instantaneous luminosity.

Afterwards, to extend its discovery potential and/or characterize any new signal possibly discovered, the LHC will need a major upgrade to increase its instantaneous luminosity by a factor of 10 beyond its design value, this period is also referred to as the LHC phase 2 period. The high-luminosity project of LHC (HL-LHC) [78] installation will start approximately in

2024 and general-purpose experiments are expected to reach about 3000 $\mathrm{fb}^{-1}$ of integrated luminosity each in ten years.

Fig. 5.1 illustrates the increase of integrated and instantaneous luminosity and center-of-mass energy at LHC over the years.

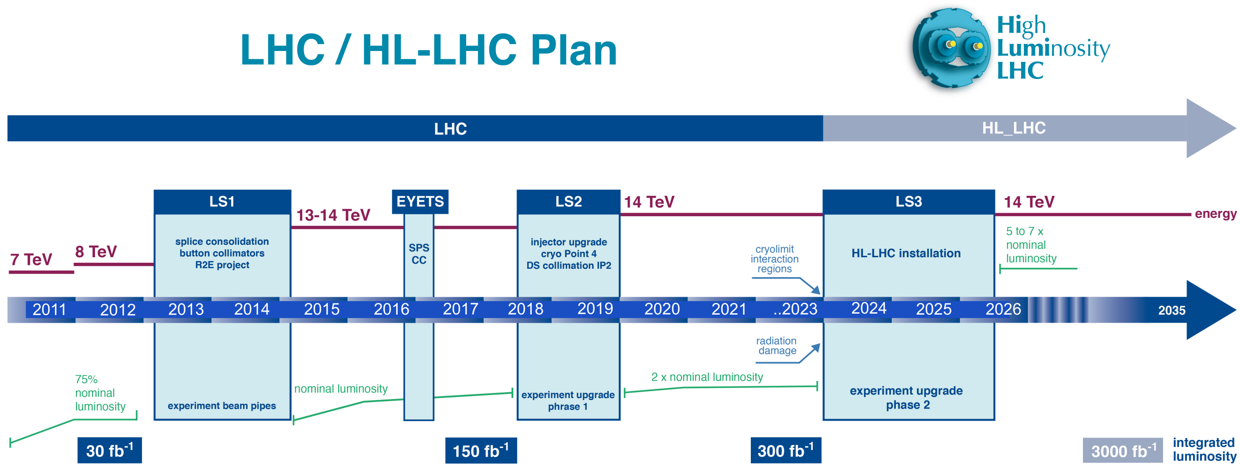


Figure 5.1: Increase of integrated and instantaneous luminosities and center-of-mass energy at LHC over the years.

One of the main challenges of the LHC at phase 2 is the increase of PU events, from the averaged number of 21 (for 2012 data) to about 200 (expected at HL-LHC). The increase of PU interactions will be an issue for triggering events, for the object reconstruction, and for all the physics objects isolation quantities. It is therefore fundamental to tag and remove the extra activity from PU interactions in order to correct the measurement of the relevant variables.

The tracker information is the most effective way to associate particles to different primary vertices, but it is limited by the PU activity (charged particles) in the tracker acceptance. The complementary use of precise calorimeter timing measurement to associate the reconstructed particles to their collision vertices [79, 80] has been investigated. This method can be used for both charged and neutral particles.

The studies discussed in this section show how the reconstruction performance improves when adding the time information. While the specific technology to be used for this purpose is not discussed in details, there are few possible options to be investigated, as for example Microchannel Plate [81], Micro Pattern Gas Detector [82], or Micro-Pattern Device [83]. For instance, a preshower detector containing one or more layers of Microchannel Plates could replace the current preshower in the endcap region, providing a time measurement with a time resolution up to 30 ps. These options will be presented in a scope document by the end of December 2015, that will complement the technical proposal for HL-LHC [84].

In order to properly evaluate the impact of the timing, studies based on simple emulation of a possible timing detector could not be used. This is because the effect of low energy interactions due to particles from pile up cannot be emulated in a simple fashion. In addition the energy deposits and their timing profile is not trivial for hadronic showers. The strategy has been then to use full simulation. Instead of inserting an alternative detector for timing, the present ECAL detector and geometry were used. At this stage we care more of the general characteristics of timing. It has been first studied the time profile of photons, jets, and a minimum ionizing particles into an active material. The material used is the $PbWO_4$ of the ECAL crystals, because of the easy access to the shower development through the Geant4 simulation.

From these studies, described in Sec. 5.2, it has been extracted a single time measurement to be associated to each particle crossing the ECAL. Sec. 5.3 shows how this additional information can be exploited to improve the object reconstruction and to mitigate the impact of PU:

- It could provide an alternative vertex determination, based on pure timing information, with a O(cm) resolution. This is particularly relevant in events with low track multiplicity (e.g. $H \to \gamma\gamma$), where the vertex cannot be precisely determined with tracking information;

- A time requirement can be also used to reduce the ECAL occupancy, removing the energy deposited in a time not compatible to the one of a particle coming from the hard interaction. This may have important consequences in many respects: reduction of event size, improvement of photon and jet energy resolution;

- The timing information of the ECAL energy deposits belonging to a jet can be used to implement a tagging algorithm aimed to identify jets which are not originating from the hard interaction.

Even if a time measurement is expected to be of particular utility at high $\eta$, because of the higher pileup occupancy and the absence of the tracker, the following studies will consider particles lying in both the ECAL barrel and endcaps. The reason for not considering only the endcap region is to provide a comparison between the performance using time and the performance using the tracker information in a region where both are fully efficient.

## 5.2 ECAL shower timing studies

We discussed in Sec. 3.2.2 the detector simulation program called Geant4 [52]. When a particle enters the ECAL, its interaction with the crystals is simulated with the Geant4 program. Multiple information is stored. The only one relevant for this studies is represented by the single particle interaction, called *Geant Step*. Each Step can be seen as an energy deposit in a given position at a given time. The full energy deposit of the particle, which can be for instance represented by an electromagnetic shower or energy loss by a charges particle, is made of several Geant Steps. The shower development in space and time can be then studied from the analysis of these Steps.

In order to determine how the particles behave, samples with a single photon ($\gamma$), electron ($e$), muon ($\mu$), pion ($\pi^-$, $\pi^+$), jet per event have been generated. For each particle type, samples with different transverse momenta have been created (from 3 to 50 GeV).

For this basic study, in all samples used in this section the vertex position has been fixed to the geometrical center of CMS, the tracker has not been included into the geometry (to avoid photon conversions), and pileup interactions have not been generated. Since all crystals are similar, each particle does not have any strong dependence on the entrance point into the crystal, each particle has been generated towards the center of a specific crystal in the ECAL barrel corresponding to $\eta = 0.135$ and $\phi = -0.041$ coordinates. In the following, every time a particle has been generated with such coordinates, it will be referenced as generated *toward the central barrel*.

To study the shower propagation inside the ECAL crystals, events with a single photon with a $p_T$ of 50 GeV have been generated towards the central barrel. Fig. 5.2 (top) shows the Geant Step multiplicity for a single photon event into the transversal section of the ECAL barrel. The $x$ and $y$-axis of the plot correspond to $X$ and $Y$ reference axes of CMS (see Sec. 2.2.1), while the $z$-axis shows the Geant Steps occupancy. Back-scattered particles produce some interactions in the surrounding ECAL crystals. Fig. 5.2 (bottom) shows the same view for a single jet event with a $p_T$ of 80 GeV generated with a different angle $\phi$.

Fig. 5.3 (left) shows the depth of Geant Steps with respect to the front-face of the crystal. The time distribution, where the zero corresponds to the time of the particle creating a the primary vertex, is presented in Fig. 5.3 (right). Both distributions have been weighted by the energy deposit of the Geant Step. It can be noted that the maximum of the energy deposit occurs after 8 cm, i.e. 7-8 radiation lengths. The shower starts at about 4.3 ns, that corresponds to the time the photon needs to reach that particular region of the detector, which is 130 cm far from the hard interaction. The depth corresponding to the first interaction of the photon inside the crystal should follow a decreasing exponential distribution

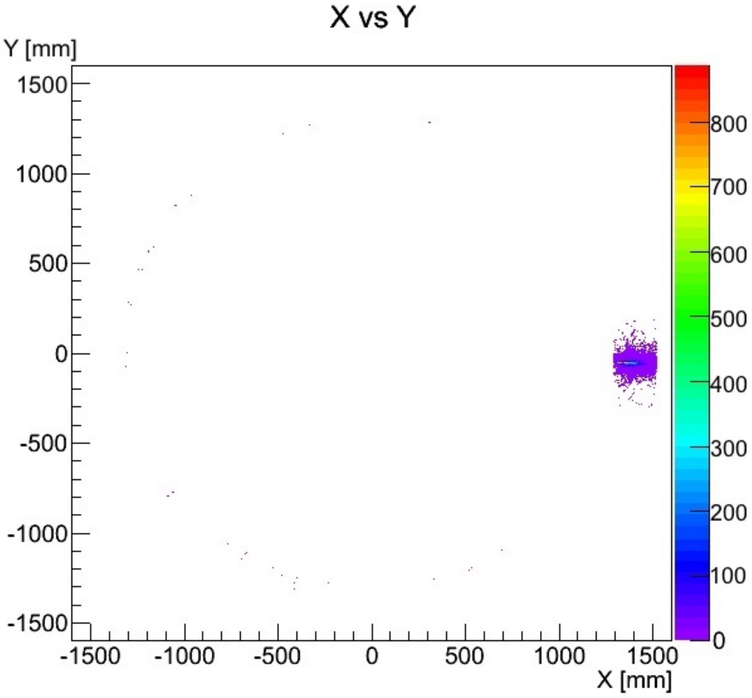


Figure 5.2: Hits multiplicity into the transversal section of the ECAL barrel in case of a single photon event (top), generated toward the central barrel with a $p_T$ of 50 GeV, and a single jet event (bottom), generated with a $p_T$ of 80 GeV and a different $\phi$. The $x$ and $y$-axis of the plot correspond to $X$ and $Y$ reference axis of CMS, while the $z$-axis shows the Geant Steps occupancy. Back-scattered particles produce some interactions in the surrounding ECAL crystals.

with a $\tau$ that represent the photon conversion length, that can be approximated with $\frac{9}{7}$ of the electron radiation length $X_0$ in the for $PbWO_4$, which is 0.89 cm. This distribution has been fitted with an exponential distribution in Fig. 5.4; the $\tau$ parameter from the fit is 1.2 cm, in agreement with the expected value.

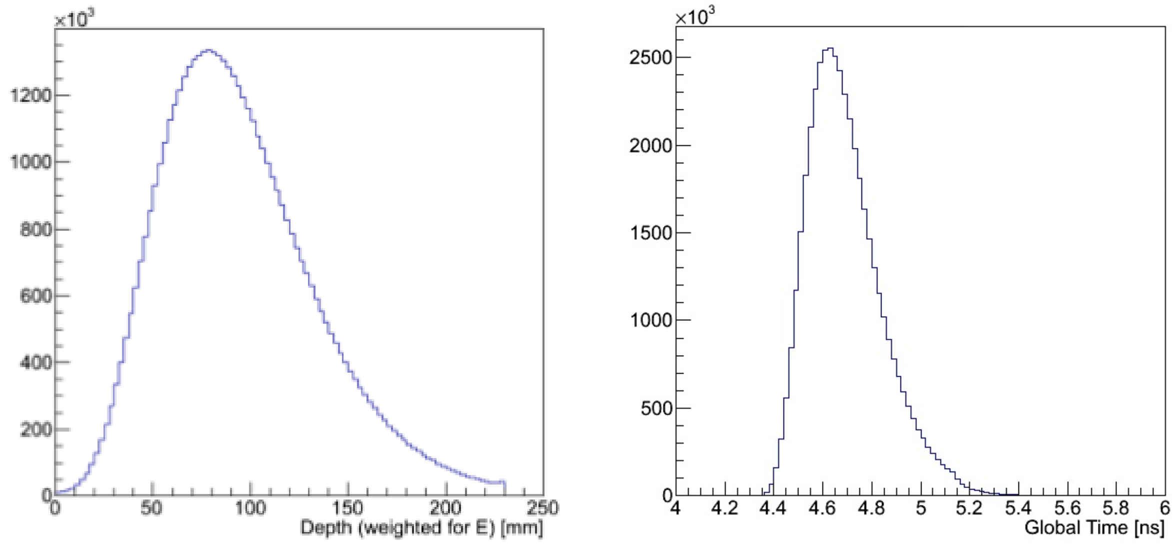


Figure 5.3: Distribution of the depth of every Geant Step, weighted by the energy deposit, starting from the front-face of the crystal (left). Time distribution of every Geant Step, weighted by the energy deposit, where zero defines the time of the hard interaction (right). Both plots refer to one single photon event generated toward the central barrel with a $p_T$ of 50 GeV.

The velocity of the shower along the longitudinal and transversal directions is an important information that can be used to characterize the shower for different objects. We analyse the events dividing the crystals in 1 cm layers along the depth. For each cell the mean time of the Geant Steps, weighted by the energy deposit, has been computed. Fig. 5.5 (left) shows that the longitudinal velocity of the shower corresponds to the speed of light (shown as the red line), that is 0.03 $\frac{\text{cm}}{\text{ps}}$. Fig. 5.5 (right) shows the velocity along the transversal side ($\Delta R$ from the shower axis). As expected, the transversal velocity was found to be quite lower than the speed of light (about 0.02 $\frac{\text{cm}}{\text{ps}}$ after the first crystal).

In Fig. 5.6 the averaged time on all the Geant Steps has been computed for each crystal, in order to see how the shower propagates from crystal to crystal. All the crystal times refer to the time of the central crystal.

The time measured in a real time detector, independently from the specific technical choice, strongly depends on the amount of material in front of the detector, and the amount of active material collecting the energy deposition. To study these two effects, we now use

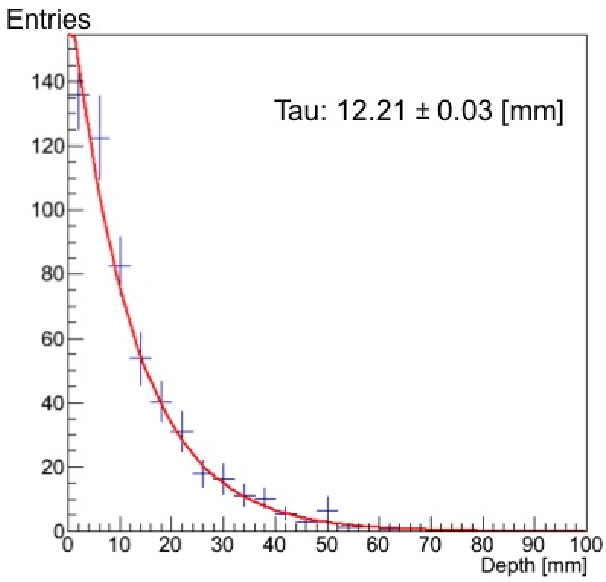


Figure 5.4: Depth distribution of the first interaction of the incoming photon into the crystal. The origin of the depth measurement starts from the front-face of the crystal. The plot refers to single photon events generated toward the central barrel with a $p_T$ of 25 GeV.

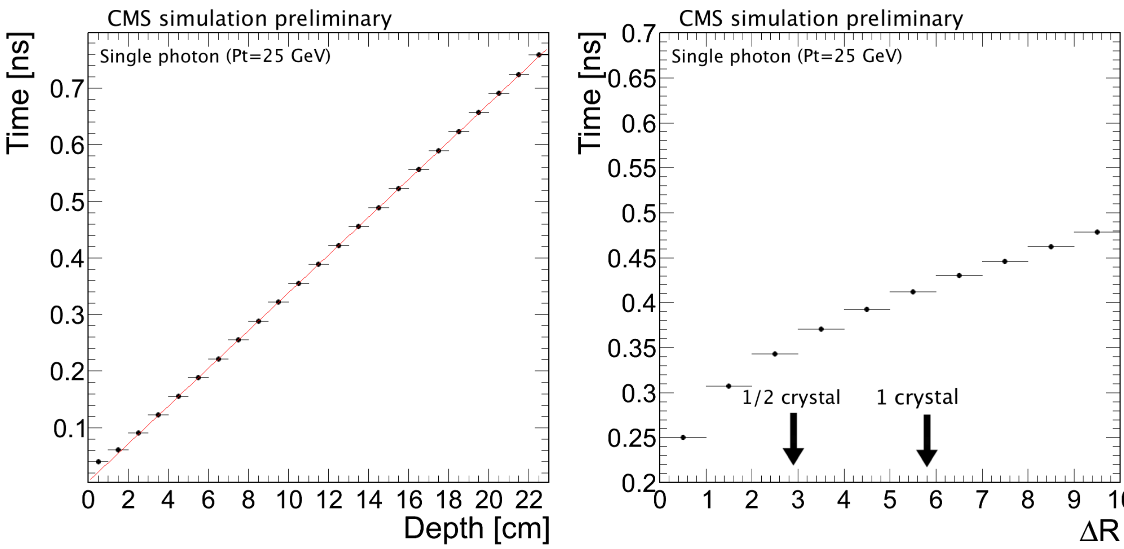


Figure 5.5: ECAL shower development along the longitudinal (left) and transversal (right) direction. On the left plot, the cells are layers of one cm along the depth. On the right plot, the cells are layers in interval of $\Delta R$ from the central axis of the shower, where each bin is $\Delta R = 0.03$ and 3 bins are about half of a crystal (1.1 cm). The plots refer to single photon events with a $p_T$ of 25 GeV in the central barrel.

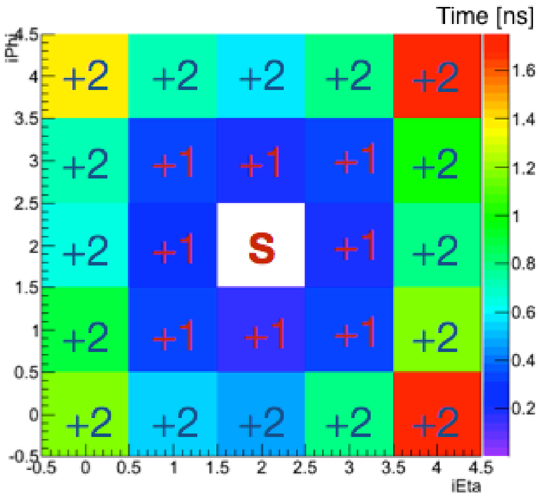


Figure 5.6: Average time, computed weighting all the Geant Steps time for the energy deposit, for each crystal of a shower, for one single photon event with a $p_T$ of 25 GeV in the central barrel. All the crystal times refer to the time of the central crystal.

the times associated to the Geant Steps to define a single time value for each ECAL crystal. This single time is defined as the time average of all the Geant Steps, weighted by the energy deposited into a region of the crystal. There are several ways to define a region where the average of the Geant Steps are performed: it could be the whole crystal, but also different longitudinal or transversal segmentations. Each choice has a different time resolution. The time resolution is defined simulating thousands of single photons events with a $p_T$ of 25 GeV in the central barrel, and measuring the time for each event. The RMS of the time distribution will be referred to as the time resolution.

The first segmentation studied corresponds to the whole crystal. The time resolution in this configuration, computed as just described, is about 45 ps and it is shown in Fig. 5.7. There are two effects contributing to this value. The first contribution is introduced from the fact that each photon starts showering at slightly different depth inside the crystal, as shown in Fig 5.4; this causes a shift on the shower distribution, and introduces a fluctuation on the mean time measured. The second contribution arises from the fact that even if two showers start at the same depth, they will have always a different evolution. This can be observed in Fig. 5.8, where five single-photon events with a $p_T$ of 25 GeV have been generated toward the same central barrel crystal. Their Geant Steps have been corrected to reproduce showers starting at the same time in the front face of the same crystal.

We then evaluated the time resolution using different longitudinal segmentations. In this configuration the crystal is divided longitudinally in layers with the same transversal size of

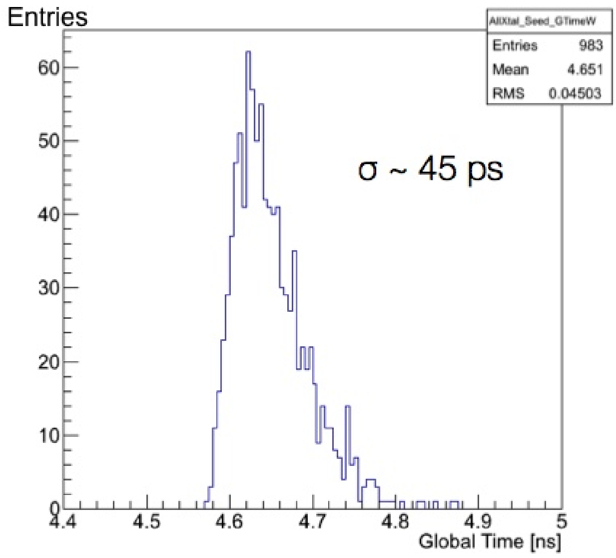


Figure 5.7: Distribution of the average of the Geant Step time value for about one thousand single-photon events with a $p_T$ of 25 GeV in the central barrel. The 45 ps RMS of the distribution represents the time resolution related to the configuration that use the whole crystal to estimate the time measurement.

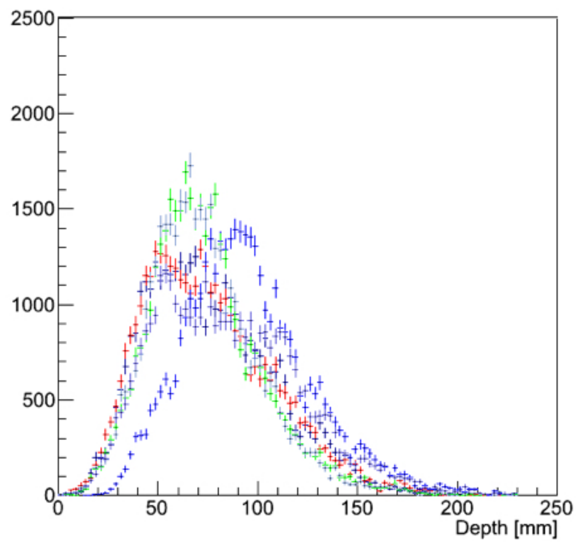


Figure 5.8: Depth, from the front face of the crystal, of all the Geant Steps forming the electromagnetic shower of five single-photon events with a $p_T$ of 25 GeV, generated in the same central barrel crystal. Different colors correspond to different single-photon events. All the depths have been corrected in order to simulate a photon showering exactly from the front face of the crystal.

the crystals and with a thickness ranging between 1 mm to 3 cm. The time can be extracted in each layer, and therefore the time resolution can be measured as a function of the depth.

In Fig. 5.9 this time resolution is shown as a function of the depth. Different colors correspond to different thickness values for the layers. The best time resolution is measured after 7 or 8 radiation lengths, corresponding to the maximum development of the shower. Already after few centimeters the intrinsic time resolution is below 10 ps. Comparing different thicknesses we notice an interplay between two effects. On one hand the number of Geant Steps collected by a layer is smaller in finer layers, affecting statistically the mean time computed. On the other hand the largest layers are more sensitive to the shower fluctuations, as in the case of the whole crystal. The layer that represents the best compromise between these two effects corresponds to the 1 cm layer.

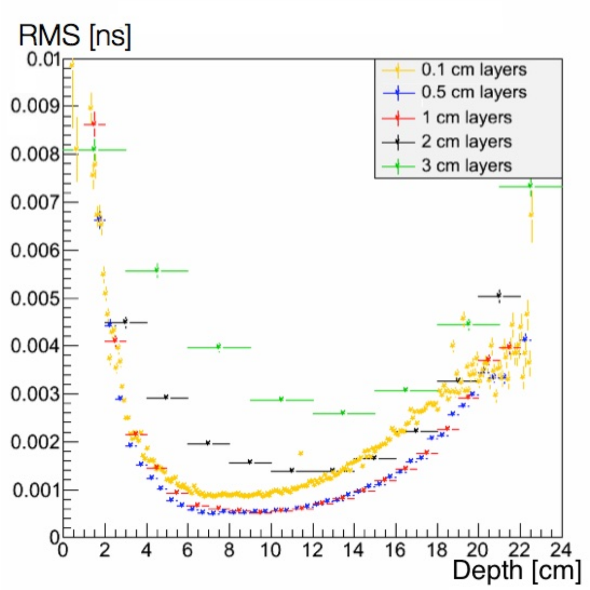


Figure 5.9: Time resolution obtained in different layers as a function of the depth for single-photon events produced toward the central barrel with a $p_T$ of 25 GeV. Different colors correspond to different layer thickness.

The segmentation of 1 cm layers has been used also in the case of positive charged single-pion events, generated in the central barrel with a $p_T$ of 25 GeV, (Fig. 5.10, left). The distribution has been compared to single-photon events with the same $p_T$ and $\eta$ (Fig. 5.10, right). Given that the charged pion starts the hadronic shower at different depths (or can even pass the crystal without interacting hadronically) while it is ionizing, the time distribution is much wider, compared to the photon one.

Once the thickness and the position of the layer in the crystal has been chosen, respectively 1 cm and 8 $X_0$, the study has been repeated with different incoming energies for

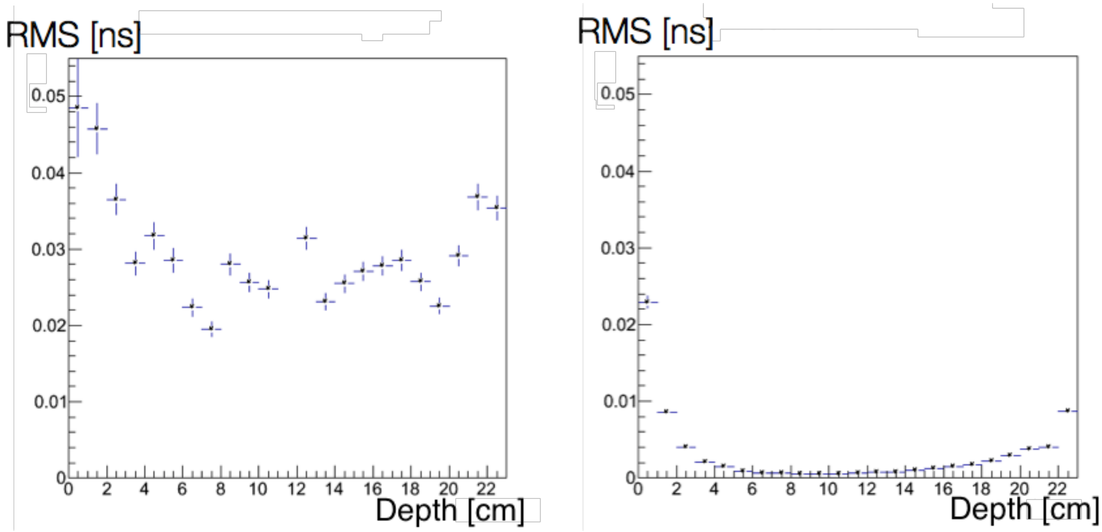


Figure 5.10: Time resolution measured at different depth in one cm layers for positive charged single-pion events (left) and for single-photon events (right). Both plots refer to events with one particle generated toward the central barrel with a $p_T$ of 25 GeV. The error bars represent the statistical error of the time resolution.

single-photon events. Fig. 5.11 shows the best time resolution obtained using 1 cm layers, (left) for photons with different $p_T$ (3, 10, 25 and 50 GeV). The same distribution is presented taking the resolution always from the sixth layer (right).

To better understand the worsening of the time profile introduced by the transversal propagation of the shower, the crystal has been segmented into $\Delta\eta$ and $\Delta\phi$, starting from the axis that represents the center of the shower energy deposition. Such configuration does not offer a good time resolution (Fig. 5.12) compared to the longitudinal segmentation, since the shower fluctuations described in Figs. 5.7 and 5.8 are not removed. However the transversal profile of the shower could offer a precious information for particle identification. An example of this is shown in Fig. 5.13, where the mean time measured in each transversal cell is shown for a photon and a jet. As it can be observed, the photon shower is originated from a single object spreading into the crystals. The jet instead, is composed of different particles, that reach the ECAL at the same time, leading to a time profile flat in the transversal direction. The transversal time profile can thus helps in particle identification.

The studies presented in this section give important information about the time profile of electromagnetic and hadronic showers, and they can help in the future choice of a time detector, and in the choice of its segmentation and position. The time profile versus the depth is close to the speed of light, but the shower development in the transversal plane is slower. The best longitudinal segmentation to estimate the time of a shower is around 1 cm, that represents a good compromise between the statistics collected and the minimiza-

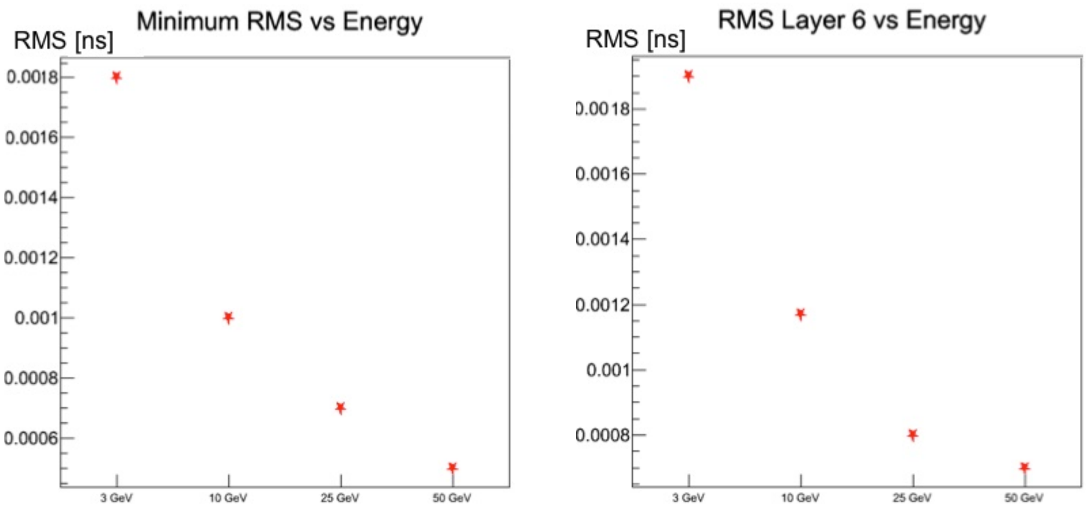


Figure 5.11: Time resolution for photons with different $p_T$ (3, 10, 25 and 50 GeV) in the central barrel. The time resolution is obtained using one-centimeter layers and taking the layer corresponding to the minimum resolution (left) and corresponding always to the sixth layer (right).

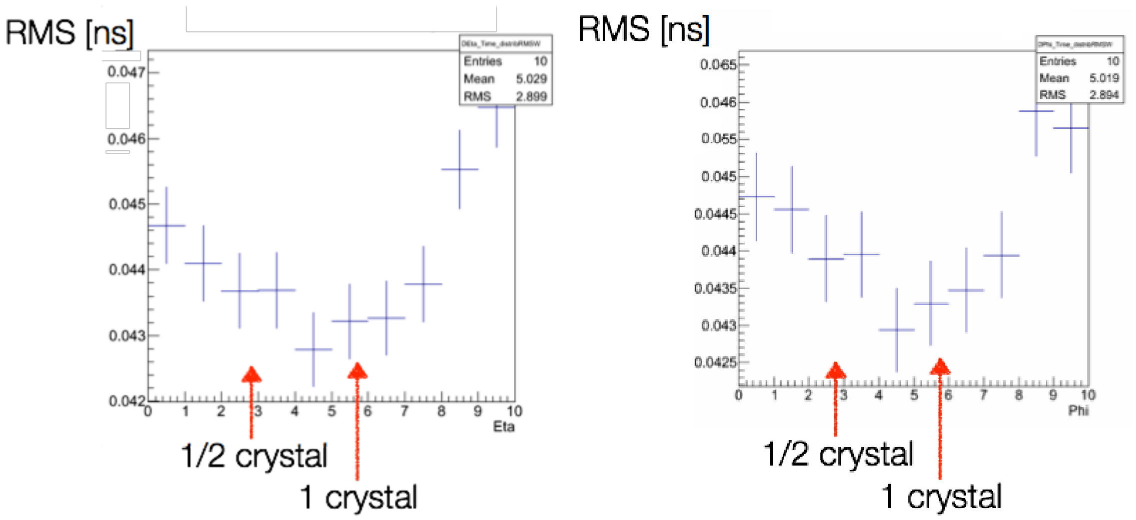


Figure 5.12: Time resolution measured in different transversal layers as a function of $\eta$ (left) and $\phi$ (right) for single-photon events produced toward the central barrel with a $p_T$ of 25 GeV.

tion of the shower deposit fluctuation. The best place to estimate the time is after 7 or 8 radiation lengths, where the shower is at the maximum of its development. Already after few centimeters, the intrinsic time resolution is below 10 ps. The lateral profile is different in the case of single-photon, single-jet, and single-pion events, and this information could help for particle identification. Selecting the averaged Geant time in one-centimeter layer

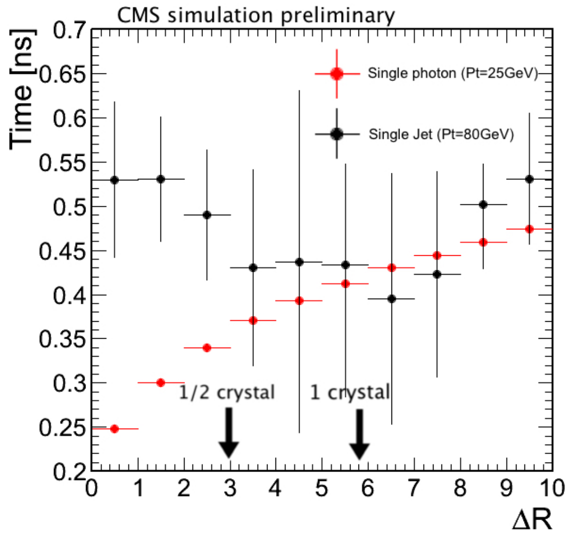


Figure 5.13: Mean time measured in each transversal cell for one single-photon event (red line) compared to one single-jet event (black line).

at the shower maximum, we are able to link each ECAL crystal to a time measurement. As we mentioned before, during HL-LHC the time measurement will come from a dedicated detector, with a time resolution of the order of tens of ps. The improvement on the particle reconstruction and pileup mitigation strongly depends on the time resolution will be achieved. In order to quantify the benefits of a time measurement as a function of the time resolution achieved, we will smear the time estimated from the ECAL crystals, and we will compare the reconstruction performances for different time resolutions.

## 5.3 Reconstruction performance using timing

In this section we present the improvement obtained adding a timing information to the reconstruction and particle identification algorithms. In this case a full simulation of the CMS detector has been used. The impact of the photon conversions due to the tracker presence on the time estimation has been found negligible. In Sec. 5.3.1 we study the determination of the the z-vertex position, in $H \to \gamma\gamma$ events, using the time associated to the photons from the $H$ boson decay. In Sec. 5.3.2 we show the pileup mitigation obtained with a selection based on the time associated to the jets, using a sample of multi-jet events from QCD processes with 20 additional pileup vertices. In Sec. 5.3.3, we show how to reduce the ECAL occupancy removing the energy deposit with a time not compatible with the one of a particle coming from the hard interaction. Finally in Sec. 5.3.4, we use the time information to correct the energy of the photons from the $H$ boson decay for the pileup contribution, improving the resolution in the $H$ boson mass measurement.

### 5.3.1 Vertex reconstruction

In processes where the number of charged particles from the primary interactions is limited (e.g. $H \to \gamma\gamma$), a precise time associated to neutral particles could help in the $z$ vertex position determination. Since each vertex produced in the bunch crossing is created at a different time, the occurrence time of the hard interaction ($T_0$) is an additional parameter that has to be determined. For this purpose $H \to \gamma\gamma$ events ($m_H = 125$ GeV) with 20 additional PU vertices have been generated.

The CMS reconstruction process has been modified to save for each crystal the time extracted from Geant as described in the previous section (using the average time of all the Geant Steps in the crystal material between 7 and 8 cm depth).

As shown in Fig. 5.6, the lateral propagation of the shower introduces a delay in the time of the shower. To avoid such effect, for the future we will refer to the time of an object, as the time associated to the most energetic ECAL crystal belonging to the object (further referred to as seed). This allows to associate a photon, to a time with a resolution of few ps. This is shown in Fig. 5.14 left, where the time of flight (TOF), that represents the time for a photon to travel from the vertex to the ECAL, and the time of the vertex creation $T_0$, have been subtracted.

Fig. 5.14 (right) shows the true z-position of the vertex on the x-axis, compared to the one derived from a minimization that takes as inputs the times and the positions of the energy deposits of the two seeds of the photon showers. The function that has been minimized is the following:

$$\chi^2(z, T_0) = \frac{(T_{meas,1} - T_{expec,1}(z, T_0))^2}{\sigma_T^2} + \frac{(T_{meas,2} - T_{expec,2}(z, T_0))^2}{\sigma_T^2} \tag{5.1}$$

where $T_{meas}$ represents the time measured, $T_{expec}$ represents the time expected from a particle coming from a vertex created at $T_0$ and in $z$ along the beam axis, and $\sigma_T$ is the resolution on the time.

A real detector will have a time resolution much larger than the ideal one we obtained from Geant. For this reason the time extracted from the simulation has been smeared in order to test the vertex resolution as a function of a realistic time resolution. The smearing is performed by using a Gaussian distribution centered on the reconstructed time value, with a width corresponding to the time resolution to be tested.

Two parameters can be extracted from the minimization: the $H \to \gamma\gamma$ z-vertex position

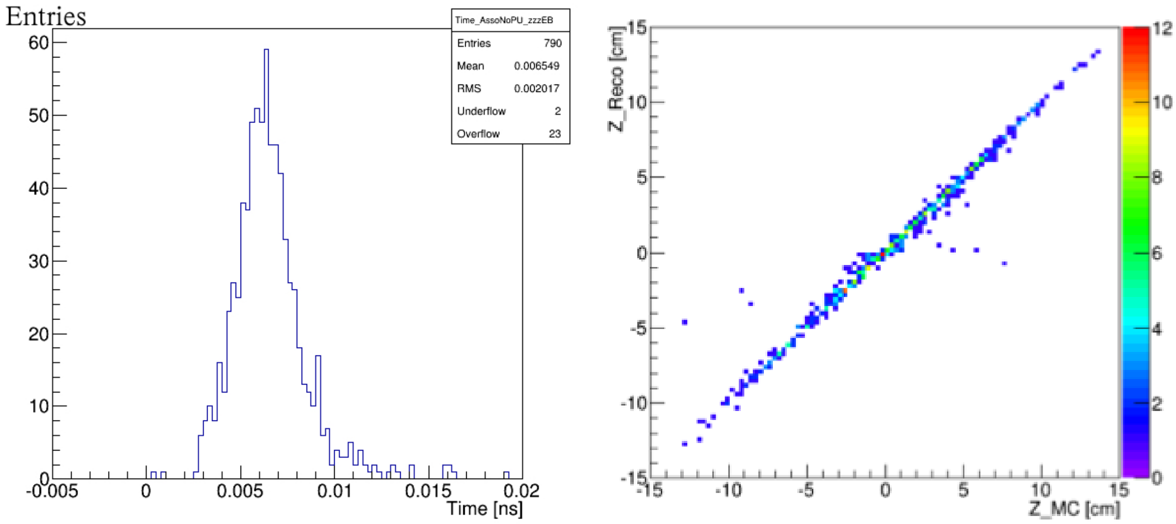


Figure 5.14: Time of the seeds of the two photons from the $H$ boson decay, where the time for a photon to travel from the vertex to the ECAL has been subtracted (left). The true z-position of the vertex compared to the z-position derived from the time of the seed crystals from the two photon showers (right).

and the time of the interaction $T_0$. In Fig. 5.15, the vertex resolution as a function of the time resolution is shown fixing $T_0$ to the correct values (left) or letting $T_0$ free to vary (right) for $H \to \gamma\gamma$ events with additional 20 pileup vertices. The figure shows inclusively photons reconstructed into the ECAL barrel and endcaps. Letting $T_0$ free causes a degradation of the resolution by a factor $\sqrt{2}$.

In general, different performances are expected for photons emitted in the barrel and endcap directions. At high $|\eta|$, the $z$ vertex position resolution is expected to improve, since the difference in time due to different $z$ positions of the vertices increase as $z \propto cos(\theta)$. In Fig. 5.16 the vertex resolution as a function of the time resolution is given separately for events with the two photons in the barrel (left) and with at least one photon in one endcap (right). For a time resolution of 25 ps, we obtain a resolutions on the $z$ vertex position of 0.82 cm for photons in the barrel and 0.62 cm for events with at least one photon in one endcap. These studies have been performed also generating 70 and 140 simultaneous PU interactions, proving that the results are stable with the number of pileup activity in the event.

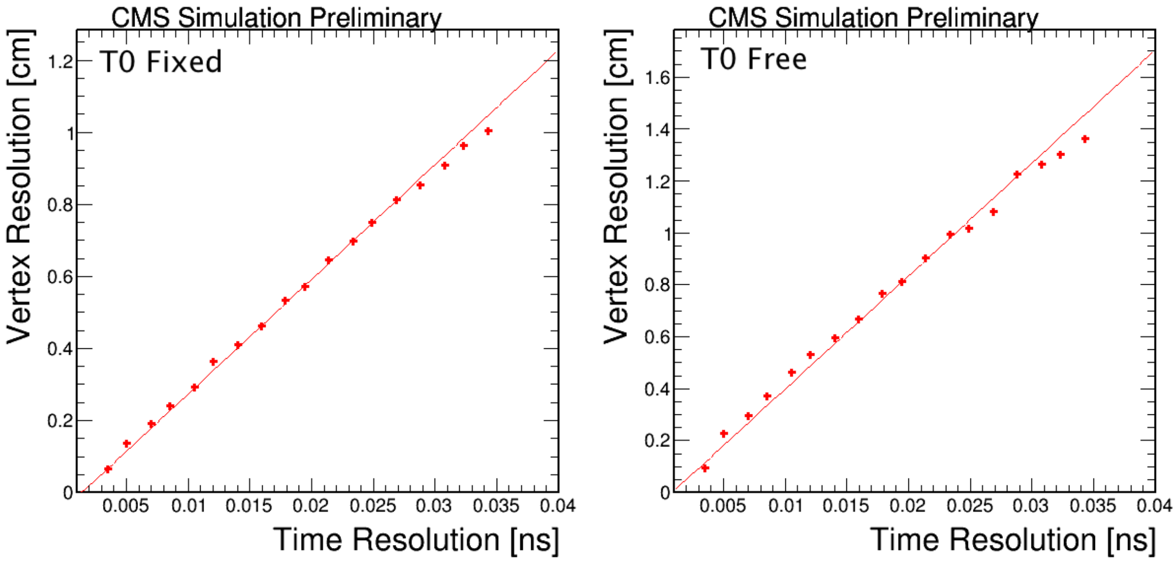


Figure 5.15: Z vertex position resolution as a function of the time resolution, that runs from few ps to 40 ps. The $T_0$ parameter is fixed to the true value (left), and free to vary and extracted from the minimization (right). The figure shows inclusively photons reconstructed into the ECAL barrel and endcap.

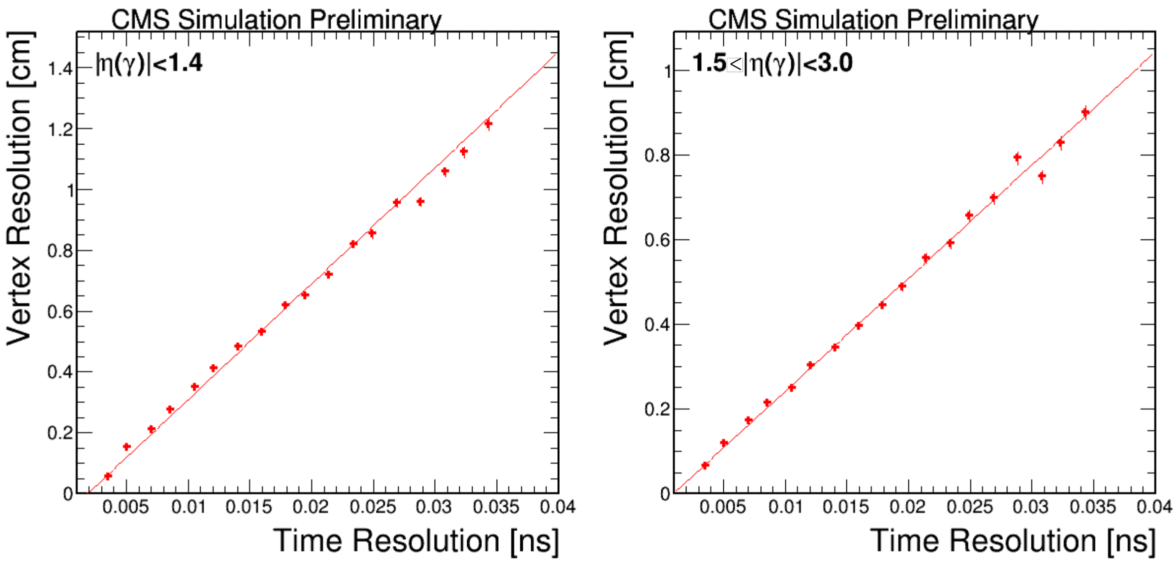


Figure 5.16: Z vertex position resolution as a function of the time resolution, that runs from few ps to 40 ps, for events with the two photons in the barrel (left) and with at least one photon in one endcap (right) [80]. The T0 parameter is fixed to the true value.

### 5.3.2 Removal of pileup jets

The time associated to the electromagnetic component of a jet can discriminate between jets coming from the hard interaction (signal) and the others coming from PU interactions (background). Once again the time associated to a jet is the time of the most energetic crystal belonging to its electromagnetic component. A sample of multi-jet events from QCD processes (referred to as QCD sample) with 20 additional pileup vertices has been generated in a $p_T$ range from 80 to 120 GeV for the initial partons. A cut of 20 GeV on the jet $p_T$ is applied to the reconstructed jets.

The time distribution for the jets from the hard collision (red), and for the pileup jets (blue), are shown in Fig. 5.17 for jets in the barrel (left) and in the endcaps (right). The signal distribution starts from zero, since the TOF for a particle traveling at the speed of light and coming from the primary vertex has been subtracted. Pileup jets have a much larger distribution due to the spread of the vertex position. This effect is more visible in the endcaps since the difference in time due to different $z$ positions of the vertices increase as $z \propto cos(\theta)$. The time resolution considered here is of few picoseconds.

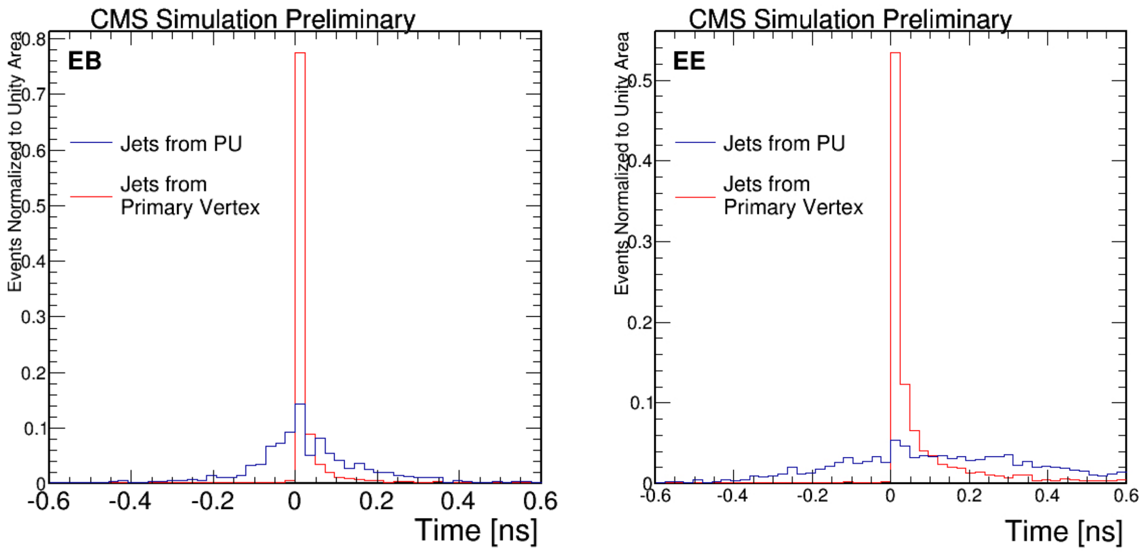


Figure 5.17: Time distribution for the most energetic crystal of jets from hard interaction (red) and from PU (blue) considering only jets in the barrel (left) and endcaps (right).

A selection based on timing is implemented. A simple window around the maximum of the signal distribution in Fig. 5.17 is defined. The width of the window is varied and the performance of the selection is studied plotting the signal efficiency, as a function of the background efficiency, for different selections in a distribution called Receiver Operating Characteristic (ROC) curve. Since the time distribution for the signal has a tail on the right, the time window used for the selection is not symmetric around zero. The efficiencies are computed as the number of jets passing a selection based on time, over the total number of jets.

The time selection has been compared to algorithms that use the reconstructed tracks, that is the most accurate information available. For a tracker based selection two different variables have been used. The $\beta^*$ variable, that represents the fraction of tracks inside a jet not pointing to the hard interaction, and the $pR$ variable, that represents the ratio between the sum of the $p_T^2$ of the tracks inside a jet, weighted by the square of distance in $\Delta r$ from the hard interaction, divided by the sum of the $p_T^2$ of all the tracks in the jet. They are defined as:

$$\beta^* = \frac{\sum trk(jet)_{PU}}{\sum trk(jet)_{all}} \quad ; \quad pR = \frac{\sum p_{Ti}^2 \Delta r_i^2}{\sum p_{Ti}^2} \tag{5.2}$$

where $\sum trk(jet)_{PU}$ is the number of tracks not pointing to the hard interaction, $\sum trk(jet)_{all}$ is the total number of tracks in the jet, $p_{Ti}$ is the transverse momentum of the track $i$, and $\Delta r_i$ is the distance of the track $i$ from the hard interaction. The ROC curves are obtained with a selection on $\beta^*$ required to be lower than a value between 0 and 1, while for $pR$ the selection requires the variable to be lower than a value between 0 and 0.5, that represents the cone width used to reconstruct the jets.

In Fig. 5.18 the ROC curves for $\beta^*$ and the time selection are shown for different $\eta$ regions. The plots show that in the region covered by the tracker, the timing is not able to compete to the variable based on tracks, in terms of rejection. On the other hand, in the forward region, at high pseudorapidity values ($|\eta|$) the limited tracker acceptance makes the timing much more useful. In Fig. 5.19 the time selection is compared at high $|\eta|$ with the $\beta^*$ (left) and the $pR$ (right) variable selections.

The advantage of using the time selection is that it is not limited by the tracker acceptance and not restricted to charged particles. These results show that the timing information is complementary to the one from the tracker. To further support this conclusion the background rejection, has been studied after fixing the signal efficiency to the value of 90%. It can be noted in Fig. 5.20 that for large pseudorapidities the rejection drops for the tracker method (left) while it stays quite flat for the timing algorithm (right).

The study has been also repeated varying the resolution of the time detector, up to 400ps. For each resolution value the pileup jet rejection has been studied using a selection that keeps the signal efficiency at about 85%. Fig. 5.21 shows the background rejection as a function of the time resolution. Up to 30 ps, the performances are not dramatically affected by the resolution, while at higher smearing the pileup jet rejection decreases substantially.

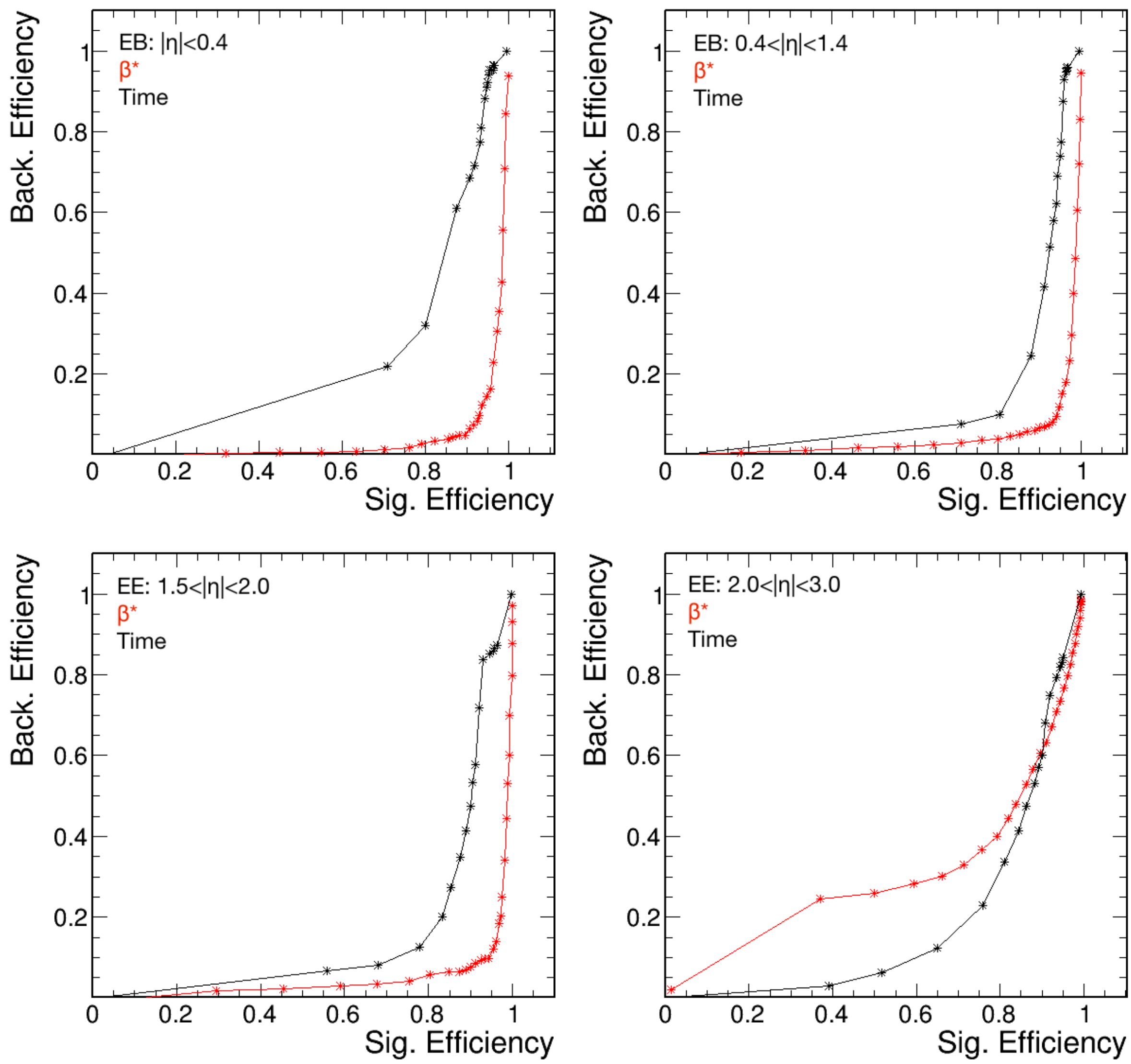


Figure 5.18: Different ROC curves for various $|\eta|$ regions. For each point a different selection has been used and the signal and background efficiency has been computed using the $\beta^*$ variable and the time information.

### 5.3.3 Occupancy reduction through time selection

A time selection can be used to perform a crystal cleaning by not measuring those with a time incompatible with the one from particles coming from the hard interaction.

We generated a $H \to \gamma\gamma$ sample ($m_H$ = 125 GeV) with and without 140 additional PU interactions. The $\Sigma E_t$ variable has been computed in both cases. The $\Sigma E_t$ variable is defined as the scalar sum of all the energy deposits in the electromagnetic calorimeter. Fig. 5.22 shows the $\Sigma E_t$ distribution in blue for the sample without PU and without any

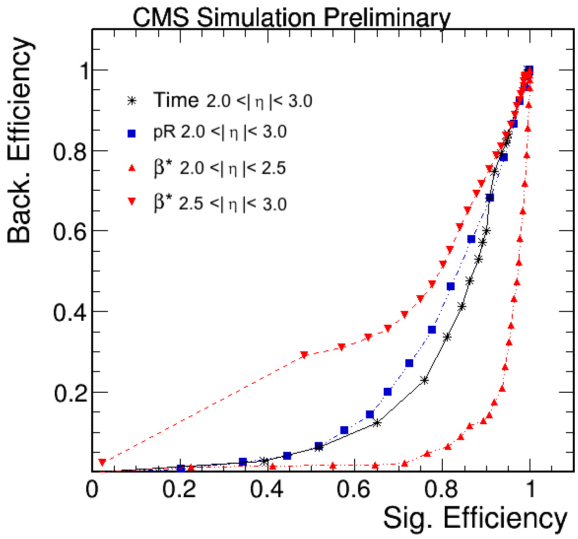


Figure 5.19: Different ROC curves for various $|\eta|$ regions. For each point a different selection has been used and the signal and background efficiency has been computed using the $\beta^*$ variable and the time information.

time selection, while the same distribution after the time selection is shown in red. The time selection simply consists in removing from the $\Sigma E_t$ computation the crystals with an energy deposit with a time outside a window of 90 ps around the expected time from a particle coming from the hard interaction. When there are no extra PU energy deposits, the two distributions are close, proving that the time requirement does not affect the signal hits. The $\Sigma E_t$ distribution for the signal with 140 PU is shown by the black distribution. A clear increase in occupancy is observed due to the activity from the pileup interactions. Applying the same time window on the 140 PU sample, we obtain the green distribution, thus reducing the occupancy significantly. In this study the time measurement has a resolution of 50 ps, in order to simulate a realistic detector. No pileup from previous bunch crossing (called out-of-time pileup) has been included in these studies.

### 5.3.4 H boson mass resolution in the $H \to \gamma\gamma$ channel

The contribution coming from PU interactions is quite isotropic, thus a bias in the ECAL cluster energy reconstruction is expected. This is due to the overlapping of PU hits to the main cluster of crystals of the electromagnetic shower (super cluster SC).

As introduced in Sec. 3.4.3, a super cluster is formed by several basic clusters of crystals. Analysing the time of each seed of the clusters contained in the SC, it is possible to remove the energy deposits not compatible with the hard interaction, cleaning the SC from the pileup contribution that otherwise would have been included into the photon energy.

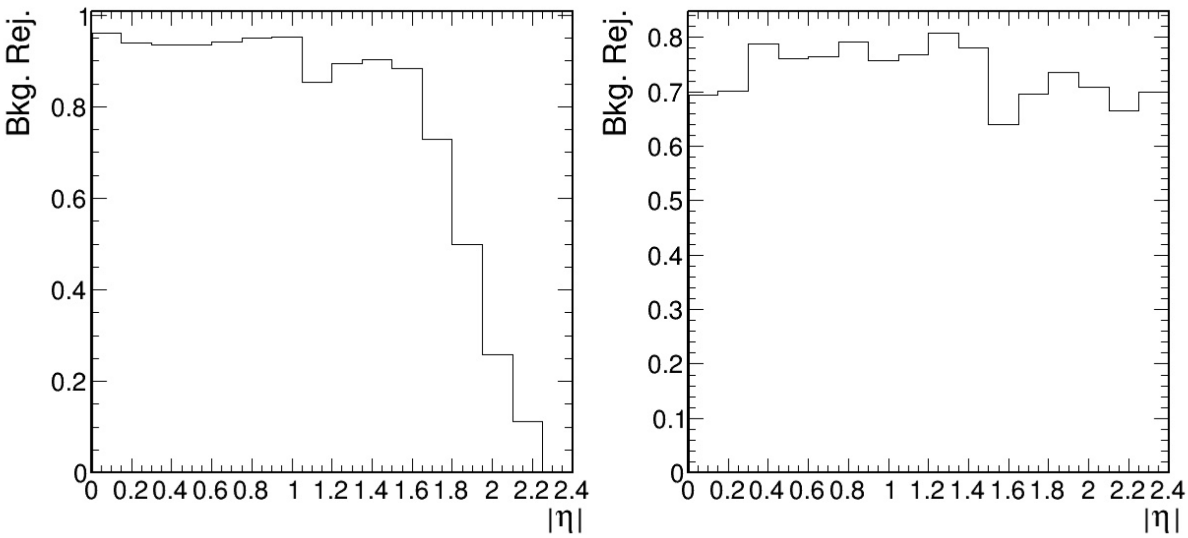


Figure 5.20: Pileup jet rejection as a function of $|\eta|$ for a signal efficiency fixed at 90%, for the selection based on the tracker (left), and on the time of the jets (right). The $p_T$ cut applied on the reconstructed jet is 20 GeV.

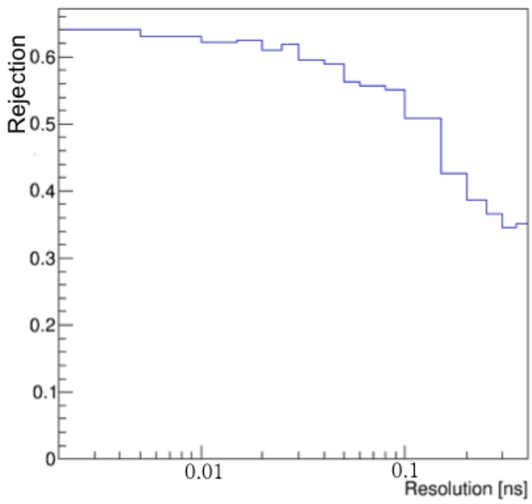


Figure 5.21: Pileup jet rejection as a function of the time resolution, for a selection that provide a QCD multi-jet signal efficiency of about 85%. The $p_T$ cut applied on the reconstructed jet is 20 GeV.

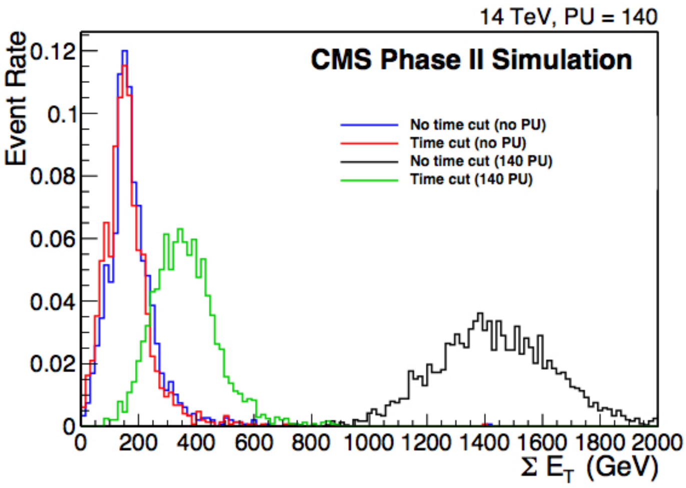


Figure 5.22: Distribution of the $\Sigma E_t$ variable for the $H \to \gamma\gamma$ process. The blue distribution is for a sample without PU and without any time selection, while the red curve represents the same distribution after the time selection. The $\Sigma E_t$ distribution for the signal with 140 PU is shown in back, and in green after the time selection. In this study the time measurement has a resolution of 50 ps, and the out-of-time PU has not been included.

For each cluster forming the super cluster, the time of the seed has been selected. If such time is contained into a time window of 180 ps around the expected time for a particle coming from the hard interaction, the cluster is kept. Otherwise the cluster is removed from the super cluster and the photon energy is recomputed.

Fig. 5.23 shows the fit to the $\gamma\gamma$ invariant mass before (left) and after (right) the super cluster cleaning procedure, in the case of no additional pileup. The distribution used for the fit to the mass distribution is a convolution of a Gaussian with a Chebyshev polynomial of second order. The mass distribution with and without the time selection looks very similar, proving that the time selection does not affect the photon energy if pileup is not present. In Fig. 5.24 the same selection has been applied on photons from the $H$ boson decay in the case of additional 140 PU interactions. As it can be seen, the time selection improves the mass resolution, and it brings the mass distribution mean closer to the simulated $H$ boson mass.

The same improvement can be seen looking at the distribution of the ratio of the reconstructed photons energy over the simulated one. In Fig. 5.25, the time selection is applied on a sample with no additional PU, proving once again that it does not affect the photons energy if pileup is not present. In Fig. 5.26, the time selection is applied on a sample generated with 140 additional pileup vertices. The resolution on the photon energy improves as a consequence of the pileup mitigation.

It is important to notice that the photon energy reconstruction algorithm used in this studies has not been tuned properly using a multivariate analysis, and thus the mass reconstructed could shift from the generated values.

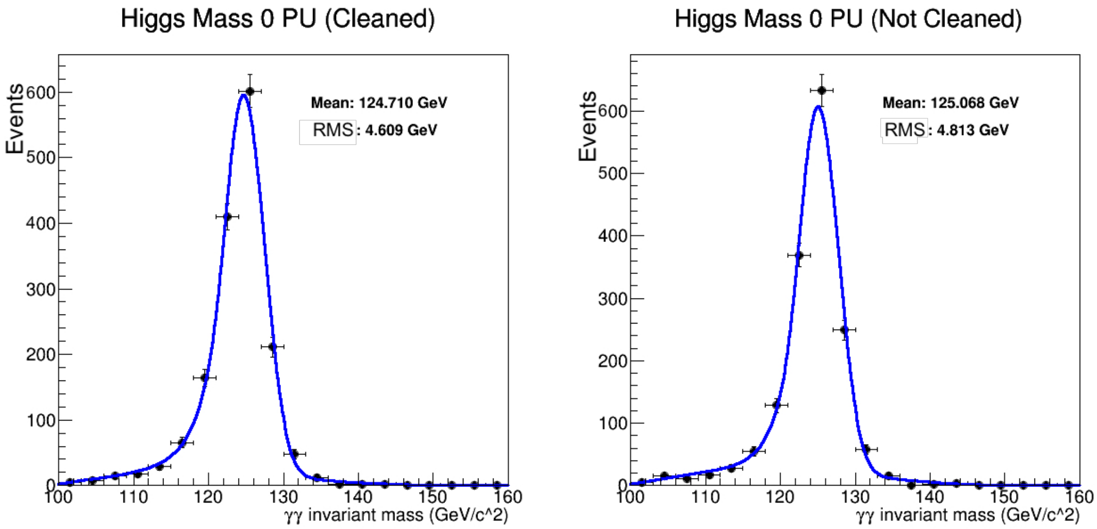


Figure 5.23: Fit to the $\gamma\gamma$ invariant mass with the super cluster cleaning procedure (left) and without (right) for a $H \to \gamma\gamma$ sample with no pileup.

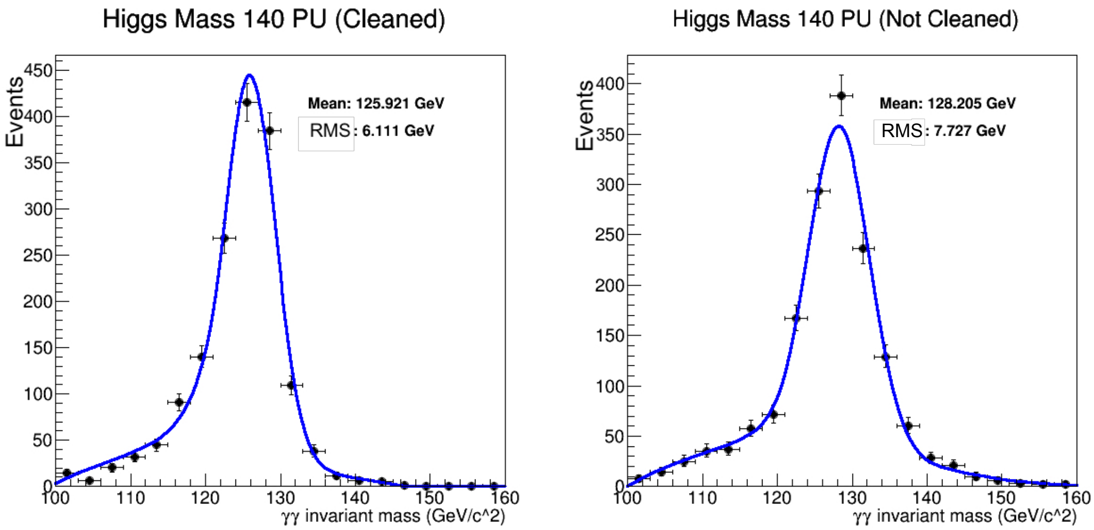


Figure 5.24: Fit to the $\gamma\gamma$ invariant mass with the super cluster cleaning procedure (left) and without (right) for a $H \to \gamma\gamma$ sample with 140 pileup interactions.

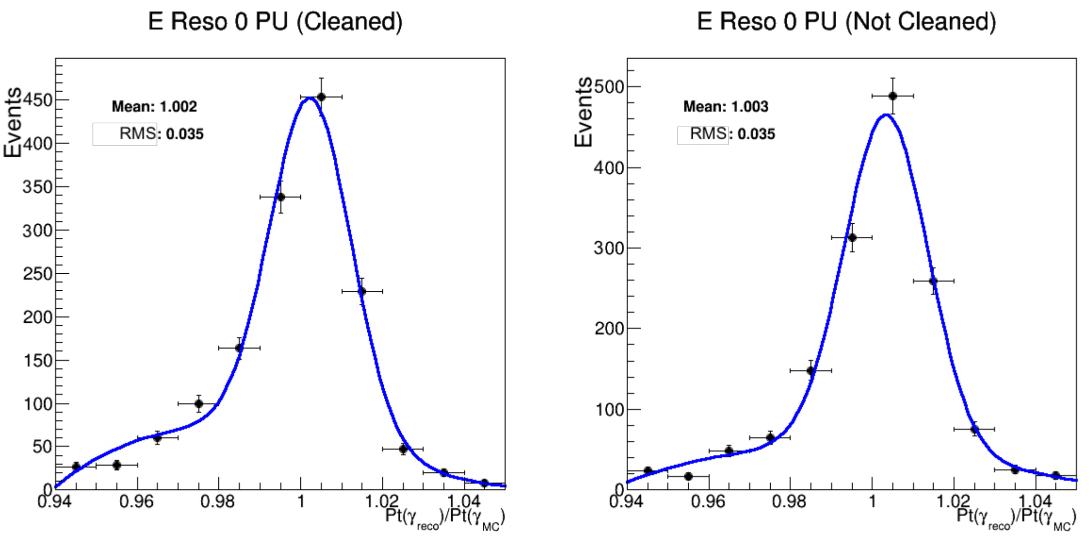


Figure 5.25: Fit to the photon energy resolution with the super cluster cleaning procedure (left) and without (right) for a $H \to \gamma\gamma$ sample with no pileup.

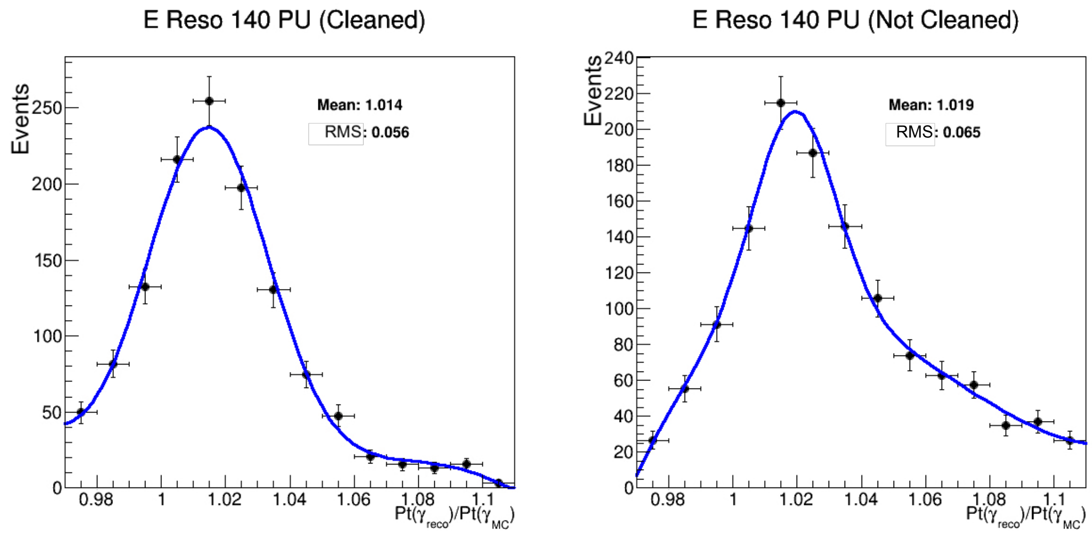


Figure 5.26: Fit to the photon energy resolution with the super cluster cleaning procedure (left) and without (right) for a $H \to \gamma\gamma$ sample with 140 pileup interactions.

## 5.4 Results and discussion

In these studies the selection used to reject pileup simply looks at the time associated to the object reconstructed. The complementarity of the time information with respect the tracker information admits the possibility to improve further the pileup mitigation combining the two information, for instance creating a multivariate analysis based on the time and tracker information, or adding the time measurement in the Particle Flow clustering algorithm. These investigations represent the next step in understanding the use of the timing information in the object reconstruction. The current results are already very promising, and motivate further studies on the use of timing in high pileup environment.

# Chapter 6

# Conclusions

We presented a measurement of the $Z$ boson pair production cross section using proton-proton collisions at 7 and 8 TeV center-of-mass energy. The $ZZ$ production cross section has been measured via the decay channel $ZZ \rightarrow 2l2\nu$. The data sample selected for our study corresponds to about 5.1 fb$^{-1}$ of integrated luminosity at 7 TeV, and about 19.6 fb$^{-1}$ at 8 TeV.

The data are selected requiring two isolated leptons of the same flavor (electrons or muons) with high transverse momentum ($p_T$). Events containing jets or additional leptons are vetoed, and additional cuts on the dilepton $p_T$, on the dilepton invariant mass, and on the transverse momentum imbalance are applied.

The main backgrounds for this measurement are the $Z/\gamma + jet$ process, the fully leptonic $t\bar{t}$ and single-top decay, and the $WW$ and $WZ$ diboson processes.

The backgrounds estimation represents the main challenge for this analysis. The $Z/\gamma{+}jet$ process has no neutrinos in the final state, but its cross section at the $Z$-peak is four orders of magnitude larger than the $ZZ$ production. Since the high $E_T^{miss}$ in $Z/\gamma + jet$ events is due to misreconstruction of physical objects, and is not well described by simulation, a high statistic control sample has to be used in order to model these tails from data.

The fully leptonic $t\bar{t}$, the single-top decay, and the $WW$ process have been estimated in a control sample obtained requiring exactly one electron and one muon in the final state. The $WZ$ process instead, has been estimated directly from the simulation.

The $\sigma(\mathrm{pp} \rightarrow ZZ)$ cross sections have been found to be $5.1^{+1.5}_{-1.4}\,(\mathrm{stat})\,^{+1.4}_{-1.1}\,(\mathrm{syst}) \pm 0.1\,(\mathrm{lumi})$ pb at 7 TeV, and $7.2^{+0.8}_{-0.8}\,(\mathrm{stat})\,^{+1.9}_{-1.5}\,(\mathrm{syst}) \pm 0.2\,(\mathrm{lumi})$ pb and 8 TeV, in agreement with theory calculations $6.2^{+0.3}_{-0.2}$ pb at 7 TeV and $7.6^{+0.4}_{-0.3}$ pb at 8 TeV, when correcting for the NLO QCD and EWK effects.

A search for anomalous triple gauge couplings (aTGC) involving the $ZZ$ final state is then performed on the very same data. In the search for aTGC, the shape of the distribution of a discriminating variable (e.g. the $Z$-boson $p_T$) has been used to derive limits on aTGC parameters, with the frequentist construction CLs. The knowledge of the $p_T$ shape distribution is fundamental to separate the contribution from standard model $ZZ$ and new physics. For this reason, a particular attention has been dedicated to the computation of the systematic error introduced on the signal $p_T$ distribution by the jet veto. Furthermore, NLO electroweak corrections have been applied to the signal simulation, since they become relevant for high $Z$-boson transverse momentum.

Finally, the $ZZ \to 2l2\nu$ final state data have been combined with the $ZZ \to 2l2l'$ final state, to increase the sensitivity on the aTGC parameters. In the absence of signs of new physics we have set limits on the relevant aTGC parameters.

The limits on the anomalous neutral trilinear $ZZZ$ and $\gamma ZZ$ couplings derived in $2l2\nu$ and $4l$ analysis are consistent at 95% C.L. with zero. The two channels have the same sensitivity to aTGC, nevertheless an under-fluctuation of data in the $2l2\nu$ analysis causes the observed limits to be tighter than the ones derived in the $4l$ analysis. Combining the two analyses, the limits improve by about 30%. The combined results represent the most stringent limits ever published.

In the last chapter of the thesis, we presented a simulation study on the use of timing in the reconstruction, in the context of High Luminosity LHC. The results obtained are a proof of principle of the utility of timing for the object reconstruction, and they motivate more specific studies simulating specific time detectors.

It has been shown that a 30 ps resolution on the time measurement would allow to extract the vertex position with a resolution of the order of the centimeter, and to reject jets coming from PU interactions with a rejection factor of about three. It has been shown how to decrease the ECAL occupancy with a selection simply based on the time of the ECAL energy deposits. Finally, an improvement on the $H$ boson mass resolution has been shown, obtained with the removal of pileup contribution to the photon clusters.

The improvements shown in the object reconstruction are appreciable, even with very basic use of timing. The complementarity of the time information with respect to the tracker information allows to further improve the pileup mitigation combining the two information. For instance it is possible to create a multivariate analysis on the time and tracker information, or include the time measurement in the clustering algorithm. The current results are already very promising, and motivate further studies on the use of timing in high pileup environment.

# List of Figures

# List of Tables

# References


[1] C. Bailey, "The Greek Atomists and Epicurus," Chicago Press, vol. 13, p. 123, 1929, link. 4

[2] D. Rouvray and R. B. King, "The periodic table: into the 21st Century," Researcher Studies Press, vol. 83, p. 48, 2005, link. 4

[3] J. Buchwald and A. Warwick, Histories of the electron : the birth of microphysics. MIT Press, 2001, link. 4

[4] P. J. Nahin, "Maxwell's grand unification," IEEE Spectrum, vol. 29, p. 45, 1992, link. 4

[5] W. N. Cottingham and D. A. Greenwood, An Introduction to the Standard Model. Cambridge, 2003, link. 4

[6] The LHC Project, "LHC Machine," JINST 3, S08001, 2008, link. 4, 21, 22, 23, 150, 159

[7] F. Englert and R. Brout, "Broken Symmetry and the Mass of Gauge Vector Mesons," Phys. Lett., vol. 13-9, pp. 321–323, 1964, link. 5, 7

[8] P. W. Higgs, "Broken Symmetries and the Masses of Gauge Bosons," Phys. Lett., vol. 13-16, pp. 508–509, 1964, link. 5, 7

[9] CMS Collaboration, "Observation of a new boson at a mass of 125 GeV with the CMS experiment at the LHC," Phys. Lett., vol. B716, p. 30, 2012, link. 5

[10] ATLAS Collaboration, "Observation of a new particle in the search for the Standard Model Higgs boson with the ATLAS detector at the LHC," Phys. Lett., vol. B716, p. 1, 2012, link. 5

[11] S. Weinberg, "A model of leptons," Phys. Lett., vol. 19, p. 1264, 1967, link. 7

[12] A. Salam, S. Weinberg, and J. Goldstone, "Broken Symmetries," Phys. Lett., vol. 127, p. 321, 1962, link. 7

[13] K. Hagiwara et al., "Probing the weak boson sector in $e^+e^- \to W^+W^-$," Nucl. Phys. B, vol. 282, p. 253, 1987. 10

[14] Y. Ashie et al., "Evidence for an oscillatory signature in atmospheric neutrino oscillation," Phys. Rev., vol. 93, p. 101801, 2004, link. 10

[15] A. G. Riess et al., "Observational Evidence from Supernovae for an Accelerating Universe and a Cosmological Constant," The Astronomical Journal, vol. 116, p. 3, 1998, link. 10

[16] C. W. John M. Campbell, R. Keith Ellis, "Vector boson pair production at the LHC," JHEP 10 018, vol. 1107, 2011, link. 11, 14, 48, 50, 96, 109, 159

[17] A. Bierweiler, T. Kaspriz, and J. H. Kuhn, "Vector-boson pair production at LHC to O($\alpha^3$) accuracy," JHEP 12 071, 2013, link. 11, 13, 14, 16, 17, 99, 150, 159

[18] J. C. Collins, D. E. Soper, and G. F. Sterman, "Factorization of Hard Processes in QCD," Adv. Ser. Direct. High Energy Phys., vol. 5, p. 1, 1989, link. 12

[19] S. D. Drell and T.-M. Yan, "Massive lepton-pair production in hadron-hadron collisions at high energies," Phys. Rev., vol. 25, p. 316, 1970, link. 12

[20] G. Altarelli and G. Parisi, "Asymptotic Freedom in Parton Language," Nucl. Phys., vol. B126, p. 298, 1977, link. 13

[21] J. Baglio, L. D. Ninh, and M. M. Weber, "Massive gauge boson pair production at the LHC: a next-to-leading order story," Phys. Rev. D88 (2013) 113005, 2013, link. 13, 14, 99, 150

[22] A. D. Martin, W. J. Stirling, R. S. Thorne, and G. Watt, "Parton distributions for the LHC," Eur. Phys., vol. C63, p. 189, 2009, link. 14

[23] J. Alwall, M. Herquet, F. Maltoni, O. Mattelaer, and T. Stelzer, "MadGraph 5 : Going Beyond," JHEP, vol. 1106, p. 128, 2011, link. 16, 48

[24] G. Gounaris, J. Layssac, and F. Renard, "New and standard physics contributions to anomalous Z and gamma selfcouplings," Phys. Rev., vol. D62, p. 073013, 2000, link. 17, 19, 20, 122, 150

[25] J. Alcaraz et al., "A Combination of preliminary electroweak measurements and constraints on the standard model," CERN PH EP-2006-042, 2006, link. 19, 20

[26] A. Robson, "Diboson Physics at the Tevatron," EPJ Web Conf., vol. 28, p. 06001, 2012, link. 19, 20

[27] D0 Collaboration, "Search for $ZZ$ and $Z/\gamma^*$ production in $p\overline{p}$ collisions at $\sqrt{s} = 1.96$ TeV and limits on Anomalous Couplings," Phys. Rev., vol. 100, p. 131801, 2008, link. 19, 20

[28] CMS Collaboration, "Measurement of the pp to ZZ production cross section and constraints on anomalous triple gauge couplings in four-lepton final states at $\sqrt{s} = 8$ TeV," Phys. Lett., vol. B740, p. 250, 2014, link. 19, 111, 114, 121, 122

[29] ATLAS Collaboration, "Measurement of $ZZ$ production in pp collisions at $\sqrt{s}$ =7 TeV and limits on anomalous $ZZZ$ and $ZZ\gamma$ couplings with the ATLAS detector," JHEP, vol. 03, p. 128, 2013, link. 19, 20

[30] CMS Collaboration, "The CMS experiment at the CERN LHC," JINST 3, S08004, 2008, link. 23, 25, 151

[31] ATLAS Collaboration, "The ATLAS Experiment at the CERN Large Hadron Collider," JINST 3, S08003, 2008, link. 23

[32] LHCb Collaboration, "The LHCb Detector at the LHC," JINST 3, S08005, 2008, link. 23

[33] ALICE Collaboration, "The ALICE experiment at the CERN LHC," JINST 3, S08002, 2008, link. 24

[34] CMS Collaboration, "The Magnet Project: Technical Design Report," Tech. Rep., 2008, link. 26

[35] CMS Collaboration, "The Tracker Project: Technical Design Report," Tech. Rep., 1998, link. 26

[36] CMS Collaboration, "Description and performance of track and primary-vertex reconstruction with the CMS tracker," JINST, vol. 9, no. 10, p. P10009, 2014, link. 27, 28, 55, 151

[37] CMS Collaboration, "The Electromagnetic Calorimeter Project: Technical Design Report," Tech. Rep., 1997, link. 29, 30, 31, 151

[38] CMS Collaboration, "Reconstruction of the signal amplitude of the CMS electromagnetic calorimeter," EPJ C, vol. 46, 2006, link. 33

[39] CMS Collaboration, "Performance of photon reconstruction and identification with the CMS detector in proton-proton collisions at $\sqrt{s}$ = 8 TeV," JINST, vol. 10, no. 08, p. P08010, 2015, link. 33, 34, 151

[40] CMS Collaboration, "The CMS electromagnetic calorimeter calibration during Run I: progress achieved and expectations for Run II," J. Phys., vol. 587, 2013, link. 35

[41] CMS Collaboration, "ECAL DPG Approved Results," Twiki, Created in 2012, link. 36, 151

[42] CMS Collaboration, "The Hadronic Calorimeter Project: Technical Design Report," Tech. Rep., 1997, link. 35, 38, 151

[43] CMS Collaboration, "Performance of the CMS hadron calorimeter with cosmic ray muons and LHC beam data," JINST, vol. 5, no. 10, p. T03012, 2008, link. 37

[44] CMS Collaboration, "Commissioning of the Particle-Flow reconstruction in Minimum-Bias and Jet Events from pp Collisions at 7 TeV," CMS PAS PFT-10-002, 2010, link. 38, 57, 60

[45] CMS Collaboration, "Determination of Jet Energy Calibration and Transverse Momentum Resolution in CMS," JINST, vol. 6, p. P11002, 2011, link. 38, 62, 101

[46] CMS Collaboration, "The Muon Project: Technical Design Report," Tech. Rep., 1997, link. 38, 39, 40, 41, 151

[47] CMS Collaboration, "The performance of the CMS muon detector in proton-proton collisions at $\sqrt{s}$ = 7 TeV at the LHC," JINST, vol. 8, p. P11002, 2013, link. 40

[48] CMS Collaboration, "Performance of CMS muon reconstruction in *pp* collision events at $\sqrt{s}$ = 7 TeV," JINST, vol. 7, p. P10002, 2012, link. 42, 54, 56, 57, 151

[49] CMS Collaboration, "CMS: The TriDAS project. Technical design report, Vol. 2: Data acquisition and high-level trigger," CERN/LHCC, vol. 026, 2002, link. 44, 151

[50] S. Alioli, P. Nason, C. Oleari, and E. Re, "A general framework for implementing NLO calculations in shower Monte Carlo programs: the POWHEG BOX," JHEP, vol. 1006, p. 043, 2010, link. 48

[51] T. Gleisberg, S. Hoeche, F. Krauss, M. Schonherr, S. Schumann et al., "Event generation with SHERPA 1.1," JHEP, vol. 0902, p. 007, 2009, link. 48

[52] S. Agostinelli et al., "GEANT4: A Simulation toolkit," Nucl.Instrum.Meth., vol. A506, pp. 250–303, 2003, link. 49, 126

[53] CMS Collaboration, "Validation and Tuning of the CMS Full Simulation," J. Phys., vol. 331, p. 032015, 2011, link. 49

[54] CMS Collaboration, "Standard Model Cross Sections for CMS at 7 TeV," Twiki, Created in 2011, link. 49, 51

[55] CMS Collaboration, "Standard Model Cross Sections for CMS at 8 TeV," Twiki, Created in 2012, link. 49, 51

[56] CMS Collaboration, "Measurement of the $W^+W^-$ Cross section in $pp$ Collisions at $\sqrt{s} = 7$ TeV and Limits on Anomalous $WW\gamma$ and $WWZ$ couplings," Eur. Phys. J., vol. C73, no. 10, p. 2610, 2013, link. 50, 51

[57] CMS Collaboration, "Measurement of the $W^+W^-$ cross section in pp collisions at $\sqrt{s}$ = 8 TeV and limits on anomalous gauge couplings," CMS-SMP-14-016, 2015, link. 50, 51

[58] CMS Collaboration, "Performance of electron reconstruction and selection with the CMS detector in proton-proton collisions at $\sqrt{s} = 8$ TeV," JINST, vol. 10, no. 06, p. 5, 2015, link. 54, 58, 80

[59] R. Fruhwirth, W. Waltenberger, and P. Vanlaer, "Adaptive vertex fitting," J. Phys., vol. G34, p. N343, 2007, link. 54

[60] W. Adam, F. Frühwirth, A. Strandlie, T. Todorov, "Reconstruction of electrons with the Gaussian-Sum-Filter in the CMS tracker at CMS," J. Phys., vol. G31, no. 9, p. 1, 2005, link. 58

[61] M. Cacciari, G. P. Salam, and G. Soyez, "The Anti-k(t) jet clustering algorithm," JHEP, vol. 0804, p. 063, 2008, link. 62

[62] M. Cacciari, "FastJet: A Code for fast $k_t$ clustering, and more," p. 487, 2006, link. 62

[63] CMS Collaboration, "Identification of b-quark jets with the CMS experiment," JINST 8, P04013, 2013, link. 63, 102

[64] D0 Collaboration, "$ZZ \to \ell^+\ell^-\nu\bar{\nu}$ production in $p\bar{p}$ collisions at $\sqrt{s} = 1.96$ TeV," Phys. Rev., vol. D78, p. 072002, 2008, link. 65

[65] K. Ackerstaff et al., "Search for anomalous production of dilepton events with missing transverse momentum in $e^+e^-$ collisions at $\sqrt{s} = 161$ GeV and 172 GeV," Eur. Phys., vol. C4, pp. 47–74, 1998, link. 65, 66

[66] CMS Collaboration, "Search for the standard model Higgs boson in the $H$ to $ZZ$ to 2 $\ell 2\nu$ channel in $pp$ collisions at $\sqrt{s} = 7$ TeV," JHEP, vol. 03, p. 040, 2012, link. 67

[67] CMS Collaboration, "Measurements of the $ZZ$ production cross sections in the $2\ell 2\nu$ channel in proton-proton collisions at $\sqrt{s} = 7$ and 8 TeV and combined constraints on triple gauge couplings," 2015, submitted for pubblication arXiv:1503.05467: link. 87, 107, 109, 110, 117, 121, 122, 153, 154

[68] M. R. Whalley and D. Bourilkov, "The Les Houches Accord PDFs (LHAPDF) and Lhaglue," hep-ph/0508110, p. 8, Aug 2005, link. 96

[69] M. Botje et al., "The PDF4LHC Working Group Interim Recommendations," 2011, submitted to Phys. Rev. link. 96

[70] H.-L. Lai et al., "New parton distributions for collider physics," Phys. Rev., vol. D82, 2010, link. 96

[71] A. Martin, W. Stirling, R. Thorne, and G. Watt, "Parton distributions for the LHC," Eur. Phys. J., vol. C63, pp. 189–285, 2009, link. 96

[72] R. D. Ball et al., "Impact of Heavy Quark Masses on Parton Distributions and LHC Phenomenology," Nucl. Phys., vol. B849, pp. 296–363, 2011, link. 96

[73] I. W. Stewart and F. J. Tackmann, "Theory Uncertainties for Higgs and Other Searches Using Jet Bins," Phys. Rev., vol. D85, p. 034011, 2012, link. 98

[74] The LHC Higgs Combination Group, "Procedure for the LHC Higgs boson search combination in Summer 2011," CERN, Geneva, Tech. Rep. CMS-NOTE-2011-005. ATL-PHYS-PUB-2011-11, Aug 2011, link. 98, 108, 116

[75] CMS Collaboration, "CMS Luminosity Based on Pixel Cluster Counting - Summer 2013 Update," CMS-PAS-LUM-13-001, 2013, link. 99

[76] G. Cowan, K. Cranmer, E. Gross, and O. Vitells, "Asymptotic formulae for likelihood-based tests of new physics," Eur. Phys., vol. C71, p. 1554, 2011, link. 108

[77] ATLAS Collaboration, "Measurement of the total $ZZ$ production cross section in proton-proton collisions at $\sqrt{s} = 8$ TeV in 20 fb1 with the ATLAS detector," Tech. Rep., 2013, link. 111

[78] M. Lamont, "LHC, HL-LHC and Beyond," PoS, vol. EPS-HEP2013, p. 149, 2013, link. 123

[79] CMS Collaboration, "Studies on a precision timing electromagnetic calorimeter for the CMS upgrade," CMS DN-14-006, 2014. 124

[80] D. del Re, "Timing performance of the CMS ECAL and prospects for the future," J. Phys., vol. 587, 2015, link. 124, 138, 157

[81] L. Pernié et al., "Response of microchannel plates to single particles and to electromagnetic showers," Nucl. Instrum. Meth., vol. A, p. 216, 2015, link. 124

[82] S. White, "RandD for a Dedicated Fast Timing Layer in the CMS Endcap Upgrade," Acta Physica Polonica, vol. B7, pp. 743–751, 2014, link. 124

[83] R. De Oliveira, M. Maggi, and A. Sharma, "A novel fast timing micropattern gaseous detector: FTM," 2015, submitted to Nucl. Instrum. Methods link. 124

[84] CMS Collaboration, "Technical Proposal for the Phase-II Upgrade of the CMS Detector," CERN, Geneva. Geneva, Tech. Rep. CERN-LHCC-2015-010. LHCC-P-008, 2015, link. 125